UC San Diego

UC San Diego Electronic Theses and Dissertations

Title

A study of local and global instabilities relevant to gas turbine combustors

Permalink

https://escholarship.org/uc/item/68s860mz

Author

Weng, Yue

Publication Date

2024

Peer reviewed|Thesis/dissertation

eScholarship.org Powered by the California Digital Library
University of California

UNIVERSITY OF CALIFORNIA SAN DIEGO

A study of local and global instabilities relevant to gas turbine combustors

A dissertation submitted in partial satisfaction of the
requirements for the degree
Doctor of Philosophy

in

Engineering Sciences (Aerospace Engineering)

by

Yue Weng

Committee in charge:

Professor Abhishek Saha, Chair
Professor Boris Krämer
Professor Jose I. Restrepo
Professor Antonio L. Sánchez
Professor Kalyanasundaram Seshadri

2024

Copyright

Yue Weng, 2024

All rights reserved.

The Dissertation of Yue Weng is approved, and it is acceptable in quality and form for publication on microfilm and electronically.

University of California San Diego

2024

DEDICATION

To my grandparents, Xianpeng Fu and Qiongxian Zhang, who sparked my dreams and set my sights on the sky.

EPIGRAPH

The Way that can be told of is not an Unvarying Way;
The names that can be named are not unvarying names.

— Lao Tzu
Tao Te Ching
(Arthur Waley Translation, 1934)

TABLE OF CONTENTS

Dissertation Approval Page . . . iii

Dedication . . . iv

Epigraph . . . v

Table of Contents . . . vi

List of Figures . . . ix

List of Tables . . . xiii

Acknowledgements . . . xiv

Vita . . . xvii

Abstract of the Dissertation . . . xviii

Chapter 1 Introduction to the Dissertation . . . 1
1.1 A brief overview of gas turbine engines . . . 1
1.2 Combustion instability in gas turbines . . . 2
1.3 Research focus of this work . . . 4

Part I Unsteady premixed flame: Experiments and time scale analysis . . . 7

Chapter 2 Assessing local statistics of a premixed turbulent Bunsen flame . . . 16
2.1 Introduction . . . 16
2.2 Methodologies . . . 20
2.2.1 Experimental Setup . . . 20
2.2.2 Characterization of conditions . . . 22
2.2.3 Choosing the appropriate thickness for conditioned average . . . 25
2.3 Results and discussion . . . 27
2.3.1 Flow statistics near the flamefront . . . 27
2.3.2 Local stretch rates . . . 30
2.3.3 Lagrangian statistics using flame particles . . . 34
2.3.4 Dispersion of flame particles and flamefront wrinkling . . . 37
2.4 Conclusion . . . 40

Chapter 3 Investigating polyhedral instability in a laminar Bunsen flame . . . 42
3.1 Introduction . . . 42
3.2 Experimental setup . . . 45
3.3 Results . . . 50
3.3.1 Regime Maps . . . 51
3.3.2 Morphology analysis . . . 55

3.3.3 Scaling of the the flow rate upper limit . . . 59
3.4 Conclusion . . . 62

Chapter 4 Investigating subharmonic bifurcation in a laminar thermoacoustic system . . . 65
4.1 Introduction . . . 65
4.2 Experimental setup . . . 68
4.3 Results . . . 72
4.3.1 Dynamical regimes of the system . . . 72
4.3.2 Dynamics of individual flame . . . 75
4.3.3 Recurrence Network analysis and asymmetric couplings . . . 79
4.3.4 The physical explanation of subharmonic oscillation . . . 82
4.4 Conclusion . . . 83

Part II Exploring thermoacoustic instability through a complex systems approach: Synchronization and modal analysis . . . 85

Chapter 5 Modeling thermoacoustic instability using the framework of synchronization: Laminar system . . . 89
5.1 Introduction . . . 89
5.2 Model Construction . . . 93
5.3 Experimental Study . . . 96
5.4 Results and discussions . . . 97
5.4.1 Bifurcation analysis . . . 97
5.4.2 Synchronization behavior of p and q . . . 104
5.4.3 Distinguishing chaotic state from strange nonchaotic attractors . . . 105
5.4.4 Summary and outlook . . . 110

Chapter 6 Modeling thermoacoustic instability using the framework of synchronization: Turbulent system . . . 111
6.1 Introduction . . . 111
6.2 Model construction . . . 116
6.3 Methodologies . . . 119
6.3.1 Experimental Details . . . 119
6.3.2 Multifractal Detrended Fluctuation Analysis . . . 121
6.4 Results and discussions . . . 122
6.4.1 The temporal transition from combustion noise to periodic oscillation 122
6.4.2 The variation in the RMS and dominant frequency of the pressure and the heat release rate fluctuations . . . 124
6.4.3 Synchronization characteristics . . . 126
6.4.4 Loss of multifractality during transition . . . 128
6.4.5 Power law in self-organization . . . 130
6.4.6 Summary and outlook . . . 133

Chapter 7 Detecting early warning signals of turbulent thermoacoustic systems using modal analysis 136
7.1 Introduction 136
7.2 Experimental details 139
7.3 Methods 140
7.4 Power Law of Self-Organization 148
7.5 Regime Separation in Singular Value Spectrum 150
7.6 Synchronization Analysis 151
7.7 Discussion 159

Bibliography 160

LIST OF FIGURES

Figure 1.1. Primary elements of a standard gas generator. 2

Figure 1.2. A schematic diagram illustrating the mechanism of thermoacoustic instability. 3

Figure 1.3. Burner nozzle before (left) and after (right) experiencing damage caused by thermoacoustic instabilities [1]. 4

Figure 1.4. The logical map of the thesis. 6

Figure 1.5. Regime diagram of premixed turbulent combustion provided by Borghi (left) and Williams (right). 15

Figure 2.1. Experimental setup: The schematic plot of the Bunsen burner and a sample Mie-scattering image of reactive flow. 21

Figure 2.2. The temperature profile and corresponding flame thickness of two flame conditions: 19% oxygen (left) and 21% oxygen (right). 23

Figure 2.3. The energy spectra of cold flow at different conditions. 25

Figure 2.4. The distribution of x coordinate of the edge from case $T_L O_L$ 26

Figure 2.5. Sensitivity analysis of u'/u' using data from case $T_L O_L$ 26

Figure 2.6. An example of conditioned statistics: Data from a point was recorded only when it lies within the zone of influence. 28

Figure 2.7. (a) Flame-conditioned r.m.s. u'_c (in m/s), (b) cold flow r.m.s. u' (in m/s), from condition $T_L O_L$. (c) The ratio of u'_c/u', along the mean flame location. 29

Figure 2.8. The PDFs of normalized tangential strain rate ($\tilde{K_t}$), normalized normal strain rate ($\tilde{K_n}$), and normalized stretch due to curvature ($\tilde{K_c}$). . . . 32

Figure 2.9. The variances of ($\tilde{K_t}$), ($\tilde{K_n}$), and ($\tilde{K_c}$) for different Karlovitz numbers (Ka). 32

Figure 2.10. Joint PDFs of different components of the stretch rate. The flame condition shown is $T_H O_L$ 33

Figure 2.11. Persistence time scale τ_{P,K_t}, τ_{P,K_n}, and τ_{P,K_c} for different conditions . 36

Figure 2.12. A schematic of tracking neighboring particles. 38

Figure 2.13. PDF profile of stretch factor ξ. 39

Figure 3.1. Experimental setups 46

Figure 3.2. Regime map for $H_2 - O_2 - N_2$ flames at fixed Le. 53

Figure 3.3. Regime map for $H_2 - O_2 - N_2$ flames at fixed T_b. 54

Figure 3.4. Samples of Mie-scattering images of a horizontal cross-section of polyhedral flames, the numbers of edges N are noted in the images. . . . 56

Figure 3.5. Stability map as function of Le and $\dot{Q}$ 58

Figure 3.6. $\tilde{\tau}_r/\tilde{\tau}_g$ as function of $\dot{Q}$ for (a) different ϕ and (b) T_b based on the scaling analyses. $\dot{Q}$ corresponding to $\tilde{\tau}_r/\tilde{\tau}_g = 1$, refers to the theoretical estimation of $\dot{Q}_{\max}$. 61

Figure 3.7. Dispersion relation at different flame conditions using the model from the work by Pelce & Clavin [2], Matalon & Matknowsky [3, 4] and Frankel & Sivasinsky [5] 62

Figure 4.1. Schematic of the experimental setup with primary components and the side view Mie scattering images of oscillating flames. 69

Figure 4.2. Representative normalized time series, and PSDs for different cases. . 71

Figure 4.3. From left to right PSDs of $\dot{q}'_l$, $\dot{q}'_c$, $\dot{q}'_r$ with $\alpha = 10\%$, 40%, and 70% H_2, from top to bottom: left flame ($\dot{q}'_l$), center flame ($\dot{q}'_c$), and right flame ($\dot{q}'_r$). 73

Figure 4.4. $\dot{q}'$ time series for $\alpha = 70\%$. 76

Figure 4.5. Overall flame dynamics demonstration. 78

Figure 4.6. Normalized cross transitivity. **(a.)**: $\dot{q}'_{\text{total}}$ vs. p'. **(b.)** center vs. side flames 81

Figure 4.7. A simple diagram illustrating the phenomenon relates to the induced vortices. 82

Figure 4.8. The horizontal Mie scattering images of two consecutive cycles clearly show a pattern shift between the neighboring cycles. 83

Figure 5.1. Bifurcation diagrams 98

Figure 5.2. The representative normalized time series from the model. 99

Figure 5.3. The representative normalized time series from the experiments. ... 100

Figure 5.4. The representative phase plot **(a, d, g)**, phase difference ($\Delta\phi_{pq}$) **(b, e, h)**, and power spectrum density ($log|(p(f))|$) **(c, f, i)** for the model. 102

Figure 5.5. The representative phase plot **(a, d, g)**, phase difference ($\Delta\phi_{pq}$) **(b, e, h)**, and power spectrum density ($log|(p(f))|$) **(c, f, i)** for the experiment. 103

Figure 5.6. The representative diagram on 0-1 test from the model. 108

Figure 5.7. The representative diagram on 0-1 test from experiments. 109

Figure 6.1. Time series obtained from the model and experiments at different dynamical states. 123

Figure 6.2. **a(i)** and **b(i)**: RMS of p' and $\dot{q}'$ at different conditions from model and experiment. 125

Figure 6.3. The power spectra density of p' at different conditions from model and experiment. 126

Figure 6.4. PLV between p' and $\dot{q}'$ at different conditions from model (**a**) and experiment (**b**). 127

Figure 6.5. Multifractal spectrum at different dynamical states from the model (**a**) and experiment (**b**). 130

Figure 6.6. The spectral amplitude of the dominant mode (A) versus Hurst exponents (H) at different control parameters during the transition to thermoacoustic instability. 132

Figure 6.7. Scaling behaviors of spectral condensation. 134

Figure 7.1. Typical dynamics at different Re in the experiment, from top to bottom: Combustion noise, intermittency, LCO 141

Figure 7.2. Phase Space change as the system transitions from combustion noise to intermittency, and finally reaching limit cycle oscillation..... 144

Figure 7.3. Cumulative sum of normalized singular values $\hat{\sigma}_i^2$. The sum up to $n = N$ should equal 1 since we normalized the 2-norm to be 1. 146

Figure 7.4. Evolution of the first six singular values as a function of Re. 147

Figure 7.5. Experimental Data overlapped with theoretical lines (Eqns. (7.12), and (7.13)) 149

Figure 7.6. An example of the PSD of the original time series and the first 6 modes after PCA. 151

Figure 7.7. PSD of the pressure time series their PCA components at different Re. 152

Figure 7.8. Dominant frequencies of low-rank time series. 155

Figure 7.9. Example time series for p'_{34} and $\dot{q}'_{34}$, and their full order time series in low Re regimes ($Re = 1.47 \times 10^4$). 156

Figure 7.10. Phase Locking Valve vs. Re. The low-rank time series is reconstructed from the low-rank Hankel matrix 157

LIST OF TABLES

Table 2.1. List of experimental conditions for Chapter 2. 24

Table 3.1. List of experimental conditions for Chapter 3. 49

Table 4.1. List of experimental conditions for Chapter 4. 68

ACKNOWLEDGEMENTS

First and foremost, I would like to express my sincere gratitude to my advisor Prof. Abhishek Saha for his continuous support throughout my journey at UCSD. His guidance was invaluable, and this study would have been impossible without him.

I would also like to thank the rest of my thesis committee, namely Prof. Antonio L. Sanchez, Prof. Kalyanasundaram Seshadri, Prof. Boris Kramer, and Prof. Jose I. Restrepo for their insightful comments, and encouragement to widen my research horizons.

A special thank you goes to Prof. R. I. Sujith for the time he devoted to offering insights into our research. Our discussions about the complex system greatly broadened my perspective.

My deepest thanks go to Dr. Vishnu R. Unni, my dear mentor, collaborator, and one of my closest friends. His immense academic expertise and unwavering support, both in academia and in life, were invaluable throughout my Ph.D. journey.

Additionally, I would like to express my appreciation to all the members of the Flame-Fluids-Energy Lab for sharing their insights and experiences. Their companionship made working together not only productive but also enjoyable. I am especially grateful to Dr. Aditya Potnis for his invaluable research expertise, assistance with experiments, and for sharing brilliant ideas, along with many cherished memories outside the lab. My heartfelt thanks also go to my undergrad mentee, Yihong Zhu, for the wonderful collaboration—keep pushing forward, future AEROPHD! I also want to acknowledge my current and past lab mates, Xian, Stacho, Sombuddha, Patrick, Brooklyn, Jose, and Blake for their valuable contributions.

Special thanks to Prof. Yousef M. Bahadori. I will always cherish the memories of being his student and serving as his teaching assistant. Working with him sparked my love for teaching and taught me how to be a good teacher.

In addition to my lab mates, I'd like to express my gratitude to my friends at UCSD—Dr. Liang Ji, Iris, Boya, Tao, Obed, Richard, Bhanjan, and Kevin—for their

companionship and for making life more enjoyable. A special shout-out goes to my dear friends from our high school days, Luorao Bian, Chaoyu Zhang, and Hexuan Yu, for always standing by my side.

Last but not least, I am grateful to my family for all the encouragement they gave to me throughout my journey, and their love and support throughout my stay at UCSD.

The completion of this Ph.D. is a testament to the collective support and contributions of everyone I have met throughout this journey. I am profoundly grateful to all who have been an essential part of this remarkable experience.

I sincerely acknowledge the funding support provided by the U.S. National Science Foundation, the Jacobs School of Engineering at UC San Diego, and the Department of Mechanical and Aerospace Engineering.

Below is the information on the published and ongoing journal articles associated with this thesis.

Chapters 2, 3, 5, and 6 are reprints of the following published articles:

Weng, Y., Potnis, A., Unni, V. R., Saha, A. (2024) Assessing local statistics of a premixed turbulent Bunsen flame. *AIAA Journal*, 1-9.

Weng, Y., Potnis, A., Saha, A. (2023). Regime and morphology of polyhedral Bunsen flames. *Combustion and Flame, 248*, 112585.

Weng, Y., Unni, V. R., Sujith, R. I., Saha, A. (2023). Synchronization-based model for turbulent thermoacoustic systems. *Nonlinear Dynamics, 111*, 12113–12126.

Weng, Y., Unni, V. R., Sujith, R. I., Saha, A. (2020). Synchronization framework for modeling transition to thermoacoustic instability in laminar combustors. *Nonlinear Dynamics, 100*, 3295-3306.

Chapters 4 and 7 are part of the following ongoing research and are currently being prepared for submission for publication:

Weng, Y., Zhu, Y., Saha, A. Vortex-driven subharmonic bifurcation in a Multi-flame Rijke Tube. Under preparation

Weng, Y., Zhu, Y., Unni, V. R., Sujith, R. I., Saha, A., Deriving early warning signals for turbulent thermoacoustic systems using principal component analysis. Under preparation

VITA

2018	Bachelor of Science in Aircraft Propulsion Engineering, Beijing University of Aeronautics and Astronautics, Beijing, China
2020	Master of Science in Engineering Sciences (Aerospace Engineering), University of California San Diego
2024	Doctor of Philosophy in Engineering Sciences (Aerospace Engineering), University of California San Diego

PUBLICATIONS

Weng, Y., Potnis, A., Unni, V. R., Saha, A. (2024) Assessing local statistics of a premixed turbulent Bunsen flame. *AIAA Journal*, 1-9.

Weng, Y., Unni, V. R., Sujith, R. I., Saha, A. (2023). Synchronization-based model for turbulent thermoacoustic systems. *Nonlinear Dynamics, 111*, 12113–12126.

Weng, Y., Potnis, A., Saha, A. (2023). Regime and morphology of polyhedral Bunsen flames. *Combustion and Flame, 248*, 112585.

Weng, Y., Unni, V. R., Sujith, R. I., Saha, A. (2020). Synchronization framework for modeling transition to thermoacoustic instability in laminar combustors. *Nonlinear Dynamics, 100*, 3295-3306.

Weng, Y., Zhu, Y., Saha, A. Vortex-driven subharmonic bifurcation in a Multi-flame Rijke Tube. Under preparation

Weng, Y., Zhu, Y., Unni, V. R., Sujith, R. I., Saha, A. Deriving early warning signals for turbulent thermoacoustic systems using principal component analysis. Under preparation

ABSTRACT OF THE DISSERTATION

A study of local and global instabilities relevant to gas turbine combustors

by

Yue Weng

Doctor of Philosophy in Engineering Sciences (Aerospace Engineering)

University of California San Diego, 2024

Professor Abhishek Saha, Chair

Modern gas turbine combustors are prone to combustion instabilities characterized by large pressure fluctuations, which can compromise safe and efficient operation and potentially cause severe hardware damage. This phenomenon, known as thermoacoustic instability, results from the interaction between the acoustic field and unsteady heat release. In recent decades, the widespread adoption of LPP (lean premixed pre-vaporized) combustors in gas turbines has significantly reduced greenhouse gas emissions. However,

the increased susceptibility of these lean premixed flames to perturbations also heightens the risk of thermoacoustic instability, spurring extensive research in this field.

Given the critical role of combustion instability in gas turbines, this study provides a comprehensive analysis from multiple perspectives. In the first part, we conducted multiple experimental investigations to explore the unsteady flame dynamics resulting from various perturbations, including turbulence, unequal mass and thermal diffusion, and the nonlinear coupling of multi-flame configurations with acoustic interactions.

In the second part, we shifted our focus to investigating the complex dynamics of thermoacoustic instability from a dynamical system perspective. We developed a phenomenological framework based on synchronization theory to model thermoacoustic instability, which effectively captured the dynamical behavior in both laminar and turbulent thermoacoustic systems. Additionally, we introduced a data-driven modal analysis for thermoacoustic instability, enabling the identification of early warning signals for the onset of instability.

Chapter 1

Introduction to the Dissertation

1.1 A brief overview of gas turbine engines

Since Frank Whittle first ran the gas turbine engine in 1937, it has undergone dramatic improvements, securing a significant role in both propulsion and power generation. Modern gas turbine engines now produce substantial power with high energy conversion efficiency and low maintenance costs [6]. They have revolutionized air travel by making it more efficient, facilitated the long-distance transportation of natural gas, and enabled the generation of affordable and flexible electricity. Beyond these applications, gas turbines are also integral to various industrial processes, contributing to overall economic growth and technological advancement. In short, gas turbines play a crucial and multifaceted role in contemporary life.

Gas turbine engines are categorized into several types based on their configurations, including turbofan, turbojet, and turboprop for aircraft propulsion, and turboshaft for helicopters or power generation. Despite these variations, the core of a typical gas turbine remains consistent, comprising the gas generator and the associated power cycle. As depicted in Fig. 1.1, the basic components of a gas generator include the compressor, combustor, and turbine.

The operation of a typical gas turbine is based on the Brayton cycle [6, 7]. In this cycle, atmospheric air is first compressed by the compressor and then directed into

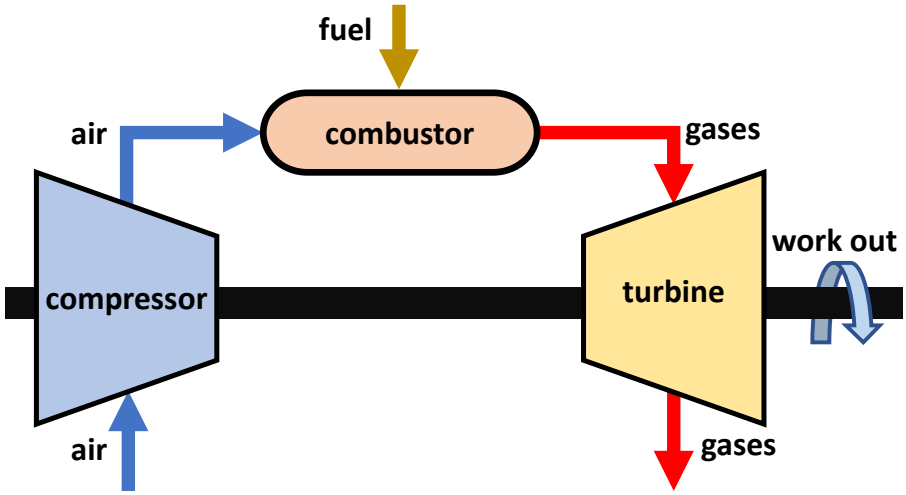


Figure 1.1. Primary elements of a standard gas generator include the compressor, combustor, and turbine. These components work in tandem to facilitate the combustion process, driving the engine's power output.

the combustor. Here, fuel is added to the compressed air and ignited, increasing the temperature and energy of the gas. The resulting high-temperature, high-pressure gas flows into the turbine, where it expands through its stages, producing shaft work that drives the compressor. The remaining gas either expands and accelerates through a nozzle to generate thrust (as in a turbojet) or produces net torque (as in a turboshaft) [8, 9].

1.2 Combustion instability in gas turbines

Within the components of a gas turbine, the combustion system holds paramount importance, particularly in modern turbines boasting high energy density. The primary objective of a combustor is to convert chemical energy into heat energy, and thus add energy to the compressed gas to power the turbine and/or generate thrust. Among many considerations of the combustor design, operational reliability is the most important one. The flame must be held steadily in the combustor and flame-out should be avoided. To ensure operational reliability, the combustion process needs to work in the stable mode in all the possible working and operating conditions [8]. Generally speaking, the main

objective is to achieve a stable and efficient combustion process.

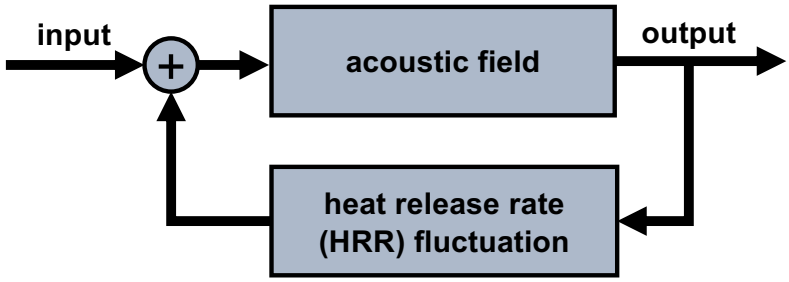


Figure 1.2. A schematic diagram illustrating the mechanism of thermoacoustic instability.

In modern combustion devices, where combustion typically occurs in confined spaces with high energy density, fluctuations in the unsteady heat release rate can interact with the acoustic modes of the chamber, potentially forming a feedback loop. If this feedback loop is positive, it can cause the amplitude of the fluctuations to increase, leading to a phenomenon known as thermoacoustic instability. Many combustion devices, such as gas turbines, rocket engines, and industrial furnaces, are susceptible to thermoacoustic instabilities [1, 10–12].

When thermoacoustic instability occurs, the resulting violent pressure oscillations can compromise the safe operation of aircraft and power stations [13], and in some cases, may lead to severe damage to engine hardware, example shown in Fig. 1.3. Over the past few decades, with the increasing demand in fuel economy and reduced emission, and cleaner combustion, the lean premixed prevaporized combustors are becoming widely popular.

In fuel-lean conditions, the flame weakens and becomes more sensitive to unsteady input perturbations. Notably, both local or global fluctuations can lead to significant variations in heat release rates. Addressing this issue is crucial to ensuring reliability and safety, making it a critical focus in the development of contemporary gas turbine technology [1].

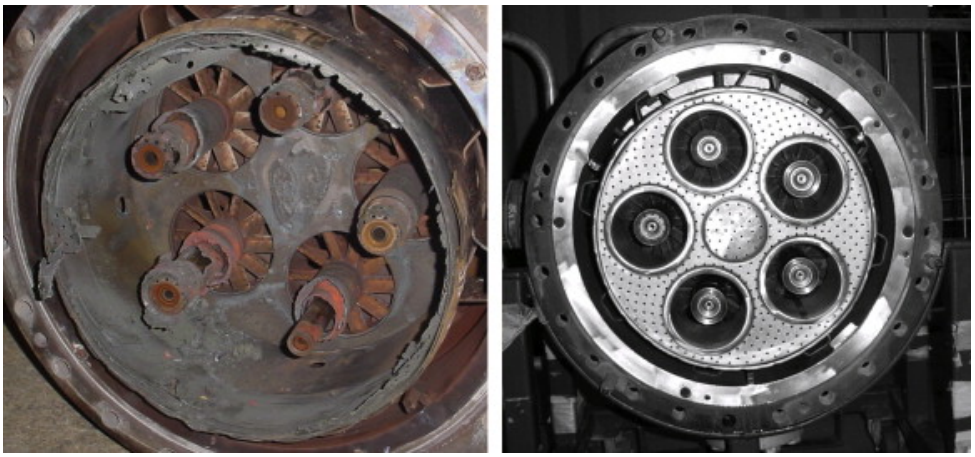


Figure 1.3. Burner nozzle before (left) and after (right) experiencing damage caused by thermoacoustic instabilities [1].

1.3 Research focus of this work

Recognizing its severity and impact on the operation and safety of modern gas-turbine combustors, this thesis aims to investigate the phenomenon from multiple perspectives. The investigation will be primarily divided into two parts. The key components of these two parts and their synergistic relationships are depicted in Fig. 1.4. Below, we provide a brief overview of our approaches in each section.

In **Part I**, we conduct experiments and investigate flame instabilities from a traditional combustion study perspective, focusing on the factors that drive unsteadiness in heat release rates and flame propagation. Recognizing that the combustors operate in a strong turbulent environment, we will focus on the effect of flame-turbulence interactions on local flame geometry and flame morphology. Besides, we also identify how intrinsic cellular instabilities in premixed flames can modify the flame dynamics, in laminar and turbulent environments. In addition, since the acoustic perturbation can significantly change the flame topology and hence alter the heat release rate, it is important to investigate the response mechanism. Specifically, we studied the nonlinear coupling between the flame and acoustics, with a particular focus on examining subharmonic behavior in a Rijke tube

from the flame's perspective. Subharmonic bifurcation is a well-known pathway to chaos, as highlighted in numerous studies. Our objective is to understand why the flame in a Rijke tube system can exhibit subharmonic oscillations and to gain deeper insights into the nonlinear interactions between the flame and the acoustic field.

In **Part II**, we investigate thermostatic instability from a dynamical system perspective and intend to build a framework for model reduction. Specifically, we introduce a framework based on synchronization to model the transition to thermoacoustic instability in both laminar and turbulent combustors. Our goal is to create a framework that integrates the flame dynamics and coupling mechanisms discussed in **Part I**, with an emphasis on capturing the complex dynamics of both laminar and turbulent thermoacoustic systems. Additionally, by applying modal analysis to quantify the transitional dynamics in turbulent thermoacoustic systems, we are able to identify early warning signals for impending instability.

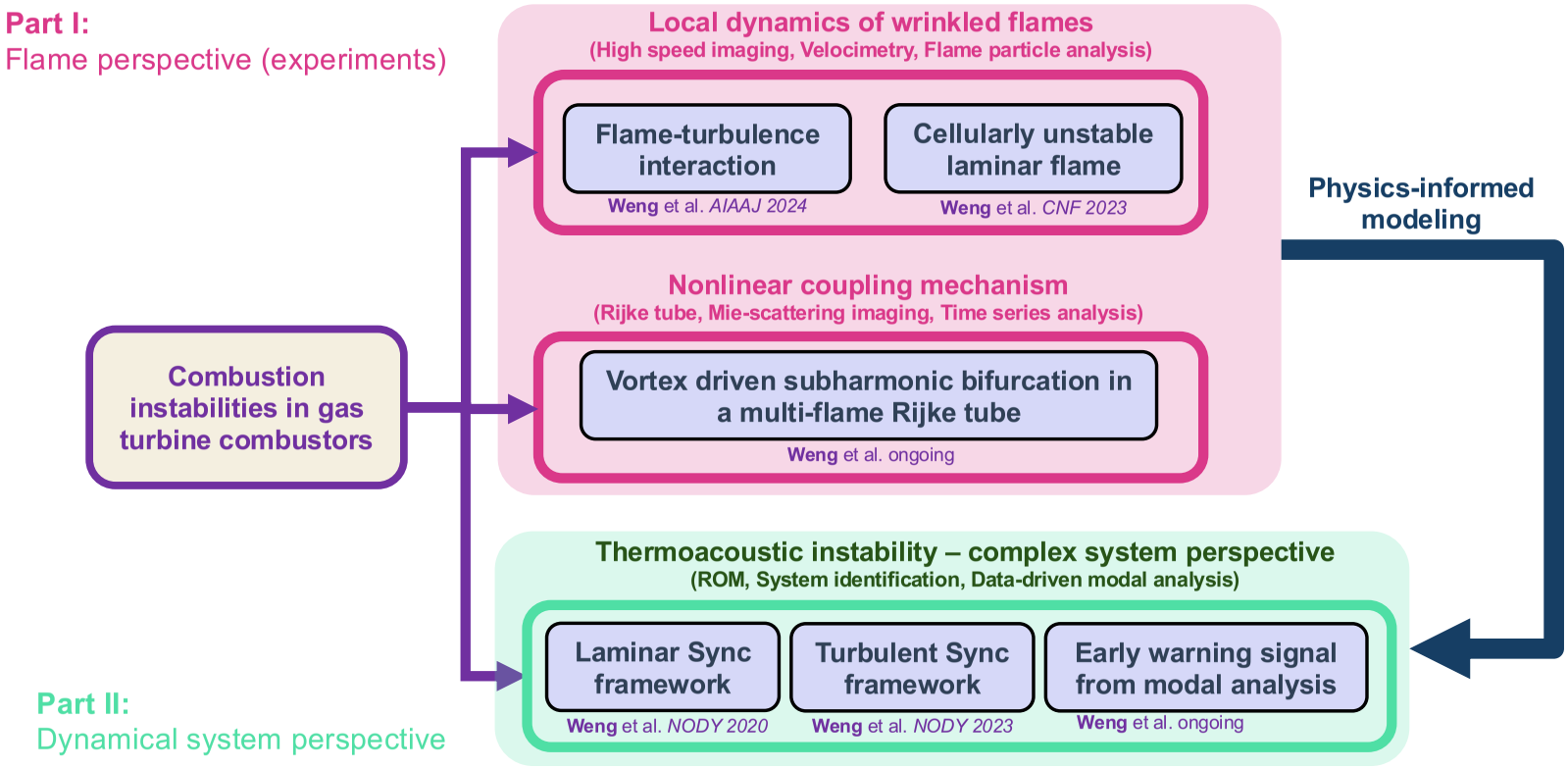


Figure 1.4. The logical map of the thesis.

Part I

Unsteady premixed flame: Experiments and time scale analysis

Brief overview of Part I

The complexity of reactive flow in practical combustors is driven by various factors, including flame dynamics, hydrodynamics, and turbulence. Each of these factors can wrinkle the flame front, altering the flame surface area and, consequently, the heat release rate. Many of these factors exhibit significant nonlinearity and possess unique time and length scales, leading to intricate and dynamic behavior. This research primarily focuses on investigating flame instability without acoustic forcing, with particular emphasis on understanding instabilities arising from the interaction between flame turbulence and the unequal diffusion of mass and heat.

The practical combustion process can be classified into three types based on the mixing method of fuel and oxidizer: premixed combustion, non-premixed combustion, and partially premixed combustion [14, 15]. In modern gas turbines, the operation is primarily in premixed modes, though locally it may also involve partially premixed or non-premixed conditions. Therefore, understanding premixed combustion under engine-relevant conditions is crucial.

Regimes of premixed flame

Under different operating conditions, the premixed flame can be distorted by various factors within the surrounding flow field. The interaction between the flow and premixed flames, along with the resulting flame dynamics, can be theoretically categorized into different regimes using the well-known turbulent flame regime diagram (Fig.1.5) [16, 17]. Although depicted with two sets of different independent variables, the two versions of the regime diagram in the figure highlight similar dynamics. The turbulent Reynolds number (Re) differentiates between laminar and turbulent flame regimes, where Re is defiend as:

$$Re = \frac{u_0' \lambda_I}{\nu} \tag{1.1}$$

where u_0' is the root-mean-square (RMS) of the fluctuating velocity, and is a measure of turbulence intensity, λ_I is a characteristic length scale of the turbulence, often taken as the integral length scale or the size of the largest eddies, ν is the kinematic viscosity of the fluid. The boundary at $Re = 1$ marks the transition between laminar and turbulent flame regimes. Within the turbulent flame regime, a key parameter that distinguishes different combustion behaviors is the Karlovitz number (Ka), defined as:

$$Ka = \frac{t_F}{t_\eta} \tag{1.2}$$

where t_F is the chemical time scale and t_η is the Kolmogorov time scale, which represents the smallest scale of turbulence. Ka characterizes the interaction between turbulence and chemical reaction rates in a flame. Another important parameter in the regime of turbulent combustion is the ratio u_0'/S_L, where S_L is the laminar flame speed. This ratio reflects the interaction between turbulence intensity and the laminar flame speed.

In the regime of wrinkled flamelets, with $Ka < 1$ and $u_0'/S_L < 1$ [18, 19], turbulence can wrinkle the laminar flamelets. However, because the turbulence is relatively weak, even the turnover velocity u_0' of the largest eddies is still too small compared to the laminar burning velocity S_L, thus turbulent mixing cannot interfere with chemical reactions. In other words, the time scale of the chemical reaction is way smaller than that of turbulence. Therefore, in the regime of wrinkled flamelets, laminar flame propagation is invariant to the effects of turbulence.

As u_0'/S_L becomes greater than one, the flame enters the regime of corrugated flamelets. In this regime, large eddies can have greater velocities than S_L, and thus the flamefront can be distorted by these eddies [20, 21]. However, because $Ka < 1$, the flame time scale is still smaller than the flow time scale, and thus turbulent fluctuations are unable to perturb the chemical reaction, and the flame structure remains quasi-steady.

The boundary between corrugated flamelets and the thin reaction zone is determined

by $Ka = 1$, also called the Klimov-Williams criterion. In the regime of the thin reaction zone, $Ka < 1$ suggests that turbulence has a smaller time scale than the combustion process. Also, it indicates that the Kolmogorov length scale of the turbulence is smaller than the flame thickness, thus smaller eddies can enter the reactive-diffusive structure of the flame. Because η is still larger than the thickness of the inner layer δ, even the smallest eddies are unable to penetrate the layer. Thus, in this regime, only transport processes are modified by turbulence. By enhancing heat transport from the reaction zone to the preheat zone, the chemical reaction is accelerated [22].

As Ka_δ reaches 1, the flame enters into the regime of broken reaction zones (also called distributed reaction zones). Since the dimensionless thickness of the inner layer, δ is usually considered as 1/10, the line of $Ka_\delta = 1$ is equivalent to $Ka = 100$. In this regime, λ_I is smaller than δ, and since eddies are smaller than the thickness of the inner layer, the turbulence not only enhances transport but also dominates the chemical reaction by introducing turbulent mixing [20, 23].

Various studies have investigated the effect of cellular instability on flame propagation in turbulent premixed flame [24, 25]. The study showed that cellular instability is able to compete with turbulence in inducing corrugation on the flamefront. Based on the contribution of turbulence and DL instability to the increase of surface area, a new boundary was introduced, which serves to separate the regime of wrinkled flamelets into turbulence dominated and DL instability dominated [24, 25]. This boundary is also shown in Fig. 1.5

Flame turbulence interaction

Although there are numerous configurations of combustors with vastly different flow and combustion characteristics, in modern gas turbines, an overwhelming majority of them involve turbulent combustion [21]. Turbulent combustion has always been a challenging topic, not only due to the inherent complexity of turbulent flows [26], but also due to

the non-linearities of flame-turbulence coupled interactions. In the early studies, several important non-dimensional parameters have been used to delineate turbulent combustion. Based on these parameters, turbulent premixed flames can be characterized into different regimes [27–29]. Among the studies, the non-dimensional parameter u'_0/S_L was found to play an important role in governing the ratio of turbulent flame speed to laminar flame speed S_T/S_L, especially for the case of high pressure and weak turbulence [30]. In turbulent flames, the flamefront surface can be strained due to the existence of velocity gradients, which are produced either as a direct consequence of the turbulence or indirectly through the turbulence-induced hydrodynamic instabilities [31].

Meanwhile, from the perspective of determining how flame alters flow structures, and thus dynamics of the turbulence, it is found that in a freely propagating flame, the turbulence intensity increases when crossing the flame. At the same time, this increment is found more prominent in the normal direction, and hence causes after-flame turbulence anisotropic [32]. In another study, using direct numerical simulation (DNS), the effect of flame on turbulence is found to strongly depend on the heat release, which through alteration of the pressure-related term exerts the flame's effect on turbulence [33]. Later, both hydrodynamic instabilities and diffusive instabilities were found to significantly contribute to the formation and propagation of wrinkles on the flame surface [34]. Furey did a large eddy simulation on a plane-symmetric dump combustor and investigated the fractal-based flame wrinkling of lean premixed flame [35]. Hamlington et. al. [36] studied an H2-air premixed turbulent flame and investigated the flame-turbulence interaction at high Ka. Also at high Ka, Bobbitt et. al. [37] found enstrophy transport can be balanced by the viscous dissipation and stretching terms of production/vortex. Recently, S_T obtained for both expanding flames and Bunsen flame have been universally classified by a flame length scale based turbulent Reynolds number [38]. Recently, Liu et. al. studied flame-generated "turbulence" in an expanding laminar flame [39], they found the energy spectrum of the generated turbulence is driven by the cellular instabilities of the

flamefront.

Since the local interactions between the flamefront and turbulence control the dynamics, morphology, and propagation of a premixed turbulent flame. To investigate such complex dynamics of flame-turbulence interaction, we present an experimental exposition of a premixed turbulent Bunsen flame. Several quantities have been evaluated to assess the flame-turbulence interaction. We first measured the statistics of the flow field adjacent to the flame and compared it with the cold flow. This allowed us to evaluate the effect of the flame on the upstream turbulence. Subsequently, we performed statistical analyses of the local values of various stretch rates and quantified how their distribution changes with turbulence intensity and flame temperature. We also evaluated the pairwise relation between various stretch rates to assess their dependence on each other. Finally, we used flame particles to evaluate the Lagrangian evolution of stretch rates conditioned on flamefronts. All the analyses presented in this work point out Karlovitz number as a key factor in determining the flame-turbulence interaction. Specifically, we observe a stronger influence of turbulent eddies on flames with increasing Karlovitz number, as evidenced by the reduced effect of flame on upstream flow, wider PDFs of stretch rates, and increased persistence time scales for stretches.

Intrinsic flamefront instability

In a premixed flame, fuel and oxidizer are thoroughly mixed before the reaction occurs, with the chemical reaction primarily taking place in a thin reaction zone that separates the burned and unburned regions. This reaction zone, or flame front, determines the rate of chemical reactions, influencing the burning rate and heat release. The flame front's geometry can change over time and space due to both intrinsic and extrinsic factors. Turbulence in the surrounding flow can wrinkle the flame front through the action of eddies of various scales. Additionally, intrinsic instabilities, such as the Darrieus-Landau instability from sharp density gradients and the diffusional-thermal instability

from mismatched thermal and mass diffusion, can also wrinkle the flame front without external influences. These wrinkled flames, with their increased surface area, burn faster than smooth laminar flames, making it essential to understand their dynamics for assessing flame stability and heat release [40, 41].

This part of the thesis investigates the local dynamics of flame wrinkling due to cellular instabilities. Intrinsic cellular instabilities can wrinkle otherwise smooth laminar flame fronts, increasing their surface area and, consequently, the burning rate. These instabilities are significant because they enhance flame propagation and burning rate without external influences like turbulence, making them of both fundamental and practical interest. While often studied in freely propagating flames, cellular instabilities can also occur in burner-stabilized premixed flames. This study presents an experimental investigation of polyhedral flamefront instability in premixed Bunsen flames for lean hydrogen mixtures. Through systematic experiments, we explore how flame temperature, Lewis number, and flow rate affect the stability and morphology of these flames. The findings are presented as regime maps, highlighting conditions that trigger instabilities and showing how transitional boundaries shift with varying experimental conditions. Additionally, we examine changes in the polyhedral flame structure under different operating conditions and explain the observed dynamics through dispersion relation analysis and residence time considerations.

Subharmonic flame dynamics in a multi-flame Rijke tube

Besides turbulence and unequal thermal-mass diffusion, external acoustic perturbations can alter flame topology and subsequently change the heat release rate. The flame's response to acoustic perturbations has been extensively studied, often using quasi-linear response methods that focus on the flame's reaction to the same input frequency, with variations only in gain and phase. However, many investigations have shown that the flame can exhibit nonlinear responses to acoustic forcing, even without considering bidirectional couplings [42]. For example, higher harmonic responses of the flame are commonly observed

in various scenarios and have been well-studied [43]. Meanwhile, subharmonic behaviors of the flame remain relatively less explored. Given that subharmonic bifurcation is a common pathway to chaos, as identified in previous studies, we aim to investigate the factors that cause the flame to exhibit such subharmonic behaviors [44].

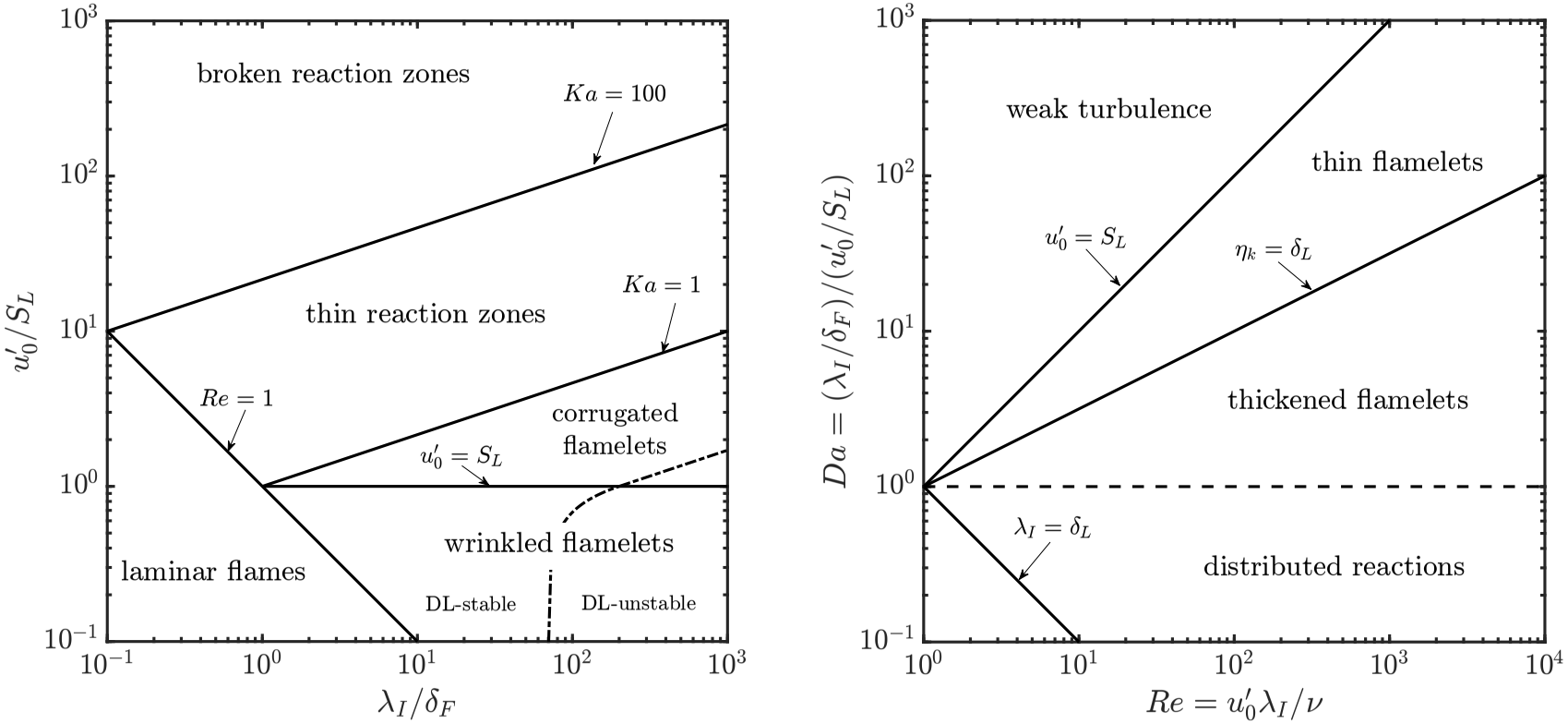


Figure 1.5. Regime diagram of premixed turbulent combustion provided by Borghi (left) and Williams (right).

Chapter 2

Assessing local statistics of a premixed turbulent Bunsen flame

2.1 Introduction

Turbulent combustion is ubiquitous in many practical devices, including gas turbines, rocket engines, automotive engines, and industrial burners. Due to the complexity arising from turbulence and its interaction with the combustion processes, turbulent combustion remains a challenging topic [45, 46]. A turbulent flow contains eddies of a multitude of lengths and timescales, which causes local unsteadiness. These eddies cause the wrinkling of a premixed flamefront within a turbulent flow, altering its shape and structure, which, in turn, results in the modification of several key behaviors, including transport process, propagation speed, fuel consumption rate, etc. [47]. Due to its importance in assessing the performance, stability, and reliability of combustors, a considerable amount of research has been conducted to quantify the global dynamics of turbulent flames, using theory, experiments, and numerical simulations [47–53].

The propagation of a premixed turbulent flame largely depends on the wrinkling caused by the turbulent eddies, altering the flamefront surface area and, thus, the burning rate [21, 54]. The degree of wrinkling on the flamefront is influenced by several factors, including characteristic length and time scales of flame and turbulence. By employing order-of-magnitude analyses of these scales, it can be shown that premixed turbulent

flames can theoretically be categorized into several regimes with various structures and morphologies, as portrayed in the famous Borghi diagram [21, 55]. While this regime diagram is widely utilized for identifying the global dynamics of turbulent flames, researchers have experimentally and numerically demonstrated that local flame dynamics are more complex, with several exceptions reported in regime boundaries [56, 57]. Additionally, the flamefront cellular instabilities provide another mechanism for the wrinkling of local flamelets [58–60]. When accounted for, the effect of cellular instabilities leads to modified global dynamics, and hence, regime maps for premixed turbulent flames [25, 61, 62]. Consequently, understanding the local statistics of flamefronts becomes crucial to comprehend the competitive role of turbulence and instabilities in flame dynamics. Furthermore, the accuracy of Large Eddy Simulations (LES), wherein the flame and flow dynamics are resolved only to limited scales, depends on accurate sub-grid scale models that describe the physics in the scales not resolved in simulations [53]. These sub-grid scale models are constructed based on the physics of local flamefront dynamics.

Owing to its importance, the flamefront wrinkling and its effect on local flamelets were the focus of several numerical studies, where sub-grid scales models were proposed using the equilibrium assumption [63], conditional filtering [64], and fractal dimension of local flamelets [65]. Some studies also focused on the interaction of laminar flamelets and vortices to provide critical physical insights [66, 67]. Meanwhile, recent investigations have found that the wrinkled flamefront may exhibit non-locality, or "memory effects," in that the wrinkling is affected by local flow structure and the upstream flow conditions [47, 68]. Hemchandra et al. [69] demonstrated that such dynamics stem from the propagation of flamefront wrinkles in the direction of the mean tangential flow. The ambient pressure can significantly influence the wrinkling process. In particular, at higher pressures, the flamefront becomes thinner and, thus, exhibits finer corrugations [70–72]. On the other hand, the propagation and wrinkling of a turbulent flamefront also influence the upstream turbulence. Since the flamefront interacts with the turbulent eddies, a modification in

flame geometry, and hence local heat release, can affect the local flow behavior. Such effects on turbulence have been characterized by changes in vorticity and strain rates [39, 47]. In a freely propagating flame, the flame may affect the flow field in its vicinity due to thermal expansion and the associated stretching of eddies, which can modify the turbulence characteristics of the flow [73]. This change is particularly pronounced in the normal direction, with isotropic turbulence in the upstream flow becoming altered to anisotropic turbulence in the post-flame region [32]. Furthermore, recent developments in 3D measurement techniques, including tomographic PIV [74–76], sparse particle flow velocimetry (SPFV) [77], high frequency swinging Mie-scattering [78, 79], have led to several new insights. These studies not only highlighted the structure of the flames in 3D space [76, 80], but also showed the three-dimensional effects on the important quantities such as turbulent kinetic energy [74], flame speed [78, 81], and flame surface density [79].

The above short review of the literature demonstrates a few important findings. First, the global behavior of turbulent flames arises from the collective dynamics of local flamefronts, often termed flamelets. Furthermore, flame-turbulence interaction is a two-way coupled process. Hence, it is important to investigate the effect of the flame on the adjacent flow field, in addition to the commonly studied aspects of the influence of turbulence on the flame properties. The evaluation of flame-turbulence interaction becomes particularly critical for developing reduced-order models, where flame dynamics are captured in simple correlations and used as subgrid-scale models. Since the evolution of local statistics can be used as key parameters in quantifying flame-turbulence interaction, Lagrangian-based analyses gained interest among researchers. For example, Steinberg et al. [82] used Lagrangian tracking of fluid particles in turbulent flames to extract the evolution of principal strain rates. Hamlington et al. [83] used the Lagrangian particle tracking to show that fluid parcels follow a longer path in turbulent flames than laminar flames due to local flow straining. While these studies used fluid particles, there is another approach with fictitious particles, limiting the particle locations on flamefronts. Such an

approach of tracking hypothetical *flame particles* is useful to study the local evolution of a flamefront. This approach was introduced by Pope [84] to analyze the evolution of properties of a hypothetical surface point on an isosurface in a turbulent flow, which moves relative to the fluid in the local normal direction to the surface. Subsequently, the propagation of the isosurface as it evolves was analyzed. As an extension of this concept, Chaudhuri [85] defined a *flame particle* as a surface point embedded and evolving on an isoscalar surface representing the flame. Despite the non-physical nature of such particles, the ability to track their movement enables the investigation of local changes in flame topology and its memory effects over time. This technique also facilitates the study of how incoming turbulence affects a flame element and allows for the identification of changes in properties on the flamefront, such as local stretch rate, which is critical for assessing the evolution of the flamefront. The study by Chaudhuri [85] on flame particle tracking in a turbulent premixed flame using direct numerical simulation revealed that these particles could experience a gradual increase in tangential strain rate and negative curvatures, ultimately leading to the local annihilation of the flame surface. Similarly, an experimental investigation utilizing the flame particle tracking on experiments of expanding premixed flames revealed distinct persistence time scales associated with the evolution of local curvature and strain rates [86].

In this study, we will explore key dynamics discussed in the above review within the context of a turbulent Bunsen flame. We aim to investigate the flame-turbulence interaction by studying local flow and flame statistics. This will be achieved by employing the high-speed velocity measurements performed on our turbulent flame in a Bunsen burner. First, we will assess how local turbulence is affected by flame propagation, comparing the statistics obtained with and without the flame. Next, we will quantify the flame-turbulence interaction by evaluating the statistics of three stretch rates conditioned on the flamefront. Finally, we will employ flame particle tracking to extract the progression of local stretch rates and delineate the characteristics and time scales associated with this evolution.

2.2 Methodologies

2.2.1 Experimental Setup

In this study, we use a piloted Bunsen burner with a nozzle diameter of 15.24mm to explore the dynamics of a premixed turbulent flame. The burner consists of a central tube that supplies the primary mixture and an annular slot for the co-flow. Turbulence in the unburned mixture was created by placing a stack of 3D-printed grids in the central tube upstream of the nozzle exit. The turbulence intensity could be varied by changing the number of grids in the stack. A premixed stoichiometric propane/oxygen/nitrogen ($C_3H_8/O_2/N_2$) mixture was supplied through the central tube and was ignited using a spark igniter to establish a stable flame. By changing the ratio of fuel and oxidizer ($C_3H_8 : O_2$), the equivalence ratio of the mixture can be modulated. For this study, the stoichiometric (unity equivalence ratio) mixture was chosen to keep the Lewis number, defined as the ratio of thermal and mass diffusivity of the mixture, close to unity. The adiabatic flame temperature (T_b) was modulated by changing the oxygen-to-nitrogen ratio ($O_2 : N_2$) in the mixture. Alicat mass-flow controllers were used to monitor and control the individual gas flow rates (Alicat MCR: $\pm 0.2\%$ full scale). Compared to laminar Bunsen flames, relatively high flow rates were required to establish a turbulent flame. In our experiments, the flow rate of 35SLPM was maintained, which resulted in a bulk velocity ($\bar{U}$) of 3.2m/s. At such flow rate, the flames are prone to blow off. To increase the stability and avoid blow-off, a pilot flame was created by burning a stoichiometric methane-air (21:79 of O_2 and N_2 moles) mixture at a low flow rate (10 SLPM) through the annular co-flow space. A constant flow rate of cooling water is supplied to the burner's inner channel to prevent overheating of its walls and protect it from damage. This cooling water also maintains the temperature of the premixed gas to remain constant throughout the experiments.

We used Mie-scattering imaging and Particle Image Velocimetry (PIV) to visualize the dynamics of the turbulent flamefront and measure the flow velocities. The premixed

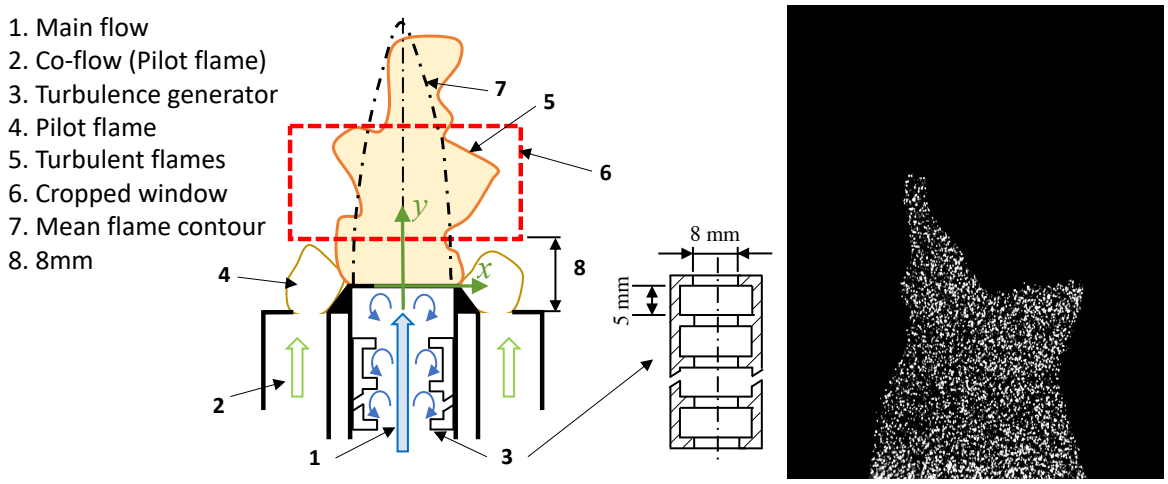


Figure 2.1. Experimental setup: The schematic plot of the Bunsen burner and a sample Mie-scattering image of reactive flow.

gas in the main flow was seeded with Di-Ethyl-Hexyl-Sebacat (DEHS) droplets for this purpose. A high-speed dual-head Nd-YLF laser and necessary optics were used to create a vertical 2D laser sheet (Sheet thickness: FWHM: $\sim 400\mu m$) placed above the burner as shown in Fig. 2.1. Our zone of interest of the turbulent Bunsen flame had dimensions of 25×15mm, which was located 8mm above the nozzle. This location was selected to minimize the influence of the pilot flame on the observed flame dynamics. A high-speed camera synchronized with laser pulses recorded the Mie-scattering images. The frame-straddled mode facilitated appropriate particle displacements between correlated image pairs, limiting errors in PIV measurements. Successive laser pulses were separated by a time interval of 50 μs. Depending on the analysis, the frame rates for the data acquisition were changed between 500 to 18000 Hz. To obtain the velocity vectors, the correlated Mie-scattering image pairs were processed using the PIV algorithm of LaVision's DaVis software with the final interrogation window size of 24 pixel $\times$24 pixel ($\sim 720\mu m \times 720\mu m$) with a 75% overlap. This results in approximately $180\mu m$ spacing between PIV vectors. PIV was performed for both conditions, i.e., with flame (hot flow) and without flame (cold flow). Since the DEHS droplets evaporate near the flame, Mie-scattering images display a clear flame boundary (Fig. 2.1b), which was tracked using custom Matlab image processing

codes. The identified flamefront is essentially the isothermal surface at which the droplets evaporate (close to the saturation temperature of DEHS). This method was previously used successfully to analyze the geometry and statistics of flamefronts [62, 86–89]. The concentration of the seeding droplet is small, and as such, their evaporation should not have significant effects on the flowfield.

2.2.2 Characterization of conditions

This study investigated four flame/flow conditions using two levels of turbulent intensities (low, T_L, and high, T_H) and two different flame temperatures or oxygen percentages (low, O_L, and high, O_H). These conditions and their corresponding characteristics scales are detailed in Table. 2.1. According to previous studies, turbulent flames can be theoretically categorized into various regimes based on several important non-dimensional parameters [17, 21, 28, 29] including the turbulent Damköhler number, $Da = t_I/t_F$, the Karlovitz number, $Ka = t_F/t_\eta$, the turbulence intensity, u'_0/S_L, and the normalized length scales, L_I/δ_L, where t_I is the integral time scale, $t_F = \delta_L/S_L$ is the flame time scale, t_η is Kolmogorov time scale, u'_0 is RMS or turbulent velocity fluctuations, S_L is laminar flame speed and δ_L is the laminar flame thickness.

To obtain the fundamental flame properties, i.e., planar laminar flame speed (S_L), flame thickness (δ_F), a 1D Chemkin simulation of an unstretched laminar planer premixed flames was performed using *GRI-Mech 3.0* chemical mechanism [90]. Laminar flame thickness δ_F is calculated from the temperature profile of 1D unstretched laminar flames using the following equation:

$$\delta_F = (T_b - T_u)/(dT/dx)_{max} \tag{2.1}$$

where T_b is the burned flame temperature, T_u is the unburned flame temperature and $dT/dx|_{max}$ is the maximum temperature gradient [91], as shown in Fig. 2.2. The charac-

teristics time scales for these flames, $t_F = \delta_F / S_L$, were also evaluated.

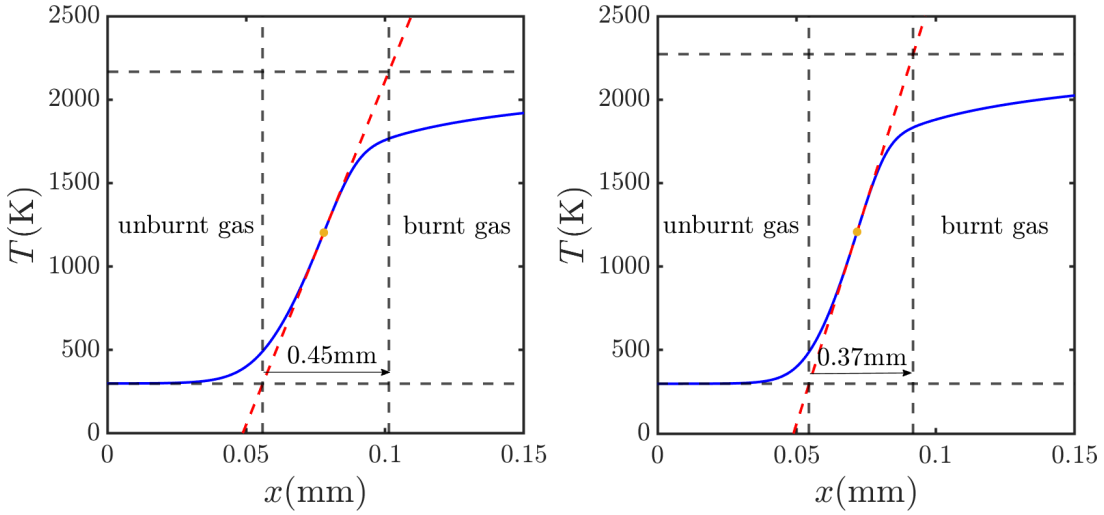


Figure 2.2. The temperature profile and corresponding flame thickness of two flame conditions: 19% oxygen (left) and 21% oxygen (right).

The turbulence characteristics of the flow field can be quantified by the overall root mean square (r.m.s.) of velocity fluctuation, defined as

$$u'(x,y) = \sqrt{\frac{\left\langle \left(u_x(x,y) - \langle u_x(x,y)\rangle\right)^2 \right\rangle + \left\langle \left(u_y(x,y) - \langle u_y(x,y)\rangle\right)^2 \right\rangle}{2}} \tag{2.2}$$

Here, the instantaneous values of velocity components in transverse and axial directions are $u_x(x,y)$ and $u_y(x,y)$, respectively. $\langle u_x \rangle$ and $\langle u_y \rangle$ are their time-averaged values. We defined the origin of the coordinate system, i.e., $x = 0$ and $y = 0$ at the center of the nozzle exit. The global conditions from the nozzle were identified by the r.m.s. of velocity at the nozzle exit $u'_0 = u'(0,0)$ (Eq. 2.2). The integral length scales $(\lambda_I)_{ij}$ were evaluated using the auto-correlation function of velocity fluctuations using the definitions from Pope [26]. The overall integral length scale, λ_I is defined as the mean of $(\lambda_I)_{ij}$, where $i = x, y$ and $j = x, y$. The energy spectra from PIV measurements evaluated for the cold flow conditions showed a fully developed turbulence behavior, i.e., near -5/3 power-law dependence with the wavenumber [26]. Some of these spectra are shown in the supplementary material. The

Kolmogorov timescale (t_η) is evaluated assuming self-similarity in dissipation of isotropic homogeneous turbulence [26]:

$$\tau_\eta = (\nu \lambda_I / {u_0'}^3)^{\frac{1}{2}} \tag{2.3}$$

Here, ν is the kinematic viscosity of the premixed gas. We also evaluated the Karlovitz number ($Ka = t_F/t_\eta$) to quantify the differences in timescales of flame and turbulence. The characteristic parameters for the four experimental conditions are listed in Table. 2.1.

Table 2.1. Relevant parameters of four experimental flame conditions, Re_T here is the turbulent Reynolds number, which is defined as $Re_T = u_0' \lambda_I / \nu$

Condition	$\frac{O_2}{O_2+N_2}$	$\bar{U}$ (m/s)	T_b (K)	u_0' (m/s)	S_L (m/s)	t_F (ms)	δ_F (mm)	λ_I (mm)	t_η (ms)	Re_T	u_0'/S_L	Ka
$T_L O_L$	19%	3.2	2169	0.26	0.31	1.47	0.45	1.56	3.53	27	0.84	0.42
$T_L O_H$	21%	3.2	2271	0.26	0.40	0.94	0.37	1.56	3.64	27	0.65	0.26
$T_H O_L$	19%	3.2	2169	0.89	0.31	1.47	0.45	1.39	0.54	80	2.87	2.73
$T_H O_H$	21%	3.2	2271	0.89	0.40	0.94	0.37	1.39	0.56	80	2.22	1.67

The energy spectra derived from PIV measurements in the cold flow (Fig. 2.3) experiments exhibited characteristics indicative of fully developed turbulence, specifically, a power-law dependence near -5/3 with respect to the wavenumber [26].

The integral length scales λ_I were evaluated using the auto-correlation function of velocity fluctuations using the definitions from Pope [26].

$$\lambda_I = \int_0^\infty \rho(r)\, dr \tag{2.4}$$

where $\rho(r)$ is the normalized autocorrelation function

$$\rho(r) = \langle u'(x) u'(x+r) \rangle / \sigma_u^2, \tag{2.5}$$

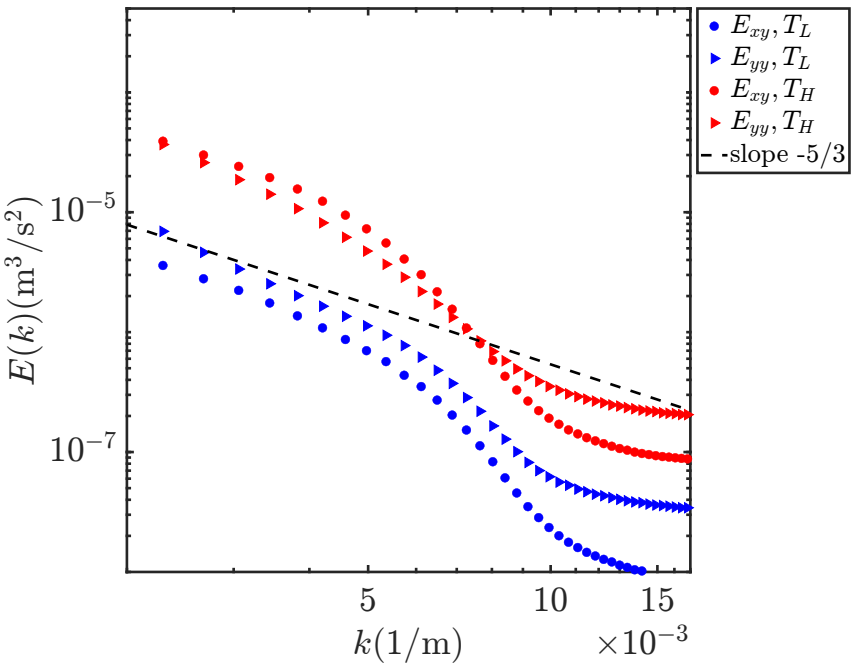


Figure 2.3. The energy spectra of cold flow at different conditions. Here, we are showing only spectra of both horizontal (u_x) and vertical (u_y) velocities in the vertical direction (y), i.e., E_{xy}, and E_{yy} for two turbulence levels used for the study.

and σ_u^2 is the variance of u'.

2.2.3 Choosing the appropriate thickness for conditioned average

The primary goal here is to capture statistics closest to the flame front. Naturally, we aimed to minimize the thickness of the zone of influence. However, if the zone is too thin, there might not be sufficient data points in the time series to attain a statistical convergence. Because the flame edge distribution conforms to a Gaussian distribution (shown below), we settled on using the thickness of one standard deviation ($\pm\delta_T$) to strike a balance. This thickness is close enough to attain strong effects of the flame ($\sim 67\%$ of the probability), yet it is enough for attaining statistical convergence. We are also limited by image and velocity vector resolutions, which restricts reducing the zone thickness further.

Also we carried out a sensitivity analysis. As illustrated in Fig. 2.5, increasing the thickness from δ_T to $1.5\delta_T$ and $2\delta_T$ does not alter the trend of the data. We do observe a

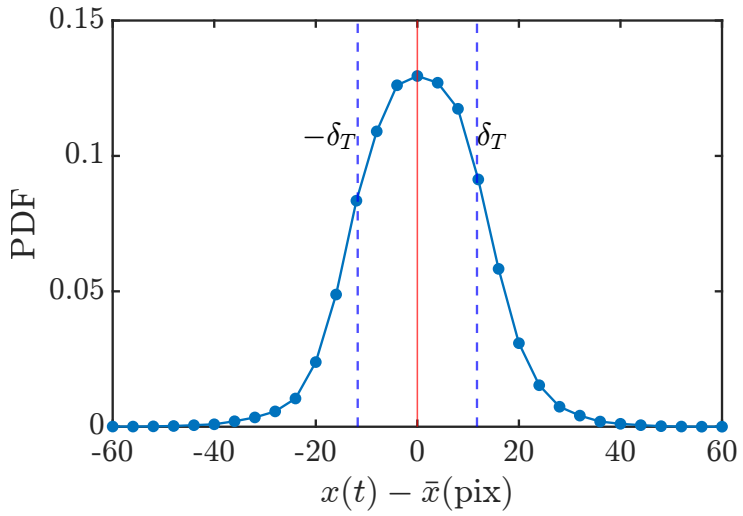


Figure 2.4. The distribution of x coordinate of the edge from case $T_L O_L$

minor rise in the overall u'/u'_c. This is expected ad the inclusion of more points away from the flamefront will diminish the impact of the flamefront, i.e., reduction in r.m.s.

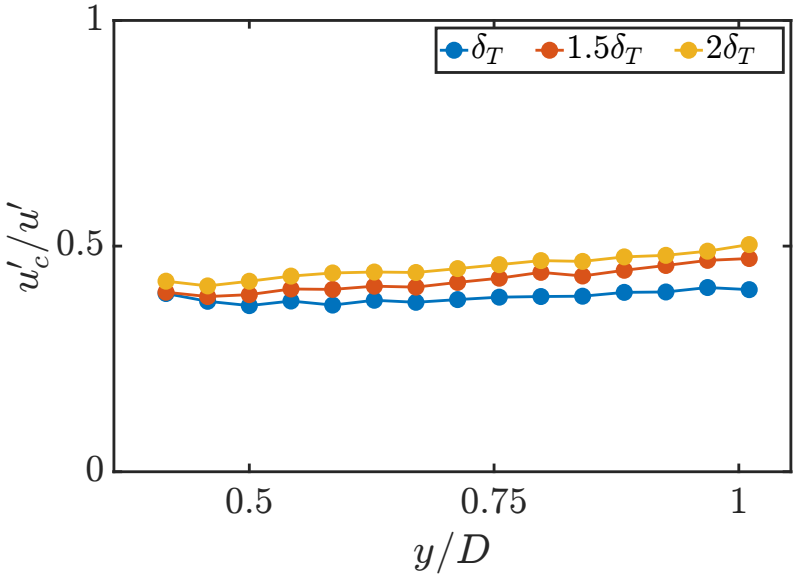


Figure 2.5. Sensitivity analysis of u'/u' using data from case $T_L O_L$

2.3 Results and discussion

2.3.1 Flow statistics near the flamefront

To assess the effect of turbulence on flame dynamics, relevant quantities are often presented as functions of either turbulence intensity or r.m.s. of flow velocity. For example, one of the commonly used scaling relations for turbulent flame speed (S_T) is $S_T/S_L \approx (u_0'/S_L)^n$ [47, 53, 68], where u_0' is the r.m.s. of the turbulent flow field. For expanding turbulent flames, it was theoretically and experimentally shown that the normalized turbulent flame speed can be expressed as follows [38, 72, 92]:

$$S_T/S_L \approx \sqrt{(u_0' R_f)/(S_L \delta_L)} \tag{2.6}$$

where R_f is the mean radius for expanding flames. However, in these correlations, it is customary to use the u_0' measured for cold flow without the presence of flames. This is primarily due to the difficulty in performing the flow measurements in the presence of the flame in experiments. In theoretical analyses, the turbulence intensity is used as a fixed boundary condition and is commonly assumed to be constant. Moreover, for flame configurations that involve a burner and mean flow (e.g., jet flames or Bunsen flames), the measurements are performed at the nozzle exit, which may be far from the flame. Naturally, one question that arises from this discussion is whether the turbulence characteristics, especially r.m.s. of velocity, will remain the same if the measurements were to be performed for hot flow and in the vicinity of the flame locations. This will significantly impact the prediction of flame dynamics, as the correct evaluation of u' that the flame experiences is important. We will address and assess this possible mismatch by using the experimental data obtained in our experiments on turbulent Bunsen flames. Since our experimental method allows us to measure the velocity field in the upstream unburned mixture in the presence of the flame, we were able to quantify the effects of

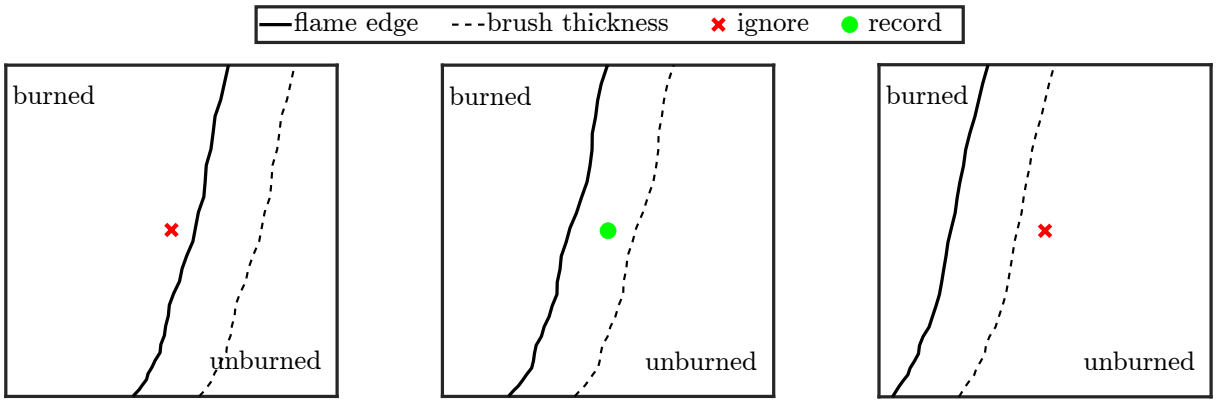


Figure 2.6. An example of conditioned statistics: Data from a point was recorded only when it lies within the zone of influence.

flame on the flow turbulence due to their interactions. We first extracted the flamefront locations from the Mie-scattering images using edge detection over a long time series to ensure statistical convergence. The mean flame location was then evaluated from the time-averaged flame position as a function of the vertical distance (y) from the burner exit. On the other hand, the standard deviation of the instantaneous flame locations at each y location was used to define the brush thickness (δ_T). We defined a zone of influence as an area that is located within the brush thickness ($\pm\delta_T$) measured from the mean flame location. Next, we extracted the flow velocities (i.e., u_x and u_y) on the flamefront using PIV data and flame location identified from the Mie-scattering images. It is to be noted that due to the unsteadiness of the turbulent flame, the flamefront oscillates about the mean flame position. Since we are interested in the effects of flame on the flow, we limited our analysis only to the instances when the flamefront was located within the zone of influence, as shown in Fig. 2.6. Long duration for PIV measurements was used to ensure that the velocity time series contained more than 1000 data points for each spatial location, which ensured statistical convergence. Measurements were also carried out for cold-flow conditions, i.e., when the flame was absent.

Fig. 2.7 displays the spatial distributions (a) r.m.s. of velocity in the vicinity of the flame, u_c' and (b) r.m.s. of velocity at the same locations in the cold-flow, u' for

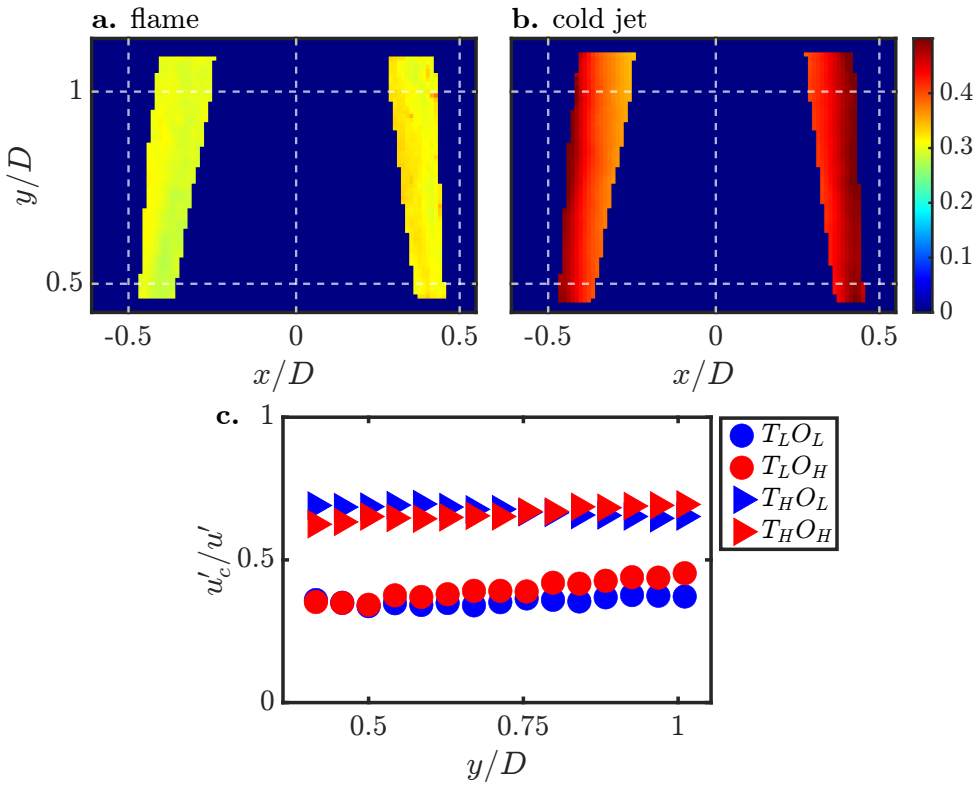


Figure 2.7. (a) Flame-conditioned r.m.s. u'_c (in m/s), (b) cold flow r.m.s. u' (in m/s), from condition T_LO_L. (c) The ratio of u'_c/u', along the mean flame location.

low temperature and low turbulent condition (T_LO_L, see Table 2.1). Although there are small spatial variations in r.m.s. of velocity fluctuation, it is clear from the color maps that the r.m.s. of the velocity decreases in the presence of flame. This weakening can be associated with the thermal expansion effect. Thermal expansion creates a local flow in front of the flamefront, weakening upstream turbulence. To compare this reduction in turbulence strength across different experimental conditions, we plotted the ratio of r.m.s. of velocities with and without the flame (u'_c/u') measured along the mean flame location in Fig. 2.7c. We notice that the flame has weakened the turbulence for all conditions, i.e., $u'_c/u' < 1$. Furthermore, for a given condition, the degree of weakening of turbulence seems to be constant along the flame and, hence, independent of distance from the nozzle (y/D). However, the degree of weakening does depend on the flame condition. Specifically, it is noticed that low turbulence conditions (both high and low flame temperature), i.e., T_LO_L

and T_LO_H have significantly lower values of u'_c/u', compared to high turbulence conditions, i.e., T_HO_L and T_HO_H. The relative strengths and responses of flame and turbulence can be quantified by the Karlovitz number (Ka), defined by the ratio of characteristic time scales. The T_LO_L and T_LO_H conditions have sub-unity Karlovitz number ($Ka < 1$, see Table 2.1), which denotes faster response time for flame compared to the turbulence. Thus, the damping effect of flame due to thermal expansion is stronger and hence lower u'_c/u'. On the other hand, for T_HO_L and T_HO_H conditions, the flame response is slower compared to the turbulence ($Ka > 1$), thus turbulence can resist the weakening effect induced by flame, leading to higher u'_c/u'. It is to be noted that the reduction in turbulence level can significantly decrease the effective Re_T. This may render a far field weakly turbulent flow condition laminar ($Re_T < 1$) near the flamefront.

2.3.2 Local stretch rates

Next, we will analyze the statistics of flame stretch, which quantifies the rate of increase in flame surface area (A) and can be mathematically expressed uisng the following equation [15, 93]:

$$K = \frac{1}{A}\frac{dA}{dt} \tag{2.7}$$

As defined, the flame stretch rate can be broken down into three components: the normal and tangential strain rates from the velocity gradient of the flow: K_n and K_t, and the stretch rate resulting from the curvature of the flame edge: K_c [94, 95].

$$K = \underbrace{S_L\kappa}_{K_c} + \underbrace{(-\mathbf{v}\cdot\mathbf{n})\kappa}_{K_n} + \underbrace{\bigtriangledown_t\cdot\mathbf{v}_t}_{K_t} \tag{2.8}$$

where κ is the curvature of flamefront, $\mathbf{v}$ is local flow velocity, $\mathbf{n}$ it a unit vector normal to the flamefront, and subscript t denotes tangential direction. Since stretch rates quantify the changes in flamefront due to unsteady and non-uniform turbulent flow, their statistics

can be used as a measure of flame-turbulence interactions [96]. In our study, as mentioned before, the edge of the flame in each Mie-scattering image is extracted by locating the maximum particle density gradient. The flamefront is then superimposed on the velocity vector field obtained from PIV. Once the flamefront geometry and the local instantaneous velocity vectors on the flamefront are obtained, the curvature and strain rates can be evaluated using Eq. 2.8. The *probability distribution functions* (PDFs) of each component of the stretch rate for all four experimental conditions are plotted in Fig. 2.8. In general, the stretch rates are affected by both turbulence and flame characteristics. Since we are interested in evaluating the effect of flame-turbulence interaction, we eliminated the pure effects of laminar flame dynamics (i.e., S_L and δ_F) by plotting a normalized stretch rate ($\tilde{K} = Kt_F$). The PDFs for all three stretch rates are symmetric, about 0. The PDFs also display long tails at extreme (high positive and negative) values. Such stretching of PDFs occurs due to intermittency, a hallmark of fully developed turbulence [97]. However, the width of the PDFs and the variance changes between different experimental conditions. This is further illustrated in Fig. 2.9, where we plotted the variance of $\tilde{K_c}$, $\tilde{K_n}$ and $\tilde{K_t}$ as function of Ka. It is apparent from the figure that the variance for all three stretch rates increases with Ka. For smaller $Ka(= t_F/t_\eta)$ conditions, the turbulence is relatively slower than flame propagation. This limits the degree of wrinkling of the flamefront and, hence, reduces the local non-uniformity in flame geometry and flow velocity. This also limits the stretch rates to a smaller range, resulting in a narrower PDF and smaller variance. With the increase in Ka, turbulence eddies become faster than flame propagation, imposing higher degrees of curvature and strains on the flamefront. This leads to wider PDFs and greater variance.

Next, we investigate the joint distribution of a pair of stretch rates to examine if there is any pairwise correlation between them. In Fig. 2.10, we show the scatter plots of two pairwise stretch rates, (a) $\tilde{K_n}$ vs. $\tilde{K_t}$, and (b) $\tilde{K_c}$ vs. $\tilde{K_n}$. The density of scatter points denotes the probability of the stretch rate values. These plots depict a clear pairwise link

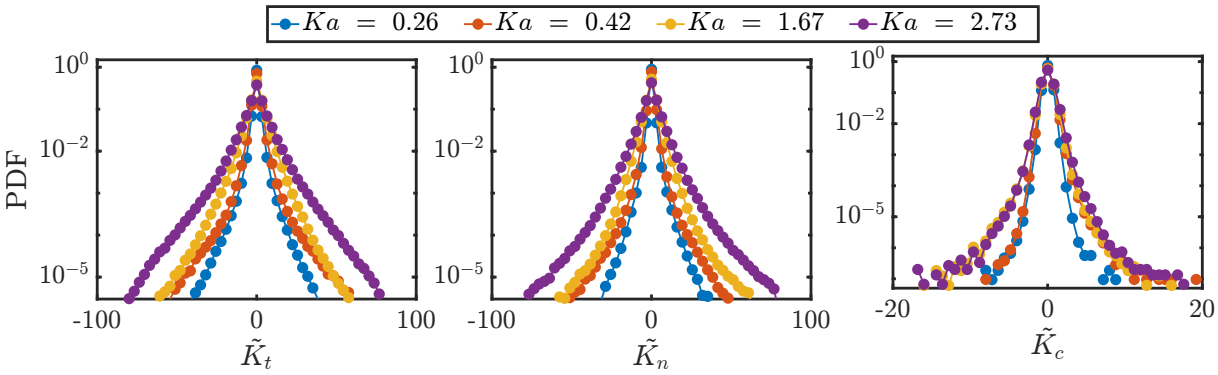


Figure 2.8. The PDFs of normalized tangential strain rate ($\tilde{K}_t$), normalized normal strain rate ($\tilde{K}_n$), and normalized stretch due to curvature ($\tilde{K}_c$).

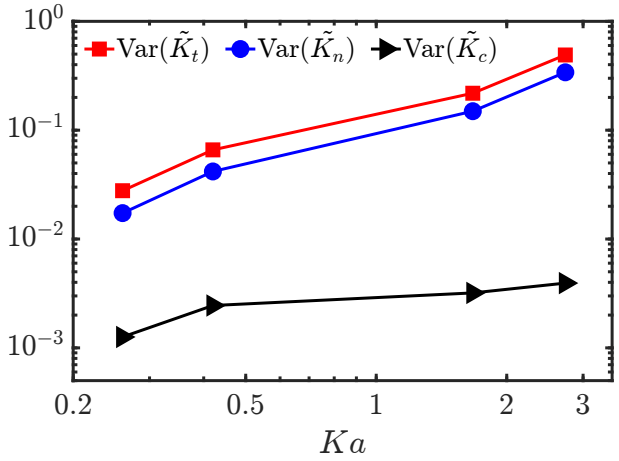


Figure 2.9. The variances of ($\tilde{K}_t$), ($\tilde{K}_n$), and ($\tilde{K}_c$) for different Karlovitz numbers (Ka).

among the stretch rates. Figure 2.10a shows that the values of $\tilde{K}_n$ and $\tilde{K}_t$ follow almost a linear relation with a negative slope. To analyze these dynamics, we revisit the definitions of the stretch rates. The stretch rate due to the normal strain is defined as follows:

$$K_n = (-\mathbf{v} \cdot \mathbf{n})\kappa \tag{2.9}$$

where, for the curvature,

$$\kappa = (-\nabla \cdot \mathbf{n}) \tag{2.10}$$

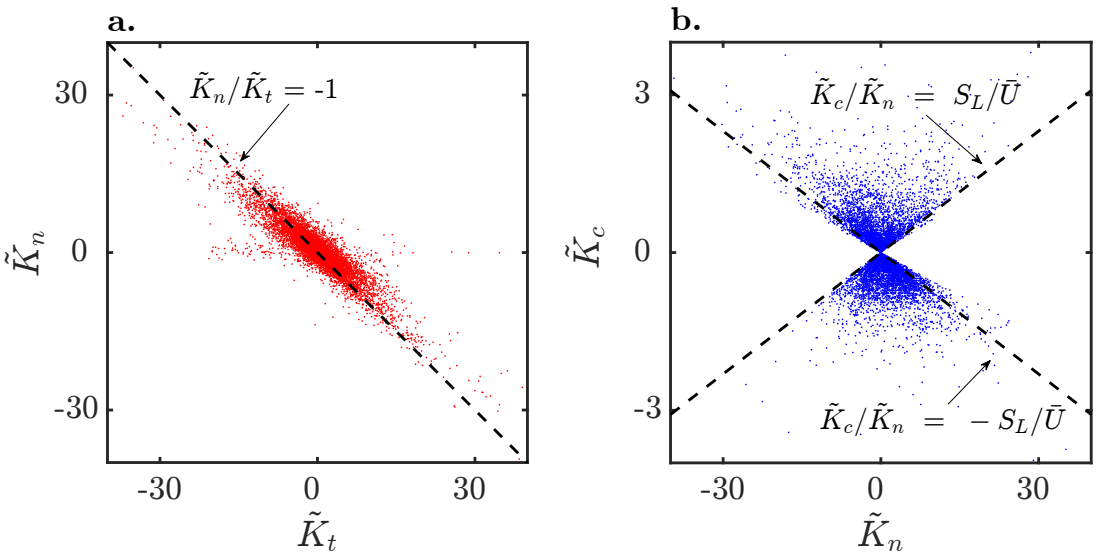


Figure 2.10. Joint PDFs of different components of the stretch rate. The flame condition shown is $T_H O_L$

Thus,

$$K_n = (\mathbf{v} \cdot \mathbf{n})(\nabla \cdot \mathbf{n}). \tag{2.11}$$

On the other hand, the stretch rate due to tangential strain rate is defined as

$$K_t = \nabla_t \cdot \mathbf{v}_t = -\mathbf{n} \cdot \nabla \times (\mathbf{v} \times \mathbf{n}) \tag{2.12}$$

which can be rewritten as

$$K_t = -(\mathbf{v} \cdot \mathbf{n})(\nabla \cdot \mathbf{n}) + (\nabla \cdot \mathbf{v}) \tag{2.13}$$

By comparing K_n and K_t, we find

$$K_t = -K_n + (\nabla \cdot \mathbf{v}) \tag{2.14}$$

Since the second term on the right-hand side, $\nabla \cdot \mathbf{v}$ is relatively small in a Bunsen flame, we expect K_n and K_t to be negatively correlated, i.e. $K_n \approx -K_t$. As shown in the figure,

the slope between them is, indeed, close to -1. We also observe that the pairwise values of $\tilde{K_c}$ and $\tilde{K_n}$ are bounded by two lines (Figure 2.10b). Using their definitions, it can be shown that

$$\frac{K_n}{K_c} = -\frac{\mathbf{v} \cdot \mathbf{n}}{S_L}. \tag{2.15}$$

Here $\mathbf{v} \cdot \mathbf{n}$ is the normal component of the flow velocity on the flamefront. One can imagine that the maximum (and minimum) values of the mean flow velocity normal to the flamefront will be related to the flow velocity at the nozzle ($\bar{U}$), or

$$-\bar{U} \leq \mathbf{v} \cdot \mathbf{n} \leq \bar{U} \tag{2.16}$$

Based on these considerations, theoretical bounds for the pairwise scatter plot of K_c and K_n are defined by:

$$-\frac{S_L}{\bar{U}} \leq \frac{K_c}{K_n} \leq \frac{S_L}{\bar{U}} \tag{2.17}$$

where $\bar{U}$ and S_L are constants for a given experiment.

2.3.3 Lagrangian statistics using flame particles

The PDFs of stretch rates, discussed and analyzed in the previous section, highlight the effect of turbulence on the local statistics. However, these statistics do not provide information on temporal evolution. For instance, while the PDFs reveal that an increase in turbulence level corresponds to broader values of stretch rates, they do not indicate how quickly the instantaneous stretch rate at a specific point on the flamefront changes. To answer this question, we need to analyze the temporal evolution of quantities at a location on the flamefront, generally obtained from Lagrangian statistics. In fluid dynamics, such analyses are often performed by tracking fluid particles, which move

with the local flow velocity. However, in a turbulent flame, fluid particles do not remain on the flamefront, preventing the acquisition of statistics conditioned on the flamefront through particle tracking. Therefore, we will use the concept of flame particles. Flame particles are defined as a series of surface points that follow two rules: (1) they are always embedded on the flamefront, and (2) they co-move with it [84]. Since flame particles move with the flamefront, the time history of these particles and their properties (e.g., stretch rates, alignments) enable Lagrangian analysis. This, in turn, allows us to see how local segments of a flamefront evolve in time [85]. Flame particle tracking can be performed with great accuracy from the numerical simulation data due to its high temporal and spatial resolutions. While tracking from 2D high-speed PIV data is limited to the measurement plane, our previous study has shown that flame particle tracking from experimental data, which generally has lower spatial and temporal resolution than simulations, can still provide key insights [86].

In this study, to perform flame particle tracking using the 2D high-speed PIV data, we follow the methodology outlined by Chaudhuri et al. [86]. The movement of a 2D surface particle can be described as [85]

$$\frac{d}{dt}\mathbf{X}_{2D}^{F}(t) = \mathbf{U}_{2D}\left(\mathbf{X}_{2D}^{F}[t], t\right) + S_d\left(\mathbf{X}_{2D}^{F}[t], t\right)\mathbf{n}_{2D}^{F}\left(\mathbf{X}_{2D}^{F}[t], t\right) \tag{2.18}$$

Here $\mathbf{X}_{2D}^{F}$ is the location vector of a flame particle on the flamefront, $\mathbf{U}_{2D}$ is the local velocity vector, $\mathbf{n}_{2D}^{F}$ is the local surface normal, and S_d is the local displacement speed. The local displacement velocity can be calculated using the relation $S_d = S_L(1 + M_k\tilde{K})$, where M_k is the Markstein number. Further details of this tracking process can be found in [85]. Since the mixture used for this study has a Lewis number close to unity, we assume the Markstein number to be 0. We initiate a number of flame particles positioned on the flamefront near the bottom section of the flame and then allow them to evolve using Eq. 2.18. By identifying their locations on the flamefront and flame-conditioned variables

(e.g., stretch rates) at each instance, we build a time series for each particle. This process was then repeated over a long series of the PIV data to obtain the temporal evolution of flame-conditioned statics.

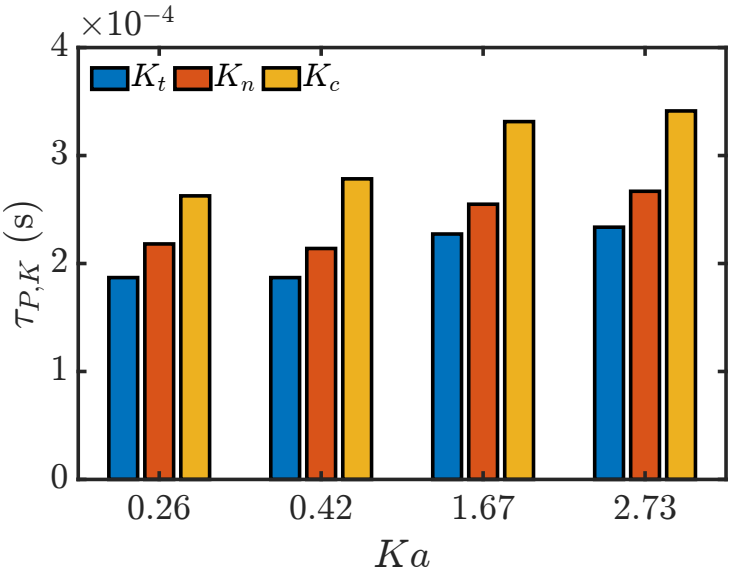


Figure 2.11. Persistence time scale τ_{P,K_t}, τ_{P,K_n}, and τ_{P,K_c} for different conditions

To quantify the evolution or time history of the stretch rates conditioned on these flame particles, we computed the persistence timescale τ_P for each component of the stretch rate. The persistence time scale for stretch rates was calculated by integrating the auto-correlation function [86],

$$\tau_{P,K_i} = \overline{\int_0^\infty \left\langle \frac{K_i\left(\mathbf{X}_{2D}^F[t],t\right) \times K_i\left(\mathbf{X}_{2D}^F[t+\tau],t+\tau\right)}{\mathrm{var}\left(K_i\right)} \right\rangle d\tau}. \tag{2.19}$$

Here $K_i(t)$ is the i^{th} stretch rate ($i \in \{c,t,n\}$) measured for at an instance t on a flame particle. $\langle . \rangle$ and $\overline{(\ .\ )}$ denote averaging over time and various flame particles, respectively.

In the statistical sense, the persistence time scale denotes the duration for which a parameter's value remains sustained. In Fig. 2.11, we compare the τ_{P,K_t}, τ_{P,K_n}, and τ_{P,K_c}, for all four experimental conditions. A few interesting observations can be made by comparing persistence time scales. First, we notice that, among the three components, τ_{P,K_c}

consistently had the largest value, while τ_{P,K_t} had the smallest value, with a difference of a factor of about 1.5. This suggests that pure curvature is more persistent than tangential and normal strains. In other words, the local curvature of the flamefront resists changes due to local turbulent fluctuations, which is also reflected in smaller variances in the PDFs of $\tilde{K_c}$(Fig. 2.9). On the other hand, the tangential strain rate is more responsive to turbulent fluctuations, and hence the shorter τ_{P,K_t} (Fig. 2.11) and larger variance in PDFs (Fig. 2.9). Moreover, we observe that the persistence time scales for all stretch rates increase with Ka. This suggests that, as the turbulence intensifies, the rate of decay for the local stretch rate slows down, which can be attributed to the weakened kinematic restoration [69]. Physically, the turbulence induces strains at multiple length scales, resulting in the wrinkling of the flamefront. As the flame propagates these wrinkles are gradually smoothed out. With an increase in Ka, the turbulence time scales become shorter than the flame time scales. Thus, the relaxation process due to flame propagation becomes slower, leading to longer persistent timescales.

2.3.4 Dispersion of flame particles and flamefront wrinkling

Next, we will analyze the dispersion of flame particles and relate them with local stretch in flamefronts. For Lagrangian fluid particle tracking in incompressible flows, it can be shown that the area (for 2D) or volume (for 3D) constructed by a fixed number of neighboring fluid particles remains constant. Thus, if the distance between two particles increases in one direction, it must decrease in at least one of the other two orthogonal directions. Based on this, the local stretching of fluid elements can be evaluated by tracking a set of fixed fluid particles in an unsteady, non-uniform flow. This approach has been used in many fluid problems to understand the underlying Lagrangian coherent structures (LCS) [98–100].

Naturally, an immediate question arises: can the straining on the flamefront be evaluated similarly by tracking flame particles? We recognize that the flame particles

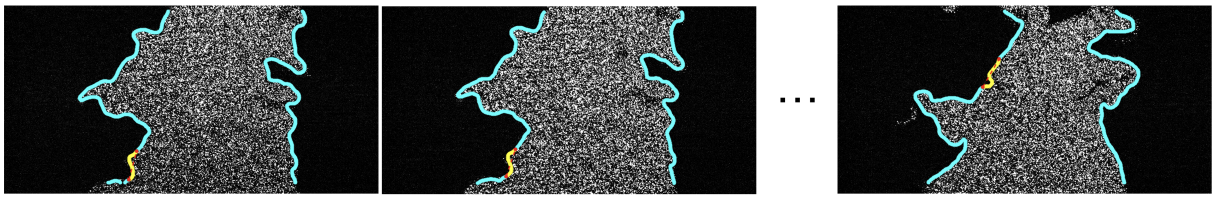


Figure 2.12. A schematic of tracking neighboring particles.

have additional constraints compared to fluid particles, as the former is conditioned to be on the flamefront. Because of this, the area or volume conformed by the neighboring flame particles is not conserved or constant, and thus, an LCS type of analysis cannot be performed with flame particles. However, we can track the distance between the individual particle pairs and quantify their dispersion.

This can be achieved by positioning two flame particles on the flamefront at an initial time $t = 0$, then tracking them until a fixed time, $t = T$. As the flame particles evolved, we recorded the length along the flamefront between the particle pairs, as shown in Fig. 2.12. We introduced the parameter "stretch factor", denoted as

$$\zeta = \frac{\Delta S_T}{\Delta S_0}, \tag{2.20}$$

where ΔS_0 represents the initial length of the flamefront between the two flame particles, and ΔS_T corresponds to the length at time T. Physically, ζ represents the degree of extension or compression (straining) of the flame segment between a fixed flame particle pair. By tracking a large number of flame particle pairs spanning over a long time recording, we can build the statistics of ζ. Special consideration was taken in optimizing the selection of T. As time progresses, flame particles on a Bunsen flame typically migrate toward the flame's tip. For a very large T, the tracked flame particles may, eventually, leave the image plane. On the other hand, a short T will limit the evolution of local wrinkles or straining of the flamefront. Since the persistent time scales for all the stretches were found to be roughly around 0.2-0.35 ms, we used $T = 1$ms. Note that we chose the value of T such that

it is sufficiently long to induce flamefront wrinkling and facilitate statistical convergence yet short enough to prevent particle pairs from leaving the image plane. Moreover, we examined the selection of $T = 1$ms and verified that slight changes in its value do not significantly influence the statistical results.

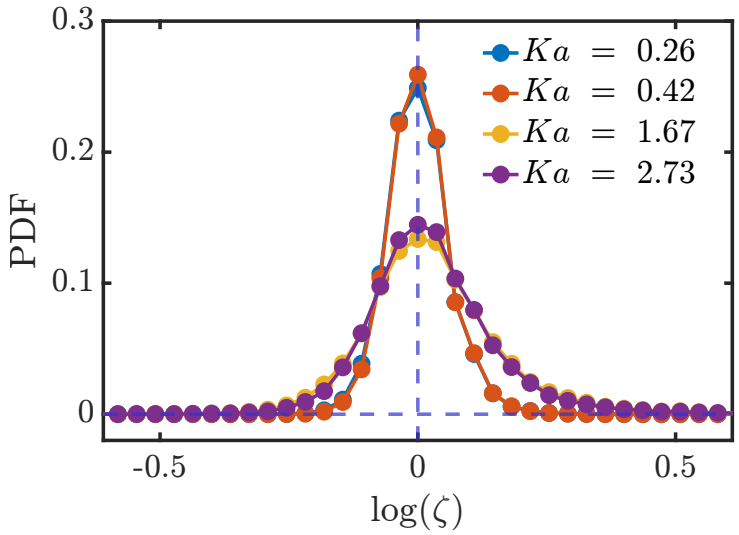


Figure 2.13. PDF profile of stretch factor ξ, note that all four profiles follow a log-normal distribution.

In Fig. 2.13, we compare PDFs of the logarithm of ζ for all four experimental conditions. Several interesting observations can be made from the comparison. First, we note that ζ can have > 1 ($\log(\zeta) > 0$) and < 1 ($\log(\zeta) < 0$) values, i.e., the flame length between two paired flamed particles can increase and decrease. The wrinkling of the flamefront due to turbulent eddies can stretch the local flamefront positively and negatively, thereby increasing or decreasing the flamefront length (or surface area), respectively. The mechanism of generating and destroying the flame surface area and particles has been studied in detail for a statistically planar turbulent flame by Daveynate et al. [101]. Second, it is evident that ζ follows a log-normal distribution (or $\log(\zeta)$ follows a normal distribution) for all four conditions. In turbulence, the cascading processes of eddies drive dissipative processes (e.g., of kinetic energy), and they can be modeled as log-normal distributions [102, 103]. Later, it was shown that scalar quantities also follow a log-normal

distribution [104]. Given that the generation and destruction of flamefronts in a turbulent flame are driven by eddies and their cascading processes, the PDFs of ζ display a log-normal distribution. Although kinematic restoration of flamefronts can be an additional mechanism for reducing wrinkled flamefronts, a log-normal distribution of ζ suggests a stronger effect of turbulent eddies. This is also evident from the third observation. The PDFs of ζ are almost identical across different T_bs for the same turbulence intensity or u'_0. For example, the conditions of Ka=0.26 and 0.42 have lower u'_0, and their PDFs of ζ are identical and narrower compared to the almost identical PDFs of Ka=1.67 and 2.73 conditions, which have higher u'_0. As the u'_0 or the turbulent Reynolds number (Re_T) increases, the scales of energetic eddies increase, which leads to a broader distribution of wrinkling. Consequently, the profile of the log-normal distribution becomes wider. The lack of variations in the PDF of ζ at various T_b (and S_L) suggests that the turbulent eddies are the primary mechanism for extending and contracting flamefronts in our experimental conditions.

2.4 Conclusion

In summary, we presented an experimental investigation of a turbulent Bunsen flame to evaluate various flame-conditioned statistics to assess flame-turbulence interactions. Below, we summarize the major findings of our investigation.

- First, we compared the velocity statistics near the flamefront with the statistics of the cold flow. This revealed a decrease in local r.m.s of velocity due to the flame, which can be attributed to thermal expansion. Furthermore, we observed that stronger turbulence intensity or a larger Karlovitz number weakens this effect of flame.

- Next, we analyzed the PDFs of different stretch rates, which were evaluated from the experimental data. The PDFs show long tails, a feature often observed in statistics measured in turbulent flows due to intermittency. Moreover, due to the broadening

of turbulent scales, the PDFs for stretch rates become wider with an increase in the Karlovitz number. Additionally, the joint scatter plots between pair-wise stretch rates display preferential distributions. The theoretical definitions of various stretch rates were then used to identify relations that describe such patterns.

- Finally, we used flame particle tracking to assess Lagrangian statistics. The temporal evolution of stretch rates conditioned on flame particles, which co-move with the flamefront, allows us to evaluate the persistent time scales. We found that the stretch rate due to curvature has a longer persistence time, making it the most resistant to change, compared to stretch rates due to normal and tangential strains. With an increase in Karlovitz number, the persistence time scale for all stretch rates increases due to the increased strength of turbulent eddies compared to flame propagation. By tracking the flame length between two flame particles over time, we also evaluated a stretch factor, which follows a log-normal distribution. This indicates that turbulence is the dominant mechanism in controlling the wrinkling of the flames for the conditions explored in this study.

This chapter is a reprint of the following published article:

Weng, Y., Potnis, A., Unni, V. R., Saha, A. (2024) Assessing local statistics of a premixed turbulent Bunsen flame. *AIAA Journal*, 1-9.

Chapter 3

Investigating polyhedral instability in a laminar Bunsen flame

3.1 Introduction

With the growing concern about the environmental impacts of traditional combustion processes, in recent years, close attention has been paid to reducing carbon emissions from energy-producing devices. Besides initiating programs on the development of renewable energies, strict regulations and restrictions are being placed on the combustion of fossil fuels. Although the usage of renewable energy, including wind and solar, has gained momentum in the last few years, it is generally believed that combustion will still occupy the largest share of the energy supply for the next few decades. Thus, the development of new strategies for producing cleaner energy from combustion becomes critical in meeting the world's energy demand with limited negative impacts on the environment. With its capability to produce zero carbon emission, hydrogen has gained global attention as a future energy-friendly fuel [105–108]. In particular, lean premixed hydrogen combustors are becoming increasingly popular for gas turbines and other industrial applications [109]. However, using hydrogen poses certain challenges for its usage as a sustainable energy source, including its lower explosion limits and, thus, difficulty in storage. Moreover, because hydrogen is significantly lighter than the air, hydrogen/air mixtures are susceptible to combustion instabilities, including flamefront instability. Once the flamefront instability

is triggered, cellular patterns appear on the flamefront and modify the smooth morphology of the premixed laminar flame. This wrinkling of the smooth flamefront, even in the absence of any external influences, increases the flame surface area and significantly alters the burning rate.

Flamefront cellular instabilities can be of two modes [110, 111]. The Darrieus-Landau (hydrodynamic) instability occurs due to a sharp temperature gradient across the flamefront and is particularly critical at high-pressure conditions [112, 113]. The diffusional-thermal cellular instability, on the other hand, occurs as a result of stronger thermal diffusion than mass diffusion, as noted by the sub-unity Lewis number, $Le < 1$ [114–116]. Here, Le is defined as the ratio between thermal to mass diffusivities of the mixture. Modern combustors operate at high-pressure, and crucially, combustion occurs at off-stoichiometric conditions (and hence non-unity Le), both of which increase the likelihood of cellular instabilities. Further, in these systems, these instabilities compete with turbulence to become the dominating mechanism that controls the dynamics of flame propagation [25, 61, 117, 118]. Thus, cellular instabilities are practically relevant from the perspective of the performance and operation of these devices. To that end, a large volume of theoretical, modeling, and experimental research has been devoted to various aspects of cellular instabilities, particularly in the context of idealized planar flames and unbounded propagating expanding flames. These studies have identified critical parameters to describe the onset of instabilities [119–121], their growth [122–127], stages of propagation [128], degree of acceleration [125, 128–130] as well as flame-induced turbulence [39, 131, 132].

The previous discussion and review illustrate the popularity of spherically expanding premixed flames to study cellular instabilities. These instabilities, however, also manifest in burner-stabilized flames, for example, Bunsen flames. A typical laminar Bunsen flame is usually axisymmetric and constitutes a smooth cone-shaped flamefront. However, under certain conditions, a polyhedral structure may appear, where the otherwise smooth cone-shaped flame becomes wrinkled. Several straight ridges appear from the bottom and extend

all the way to the tip of the conical flame and conform to a polyhedral geometry. Unlike the well-studied positively stretched expanding flame, the Bunsen flame has a dominant axial flow close to the nozzle [133], and the flame surface is negatively stretched. The cellular instabilities are promoted by negative stretch [134], and thus, they predominantly appear along radial lines in a Bunsen flame, which results in the structure of a polyhedral flame. Such polyhedral structure in a Bunsen flame was first observed by Smithells and Ingle [135] in rich benzene, pentane, and hexane mixture, which was subsequently confirmed to be caused due to a diffusive-thermal cellular instability.

Although relatively less-explored compared to its counterpart, the expanding flame, there have been a few foundational studies that paved the way for our current understanding of polyhedral Bunsen flames. For example, Markstein [136] reported that the transition between smooth and polyhedral flames can occur due to changes in flow rate, while Buckmaster [137] reported that the number of sides can vary greatly under various conditions. It was also shown that regions of polyhedral flames can have augmented or weakened burning, manifested by bright and dark edges, respectively, on flame chemiluminescence images [40, 138]. It was also reported that the location of ridges in a polyhedral flame may not be stable, as evidenced by unidirectional, bi-directional, or chaotic rotation of the edges with rapid changes in fuel concentration [138]. The stability of polyhedral flames, in general, was shown to be strongly dependent on the amount of heat loss to the burner and hence influenced by burner (nozzle) geometry. Buckmaster [137] used linear stability analysis to determine several key parameters to identify the critical condition for the manifestation of polyhedral flames. Furthermore, the rotational instability of the polyhedral structures was analyzed by considering the interaction of two harmonic unstable modes. Subsequently, the rotation instability was further investigated by Gorman et al. [139].

While the above discussion highlights the detailed work that investigated polyhedral flames, there is a lack of systematic study to delineate the effects of various operating

parameters on the stability and morphology of these flames. For example, in most studies, the experiments were conducted while changing two or more operating parameters, and hence, identification of their individual effects becomes challenging. Thus, we present a detailed experimental investigation of the dynamics and morphology of polyhedral flames and the effects of the adiabatic flame temperature (T_b), equivalence ratio (ϕ), and flow rate ($\dot{Q}$) on them. We conduct the study with practically relevant lean hydrogen and methane flames.

The rest of the manuscript is put forward in several sections. First, we discuss the experimental setup, diagnostic methods, and the mixture conditions studied. Subsequently, we present our primary findings and discuss the results in the context of flame theories. Finally, we conclude the manuscript with a summary of our investigation of polyhedral flames.

3.2 Experimental setup

Our experiments were conducted using a Bunsen burner designed with a cooling jacket to ensure constant temperature and prevent overheating of the burner tip. The detailed schematic of the experimental setup, along with the primary optical setup, is shown in Fig. 3.1. The central nozzle has an outer diameter of 15.2mm, while the inner diameter $D = 12.4$mm. We used a flat burner tip, which is made of brass. The geometry of the tip is critical since the flow field near the burner exit influences the flame configuration and stability.

The gaseous fuel (Hydrogen, H_2 or Methane, CH_4), Oxygen (O_2), and inert gases (Nitrogen, N_2 or Argon, Ar) were supplied in appropriate proportion from separate gas cylinders and were mixed in a small mixing chamber located upstream, before passing through the burner nozzle. The individual flow rates of these gases and the total volume flow rates were controlled by a number of digitally controlled mass flow controllers (Alicat

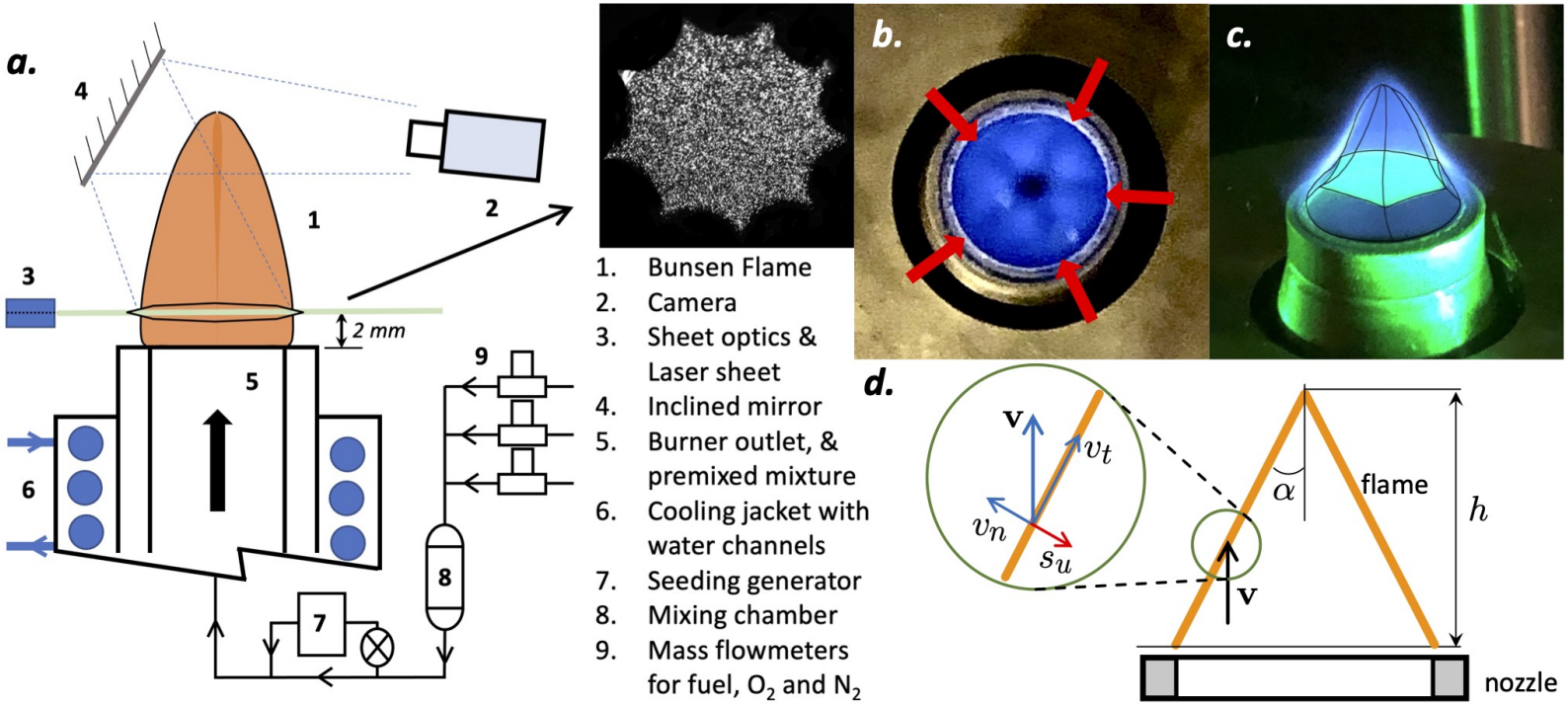


Figure 3.1. **(a.)** Schematic of the experimental setup with primary components and flow controllers. (inset: a typical Mie scattering image of a polyhedral flame). **(b.)** The top view chemiluminescence of a polyhedral flame (lean $CH_4 - O_2 - Ar$ mixture). The flame is split into 5 cells, whose ridges are marked by arrows. **(c.)** Side view of the same flame displaying planar Mie-scattering of horizontal cross-section as illuminated by the laser sheet. **d.** Schematic showing the coordinate system for the laminar Bunsen flame.

MCR: ±0.2% full scale). Since we intend to study the dynamics of laminar flames, the total flow rate ($\dot{Q}$) was maintained to be smaller than 30SLPM, beyond which the flame loses its steady shape and shows turbulent-like behavior. Note that the transition to turbulent flame can be identified from high-speed side view images as the conical steady Bunsen flame geometry transforms into a highly unsteady wrinkled structure with a large brush thickness and short flame length. One can define a Reynolds number as $Re = \rho U D/\mu$, where ρ and μ are the density and dynamic viscosity of the premixed gas, and the mean velocity (U) is related to the total volumetric flow rate by $U = 4\dot{Q}/(\pi D^2)$.

Most of the experiments were conducted using Hydrogen (H_2)-Oxygen (O_2)-Nitrogen (N_2) mixtures, which have practical importance in carbon-less combustion. We varied the H_2 to O_2 ratio or equivalence ratio (ϕ) to modulate Le, defined as the thermal to mass diffusivity of the mixture. For hydrogen flames, it is well-known that Le of the mixture decreases (or increases) with a decrease (or increase) in equivalence ratio (ϕ). The lean ($\phi < 1$) and rich ($\phi > 1$) hydrogen flames possess $Le < 1$ and $Le > 1$ mixtures, respectively [40]. Apart from H_2, a small set of experiments were conducted using Methane(CH_4)-Oxygen(O_2)-Argon(Ar) mixtures to confirm that the observed dynamics are fuel independent. Since the Le for $CH_4 - O_2 - N_2$ mixtures are close to unity, we used a heavier inter gas (Ar) to reduce the thermal diffusivity of the mixture and obtain the $Le < 1$ condition. Irrespective of the fuel, the adiabatic flame temperature T_b of the mixture was modulated by changing the ratio of oxygen and inert gas in the mixture. The fundamental flame properties, such as unstretched planar laminar flame speed, flame thickness, and adiabatic flame temperature, were evaluated through the PREMIXED module in Chemkin-Pro software, using GRI-3.0 [90] chemistry model. The conditions used in this study and their corresponding parameters are listed in Table 3.1.

In literature, there are several theoretical methods that can be used to obtain the mixture Lewis number [140]. Some of the common methods that have been proposed by various groups include Le based on deficient species [141], heat release-based weighted

average [142], volume-based weighted average [143], the diffusivity of the fuel [144] etc. Here, we used the definition based on the global reaction scheme proposed by Addabbo et al. [145]. The effective Lewis number of the mixture is given by

$$Le = 1 + \frac{(Le_E - 1) + (Le_D - 1)\mathcal{A}}{1 + \mathcal{A}} \tag{3.1}$$

where Le_D and Le_E are Lewis numbers of the deficient and excess species, respectively. $\mathcal{A}$ is the mixture strength, where

$$\mathcal{A} = 1 + Ze(\bar{\Phi} - 1) \tag{3.2}$$

and Ze is the Zel'dovich number,

$$Ze = \frac{E(T_b - T_0)}{RT_b^2} \tag{3.3}$$

where R is the gas constant, T_b is the adiabatic flame temperature, T_0 is the unburned gas temperature, and E is the activation energy. We discuss how to evaluate the activation energy in the supplementary materials. $\bar{\Phi}$ is the mass ratio of excess, to the deficient species, with respect to the stoichiometric mixture and is equal to, and reciprocal of the equivalence ratio for the rich ($\bar{\Phi} = \phi$), and lean ($\bar{\Phi} = 1/\phi$) mixtures, respectively. Further details are provided in Addabbo et al. [145]. The calculated Lewis numbers for all the mixtures are listed in Table 3.1. As expected, for all lean $H_2 - O_2 - N_2$ mixtures, Le is smaller than unity, and as the equivalence ratio increases, the Le increases.

As mentioned before, most of the experiments were performed with H_2, for which it was difficult to capture clear (blue) chemiluminescence images due to lack of CH^* in flames. As an alternative, we used planar Mie-scattering imaging to visualize the morphology of the Bunsen flames. For the Mie-scattering imaging, an Nd-YLF laser (wavelength 527nm) along with sheet-making optics was used to create an approximately 1mm thick laser

Table 3.1. List of experimental conditions, where ϕ is the equivalence ratio and T_b is the adiabatic temperature, $s_{u,0}$ is the unstretched planar laminar flame speed.

Mixture	T_b(K)	ϕ	O_2%	Le	$s_{u,0}$(cm/s)
H_2-O_2-N_2	1300 ± 10	0.5	14.5	0.406	6.15
		0.6	12.1	0.432	6.31
		0.7	10.3	0.466	6.03
		0.85	8.5	0.562	6.04
H_2-O_2-N_2	1350 ± 10	0.5	15.4	0.412	9.11
		0.6	12.8	0.437	8.97
		0.7	11	0.474	9.02
		0.85	9	0.571	8.51
H_2-O_2-N_2	1400 ± 10	0.5	16.3	0.417	12.4
		0.6	13.6	0.443	12.38
		0.7	11.6	0.48	11.95
		0.85	9.5	0.579	11.42
H_2-O_2-N_2	1450 ± 10	0.5	17.2	0.421	16.3
		0.6	14.3	0.448	15.94
		0.7	12.3	0.487	15.96
		0.85	10	0.588	15.43
H_2-O_2-N_2	1500 ± 10	0.5	18.2	0.426	21.17
		0.6	15.1	0.454	20.43
		0.7	12.9	0.493	19.86
		0.85	10.6	0.598	20.17
H_2-O_2-N_2	1550 ± 10	0.5	19.2	0.431	26.56
		0.6	15.9	0.459	25.53
		0.7	13.6	0.5	24.91
H_2-O_2-N_2	1600 ± 10	0.5	20.2	0.436	32.52
CH_4-O_2-Ar	1888	0.5	22	0.954	22.77

sheet. The premixed gas mixture passing through the burner was seeded with D.E.H.S. (di-ethyl hexyl sebacate) droplets with a mean size of $1 - 2\mu m$, which scattered the laser

light. The resultant Mie-scattering images were captured using a DSLR camera in our experiments. Near the flamefront, due to high temperature, these droplets evaporate, limiting the high seeding density only to the unburned side. Thus, when imaged, the Mie scattering from these seeding droplets displays the contour of the flamefront [39, 146]. Since we are mostly interested in observing the polyhedral geometry, we visualized the cross-section of the flame by placing the laser sheet horizontally at a distance $\sim$ 2mm from the burner exit and imaging the illuminated zone from the top using a 45° mirror, as shown in Fig. 3.1. The inset of Fig. 3.1a shows a typical Mie-scattering image. For CH_4 flames, chemiluminescence images can also be captured to observe the global flame shape (Fig. 3.1b and c).

Evaluation of the activation energy

We calculate the ratio of the activation energy (E) and the gas constant (R), E/R using the following the equation [147]:

$$\frac{E}{R} = 2\ T_b^2\ \frac{\mathrm{d}\left(\ln\left(\rho_u s_{u,0}\right)\right)}{\mathrm{d}T_b} \tag{3.4}$$

For each mixture, we simulate the 1-D flame using Chemkin's PREMIXED package and evaluate the unstretched planar laminar flame speed at different initial temperatures. The value of E/R can be then evaluated from linear regression of $\mathrm{d}\left(\ln\left(\rho_u s_{u,0}\right)\right)/\mathrm{d}T_b$ vs. $1/(2T_b^2)$ plots.

3.3 Results

To explore the morphology and transitional boundaries of polyhedral Bunsen flames, we first established the flame at a condition with fixed ϕ and T_b, by igniting the premixed gas emanating from the nozzle. Then, while keeping the mixture condition fixed, we increased or decreased the volumetric flow rate $\dot{Q}$ in small increments using the mass flow

controllers. We waited for the flame to achieve a steady state after each incremental change and acquired images of the flame morphology at each condition. Here, it is important to note that a change in $\dot{Q}$ alters the length of a stable Bunsen flame. Furthermore, there exist two limits of $\dot{Q}$ between which a stable Bunsen flame can be established. When the $\dot{Q}$ is smaller than a critical lower limit, the flame moves inside the burner tube, and flashback is observed. We used this flow condition as the lower critical point for each case. At a very high $\dot{Q}$, blow-off is observed, in that the flame detaches from the Burner and extinguishes. There also exists a $\dot{Q}$ (approximately 30SLPM for the current Burner) beyond which the flow emanating from the Burner becomes turbulent. Recognizing that the presence of turbulence can significantly modify the transitional boundaries of cellular instabilities, in our experiments, we used this limit as the largest operational flow rate and limited our study to $\dot{Q} \leq$ 30SLPM. The general shape and strength of the flame are also sensitive to change in ϕ or Le. This is a common behavior of stretched flames and has been extensively discussed in the literature in the context of smooth, stable laminar flames. Following the above-mentioned procedure, we performed experiments at fixed ϕ (or Le) and T_b for cases detailed in Table. 3.1, and identified the range of flow rates for which polyhedral flames can be observed. Simultaneously, we also monitored the changes in the morphology of the polyhedral structures by analyzing the Mie-scattering images.

3.3.1 Regime Maps

By repeated experiments for a large range of ϕ (or Le) and T_b, we identified the range of $\dot{Q}$ over which polyhedral instabilities were observed. The observations can be presented in the form of regime maps, which we will discuss next.

T_b dependence

To delineate the effect of T_b on the polyhedral cellular instability, we plotted regime maps at fixed ϕ (or Le) for lean $H_2 - O_2 - N_2$ flames. These maps were constructed by identifying the state of the flame over a range of $\dot{Q}$ for various T_bs. The regime maps for four different ϕ (or Le) are shown in Fig. 3.2. Different symbols were used in the regime map to identify the state of the flames, e.g. stars: polyhedral flame, circles: smooth laminar flame, square: flashback. We notice that at any T_b, the lowest flow rate required for polyhedral flame ($\dot{Q}_{min}$) was limited by flashback (green circles). This observation is, in general, true for all the conditions we have studied. The regime map also shows that, with increase in T_b, the $\dot{Q}_{min}$ increases (Fig. 3.2a-d). This can be attributed to the increased flame speed ($S_{u,0}$) with T_b and hence, a larger critical flow speed (or $\dot{Q}$) required to avoid flashback.

At a fixed T_b, for $\dot{Q} > \dot{Q}_{min}$, we observe the continued existence of the polyhedral structure over a range of flow rate until we reach another critical value $\dot{Q}_{\max}$. At this critical flow rate $\dot{Q}_{\max}$, the flame becomes smooth and devoid of any polyhedral structures (Fig. 3.2 a-d). This transition from polyhedral to a smooth morphology due to an increase in flow rate was also reported in previous studies [137, 138, 148]. However, no clear explanation was provided about the underlying physics of this transition. Later in the manuscript (Section 3.3.3), we will show that this transition can be explained by an analysis of residence time.

In Fig. 3.2, we can also observe that the $\dot{Q}_{\max}$ decreases as we move to higher T_b. The flow rate regime over which polyhedral flames can be observed, thus, can be defined as

$$\dot{Q}_{min} < \dot{Q} < \dot{Q}_{max} \tag{3.5}$$

Since both the $\dot{Q}_{min}$ and $\dot{Q}_{\max}$ increase with T_b, there exists a critical value ($T_{b,m}$) for

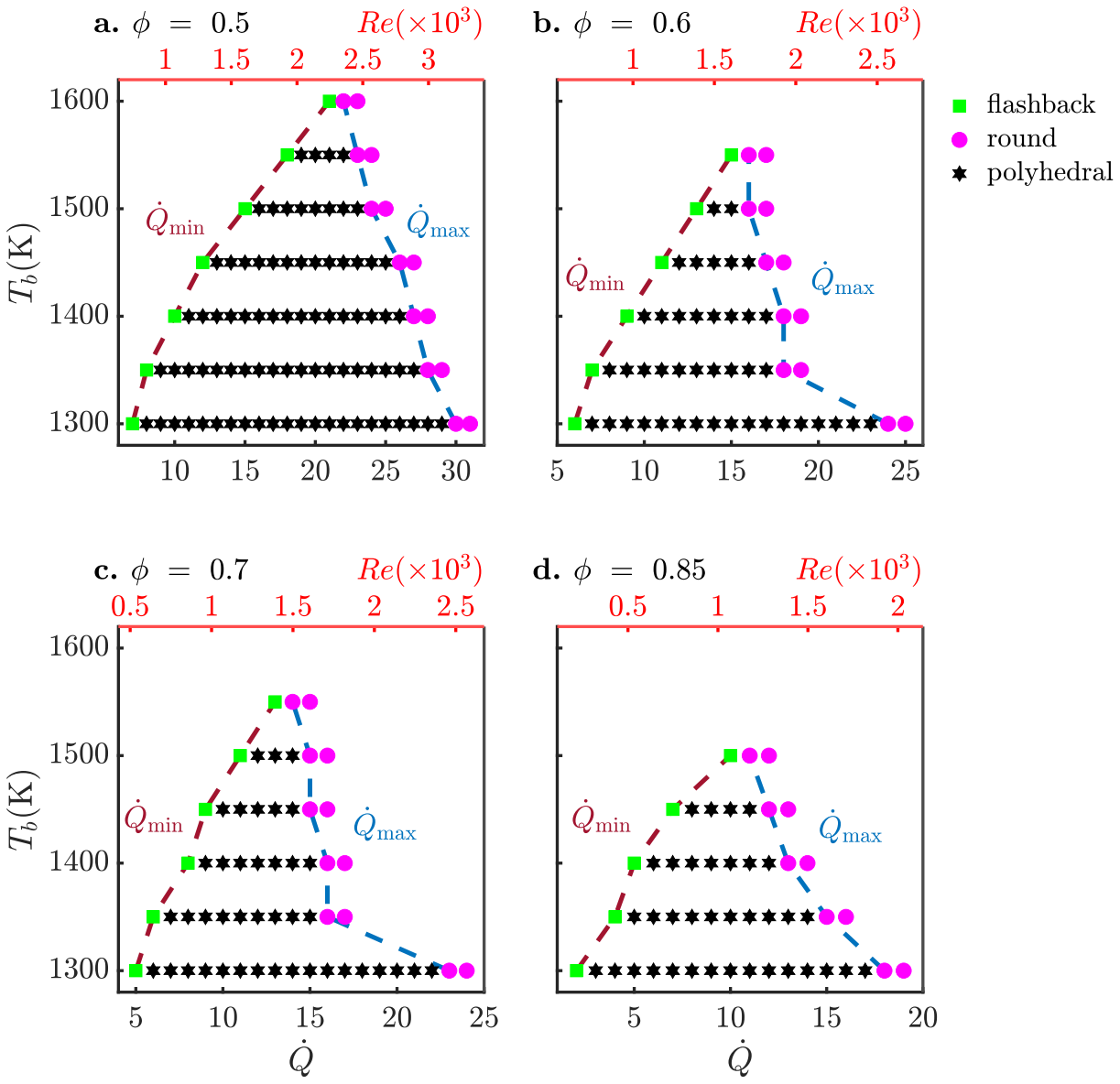


Figure 3.2. Regime map for $H_2 - O_2 - N_2$ flames at fixed Le. Flame states are shown as a function of Re and flame temperature (T_b). (**a**) $\phi = 0.5$, (**b**) $\phi = 0.6$, (**c**) $\phi = 0.7$, (**d**) $\phi = 0.85$. As T_b increases, the range of flow rate that polyhedral flames appear evidently reduces, and ultimately, no polyhedral structure can be observed above a certain T_b for the given ϕ.

a fixed ϕ (or Le), beyond which polyhedral flames can not be observed. This critical temperature, $T_{b,m}$ increases as the ϕ (and Le for H_2-flames Le) decreases ($T_{b,m} = 1600$K for $\phi = 0.5$ and $T_{b,m} = 1500$K for $\phi = 0.85$). Comparison of the regime maps for four different ϕ (or Le) (Fig. 3.2a to d) confirms that, as we decrease Le, the range of conditions

favorable for a polyhedral flame becomes larger. This extension is caused by the stronger diffusional-thermal instability for smaller Le flames.

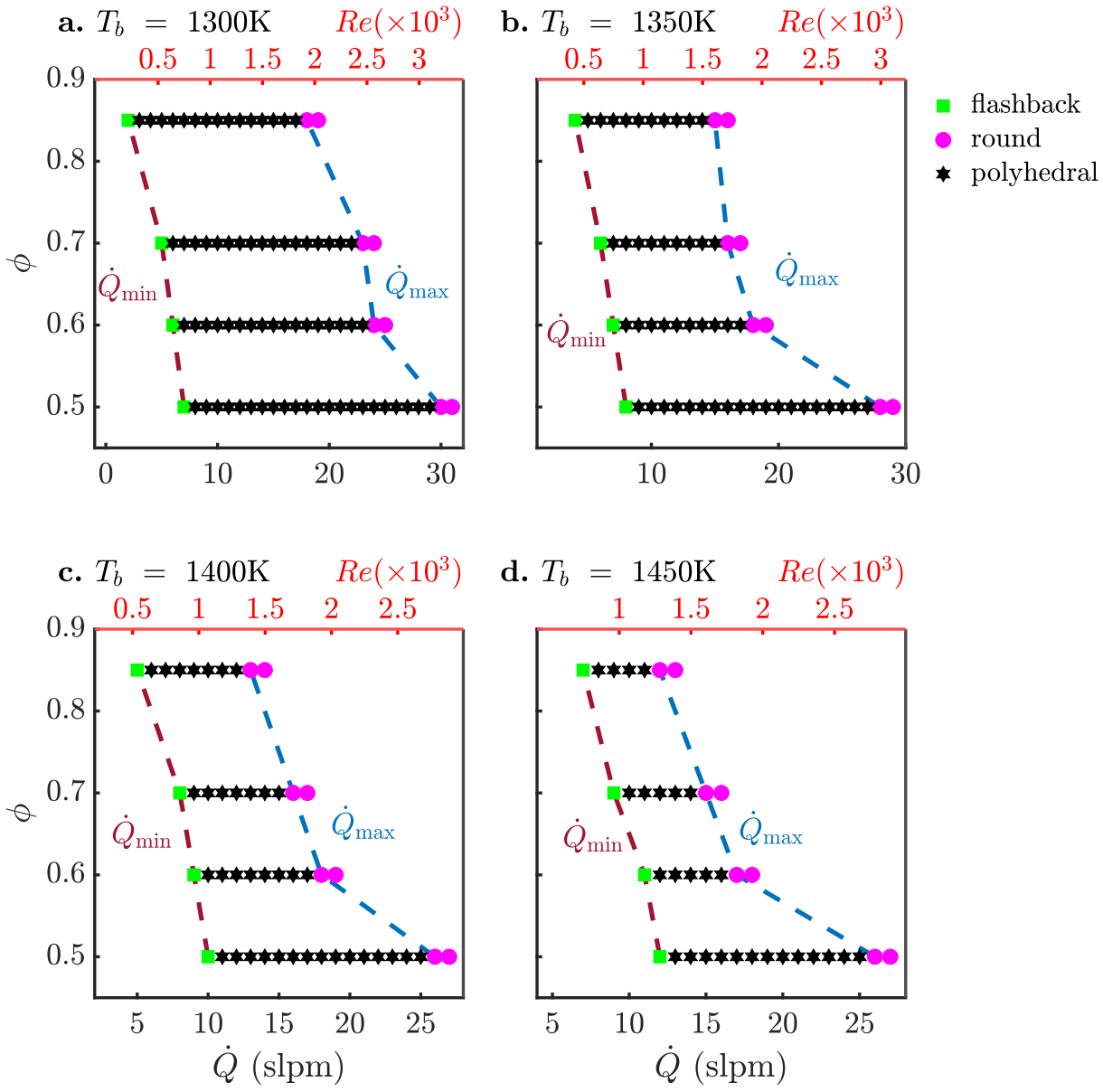


Figure 3.3. Regime map for $H_2 - O_2 - N_2$ flames at fixed T_b. Flame states are shown as functions of Re and phi. (**a**) T_b = 1300K, (**b**) T_b = 1350K, (**c**) T_b = 1400K, (**d**) T_b = 1450K.

Le **dependence**

Next, we will discuss the role of Le on the instability by potting the state of the flames as a function of ϕ and $\dot{Q}$ at fixed T_b. Figure 3.3 shows such regime maps for four different T_bs. It is to be noted that for lean ($\phi < 1$) $H_2 - O_2 - N_2$ flames, Le is less than unity, and it decreases with a decrease in ϕ [40]. In general, we observe a similar trend between all ϕ (or Le conditions) in that, at any given ϕ, the polyhedral flames are observed between an upper and lower limit of flow rates $\dot{Q}_{min} < \dot{Q} < \dot{Q}_{max}$. The $\dot{Q}_{min}$, which is bounded by flashback, decreases with an increase in ϕ or Le. This is consistent with the literature on flashback [149, 150], which has shown that the critical flow rate required for flashback decreases with an increase in Le.

At the other extreme, $\dot{Q}_{\max}$, at which the polyhedral flame transforms into a smooth flame, also decreases with an increase in ϕ or Le (Fig. 3.3). Furthermore, the overall range of flow rate for which the polyhedral flames are observed becomes larger with a decrease in T_b (Fig. 3.3a-d). We will show that the boundary depends on the residence time scale in Section 3.3.3.

3.3.2 Morphology analysis

In this section, we will discuss the changes in the morphology of the polyhedral flames with changes in the operating conditions. Previous experimental studies have shown that the mixture condition and flow rate can alter the number of ridges of a polyhedral flame. However, a detailed description and a systematic investigation are lacking. In general, at the onset of instability, the otherwise smooth conical Bunsen flame forms ridges along the length of the flame, which presents as a polyhedral structure. At this stage, the horizontal cross-section of the flame appears to be a polygon as shown in Fig. 3.1c. As we vary the $\dot{Q}$ or Le, we observe changes in the number of ridges or the number of sides of the polygon, as seen in the horizontal cross-section. Within our experimental conditions,

for lean H_2 flames, the number of the ridges (N) varied from 7 to 20, while for the CH_4 flame, the variation in N was much narrower, from 3 to 7.

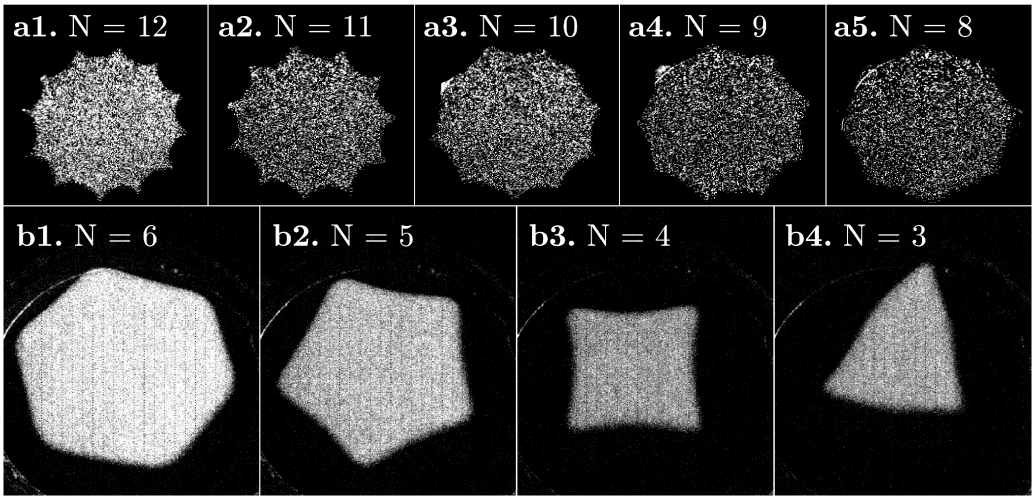


Figure 3.4. A few samples of Mie-scattering images of a horizontal cross-section of polyhedral flames, the numbers of edges N are noted in the images. The first row (from **a1** to **a5**) corresponds to a lean $H_2 - O_2 - N_2$ flame with $T_b = 1300$K, $\dot{Q} = 10$SLPM. **a1.** $\phi = 0.4$, 12 ridges; **a2.** $\phi = 0.5$, 11 ridges; **a3.** $\phi = 0.6$, 10 ridges; **a4.** $\phi = 0.7$, 9 ridges; **a5.** $\phi = 0.85$, 8 ridges. As ϕ increases, the number of edges decreases. The second row (from **b1** to **b4**) corresponds to lean $CH_4 - O_2 - Ar$ flame with $\phi = 0.5$, oxygen ratio at 22%, from left to right: $\dot{Q}$ reduces from 5 to 2SLPM. As $\dot{Q}$ decreases, the number of edges decreases.

Figure 3.4 shows the typical horizontal cross-sections of polyhedral flames. The top row consists of images from lean $H_2 - O_2 - N_2$ flames at five different ϕ or Le at fixed $\dot{Q} \approx 10$ SLPM and $T_b = 1300$K. We notice that from left to right (a1 to a5), the Le of the mixture increases, and the number of ridges of the polyhedral structure, N, decreases. In the second row of Fig. 3.4, the cross sections of CH_4 flames are shown. These images correspond to flames at different flow rates but at fixed Le ($\phi = 0.5$) and $T_b \approx 1888$K. In particular, from left to right (b1 to b4), $\dot{Q}$ is decreasing, which also reduces the number of ridges (N) in the polyhedral geometry.

To explain these observed dynamics and to analyze the flame morphologies, a dispersion relation will be used. While different forms of dispersion relations for flamefront instability have been developed by various research groups, including Pelce and Clavin [2],

Matalon and Matkowsky [151, 152] and Frankel and Sivashinsky [153], we will use the dispersion relation derived by [137]. However, other dispersion relations will qualitatively depict similar dynamics. Buckmaster [137] expressed the dispersion relation in the non-dimensional as

$$\tilde{\omega} \;=\; -4\tilde{k}^4 - \tilde{k}^2\left(1 + \frac{lJ_s}{2\tilde{T}_b^2}\right) - \frac{\theta(\tilde{T}_s - \tilde{T}_b + J_s)}{2\tilde{T}_b^2}. \tag{3.6}$$

Note that all the variables in this expression are in non-dimensional forms, as shown in [154]. $\tilde{\omega}$ is the non-dimensional growth rate, $\tilde{k}$ is the non-dimensional wavenumber. J_s is the mass flux fraction of the mixture through the burner, expressed as

$$J_s = \frac{\tilde{T}_b^2}{\theta}\sqrt{2\ Da\ Le\ \exp(-\frac{\theta}{\tilde{T}_b})}. \tag{3.7}$$

Here, $\tilde{T}_s$ is the non-dimensional temperature of the burner surface, $\tilde{T}_b$ is the non-dimensional adiabatic flame temperature, θ is the non-dimensional activation energy (a brief description of the activation energy is evaluated can be found in the supplementary material). The temperatures, in the dispersion relation, are non-dimensionalized by a temperature scale defined as $T_c = T_b - T_0$, where T_0 is the unburned gas temperature. Da is the Damkohler number and $l = \theta(1 - Le^{-1})$ is a measure of Le.

Equation 3.6 provides a range of wavenumber for which the growth rate is positive, and hence, the instability can manifest, and polyhedral structures are observed. The $\tilde{k}$ values where $\tilde{\omega} = 0$ draw the boundary of stability as shown in Fig. 3.5. The figure shows the typical range of wavenumbers, for which the flames are unstable as a function of Le (Fig. 3.5a).

The second term on the right-hand side of Eq. 3.6 demonstrates the Lewis number effect through the quantity, l. For $Le < 1$ (> 1), the l is negative (positive) which augments (suppresses) $\tilde{\omega}$, and hence the instability. This is evidenced in Fig. 3.5a in the form of a critical $Le(\approx 1)$, beyond which the flame is stable for all $\tilde{k}$.

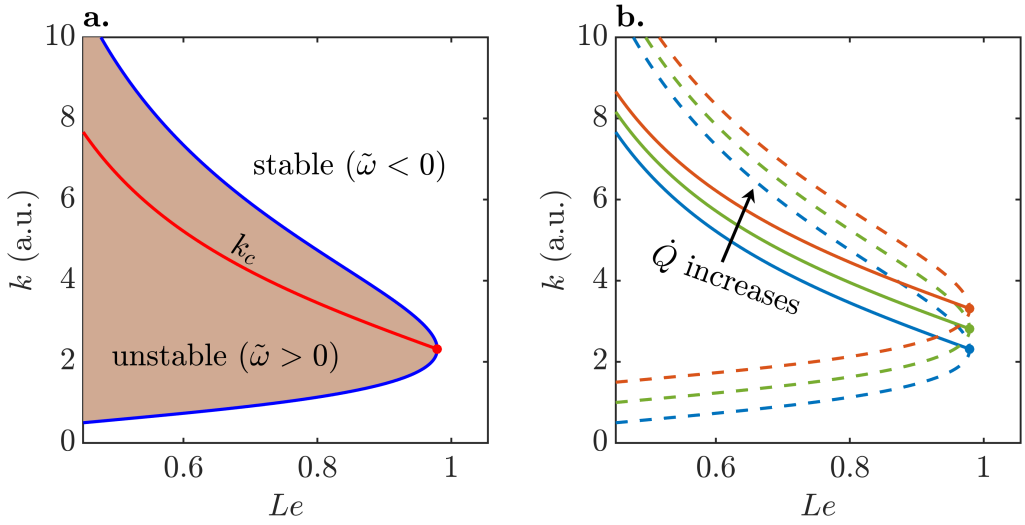


Figure 3.5. **(a.)** Stability map as function of Le indicating the unstable modes of polyhedral flames. The shaded area corresponds to conditions with a positive growth rate and denotes the presence of cellular instability and polyhedral flames. The red line indicates critical wavenumber, $\tilde{k}_c$, corresponding to the maximum growth rate, which determines the number of edges in polyhedral flames. **(b.)** Stability map as $\dot{Q}$ changes.

The number of ridges, N, however, is dictated by the critical (dimensional) wavenumber k_c corresponding to the maximum growth rate. This can be assessed by setting $\partial\tilde{\omega}/\partial\tilde{k} = 0$ in Eq. 3.6, which leads to the non-dimensional critical wavenumber $\tilde{k}_c$, where

$$\tilde{k}_c = \sqrt{(-1/8)(1 + lJ_S/(2T_b^2))} \tag{3.8}$$

By using the definition of non-dimensional wavenumber $\tilde{k}_c = k_c L_c$ [154], where $L_c = \mathcal{D}_{\text{th}}/U$ is the characteristic length scale, and $\mathcal{D}_{\text{th}}$ is the thermal diffusivity, we can express

$$k_c = \frac{4\dot{Q}}{\pi D^2 \mathcal{D}_{\text{th}}} \sqrt{-\frac{1}{8}(1 + \frac{lJ_S}{2T_b^2})}. \tag{3.9}$$

Since $N \sim Dk_c$, and D (the burner diameter) is a constant, we can expect the number of ridges to be proportional to the critical wavenumber ($N \sim k_c$). To assess the role of Le on

the number of ridges, we plotted the k_c as a function of the Le for fixed $\tilde{T}_b$ in Fig. 3.5a (red line). The plot shows that k_c decreases with an increase in Le, hence we observe a reduction in the number of edges (N) in Fig. 3.4a as ϕ (or Le) is increased for a lean H_2 flame. Equation 3.9 also shows that for a fixed Le and T_b, the k_c (and N) decreases as the flow rate $\dot{Q}$ decreases, as shown in Fig. 3.5b, which corroborates with the experimental observation for CH_4 flames (Fig. 3.4b).

3.3.3 Scaling of the the flow rate upper limit

While discussing the regime maps in section 3.3.1, we identified that there exists an upper limit of flow rate ($\dot{Q}_{\max}$), beyond which polyhedral instability disappears. This observation was reported in previous studies [137], although no quantitative reasoning was provided. In this study, we also notice that an increase in Le or T_b, $\dot{Q}_{\max}$ decreases. In the following, we will derive a scaling relation for this $\dot{Q}_{\max}$ and discuss its dependence on the operating conditions. Physically, the polyhedral instability requires a finite time (τ_g) to develop, which is inversely proportional to the maximum growth rate ($\tau_g \sim 1/\omega_c$). Here, ω_c corresponds to the maximum growth rate, which can be derived from the dispersion relation in Eq. 3.6. On the other hand, the flow emanating from the nozzle has a residence time scale (τ_r). We expect that for instability to develop, the residence time must be larger than the growth time for the inability ($\tau_r > \tau_g$). A similar argument for slot burners was also made by Rosen and Axelbaum [155] to derive the limiting condition for instabilities. In the present study, we can define the τ_r as the time taken by a fluid particle to reach the flame height h from the nozzle exit and can be expressed as

$$\tau_r \sim \frac{h/\cos\alpha}{v_t} = \frac{h}{U\cos^2\alpha} = \frac{\pi D^2 h}{4\dot{Q}\cos^2\alpha}. \tag{3.10}$$

Here, the tangential component of the flow velocity along the flame surface is $v_t = U/\cos\alpha$, where α is the half cone angle of the Bunsen flame (shown in Fig. 3.1d). By assuming the

Bunsen flame to be a perfect cone and using the theoretical relation between unstretched planar flame speed ($s_{u,0}$) and half cone angle using the following equation [40]:

$$\cos\alpha = \sqrt{1-(s_{u,0}/U)^2} \tag{3.11}$$

we can rewrite the τ_r as

$$\tau_r \sim \frac{\pi D^2 h}{4\dot{Q}\left[1-\left((\pi/4)s_{u,0}D^2/\dot{Q}\right)^2\right]} \tag{3.12}$$

Both Eqs. 3.10 and 3.12 show that the the residence time, τ_r decreases with increase in flow rate ($\dot{Q}$), for a fixed mixture condition (ϕ and T_b). When the $\dot{Q}$ becomes so large that $\tau_r < \tau_g$, the cellular structure cannot develop due to limited residence time. Thus, there exists a maximum flow rate, $\dot{Q}_{\max}$, beyond which polyhedral structure cannot be observed. This upper limit, $\dot{Q}_{\max}$, can be theoretically estimated with the limiting condition of $\tau_r/\tau_g \approx 1$. By substituting the expression for the critical wavenumber $\tilde{k}_c$ (Eq. 3.9), in the dispersion relation (Eq. 3.6), we find the non-dimensional timescale for instability

$$\tilde{\tau}_g = \tilde{\omega}_c^{-1} = \left[\frac{1}{16}\left(1+\frac{lJ_s}{2\tilde{T}_b^2}\right)^2 - \frac{\theta(\tilde{T}_s-\tilde{T}_b+J_s)}{2\tilde{T}_b^2}\right]^{-1}. \tag{3.13}$$

On the other hand, we can evaluate the non-dimensional residence time ($\tilde{\tau}_r = \tau_r/t_F$) by using Eq. 3.12. Here, $t_F = \delta_0/s_{u,0}$ is the flame timescale. In Fig. 3.6(a) we plotted $\tilde{\tau}_r/\tilde{\tau}_g$ for a fixed T_b and few different ϕ or Le. First, we observe that for any given ϕ, $\tilde{\tau}_r/\tilde{\tau}_g$ decreases with increase in $\dot{Q}$, and crosses the theoretical limit of $\tilde{\tau}_r/\tilde{\tau}_g = 1$ at a critical $\dot{Q}$. This value identifies the theoretical estimation of $\dot{Q}_{\max}$, beyond which instability cannot be observed. Furthermore, we observe that the $\tilde{\tau}_r/\tilde{\tau}_g$ lines shift to left as ϕ increases, and hence, the theoretical $\dot{Q}_{\max}$ becomes smaller with increase in ϕ or Le. This corroborates with the experimental findings in Fig. 3.2. Similarly, in Fig. 3.6(b) we plotted $\tilde{\tau}_r/\tilde{\tau}_g$ for

a fixed ϕ and a few different T_bs. We observe that, as T_b increases, the theoretical limit of the higher flow rate $\dot{Q}_{\max}$ decreases, a trend also observed in experiments (Fig. 3.3). We also notice that the theoretical $\dot{Q}_{\max}$ values are in the same range of experimentally observed values. Some discrepancies are expected as the scaling analysis involves several simplifications in assessing the timescales.

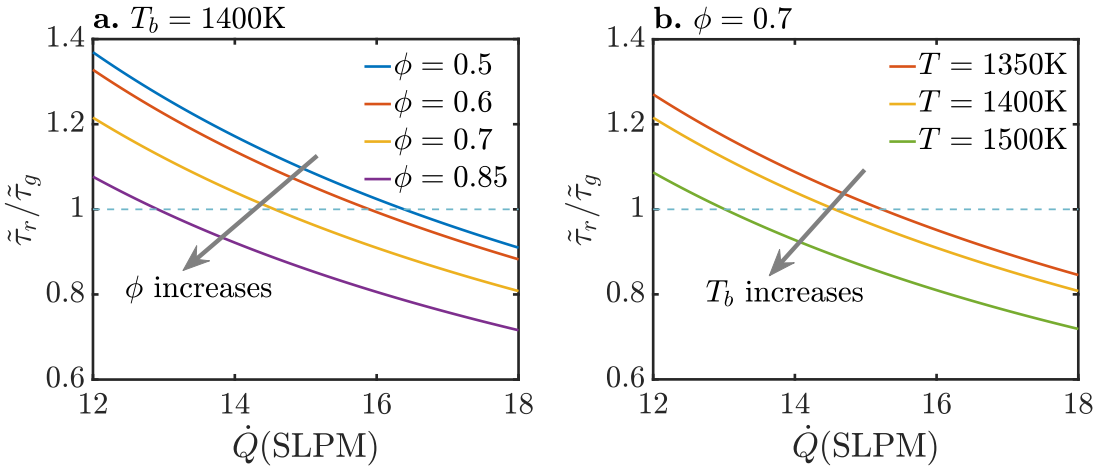


Figure 3.6. $\tilde{\tau}_r/\tilde{\tau}_g$ as function of $\dot{Q}$ for (a) different ϕ and (b) T_b based on the scaling analyses. $\dot{Q}$ corresponding to $\tilde{\tau}_r/\tilde{\tau}_g = 1$, refers to the theoretical estimation of $\dot{Q}_{\max}$.

Stability analysis using another model

Here we will discuss the dispersion relation based on work by Pelce & Clavin [2], Matalon & Matknowsky [3, 4] and Frankel & Sivasinsky [5]

$$\omega = \frac{1}{2}(\sigma - 1)s_{u,0}k - \frac{1}{2}s_{u,0}\delta_0\left(Le_{\text{eff}} - Le^*_{\text{eff}}\right)k^2 - 4\mathcal{D}_{\text{th}}\delta_0^2 k^4 \tag{3.14}$$

where σ is the ratio thermal expansion, $s_{u,0}$ is the laminar flame speed, δ_0 is the laminar flame thickness, Le_{eff} and Le^*_{eff} are the effect Lewis number and its critical value, $\mathcal{D}_{\text{th}}$ is the thermal diffusivity of the mixture. Qualitatively, the model shows a similar behavior, in that with a decrease in Le, the growth rate increases or instability become stronger.

As an example, we will plot the growth rate for some of our experimental conditions. We use the flames with a fixed flame temperature ($T_b = 1400$K), and the four different

equivalence ratios ranging from 0.5 to 0.85. The flame parameters for these flames are evaluated from Chemkin simulations. As shown in Fig. 3.7, because the conditions are with sub unity Lewis number, each curve has a range of k with a growth rate greater than zero, i.e. the flame is cellularly unstable. As the ϕ and hence, Le increases, the range of k that is with a positive growth rate becomes smaller, and the maximum growth rate also decreases, which is consistent with our experimental observation. Moreover, as the equivalence ratio increases, the critical k that corresponds to the maximum growth rate drops, which can explain the morphology change.

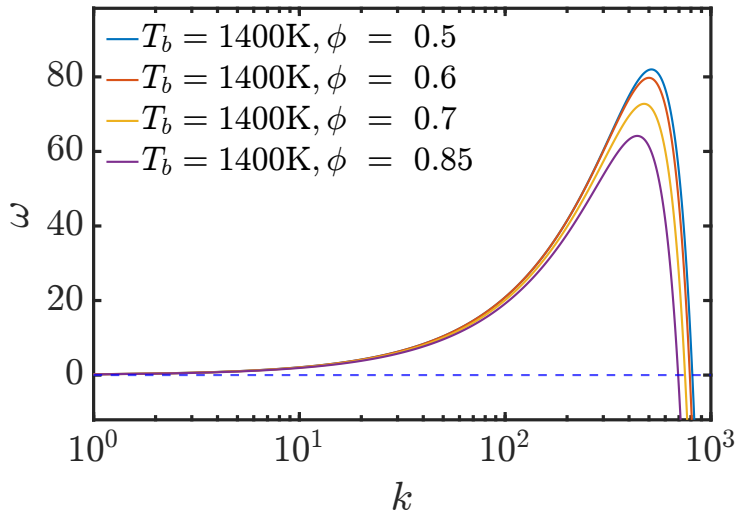


Figure 3.7. Dispersion relation at different flame conditions using the model from the work by Pelce & Clavin [2], Matalon & Matknowsky [3, 4] and Frankel & Sivasinsky [5]

In summary, the dispersion discussed above qualitatively shows similar behavior to the dispersion relation presented by Buckmaster [137]. Moreover, both of them corroborate the experimental observations.

3.4 Conclusion

In summary, we have presented a comprehensive experimental study of polyhedral Bunsen flames. Hydrogen was used as the primary fuel for the experimental investigation. Hydrogen is considered to be one of the viable alternate fuels to limit the emission of

greenhouse gases from combustors. Although preferred for reducing emissions, owing to its sub-unity Le, lean hydrogen-air mixtures are prone to cellular instabilities, such as polyhedral Bunsen flames.

We studied the dynamics and morphology of such flames for a range of equivalence ratios (or Le), T_b, and $\dot{Q}$. We discerned that the polyhedral structures of Bunsen flame can occur for $Le < 1$ conditions only for a certain range of flow rates. The lower bound of the flow rate is limited by flashback, which increases with T_b, but decreases with Le. The upper bound of the flow rate at which a polyhedral flame transforms into a smooth flame is controlled by the residence time scale τ_r. For a Bunsen flame, this upper limit decreases with both T_b and Le. This behavior can be attributed to the competition between the growth rate of instabilities and the residence time of the flow. A scaling analysis was performed to derive a theoretical estimation for this upper bound of the flow rate for which polyhedral instability can be observed. Regime maps constructed using the experimental data for a large range of conditions demonstrate that for a fixed Le, the range of flow rate for which polyhedral flames are observed decreases with an increase in T_b. Furthermore, there exists a maximum temperature beyond which polyhedral Bunsen flames are not observed for any flow rate.

Subsequently, we have also carefully identified the number of edges or ridges in the polyhedral structure formed during the instability. Experimentally, we found that the number of ridges decreases with an increase in Le at a fixed flow rate and flame temperature. On the other hand, the number of edges increases with an increase in flow rate for a fixed Le and flame temperature. These behaviors were systematically observed for both hydrogen and methane flames. A detailed analysis of the dispersion relation and the critical wavenumber for maximum growth rate was performed. The critical wavenumber corresponding to the maximum growth rate of the instability, which controls the number of edges, was shown to decrease and increase with an increase in the mixture Le and the $\dot{Q}$, respectively.

This chapter is a reprint of the following published article:

Weng, Y., Potnis, A., Saha, A. (2023). Regime and morphology of polyhedral Bunsen flames. *Combustion and Flame, 248*, 112585.

Chapter 4

Investigating subharmonic bifurcation in a laminar thermoacoustic system

4.1 Introduction

Modern combustion devices often experience large pressure fluctuations arising from the interaction between the acoustic field and unsteady heat release rate, which can cause severe damage to the engine hardware. This phenomenon, known as thermoacoustic instability, affects the performance and limits the operating conditions for devices, such as gas turbines, rocket engines, and industrial furnaces, which house flames in a closed chamber [1, 10–12, 156]. Over the past few decades, the broad adoption of LPP (lean premixed pre-vaporized) combustors for gas turbines paved the path for reducing greenhouse gas emissions. Yet, the susceptibility of these lean premixed flames to perturbations increases the risk of thermoacoustic instability, driving a significant amount of research in this area [157]. Many of these studies on thermoacoustic instability primarily focus on identifying the regime of periodic oscillation and its amplitude. However, recent experiments revealed that thermoacoustic systems can exhibit intricate dynamics beyond periodicity, including quasi-periodic oscillation [158], chaos [44, 159, 160], and strange nonchaos [161, 162].

These complex dynamics are caused by the non-linearities associated with chemical reactions, heat release, heat/mass/energy transfer [160, 163], and nonlinear couplings between the flame and the acoustic field. Exploring the fundamental physics behind these complex dynamics might uncover early warning signals for predicting thermoacoustic instability. In general, the complex nature of chemical reactions is the major cause of the inherent non-linearities of the flame and its nonlinear response to the acoustic perturbation [164]. Moreover, various parameters, including turbulence, vortex shielding, temperature fields [165], can introduce non-linearities depending on the specific setup.

In laminar thermoacoustic systems, the transition route to chaos through quasi-periodic oscillation has been observed in multiple studies, and many of which use a Rijke tube. With a special place in thermoacoustic studies, Rijke tube provides a relatively simple self-excited flame configuration where several dynamics can be triggered by modulating the axial location of the flame, flow rates, and mixture composition. Although it is likely the simplest configuration of a thermoacoustic system, among prior experimental investigations with Rijke tubes, laminar multi-flame burners are often employed in experiments where diverse and rich dynamics are observed [44, 166, 167]. Such configuration could potentially alters the behavior of the Rijke tube for two reasons. Firstly, the resulting dynamic interactions between adjacent flames can significantly change the topology of the overall flamefront and, thus, alter its characteristics, such as the surface area, and ultimately, the total burning rate [168,169]. While most studies focus on the variation of global parameters of the interacting flame, only a few discuss their effects on their response under system acoustics or thermoacoustic instability. For instance, Culler et al. [170] investigates the effect of asymmetrical and unsymmetrical equivalence ratios in a multi-flame combustor, noting that the nozzle configuration greatly influences the bifurcation as well as fuel staging for a gas turbine engine. Researchers also found the drastic changes in the flame surface area caused by flame collision can suddenly enhance the turbulence and, thus, augment the local burning rate and trigger thermoacoustic instability [171, 172]. Secondly,

most of the previous studies consider the multi-flame burner as a complete module of the thermostatic system, and thus only the total heat release rate is often discussed. However, it is to be noted that when multiple flames are placed together, interactions between adjacent flames may cause the oscillation behavior of individual flames differ to each other, resulting in a more intricate fluctuation of total heat release rate. In open-flame configurations, such interaction has been extensively studied. For example, research on candle flame oscillators has explored individual and global dynamics of multiple flames in various configurations [173, 174]. In particular, these studies used the time series of brightness and/or temperature for each flame to perform a series of time-series and network analyses to quantify the local and global dynamics. These studies have demonstrated that interactions between flames can give rise to diverse synchronization states in the system, including generalized synchronization, phase synchronization, and anti-phase synchronization, and consequently altering global dynamics [175, 176].

The above review highlights that multi-flame burner in a Rijke tube can introduce additional complexities to the system. However, their effect on combustion dynamics in a Rijke tube remains relatively unexplored. Most of these studies employ a global heat release measurement using either the camera or photo-multiplier tube (PMT) to obtain global heat release dynamics, where the influence of individual flames remains untraceable. Naturally, quantifying the individual flame dynamics and seeing how it affects the global dynamics in the Rijke tube is of practical interest. This topic is worth exploring because modern combustion devices such as gas turbines and furnaces often utilize multiple adjacent flames to optimize flame stabilization and fuel-lean operations. Thus, in this study, we focus on unveiling the key dynamics caused by interactions between adjacent flames when a multi-flame burner is placed inside a Rijke tube. Furthermore, unlike most previous studies with the Rijke tube, we use the extent of hydrogen addition to a premixed hydrocarbon (propane) flame as the control parameter while maintaining a fixed global equivalence ratio. This is practically relevant, as hydrogen addition is considered a method to reduce

the carbon footprint of current gas turbine combustors. However, the addition of hydrogen could significantly impact flame properties, including flame temperature and laminar flame speed, thereby altering the interaction between the unsteady heat release rate and the acoustic field. Our focus will be on analyzing pressure time series to identify the global dynamics while simultaneously observing the morphological changes in individual flames. Using time-series analyses, we will quantify the flame dynamics and assess its effect on the overall combustion dynamics.

4.2 Experimental setup

Table 4.1. List of experimental conditions, where $\alpha = [H_2]/([H_2] + [C_3H_8])$, Le is Lewis number, Q is the flow rate, S_L is the unstretched planar laminar flame speed, δ_F is the laminar flame thickness, and T_b is the adiabatic flame temperature.

α	Q (SLPM)	Le	S_L (cm/s)	δ_F (mm)	T_b (K)
10%	6	1.11	48.1	0.033	2266
20%	6	0.97	49.3	0.033	2268
30%	6	0.89	50.7	0.032	2270
40%	6	0.84	52.6	0.032	2272
50%	6	0.81	55.2	0.031	2275
60%	6	0.80	59.1	0.030	2280
70%	6	0.81	65.2	0.029	2287

The schematic of our experimental setup is shown in Fig. 4.1(a). The Rijke tube was constructed using a vertical circular quartz tube with an inner diameter of 50mm and a length of 0.914m. The top of the Rijke tube is open to the atmosphere, while the bottom end is covered with a solid plate. This plate contains a perfectly designed circular hole to allow an axial motion of a copper tube with inner and outer diameters of 12.7 mm and 16 mm, respectively. The multi-hole burner was mounted at the end of this copper tube, as

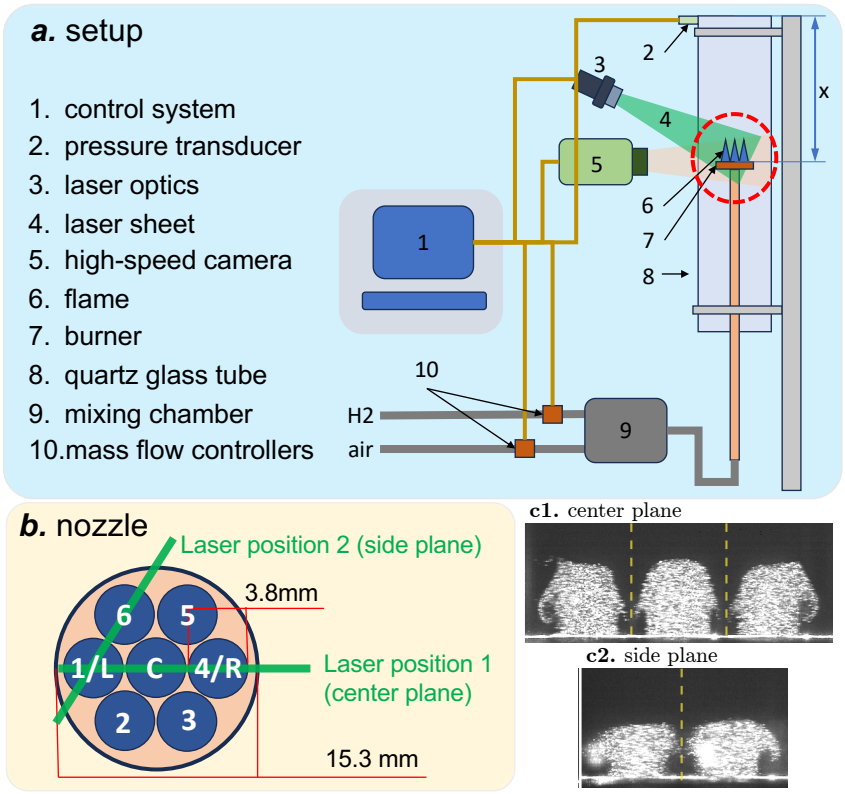


Figure 4.1. Schematic of the experimental setup with primary components and the side view Mie scattering images of oscillating flames.

shown in the schematic. Although the copper tube is long enough to place the burner at any axial location of the Rijke tube, for this study, we fixed the location of the burner at 30cm measured from the top (open) end of the Rijke tube. The burner has a 7-hole design (shown in Fig. 4.1b), where each hole has a diameter of 3.8 mm, and a center-to-center distance between holes is 4.8mm. A pressure transducer is mounted at the top of the Rijke tube to acquire the pressure time series of the combustion dynamics. A well-controlled flow of premixed gas (fuel and oxidizer) was supplied to the copper tube. We used a mixture of hydrogen and propane ($H_2 + C_3H_8$) as the fuel, while the oxidizer was air. The supply lines from gas cylinders were connected to a set of mass flow controllers (Alicat MCR: $\pm 0.2\%$ full scale), which allowed us to individually modulate the flow rates for H_2, C_3H_8, and air. In the experiments, we maintained the total flow rate ($Q = 6$SLPM) and the global equivalence ratio ($\phi = 1$) constant while we modulated the H_2 percentage, quantified by

ff = $[H_2]/([H_2] + [C_3H_8])$ in the fuel mixture. Hydrogen-blended hydrocarbons are often suggested as new fuels to reduce the production of greenhouse gases and pollutants in gas turbine operations. The parametric space of our study will show how the increase in H_2 percentage may affect the combustion dynamics.

Fundamental flame properties, including unstretched planar laminar flame speed (S_L), flame thickness (δ_F), and adiabatic flame temperature (T_b), were evaluated through the PREMIXED module in Chemkin-Pro software with GRI-3.0 [90] chemistry model. The global Lewis number (Le) of the mixtures is evaluated using the method described by Addabbo et al. [177] and Dinkelacker et al. [144]. The flame conditions applied in the experiments and corresponding parameters are listed in Table 4.1. It can be noted that the flame temperature (T_b) across our experimental conditions remains almost constant (2268-2287 K), while the global Lewis number varies from 1.11 to 0.81. It is well known that hydrogen addition can trigger cellular instabilities [178] in premixed flames. Using the dispersion relation [5], we confirmed that, for all experimental conditions, the cutoff wavelength (minimum wavelength required for the instability) is larger than the burner diameter. Thus, the flame dynamics were not affected by the cellular instabilities. The flow rates were also sufficiently low to maintain the steady laminar structure of the individual flames when operated outside the Rijke tube.

To quantify flame-flame interactions and the ensuing dynamics, the time series of heat release from individual flames is generally measured. However, due to the complex geometry of the multi-hole design, the accurate and quantitative measurement of the heat release from individual flames is difficult. To circumvent this issue, we used Mie scattering images, allowing us to observe the flamefront and its morphology. A 527nm Nd-YLF laser, coupled with sheet-making optics, was used to generate a thin vertical laser sheet, which was placed at various strategic positions with respect to the burner (shown in Fig. 4.1b) to capture the cross-sectional images from different views. Before entering the burner tube, the unburned mixture was seeded with DEHS (di-ethyl hexyl

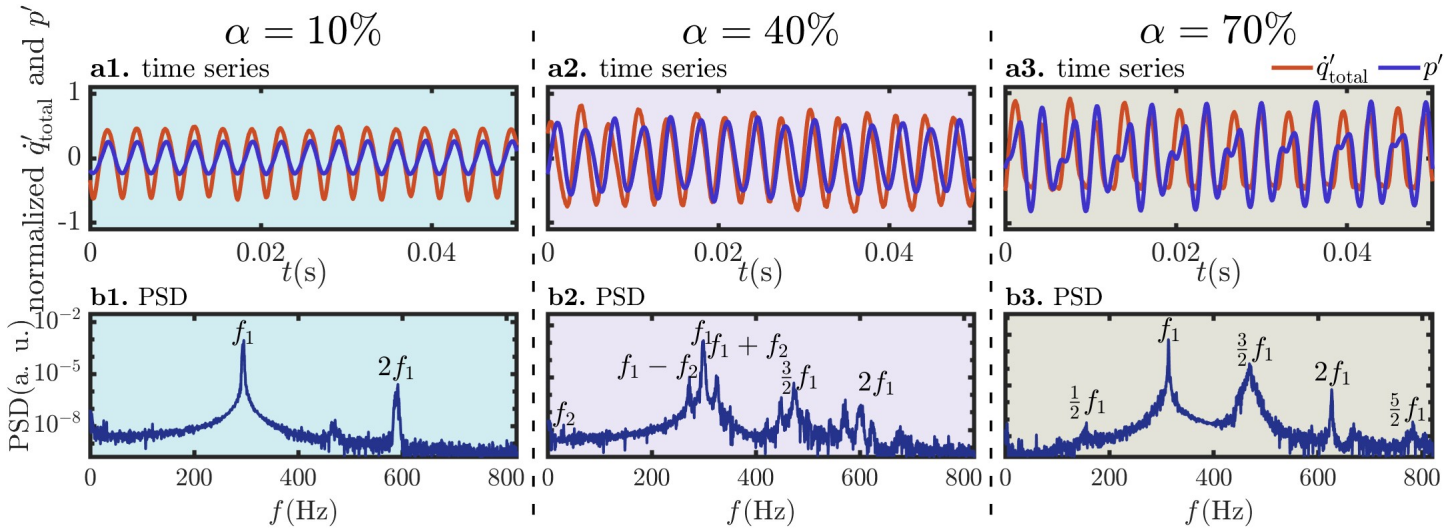


Figure 4.2. Representative normalized time series (a1, a2, a3), and PSDs for different cases (b). Figures a1, a2, and a3 show the evolution from periodic to more quasi-periodic as H_2 content increases from 10% to 70 %. The phase difference between p' and $\dot{q}'_{total}$ are shown in the supplementary material. PSDs show the richer dynamics for increasing H_2 ratio: the emergence of a second competing frequency is clear from the figure.

sebacate). The Mie scattering images were captured using a synchronized Phantom V710 high-speed camera with a sampling frequency of 10000 Hz. The imaging resolution is 640 × 552 pixels. Since the DEHS droplets evaporate near the flame, the Mie scattering images display a clear flamefront (Fig. 4.1c), essentially the isotherm where the droplet evaporates. This method has been successfully used to analyze the geometry and statistics of flamefronts in previous studies [59, 86, 179]. We will perform our analyses based on the cross-sectional area of the flames. It is to be noted that the cross-sectional area of a conical structure (individual flames) is related to the surface area. Thus, the time series of the cross-sectional area of our flames can be a qualitative measure of the heat release rate time series [180]. The three individual flames were first identified by processing the images from the center plane (Fig. 4.1b), and a threshold was set to distinguish between the background and flame. This allows us to calculate the cross-sectional area of individual flames: the left flame: $\dot{q}_l$, the center flame: $\dot{q}_c$, and the right flame: $\dot{q}_r$, when imaged the center plane. By performing measurements in both central and side planes (Fig. 4.1b), we confirmed that the six peripheral flames display alternate symmetry, i.e., flames 1, 3, and 5 show similar dynamics, and flames 2, 4, and 6 show similar dynamics. Thus, the total flame cross-sectional area can be extracted as $\dot{q}'_{\text{total}} = 3 \times \dot{q}_l + 3 \times \dot{q}_r + \dot{q}_c$. It is to be noted that the fluctuation of the $\dot{q}$ is calculated by $\dot{q}' = \dot{q} - \bar{\dot{q}}$, where $\bar{\dot{q}}$ is the time average of $\dot{q}$.

4.3 Results

4.3.1 Dynamical regimes of the system

We present the observations using the time series of pressure fluctuation (p') and the cross-sectional area ($\dot{q}'$), which is qualitatively equivalent to the heat release rate of the flames. While earlier studies on Rijke tube utilized flame location [44], equivalence ratio [167], and flow rate [164] as control parameters to obtain different dynamical states, in this study we modulated α, the H_2 percentage in the $H_2 + C_3H_8$ fuel mixture. We

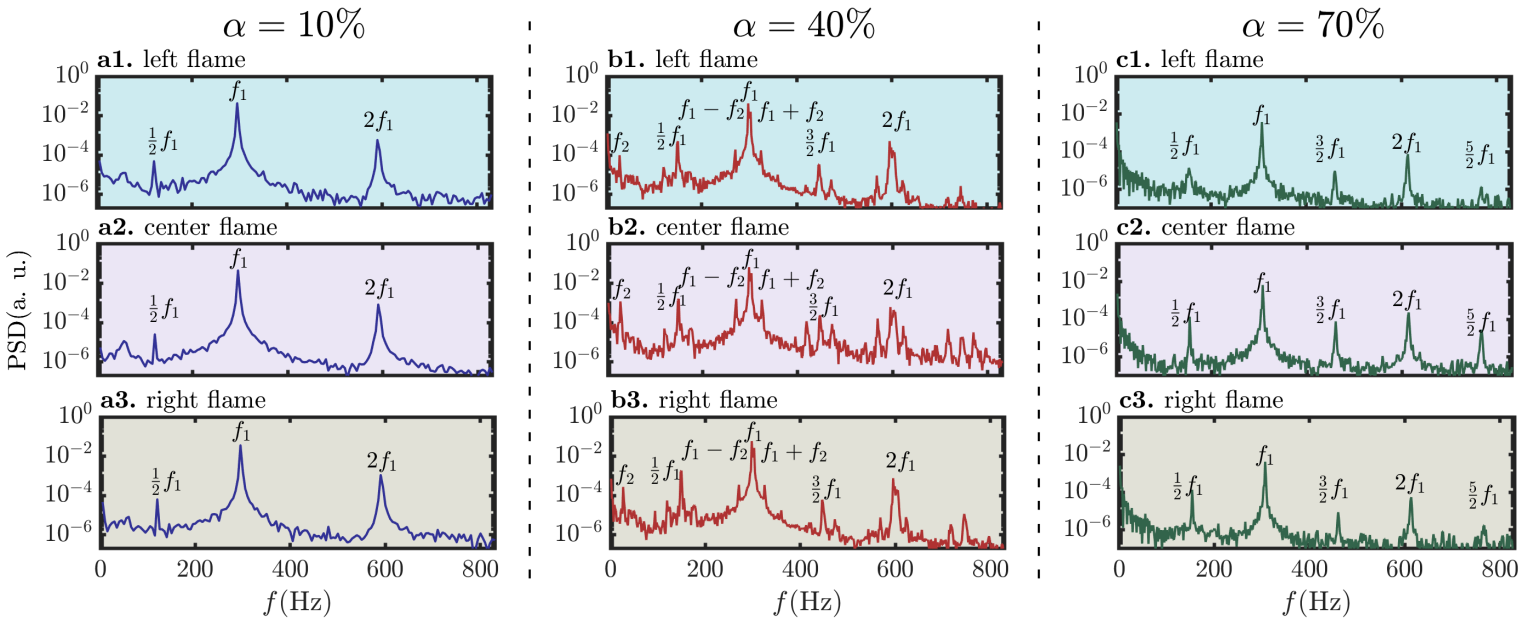


Figure 4.3. From left to right PSDs of $\dot{q}'_l$, $\dot{q}'_c$, $\dot{q}'_r$ with $\alpha = 10\%$, 40%, and 70% H_2, from top to bottom: left flame ($\dot{q}'_l$), center flame ($\dot{q}'_c$), and right flame ($\dot{q}'_r$).

obtained the p' and $\dot{q}'$ for conditions listed in table 4.1, where the H_2 percentage in fuel (α) was varied between 10% and 70% in increments of 10%. By comparing the observed dynamics in p', we can qualitatively identify three distinct regimes. The normalized time series of p' and $\dot{q}'_{\text{total}}$ for three different α's are shown in Fig. 4.2(a). The corresponding power spectral densities (PSD) of p' are presented in Fig. 4.2b.

For low hydrogen content, $\alpha = 10\%$, the p' and $\dot{q}'_{\text{total}}$ time series display Limit Cycle Oscillation (Regime I). Here, p' and $\dot{q}'_{\text{total}}$ oscillate periodically with a fixed amplitude and remain in phase (Fig. 4.2a1). This is the hallmark of the generalized synchronized state between p' and $\dot{q}'_{\text{total}}$. The PSD of p' (Fig. 4.2b1) displays two dominant peaks, $f_1 = 295Hz$, and its second harmonic, $2f_1 = 590Hz$. The fundamental frequency of the air column in our Rijke tube is around 100Hz. As the lower side is closed, and the flame location is near the node of the third harmonic, the primary dominant frequency (f_1) is closely aligned with the third harmonic of the air column (around 300Hz) [181].

As H_2 content increases, we observe quasi-periodic oscillation from both p' and $\dot{q}'_{\text{total}}$ time series (Regime II). For example, at $\alpha = 40\%$, illustrated in Fig. 4.2a2, the local amplitude of the time series is no longer constant; instead, it varies continuously within a specific range. Moreover, in contrast to the periodic state, a phase lag consistently exists between p' and $\dot{q}'_{\text{total}}$ and fluctuates over time. As displayed in the PSD of p' (Fig. 4.2b2), equally spaced frequency peaks neighboring to f_1, and its second harmonic $2f_1$ emerges. We also observe a weaker peak at $f_2 \approx 27$Hz. The neighboring peaks are located at $f_1 - f_2 = 271$Hz, $f_1 + f_2 = 325$Hz, and $2f_1 - f_2 = 569$Hz. These algebraic combinations of frequencies (compound frequencies) are typical for quasi-periodic dynamics arising from nonlinear interactions between different modes (f_1 and f_2) [160]. We also observe the emergence of a peak at $\frac{3}{2}f_1$, indicating the presence of a sub-harmonic mode. As the H_2 content increases, this peak becomes stronger. However, for $\alpha < 60\%$, the contribution from the sub-harmonic is much weaker compared to the dominant frequency, f_1, and its higher harmonics.

At higher H_2 content, specifically for $\alpha = 70\%$, the effects of the sub-harmonic frequency become more apparent. The p' time series (Fig. 4.2a3) displays alternating full and broken peaks. In the PSD, the peaks related to f_2 disappear, while new peaks are observed at $\frac{1}{2}f_1$, $\frac{3}{2}f_1$, and $\frac{5}{2}f_1$, which indicates that the dynamics of the system is locked to the sub-harmonic mode.

In summary, with the increase in the α, progressively more intricate dynamics have been observed. In particular, the system transitions from periodic oscillation to period-doubling through quasi-periodic oscillation. A similar transition in dynamical states has been reported in previous studies in various types of combustors [160, 182, 183], and is a well-known route to chaos for dynamical systems [44]. However, the pressure dynamics reported above do not explain why the sub-harmonics are observed. To provide further insights, we will need a comprehensive analysis of flame dynamics, which will be the topic of the following section.

4.3.2 Dynamics of individual flame

In order to explore the behavior of the individual flames in the multi-hole burner and their effects on the transition between various dynamical states observed in the pressure time series, we systematically analyzed the dynamics of the cross-sectional area of the flames. As described in the experimental section, when the laser sheet was positioned along the diameter of the burner (i.e., the central plane in Fig. 4.1b), the Mie scattering images revealed the shapes of three flames, i.e., two diametrically opposite flames (We will call them left and right flames), along with the center flame (Fig. 4.5a). Fig. 4.3 shows PSD of the $\dot{q}'$ of individual flames across the three dynamical regimes.

For low H_2 content ($\alpha = 10\%$), all three flames display oscillations with f_1 as the dominant frequency in the spectra (Fig. 4.3a1, a2, and a3). It is to be noted that while a weak sub-harmonic ($\frac{1}{2}f_1$) is present in the spectrum, it does not interact with either f_1 or $2f_1$ to produce dynamics at compound frequencies in this regime.

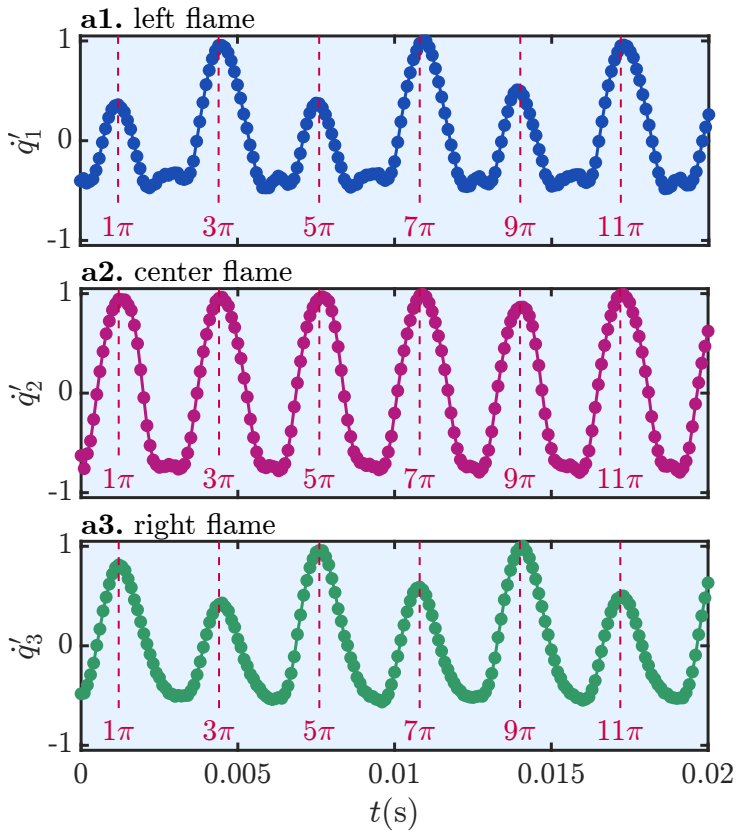


Figure 4.4. $\dot{q}'$ time series for $\alpha = 70\%$. The asymmetric oscillation between the left and right flame can be seen. The periodic of such asymmetric oscillation is 4π, where the left/right flames return to their original $\dot{q}'$ level.

In the quasi-periodic regime ($20\% \leq \alpha \leq 50\%$), multiple peaks emerge in the spectra for all three flames. While f_1 continues to dominate, f_2 becomes more visible as the second-largest peak. Moreover, f_2 interacts with the other modes f_1, its sub-harmonic ($\frac{1}{2}f_1$, $\frac{3}{2}f_1$), and higher harmonic ($2f_1$) modes, giving rise to various neighboring compound peaks with equal spacing of f_2. Furthermore, the peak of f_2 in the central flame remains one order of magnitude higher than that in the side flames, suggesting that the central flame is more responsible for generating this mode. This observation will be elaborated in the next section using network analysis. These observations suggest that the low frequency $f_2 \approx 27Hz$ originates from the individual flame dynamics. This mode actively interacts with the dominant fundamental modes of the system (f_1, $2f_1$), producing compound frequencies and, hence, quasi-periodic dynamics as observed in Fig.4.2b2.

For higher H_2 content ($\alpha \geq 60\%$), the f_2 and related compound peaks disappear, while the sub-harmonic peak ($\frac{1}{2}f_1$) and related compound peaks emerge in the spectra of $\dot{q}'$ of all three flames–a pattern also observed for p' spectra. It is to be noted that the energy of the peak at $\frac{1}{2}f_1$ from the side flames (Fig. 4.3c1, and c3) is higher than that from the central flame (Fig. 4.3c2). This suggests that the side flames are more responsible for the emergence of the sub-harmonic oscillations observed in p'. To further illustrate this point, we compare the time series of $\dot{q}'$ from these three flames in Fig. 4.4.

While the center flame displays a periodic behavior with almost fixed amplitude, the side flames show a repetition of higher and lower amplitude peaks in the time series. This is the hallmark of a signal that combines fundamental and sub-harmonic frequencies, e.g., f_1 and $\frac{1}{2}f_1$, respectively. A comparison between the time series from the left and right flames further reveals a phase lag between these two signals, in that the higher amplitude peak of the right flame arrives with the low amplitude peak of the left flame, and vice versa. This behavior is further demonstrated through a series of Mie scattering images over the two time periods ($2/f_1$) to show the alternating behavior of left and right flames in Fig. 4.5b. Furthermore, we investigated two adjacent side flames by placing the laser across them (Fig. 4.1: laser position 2). As shown in Fig. 4.5c, the two adjacent side flames also display alternate dynamics observed in diametrically opposite (left and right flames) flames, and their time series also displayed similar dynamics (not shown) as left and right flames. This alternating high-and-low amplitude dynamics displayed by adjacent and diametrically opposite side flame confirms that the sub-harmonic dynamics arise from the local flame oscillation, whose frequency is $\frac{1}{2}f_1$. Figure 4.5c schematically illustrates the effects of the subharmonic frequency on the flame dynamics. It is to be noted that this sub-harmonic mode is also present in all three regimes (PSD in Fig. 4.3a, b and c). However, for the periodic and quasi-periodic regimes ($\alpha < 60\%$), its strength is much weaker compared to other modes. But for high hydrogen content ($\alpha \geq 60\%$), the sub-harmonic mode becomes stronger and affects the pressure fluctuations. The emergence of sub-harmonic modes

was previously reported in annular combustors with multiple turbulent swirl flames [182]. The emergence of sub-harmonic modes is known to be a feature that accompanies the periodic-doubling routes to chaos in thermoacoustic systems [160, 164].

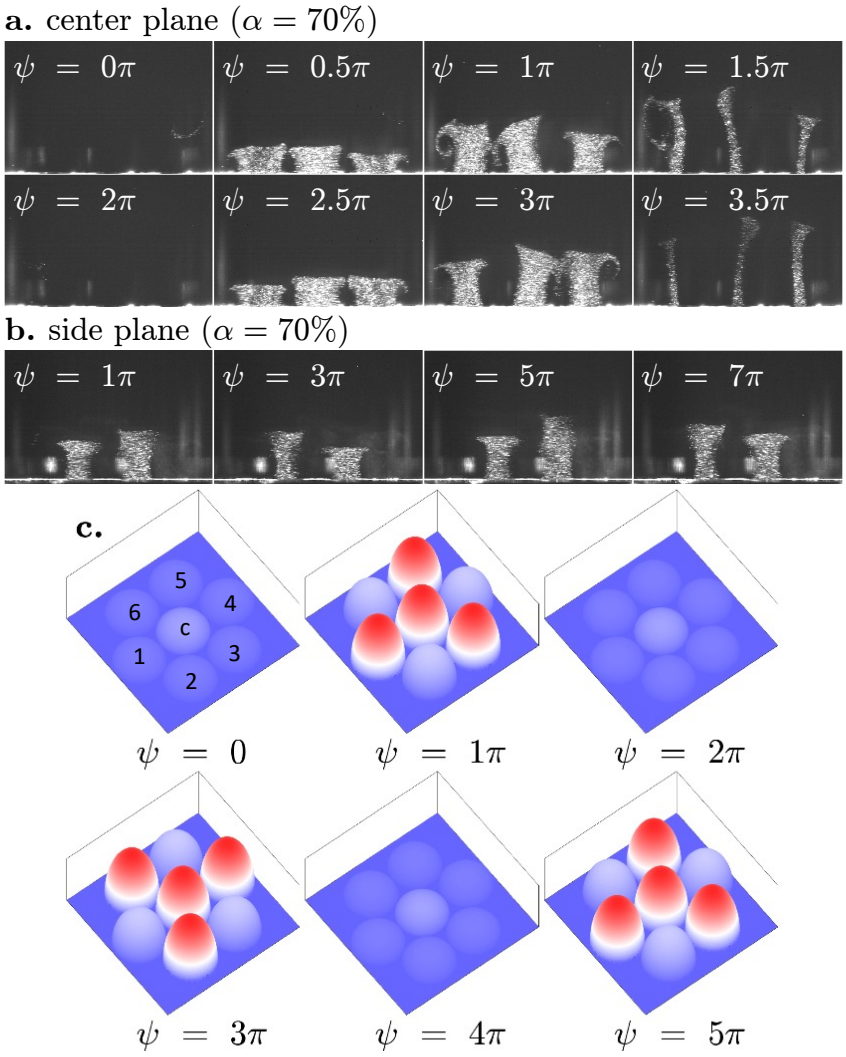


Figure 4.5. Overall flame dynamics demonstration. The oscillation mode corresponds to the solution of vibrating membranes of $m = 3$, as shown in **(a)**. Observe the alternation of flame heights at the center plane. A representative cycle of flame oscillations captured by high-speed camera. The phenomenon of alternating flame heights of left and right flames can be clearly seen in **(b)** ($\psi = 0.5\pi, \psi = 2.5\pi$) and **(c)** ($\psi = 1\pi, \psi = 3\pi$)

It is important to highlight that, despite the phase difference between the oscillations in individual side flames for $\alpha \geq 60\%$, when aggregating their respective time series to calculate $\dot{q}'_{\text{total}}$ (equivalent of global heat release rate), the lower peaks and higher peaks

of the side flames appear to complement each other, giving rise to a more periodic wave pattern, as observed in Fig. 4.2. This is why such an subharmonic mode of flame oscillation could not be identified in previous studies, where chemiluminescence was used to measure a global heat release rate measurement. As seen in Fig. 4.4, the individual flames' time series are critical to capturing the dynamics of subharmonic modes.

4.3.3 Recurrence Network analysis and asymmetric couplings

Next, we investigate the relative importance of individual flames in driving the combustion dynamics by using network analyses. Thermoacoustic instabilities are driven by bi-directional coupling between heat release and pressure oscillations. However, there can be an asymmetry in these (bidirectional) coupling strengths in that one could have a stronger influence in driving the dynamics than the other. One of the well-known methods to quantify the possible asymmetry in the coupling strength is by computing the cross-transitivity [184] using recurrence matrices, which are characteristics of any deterministic dynamical system [185]. Here, the recurrence of a measured time series was computed after reconstructing the phase space using Takens' embedding theorem [186], which involved computing the delayed vectors of the time series. Here, the set of delayed vectors is constructed with an optimum time lag (d) and optimum embedding dimensions (M) of the time series. Therefore, the delayed vector of a time series $x(t)$ can be expressed as

$$\mathbf{V}_i = [x_i, x_{i+d}, ..., x_{i+(M-1)d}]. \tag{4.1}$$

In this study, the optimum time lag d is chosen as the first minimum of the average mutual information (AMI), and the optimum embedding dimension is chosen as the first zero of the False Nearest Neighbor (FNN) [187]. The recurrence matrix R can be defined as

$$R_{ij} = \theta(\epsilon_V - ||V_i - V_j||), \tag{4.2}$$

where θ is the Heaviside function, ϵ_V is a recurrence threshold, $||V_i - V_j||$ is the Euclidean distance between two delayed vectors. If the condition, $||V_i - V_j|| < \epsilon_V$, is satisfied, V_i can be identified as recurrent. The cross-recurrence matrix (CRM) captures the recurrence properties of two time series in the same reconstructed phase space.

$$CRM_{ij} = \theta(\epsilon_{VW} - ||V_i - W_j||). \tag{4.3}$$

If $CRM_{ij} = 1$, then one oscillator recurs to the state of the other. Otherwise, the two oscillators are not linked. All ϵ in this paper are selected such that the recurrence rate (RR) of R and CRM are approximately 0.01 [188]. The recurrence rate of a recurrence matrix is defined as follows:

$$RR = \frac{1}{N^2} \sum_{i,j=1}^{N} R_{ij}. \tag{4.4}$$

Now we may quantify the directional coupling between flames using cross transitivity (τ) between two-time series, x, and y, as [184]:

$$\tau_{XY} = \frac{\sum_{v \in V_X; a,b \in V_Y} A_{va} A_{ab} A_{bv}}{\sum_{v \in V_X; a,b \in V_Y} A_{va} A_{vb}} \tag{4.5}$$

Here the cross-transitivity, $\mathcal{T}_{pq}$, represents the directional coupling strength from $\dot{q}'_{\text{total}} \rightarrow p'$. Therefore, $\mathcal{T}_{pq}/\mathcal{T}_{qp} > 1$, suggests that the coupling strength of $\dot{q}'_{\text{total}} \rightarrow p'$ is stronger than coupling strength of $p' \rightarrow \dot{q}'_{\text{total}}$, hence, $\dot{q}'_{\text{total}}$ drives that dynamics, and vice versa.

In Fig. 4.6(a), $\mathcal{T}_{pq}/\mathcal{T}_{qp}$ are shown for various α. In the periodic oscillation regime ($\alpha = 10\%$), $\mathcal{T}_{pq}/\mathcal{T}_{qp} < 1$ indicates stronger effect of p' on $\dot{q}'$. This is why, in this regime, the PSDs showed only the fundamental frequency of the tube and its higher harmonics (f_1, and $2f_1$). In the quasi-periodic oscillation regime ($20\% \leq \alpha \leq 50\%$), $\dot{q}'$ displays dominance over p' ($\mathcal{T}_{pq}/\mathcal{T}_{qp} > 1$), a behavior also observed in previous studies [189]. This also explains why the f_2 arising from flame dynamics (Fig. 4.3b) drives the compound frequencies in

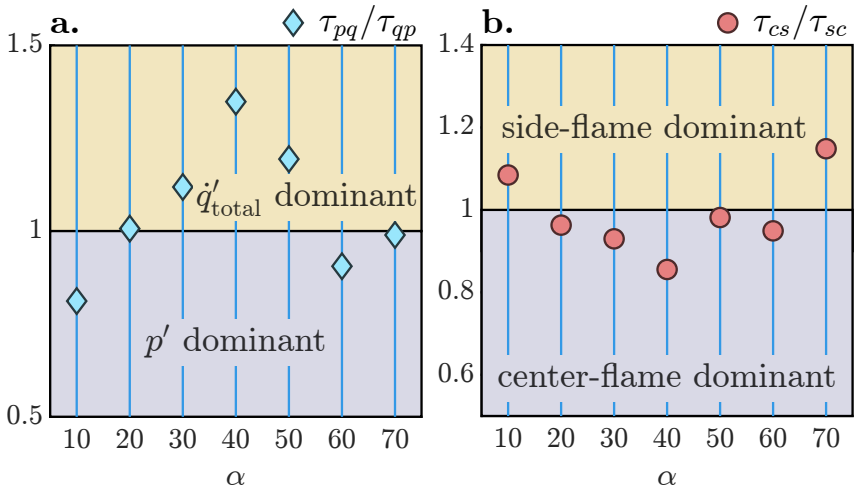


Figure 4.6. Normalized cross transitivity. **(a.)**: $\dot{q}'_{\text{total}}$ vs. p'. **(b.)** center vs. side flames

the pressure dynamics (Fig. 4.2b2). Furthermore, with the increase in H_2 content, the gradual weakening of quasi-periodic behavior occurs. At $\alpha \geq 60\%$, with the emergence of sub-harmonic frequency ($\frac{1}{2}f_1$) in the spectra, we observe $\mathcal{T}_{pq}/\mathcal{T}_{qp} < 1$ or ≈ 1. In this regime, the influence of p' and $\dot{q}'$ on each other is comparable. The flames react to pressure excitation, giving rise to the sub-harmonic response. This, in turn, affects the pressure and imposes the sub-harmonic frequencies in pressure oscillations, resulting in period doubling in the system.

Next, we evaluate the asymmetric couplings between the side (s) and the central flames (c) by calculating the cross transitivity, $\mathcal{T}_{cs}/\mathcal{T}_{sc}$. This will allow us to assess the relative importance of these flames in the global dynamics. Here, we used an average of cross-sensitivities of central (c)-left (l) flames and central (c)-right (r) flames to define $\mathcal{T}_{cs}/\mathcal{T}_{sc} = \frac{1}{2}(\mathcal{T}_{cl}/\mathcal{T}_{lc} + \mathcal{T}_{cr}/\mathcal{T}_{rc})$.

In the regime of periodic oscillation ($\alpha = 10\%$), $\mathcal{T}_{cs}/\mathcal{T}_{sc}$ is weakly greater than 1, suggesting somewhat dominant effect of side flames. In the 7-hole design, the central flame is generally affected by all the surrounding flames. The center flame starts to become more dominant ($\mathcal{T}_{cs}/\mathcal{T}_{sc} < 1$) in the quasi-periodic regime ($20\% \leq \alpha \leq 50\%$), which is driven by emergence and interaction of f_2 mode with the f_1, and $2f_1$ modes. This corroborates

the $\dot{q}'$ spectra of individual flames (Fig. 4.3b), which showed stronger f_2 peaks for the center flames compared to the side flames. As discussed in the previous section, the sub-harmonic modes in the side flames are present for all α but are relatively weaker than the other modes. For higher hydrogen percentages, i.e., higher α, the dynamics start to be dominated by the sub-harmonic oscillation. At $\alpha > 40\%$, we see that $\mathcal{T}_{cs}/\mathcal{T}_{sc}$ is increasing, suggesting that the dominance of center flames is decreasing. At $\alpha = 70\%$, we see $\mathcal{T}_{cs}/\mathcal{T}_{sc} > 1$, suggesting a strong effect of subharmonic modes, and hence, the side flames.

4.3.4 The physical explanation of subharmonic oscillation

Here, we provide a potential explanation for the subharmonic oscillation observed in the experiment. Previous studies [190] have shown that closely positioned flames affect each other through the interactions of the vortices shed by the flames.

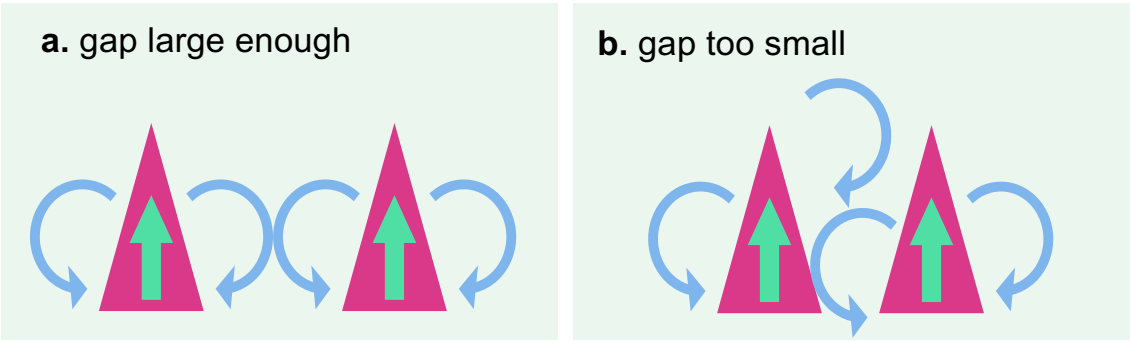


Figure 4.7. A simple diagram illustrating the phenomenon relates to the induced vortices: **a.** larger gap, **b.** small gap, with vortex appear sequentially

An oscillating isolated flame generally entrain the flow and generate vortices. When two flame are placed together and oscillate at the same frequency, with a large enough gap, the two vorticies induced by both flames could be configured horizontally together, as shown in Fig. 4.7a. However, when the distances are too small, the vortices generated by neighboring flames cannot be produced simultaneously, and as such, the vortices are shed alternatingly by the flames, as shown in Fig. 4.7b. This causes flames to oscillate

alternatingly, leading to the subharmonic oscillation. Our flames being closely packed, we observe the subharmonic peaks in flame shape at all conditions (hydrogen percentages). With increased hydrogen percentage, flame speed (s_L) increases, and flame thickness δ_F decreases. Since the vorticity across the flame scales with s_L/δ_F, the vortex becomes stronger at higher hydrogen percentages, leading to stronger sub-harmonic dynamics. This is why the sub-harmonic peaks in pressure signatures can be observed only at high hydrogen percentages when the vortices are stronger.

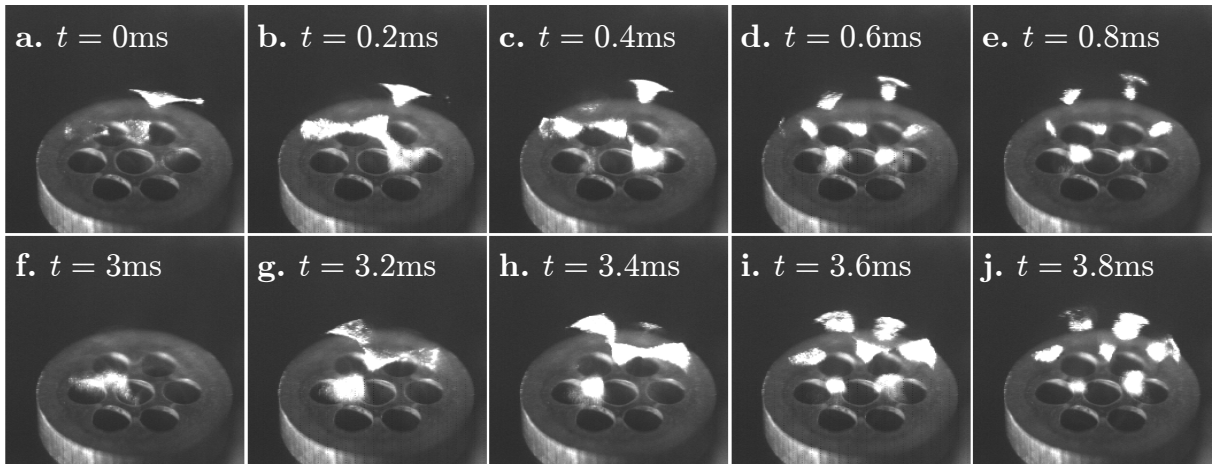


Figure 4.8. The horizontal Mie scattering images of two consecutive cycles clearly show a pattern shift between the neighboring cycles.

4.4 Conclusion

We presented an experimental investigation of a multi-flame laminar Rijke tube. Along with the traditional pressure measurement to quantify the global dynamics, we additionally employed Mie scattering imaging to assess the time series of individual flames. We identified several key dynamical states by varying the hydrogen content in hydrogen/propane/air flame. The pressure and flame time series analyses revealed how the individual flame dynamics produce complex global dynamics. The key findings can be summarized as:

- The system displays periodic behavior at low hydrogen content, where the individual flames and the pressure time series show response at fundamental mode f_1 and its higher harmonic.

- For intermediate hydrogen content, the quasi-periodic oscillations were observed when a second frequency, f_2, interacts with the fundamental modes producing peaks at algebraic combination frequencies. Analyses showed that the central flame is dominant in driving the dynamics.

- At higher hydrogen content, the side flames display a strong oscillation at a sub-harmonic ($f_1/2$) frequency. This mode in flames drives the period doubling in the global pressure dynamics.

This chapter is a part of the following ongoing research and is currently being prepared for submission for publication:

Weng, Y., Zhu, Y., Saha, A. Vortex-driven subharmonic bifurcation in a Multi-flame Rijke Tube. Under preparation

Part II

Exploring thermoacoustic instability through a complex systems approach: Synchronization and modal analysis

Brief overview of Part II

This part of the work focuses on investigating thermoacoustic instability from a dynamical systems perspective. In **Part I**, we obtained valuable insights from the flame perspective, particularly regarding the time scales related to flamefront instabilities and the nonlinear flame-acoustic coupling mechanisms resulting from multi-flame interactions. However, a crucial question remains: how do we incorporate this information into modeling thermoacoustic instability?

Synchronization framework for modeling transition to thermoacoustic instability

Traditional methods for modeling thermoacoustic instability, such as flame transfer functions (FTF) and flame describing functions (FDF), are based on linear response to forcing. These methods are insufficient for capturing the complex dynamics introduced by the system's nonlinear nature. Therefore, in this part, we present a phenomenological reduced-order model based on synchronization theory to address the transition to thermoacoustic instability in both laminar and turbulent combustors.

Instead of using the flame describing function to represent the unsteady heat release rate as the flame's response to acoustic perturbation, the new model treats the acoustic field and unsteady heat release rate as two nonlinearly coupled subsystems. By varying the coupling strength, this model can replicate the transitions observed in both laminar and turbulent thermoacoustic systems. Specifically, in the laminar thermoacoustic model, altering the coupling strength allows the capture of various dynamical behaviors, including limit cycle oscillations, quasi-periodic oscillations, strange nonchaos, and chaos. The model also qualitatively replicates the different behaviors of a laminar thermoacoustic system observed in previous experiments [44].

For the turbulent thermoacoustic model, the transition from low-amplitude chaotic

oscillations (i.e., combustion noise) to high-amplitude periodic oscillations through intermittency [191] is captured. As the system transitions to limit cycle oscillations, the pressure fluctuations lose their multifractality and increase in amplitude, mirroring the transition mechanism observed in turbulent thermoacoustic systems in previous experiments.

Data driven modal decomposition for thermostatic system

Recent research on turbulent thermoacoustic systems has revealed a fundamental universality in the self-organization behavior observed during transitions, where ordered patterns emerge from initially disordered states [192]. This phenomenon is characterized by various power laws related to spectrum condensation [193] and Hurst exponents [194], which have been identified not only in thermoacoustic systems but also in other types of turbulent systems, such as aeroelastic and aeroacoustic systems.

The studies mentioned above offer a novel perspective on transitions in turbulent environments. However, since much of this analysis relies on one-dimensional time series data, it may fall short of providing a detailed explanation of the physics behind self-organization behaviors, which generally occur in higher-dimensional space. Recognizing this limitation, we aim to reconstruct the higher-dimensional phase space and conduct modal analysis to investigate the underlying mechanisms of self-organization.

In this part of the thesis, we present a novel method for detecting early warning signals in turbulent thermoacoustic systems through modal analysis using principal component analysis (PCA). Unlike previous studies that concentrated on one-dimensional time series data, our approach reconstructs the phase space with Hankel matrices and applies PCA to extract orthogonal components. This enables the identification of modes that significantly contribute to the amplitude increase during the transition to instability. Our results reveal that the transition can be characterized by two distinct regimes. In both regimes, the mode associated with instability is consistently present, with its frequency increasing linearly with the Reynolds number. However, in the first regime, this mode does

not correspond to the first principal component (i.e., the mode with the greatest variance). It is only in the second regime that this mode becomes the first principal component, thereby becoming the primary contributor to the amplitude increase of pressure oscillations. Crucially, since the shift in the first principal component occurs well before the pressure amplitude reaches its peak as the Reynolds number increases, this shift could serve as a straightforward criterion for providing early warning signals of thermoacoustic instability. Furthermore, we analyzed the synchronization behavior between different components of pressure and heat release time series. We discovered that the instantaneous phase synchronization occurs in the mode of instability well before the pressure and heat release rate time series become fully synchronized. Additionally, we derived a two-section power law that describes the change in singular values during the transition. This power law was found to be applicable across various turbulent thermoacoustic systems.

Although this work is ongoing, these observations offer valuable early warning signals for instability and provide a new perspective for studying complex systems.

Chapter 5

Modeling thermoacoustic instability using the framework of synchronization: Laminar system

5.1 Introduction

In many engineering systems used for power generation and propulsion, such as gas turbines, rocket engines and industrial burners, combustion occurs in a confined space. In such systems, the heat release rate fluctuations can influence the acoustic field of the combustor and vice versa. Such a feedback, when positive, can result in the onset of large amplitude acoustic pressure fluctuations known as thermoacoustic instability [1], which is detrimental for both rocket engines [195] and gas turbines [196]. The resulting violent oscillations reduce the lifetime of a combustion system and can sometimes lead to serious damage to the hardware. Thus, thermoacoustic instability has become a major concern associated with modern combustor design, especially for newly designed lean-premixed-prevaporized (LPP) combustors, where combustion predominantly occurs in fuel lean conditions to reduce emissions [197].

A criterion for growth of acoustic energy in a confinement as a result of unsteady heat fluctuation was given by Lord Rayleigh [198], who explained that when acoustic pressure oscillation is in-phase with the fluctuation of heat release rate, energy is added to

the acoustic field. This results in a growth of amplitude of acoustic pressure fluctuations in a thermoacoustic system until it is limited by the nonlinear effects, thus resulting in large amplitude limit cycle pressure oscillations [198, 199]. Traditionally, the transition to thermoacoustic instability was considered as a Hopf bifurcation [200, 201], where the system transitions from a state of fixed point to limit cycle oscillations [202] as the control parameter is varied. In both experimental and theoretical studies, the transition from a stable non-oscillatory operation to a limit cycle oscillation during the onset of thermoacoustic instability has been thoroughly investigated [200, 203, 204].

To model such a thermoacoustic system, and to identify the parameter range where an onset of thermoacoustic instability is expected, the response of the heat release rate to the acoustic fluctuations is traditionally expressed as a flame transfer function (FTF) or flame describing function (FDF). FTF is a linear model of the flame defined in the frequency domain [205], as shown in Eqn. (5.1). It depicts the flame's response to small perturbations from the flow (such as pressure fluctuations, flow velocity fluctuations) as a function of frequency [206],

$$F(\omega) = \frac{q(\omega)/Q}{u(\omega)/U} = G(\omega)e^{i\varphi(\omega)} \tag{5.1}$$

Here $F(\omega)$ is the FTF, q and Q are the fluctuation and the mean of the heat release rate, u and U are the fluctuation and the mean of the velocity measured at a constant point respectively, and ω is the angular frequency [207]. FTF for a combustion system can be identified from the experiment and thus, both the excited frequency and the linear growth rate of the system can be derived. It is to be noted that FTF is defined in the limits of small perturbation. In conjunction with a model for the acoustic field in the duct, the FTF approach is able to identify the linear growth rate for acoustic oscillations and consequently, define a stability map [208]. However, FTF is unable to predict the effects of nonlinearity, such as the amplitude of limit cycle oscillations, and mode switching [209].

FDF, on the other hand, originally introduced by Dowling [210, 211], extends the framework of FTF to the nonlinear regime. Based on the theories of control system, FDF is defined as a complex harmonic response of the flame under a sinusoidal forcing and hence is a function of both the frequency and the amplitude of the forcing [212].

$$F(\omega, |u|) = \frac{q(\omega)/Q}{u(\omega)/U} = G(\omega, |u|)e^{i\varphi(\omega,|u|)} \tag{5.2}$$

Here, $F(\omega, |u|)$ is FDF, ω and u are the frequency and amplitude of the sinusoidal forcing. As a quasi-linear approach, it considers flame as a nonlinear module coupled to a linear acoustic system. Thus the heat release rate fluctuation can be expressed as a nonlinear response to the acoustic perturbation [213]. In addition to excited frequency and linear growth rate, analysis based on FDF can also predict some nonlinear behavior of the thermoacoustic system, such as the amplitude of a limit cycle oscillation at certain frequency [211]. More recently, Noiray et al. [214] introduced a unified framework of FDF incorporating the effect of delay in the response of heat release to flow fluctuations. This improved the ability of models to better approximate the experimental findings. However, since the acoustic forcing used for estimating FDF and hence the acoustic field is harmonic, the work done by the heat release rate oscillations at higher harmonics for the given forcing averages to zero over one cycle of forcing. Even though this simplifies the description of FDF, it adds a limiting assumption that acoustic field is always harmonic in time [215].

Furthermore, despite its ability to model the weak nonlinear coupling between acoustics and flame response, FDF cannot model the secondary bifurcations present in a thermoacoustic system. Experimental studies show that even laminar thermoacoustic systems with simple geometry can exhibit elaborate nonlinear behaviors. Kabiraj et al. [216] investigated various bifurcations in a laminar thermoacoustic system and established a route from self-excited periodic oscillation to chaos via the Ruelle-Takens scenario. Kasturi et al. [217] discovered bursting oscillations and mixed mode oscillation in a

laboratory combustor with a matrix flame. Intermittent oscillations were also observed in a thermoacoustic system as the system transitioned between a state of periodic oscillations to flame extinction [218]. Furthermore, Kashinath et al. [219] performed numerical experiments on a coupled flame-acoustic model representing a thermoacoustic system, and examined its dynamical behavior. They found that the thermoacoustic oscillation in a ducted premixed flame can transition to chaos via either the period-doubling route or the Ruelle-Takens-Newhouse route. Recently, strange nonchaos is also found in a self-excited laminar thermoacoustic system by Premarj et al [220]. Strange nonchaotic attractor (SNA) exhibits complex structure in the phase space. However, the corresponding system does not exhibit sensitivity to initial condition as opposed to a chaotic system [221].

Recently, Pawar et al. [222] performed experiments on a turbulent combustor with a bluff-body stabilized flame and showed that a synchronization of acoustic field and heat release fluctuation results in the onset of thermoacoustic instability. They have also shown that the synchronized and the desynchronized states correspond to thermoacoustic instability and stable condition respectively and an intermittent phase synchronization state exists between these two states [222]. Inspired from this work, Mondal et al. [223] analyzed the synchronous behaviors of pressure and heat release rate during various states of thermoacoustic oscillations reported by Kabiraj et al. [216]. They found different synchronization states including phase locking, intermittent phase locking, and phase drifting, corresponding to different dynamical states [223]. Recently, synchronization framework was introduced to model the transitions in aeroelastic system by Raaj et al. [224].

In the flame transfer function or flame describing function approach, the flame is forced at various acoustic velocities, and the response of the flame is evaluated, as a function of the forcing frequency [214]. The flame transfer function approach does not attribute inherent dynamics to the flame; instead the flame responds to the acoustic velocity fluctuations with a gain and a phase.

However, in reality the flame in itself is a nonlinear oscillator, that has its own dynamics, and needs to be described as a complete oscillator, not just a quasi-steady response to the acoustic field. This nonlinear oscillator can interact nonlinearly with the acoustic oscillator. When the flame has its own dynamics, we can have different synchronization behaviors [223]. We need a synchronization approach, primarily because we have two oscillators. Thus we attempt to model a laminar thermoacoustic system based on the framework of synchronization. We consider the onset of thermoacoustic instability as the result of synchronization between pressure fluctuation and unsteady heat release. In the present work, we are modeling the bifurcations including the secondary bifurcations and the sequence of bifurcations leading to chaos etc.

In our model, instead of representing the flame using a transfer function or a describing function, we consider the acoustic field and the unsteady flame as a pair of nonlinearly coupled damped oscillators. A bifurcation analysis is performed by varying the coupling strength. We observed that the model is able to qualitatively replicate the dynamics of thermoacoustic oscillations observed in experiments.

The rest of the chapter is organized as follows, in Sec. 5.2, we introduce our model based on the synchronization framework, in Sec. 5.3, we describe the experiment from Kabiraj et al. Then, in Sec. 5.4, we compare the dynamics observed in the model and the experiment. The results show that both bifurcations and synchronous behaviors observed in the experiment can be successfully captured in the model.

5.2 Model Construction

The objective of this work is to demonstrate that a synchronization based phenomenological model can qualitatively capture the dynamics exhibited by a laminar thermoacoustic system and can reproduce the various bifurcations in the system. In this study, we however, do not attempt to quantitatively reproduce the experimental

observations. We introduce a pair of coupled oscillators to model the thermoacoustic system. Note that for brevity, in the rest of the paper, we use $p(t)$ and $q(t)$ to represent pressure fluctuation and heat release rate fluctuation, respectively. Both the acoustic oscillator and the heat release rate oscillator are considered as damped simple harmonic oscillators that are nonlinearly coupled with each other (Eqn. (5.3), Eqn. (5.4)). Thus, when decoupled, for a laminar system, the acoustic oscillator and the heat release rate oscillator (flame) act as damped oscillators that exhibit no oscillations, once steady state is reached.

$$\ddot{p}(t) + \zeta_1 \dot{p}(t) + \omega^2 p(t) = C_{pq}(1 - q(t - \tau_2)^2) \cdot \dot{p}(t) \tag{5.3}$$

$$\ddot{q}(t) + \zeta_2 \dot{q}(t) + {R_\omega}^2 \omega^2 q(t) = R_c C_{pq}(p(t - \tau_1)^3 - 1) \tag{5.4}$$

Here,

$$\tau_1 = T_1 = \frac{2\pi}{\omega} \times 1, \quad \tau_2 = T_2 = \frac{2\pi}{R_\omega \omega} \times 1 \tag{5.5}$$

In Eqn. (5.3) and Eqn. (5.4), ω is the angular frequency of the acoustic oscillator, and R_ω is the ratio of angular frequency of the acoustic oscillator and the heat release rate oscillator. The RHS of the equations represent the nonlinear coupling between the two oscillators. We have not optimized the nonlinear terms used for the coupling. Since the main objective of the paper was to show that a laminar thermoacoustic system could be modeled in a framework of synchronization (i. e., as a set of nonlinearly coupled damped oscillators), our focus was to develop a generic model that captured the qualitative behaviors exhibited in experiments. Towards this purpose, we manually chose simple nonlinearities for pressure and heat release rate that resulted in a bifurcation route as observed in experiments. In our system, the coupling between p and q depends on the local admittance of q in the acoustic oscillator. In the experiments, local admittance varies with the location of the

flame in the combustor x_f (explained in the next section). C_{pq} (or C_{qp}) is the coupling strength from q to p (or p to q), and $R_c = C_{qp}/C_{pq}$. In this study, we consider C_{pq} as the bifurcation parameter. ζ_1 and ζ_2 are the damping parameters of the system.

Previous studies have shown that the delay in the coupling between the unsteady heat release rate and the acoustic fluctuation is an important parameter that determines the dynamics of the system [214]. Hence, we introduce time delay in the coupling terms of the model. For generality, we introduce delay in both the response of both heat release rate fluctuations to the acoustic pressure fluctuations and the response of acoustic fluctuations to the heat release rate fluctuations. This is reasonable since the delay in either of these subsystems would depend on the position of the flame within the acoustic duct. In previous studies this was not adopted since the models contained only a simple oscillator representing the acoustic field [204, 210]. While the choice of precise time scale of the delay requires further investigation, previous research shows that it is of the order of the time period of oscillation [214], and thus for simplicity, in this study the two delays τ_1 and τ_2 are considered to be of the order of time period of the oscillators. The system of differential equations is then solved using Matlab's standard delay differential equation solver DDE23, which uses a three-stage, third-order, Runge-Kutta method with variable time steps.

Since the objective of the model is to show qualitative equivalence of the dynamics of the coupled oscillator system with the thermoacoustic system, we chose a generic set of parameters that roughly follows the trends observed in the experiment. Parameters used in the model are, $\omega^2 = 160$, $\zeta_1 = \zeta_2 = 1$, $R_\omega^2 = 2.5$, $R_c = 0.9$. Note that the angular frequency ω and R_ω in experiments depends on the geometry of the flame holder and the combustor. We observe that the bifurcation diagram is largely unaffected with small variation in R_ω as long as it is of the order of 1. Then, in order to match the frequency distribution of the thermoacoustic system used in experiments, the time t in the model is rescaled. Godavarathi et al. [225] showed that the coupling between heat release rate and

acoustic fluctuation is asymmetric and that the heat release rate has a greater influence on acoustic fluctuations than vice versa. To account for this we choose the ratio of coupling strength, $R_c = 0.9$ (i.e. < 1).

In the present work, we manually tune the nonlinearities in the coupling to obtain a bifurcation diagram similar to that observed in experiments. However, in a future study the optimization of nonlinearities and the parameters of the system can be performed more systematically using data driven modeling methods and tools from machine learning.

5.3 Experimental Study

In this study, we validate the developed phenomenological model for a thermoacoustic system, using the data obtained by Kabiraj et al. [216] in their experimental study of bifurcations in a laboratory scale laminar combustor.

The experimental setup consists of a vertical glass duct of length 80 cm and inner diameter of 56.7 mm. The upper side of the duct is open, while the lower side is closed. A coaxial copper tube introduces premixed air-fuel mixture to the burner located inside the combustor. The glass duct is connected to a traverse system that is capable of adjusting the vertical position of the glass duct such that the relative location of the burner (and hence the flame location, x_f) within the duct can be varied. Liquefied petroleum gas (LPG) is utilized as the fuel and it is well premixed with air at a constant equivalence ratio of $\phi = 0.48$ prior to being introduced to the burner. The flow rate of the premixed gas mixture is fixed during the experiment. The bifurcation characteristics of the system is studied with variation in x_f.

At different values of x_f, acoustic pressure fluctuations (p) and heat release rate fluctuations (q) inside the glass duct are simultaneously measured. A pressure transducer (PCB, 103B02) mounted on the glass duct is used to measure the acoustic pressure fluctuation inside the glass duct. The heat release rate is proportional to the reaction rate.

Hence, total CH^* chemiluminesence intensity indicating the global reaction rate is used as a measure of global heat release rate in the system. CH^* chemiluminescence is measured using a photomultiplier tube outfitted with a narrow band optical filter of bandwidth of 10 nm centered around 431.4 nm. Further details of the experimental setup can be found in Kabiraj et al. [216].

5.4 Results and discussions

5.4.1 Bifurcation analysis

Figure 5.1 shows the bifurcation diagrams to track and analyze the qualitative changes in dynamics of the thermoacoustic system with variation of a control parameter. As mentioned before, the coupling depends on the admittance, which varies with flame location (x_f) in the experiment, and with the coupling strength C_{pq} in the model. Thus, C_{pq} and x_f are the control parameters in the model (Fig. 5.1(a)) and in experiments (Fig. 5.1(b)), respectively. We plot the local maxima of time series of pressure fluctuations (corresponding to the asymptotic state for a control parameter) as a function of the control parameter. The amplitude distribution of local maxima of time series of a state variable can represent a system's dynamical behavior. For example, a single local maxima represents a constant amplitude, which usually corresponds to limit cycle oscillations. A continuous line with a clear range indicates that the local amplitude varies regularly in a constant range, which may correspond to quasi-periodic oscillations. To further characterize different dynamical natures in the model and the experiment, we also reconstruct the corresponding phase space attractors and analyze the power spectrum of pressure oscillations (Figs. 5.4 and 5.5).

As we can see in Fig. 5.1(a), when C_{pq} is small enough, oscillators behave like typical damped oscillators. Since there is one point at zero amplitude for a given coupling strength, the bifurcation diagram, in this region ($0 < C_{pq} < 1$), consists of a series of

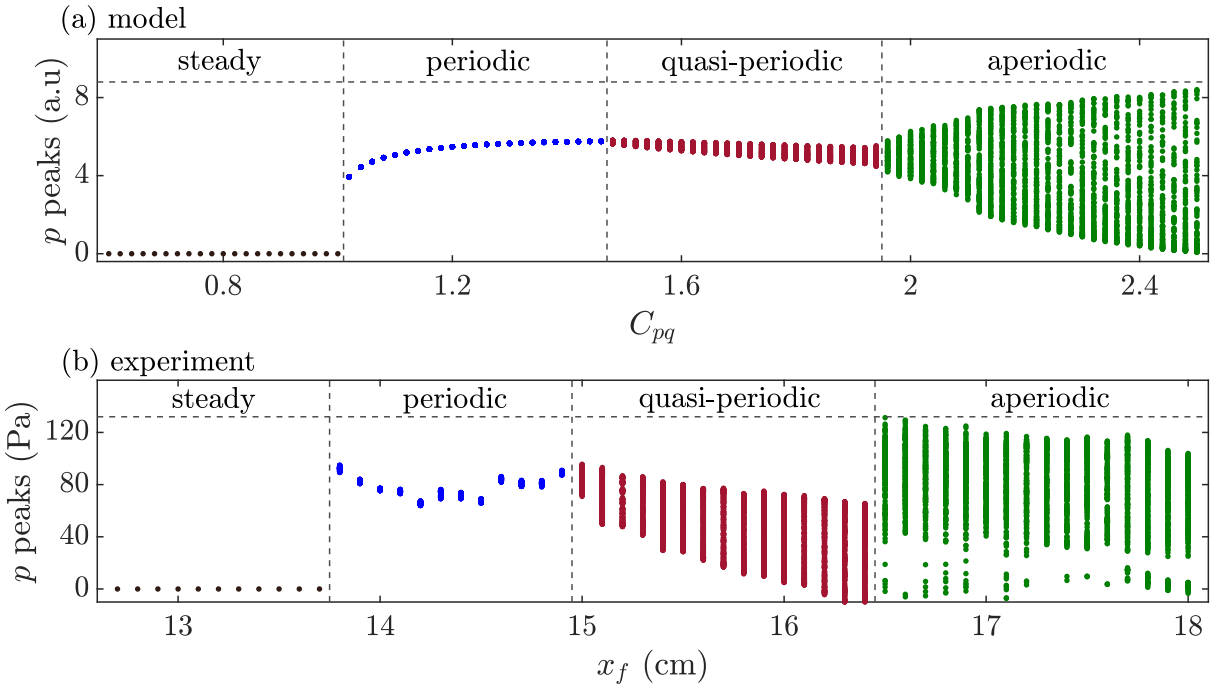


Figure 5.1. **(a)** A bifurcation diagram for the model showing the amplitude of local maxima of p as a function of coupling strength C_{pq}. **(b)** A bifurcation diagram from the experiment showing the local maxima of p as a function of x_f. In the model, as the coupling strength increases, the system transitions from limit cycle oscillation to aperiodic oscillation through quasi-periodic oscillation, which is consistent with the experiment.

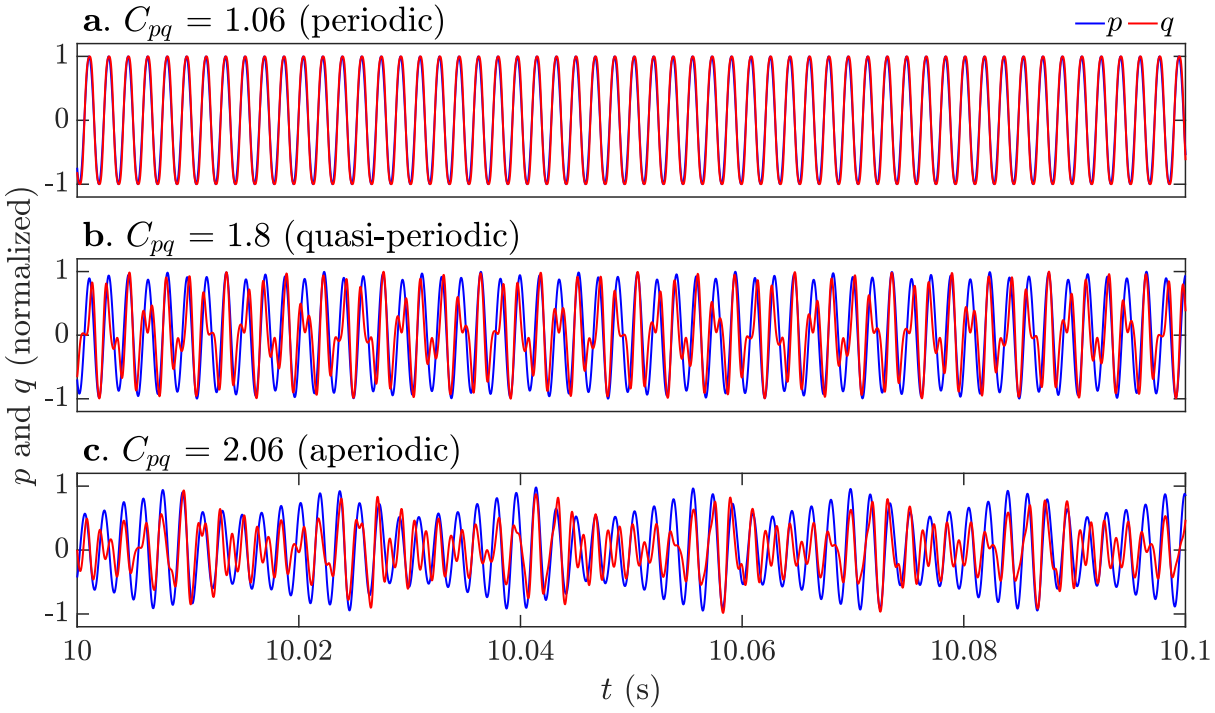


Figure 5.2. The representative normalized time series from the model: from top to bottom periodic ($C_{pq} = 1.06$), quasi-periodic($C_{pq} = 1.8$), and aperiodic ($C_{pq} = 2.06$). During limit cycle oscillation, two time series are mutually synchronized and show a strong periodicity. During quasi-periodic oscillation, irregular periodicity and recurrence are observed and the synchronization is relatively weak. During chaotic oscillation, the two time series are disordered and desynchronized.

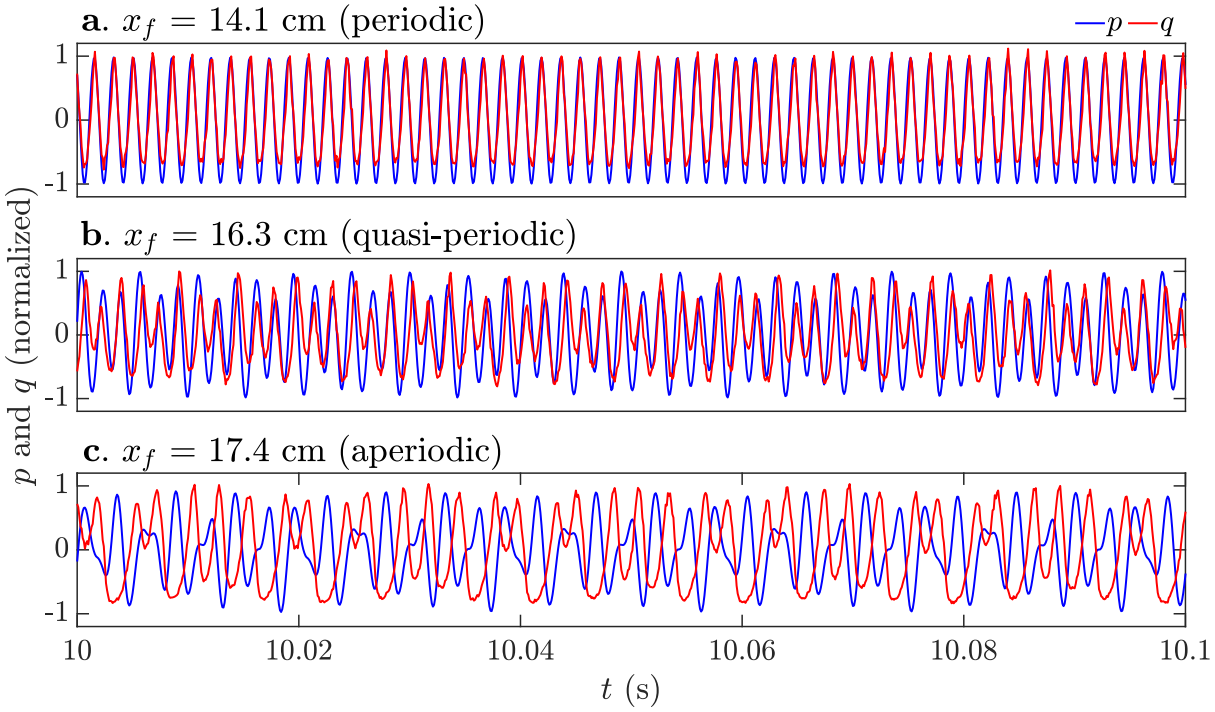


Figure 5.3. The representative normalized time series from the experiments: from top to bottom, periodic (x_f = 14.1 cm), quasi-periodic(x_f = 16.3 cm), and aperiodic (x_f = 17.4 cm).

fixed zero points (Fig. 5.1(a)). As the coupling strength C_{pq} increases, at $C_{pq} = 1$ the dynamics change qualitatively and the system exhibits limit cycle oscillations of finite amplitude (Fig. 5.2(a)). This corresponds to a subcritical Hopf bifurcation [202]. In the corresponding power spectrum, as shown in Fig. 5.4(c), there is only one dominant frequency, which is close to the inherent frequency of the oscillator. In the phase space, the corresponding trajectory is a single closed orbit Fig.5.4(a). At $C_{pq} = 1.48$, the second bifurcation occurs (Fig. 5.1(a)), instead of a series of points with constant value, the pattern on the bifurcation diagram now becomes a vertical straight line, which means the local amplitude of the time series in this region is varying continuously in a range (Fig. 5.2(b)). In the corresponding power spectrum, a second frequency peak appears (Fig. 5.4(f)), and the two frequency components are incommensurate with each other. In the phase space Fig. 5.4(d), the closed orbit now becomes a toroidal structure. These features indicate a region of quasi-periodic oscillation, which is caused by a multi-mode interaction. Beyond $C_{pq} = 1.96$, with the increase in C_{pq}, the time series of p becomes more irregular and disordered (Fig. 5.2(c)), which, in turn, extends the range of peaks in the bifurcation diagram (Fig. 5.1(a)). Moreover, in this range of C_{pq}, a broad band of frequencies can be observed in the power spectrum Fig. 5.4(i) and in the phase space, the toroidal structure breaks down to become irregular Fig. 5.4(g). These characteristics indicate that the system is in the aperiodic regime, which can be either chaos or strange nonchaotic attractors (SNAs) [220, 226]. In Sec. 5.4.2 we will characterize the dynamics in this regime in detail using the 0-1 test [227].

For the experimental data, we plot the local maxima of p as a function of the flame location x_f Fig. 5.1(b). Comparing the results from the model and the experiments, both dynamical behaviors and the transition between various dynamical states, show that they are qualitatively similar, in that the system transitions from limit cycle oscillation to aperiodic oscillation through a regime of quasi-periodic oscillation.

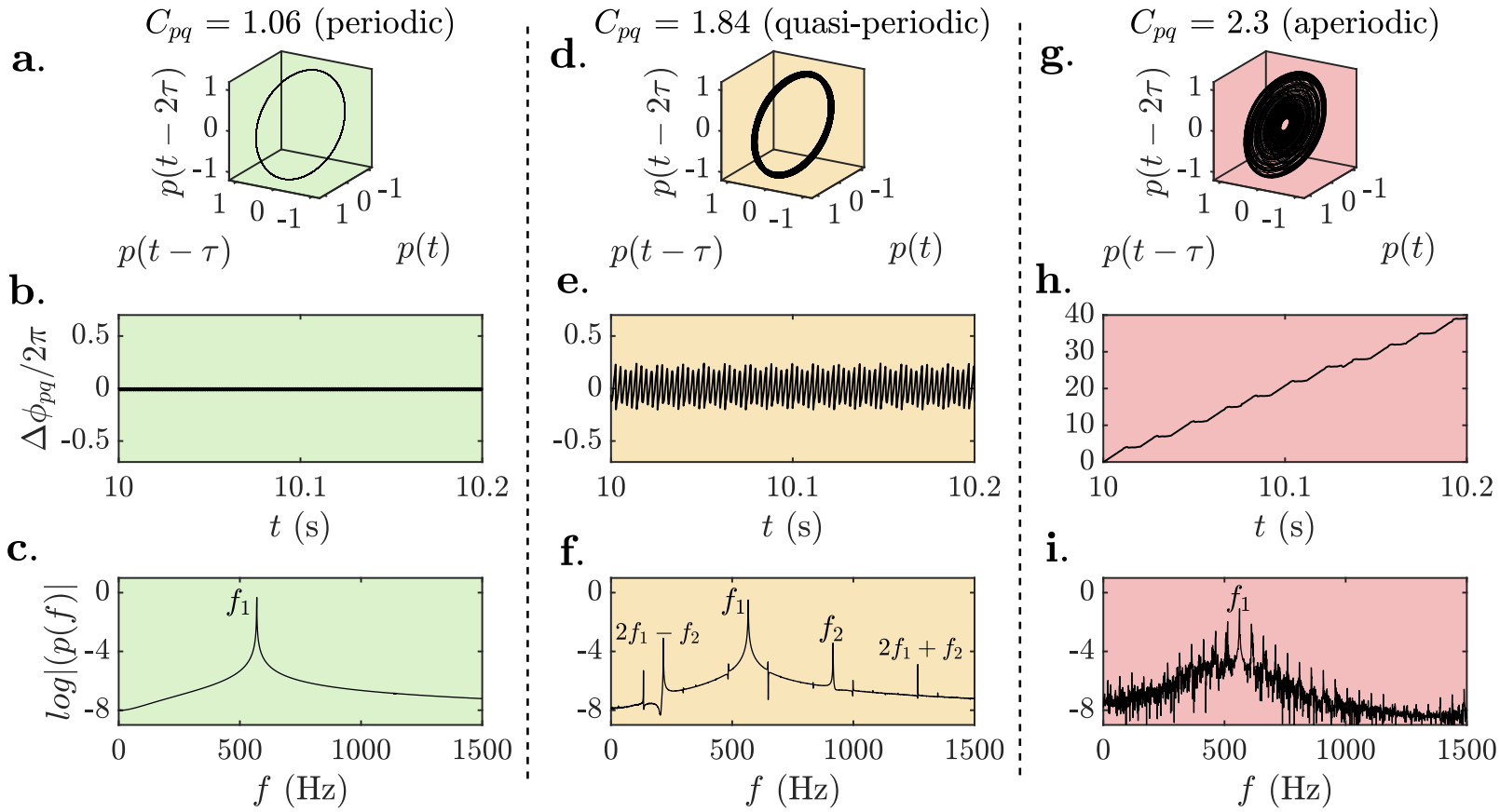


Figure 5.4. The representative phase plot **(a, d, g)**, phase difference ($\Delta\phi_{pq}$) **(b, e, h)**, and power spectrum density ($log|(p(f))|$) **(c, f, i)** are shown from top to bottom for the model. From left to right, periodic ($C_{pq} = 1.06$, $f_1 = 570\ Hz$), quasi-periodic ($C_{pq} = 1.84$, $f_1 = 566\ Hz$, $f_2 = 916\ Hz$), and aperiodic ($C_{pq} = 2.3$, $f_1 = 564\ Hz$)

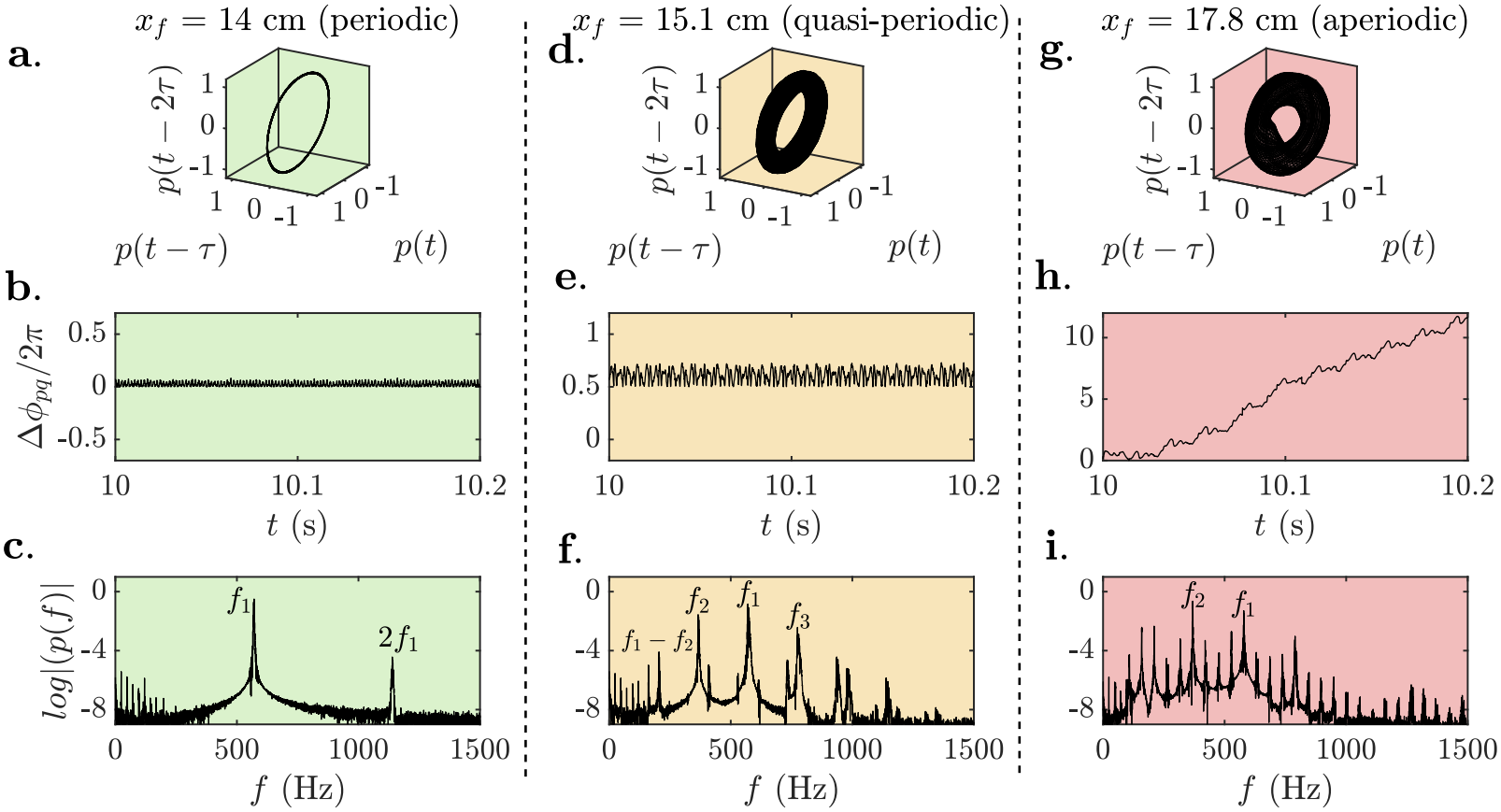


Figure 5.5. The representative phase plot **(a, d, g)**, phase difference ($\Delta\phi_{pq}$) **(b, e, h)**, and power spectrum density ($log|(p(f))|$) **(c, f, i)** are shown from top to bottom for the experiment. From left to right, periodic ($x_f = 14$ cm, $f_1 = 570\ Hz$), quasi-periodic ($x_f = 15.1$cm, $f_1 = 574\ Hz$, $f_2 = 374\ Hz$, $f_3 = 747\ Hz$), and aperiodic ($x_f = 17.8$ cm, $f_1 = 579\ Hz$, $f_2 = 368\ Hz$)

5.4.2 Synchronization behavior of p and q

In the previous section, we demonstrated that our model is able to capture the various dynamics exhibited by the pressure fluctuations. Next, we investigated the capability of model to reproduce the synchronization characteristic of p and q oscillations in the thermoacoustic system. Previously, the synchronization behavior between the pressure fluctuation and heat release fluctuation in the experimental data reported in Kabiraj et al. [216] was studied by Mondal et al. [223]. Multiple synchronous behaviors were observed from the experiment, including phase locking, intermittent phase locking and phase drifting.

To better understand the interaction between the two coupled oscillators, in Fig. 5.4(b, e, h) we plot the relative phase difference of p and q to distinguish the different synchronization states. We assess the synchronization feature of the model by analysing the variation of the unwrapped instantaneous phase difference $\Delta\phi_{p,q}(t)$ between the two oscillators.

$$\Delta\phi_{p,q}(t) = \phi_q(t) - \phi_p(t) \tag{5.6}$$

Here $\phi_q(t)$ and $\phi_p(t)$ are the phase of q and p respectively. When the system is in the region of limit cycle oscillation, the relative phase difference between two oscillators is nearly constant with fluctuations near a constant value (Fig. 5.4(b)). In other words, the phase is perfectly locked; this confirms the synchronization behavior and it is consistent with the results from experiment (Fig. 5.5(b)). Although angular frequency in the two oscillators are different, here both signals keep oscillating with the same frequency, which is close to the angular frequency of p.

As the system transitions to aperiodic regime, we observed intermittent phase locking (Fig. 5.4(h)). For a short period of time, the instantaneous phase differences of the two time series can be locked. However, occasionally, it can jump by multiples of

2π (Fig. 5.4(h)). Such jumps happen between consecutive phase locked time slots. The intermittent phase locked state will gradually transit to a phase drift state as C_{pq} increases. During the phase drift state, the relative phase difference continuously increases. These observations are also consistent with the findings from experiments (Fig. 5.5(h)). The discussion and analysis of phase difference presented in this sub-section, hence, confirms that the different dynamical states relate to different synchronous behaviors.

5.4.3 Distinguishing chaotic state from strange nonchaotic attractors

Strange nonchaotic behavior can be commonly observed in coupled nonlinear systems [228]. In such a state, a phase space attractor with a fractal geometrical structure similar to chaos usually exists. However, unlike chaotic attractors, the corresponding phase space trajectories do not exhibit sensitivity to initial conditions [229]. Such attractors, which can be identified by the lack of a positive Lyapunov exponent are commonly known as, strange nonchaotic attractors (SNAs). Previous studies have shown that flame response in laminar thermoacoustic systems subjected to either periodic acoustic forcing [226] or self-excitation [220] can exhibit SNA. Naturally, for our proposed model based on synchronization framework to be successfully used for capturing flame response in thermo-acoustic systems, it is imperative that the model captures SNA.

Ideally, as the phase space trajectories corresponding to SNAs are not sensitive to initial condition, they can be distinguished from chaos with the lack of positive Lyapunov exponent [228]. However, the data from experiments inevitably contains noise, which restricts the usefulness of the Lyapunov exponent. Hence, we use an alternate method to test chaos, known as 0-1 test [229]. In 0-1 test, two translation variables $\mathcal{P}(n)$ and $\mathcal{Q}(n)$ (Eqn. 5.7 & 5.8) are derived from a one-dimensional time series $\phi(j)$, whose properties are to be investigated. Here $j = 1, 2, ..., N$, n is an index that varies from 1 to $N/10$, and c is a random constant which needs to be chosen in a specific range [227], which we will

discuss later.

$$\mathcal{P}(n) = \sum_{j=1}^{n} \phi(j) \cos(jc) \tag{5.7}$$

$$\mathcal{Q}(n) = \sum_{j=1}^{n} \phi(j) \sin(jc) \tag{5.8}$$

The behavior of these two translation variables can determine the the dynamical states of the system. More specifically, for a periodic or quasi-periodic time series, $\mathcal{P}(n)$ and $\mathcal{Q}(n)$ are correlated, while for a chaotic time series they are uncorrelated. To further investigate the behavior of $\mathcal{P}(n)$ and $\mathcal{Q}(n)$, a modified mean square displacement can be derived,

$$M(n) = D(n) - V_{osc}(c, n) \tag{5.9}$$

where $D(n)$ is the original mean square displacement, defined as follows:

$$D(n) = \lim_{N\to\infty} \frac{1}{N} \sum_{j=1}^{N} [\mathcal{P}(j+n) - \mathcal{P}(j)]^2 + [\mathcal{Q}(j+n) - \mathcal{Q}(j)]^2 \tag{5.10}$$

and $V_{osc}(c, n)$ is the correction term to ensure convergence:

$$V_{osc}(c, n) = [\lim_{N\to\infty} \sum_{j=1}^{N} \phi(j)]^2 \cdot (\frac{1 - \cos nc}{1 - \cos c}) \tag{5.11}$$

The value of $M(n)$ should be bounded within a range around a constant value for a periodic or quasi-periodic time series, and it will linearly increase for a chaotic time series. Subsequently, the asymptotic growth rate of $M(n)$, K_c for a given c is estimated. It can be shown that K_c is the Pearson correlation between vector $\xi = (1, 2, ..., n)$ and $\Delta = (M(1), M(2), ..., M(n))$ [230]. In order to distinguish chaos from other regular dynamics without the effects of resonance, the constant c needs to vary randomly in the range of $\pi/5$ to $4\pi/5$ [227]. Because the value of K_c depends on c, it could attain different

values for a given time series. Then the median of these values needs to be calculated to conduct the testing result K, which is $K = \text{median}(K_c)$ [227]. Finally, $K = 0$ indicates that the system is nonchaotic while $K = 1$ shows the existence of a chaotic attractor [227]. To distinguish SNAs from periodic oscillations and chaos, Gopal et al. [221] showed c should be equal to $\frac{(2\pi)^2}{\omega}$, where $\omega = \frac{\sqrt{5}-1}{2}$.

Next, we use 0-1 test to various dynamical states captured by the model. The phase portraits of the translation variables $\mathcal{P}(n)$ versus $\mathcal{Q}(n)$ (Fig. 5.6(a, d, g)), modified mean square displacement $M(n)$ (Fig. 5.6(b, e, h)), and asymptotic growth rate K (Fig. 5.6(c, f, i)) for different dynamics in the model are shown in Fig. 5.6. As we can see, when the system is quasi-periodic, the trajectory of $(\mathcal{P}, \mathcal{Q})$ is like a circle (Fig. 5.6(a)), $M(n)$ fluctuates around a constant value (Fig. 5.6(b)), and the asymptotic growth rate K (Fig. 5.6(c)) is always close to zero [221]. When the thermoacoustic system transitions to chaos, the trajectory of $(\mathcal{P}, \mathcal{Q})$ fragments into inordinance (Fig. 5.6(g)) and the modified mean square displacement $M(n)$ is almost linearly increasing (Fig. 5.6(h)), which corresponds to the diffusive behavior of the chaotic attractor, thus K is always close to 1 (Fig. 5.6(i)) [220, 221]. As for SNA, it can be difficult to distinguish because it has characteristics of both chaotic attractors (strange and complicated structure) and quasi-periodic attractors (does not sensitively rely on initial condition), but it can be recognized from an oscillatory behavior of $M(n)$ (Fig. 5.6(e)). More specifically, $M(n)$ for an SNA for small n may grow linearly. However, for large n, $M(n)$ tends to be bounded within a range and oscillates around a constant value [220, 221]. Furthermore, the value of K can be lying between 0 and 1 (Fig. 5.6(f)) [231]. Such dynamical behaviors in the model has also been observed in the experimental data (Fig.5.7). Although we are able to detect SNAs in some time series from the model, we note that the range of SNAs is quite narrow in the data from both model and experiment. Thus, currently we are unable to identify a clear boundary for SNA and chaos. We will investigate SNAs predicted by this model in more detail in a future study.

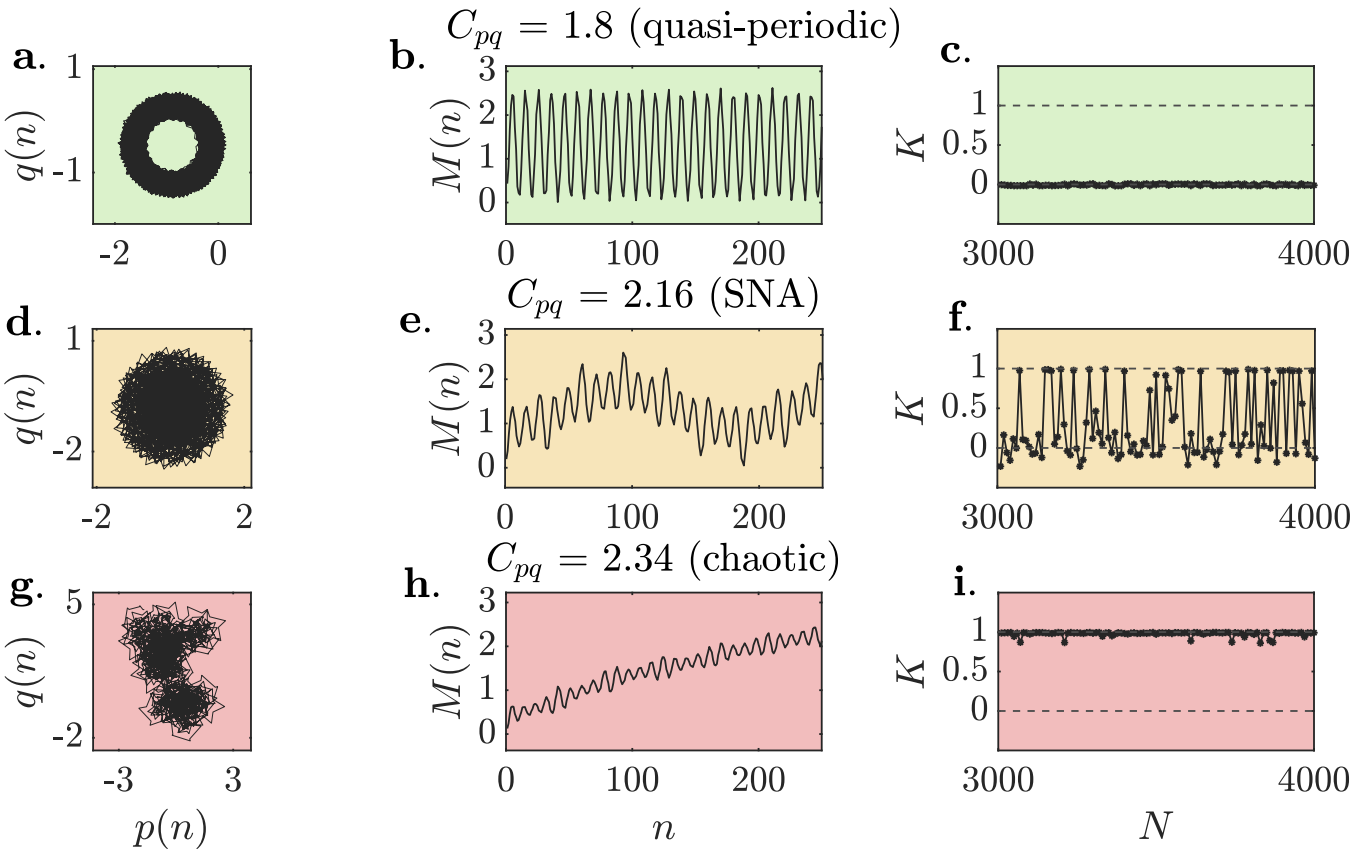


Figure 5.6. The representative diagram on 0-1 test from the model. From left to right: trajectory of translation variables $\mathcal{P}(n)$ and $\mathcal{Q}(n)$ **(a, d, g)**, modified mean square displacement $M(n)$ **(b, e, h)**, the variation of growth rate K **(c, f, i)**. Strange nonchaotic attractors are found in the model by applying 0-1 test, which is consistent with the experimental results

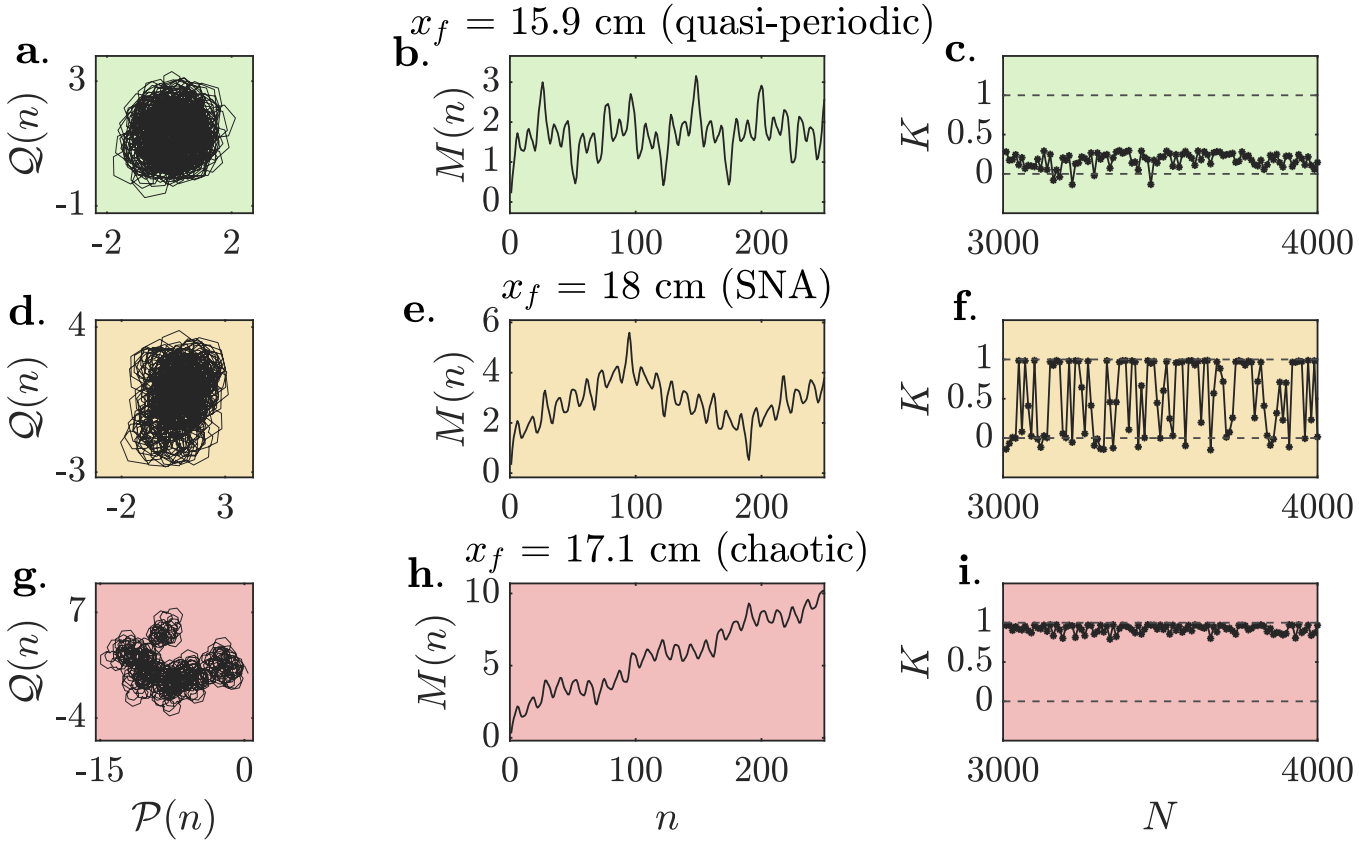


Figure 5.7. The representative diagram on 0-1 test from experiments. From left to right: trajectory of translation variables $\mathcal{P}(n)$ and $\mathcal{Q}(n)$ **(a, d, g)**, modified mean square displacement $M(n)$ **(b, e, h)**, the variation of growth rate K **(c, f, i)**

5.4.4 Summary and outlook

In this paper, we introduced a phenomenological model based on the framework of synchronization that captures the dynamical behaviors observed in a laminar thermoacoustic system. Instead of regarding the unsteady heat release rate as a quasistatic response to the acoustic perturbation, we considered the unsteady heat release rate and the acoustic field as a pair of coupled oscillators. By changing the coupling strength, we show that the the model predicts transitions from a state of limit cycle oscillation to chaos through a route of quasi-periodic oscillation, which is consistent with the experimental result observed by Kabiraj et al. [216]. In addition, strange nonchaotic attractors that appear in the experiment [220] was also captured in the model. These, in summary, confirm that the proposed synchronization based model using coupled oscillators is able to capture the nonlinear dynamical behaviors of a laminar thermoacoustic system.

The present model still has various limitations. For example, it is hard to analytically determine the expression of the unsteady heat release rate as an oscillator. We may be able to derive it using data-driven optimization methods. Secondly, the model is only tested and compared to laminar thermoacoustic instabilities, while in reality thermoacoustic instabilities usually happen in turbulent combustors. We will consider the effect of turbulence and turbulent combustion in a future work.

This chapter is a reprint of the following published article:

Weng, Y., Unni, V. R., Sujith, R. I., Saha, A. (2020). Synchronization framework for modeling transition to thermoacoustic instability in laminar combustors. *Nonlinear Dynamics, 100*, 3295-3306.

Chapter 6

Modeling thermoacoustic instability using the framework of synchronization: Turbulent system

6.1 Introduction

In many power generation devices, including gas turbines, rocket engines, and industrial burners, combustion occurs in an enclosed space. In these devices, the heat release rate fluctuations may interact with the acoustic field in the combustor, and vice versa. As a result, feedback may arise, and when this feedback is positive, there will be growth in acoustic fluctuations, which eventually saturates to limit cycle oscillations due to nonlinearities in the system. This phenomenon is known as thermoacoustic instability. The violent oscillations are usually harmful to combustion devices and can cause the extinction of the flame, or damage the hardware [1, 10–12]. In the past few decades, lean-premixed-prevaporized (LPP) combustors are widely applied in the industry to reduce emissions. The flame is inherently more sensitive to perturbation when operating in fuel-lean conditions. Thus, the LPP combustors are more susceptible to thermoacoustic instability. Because of the wide application of LPP combustors, thermoacoustic instability has become a major concern in combustor design. Numerous studies in the past have focused on predicting the onset, evasion, or suppression of thermoacoustic instabilities.

Rayleigh first explained the emergence of thermoacoustic instability in 1878. He showed that when the acoustic oscillation is in phase with the fluctuations in unsteady heat release rate, energy is added to the acoustic field; hence the amplitude of acoustic pressure will grow [232]. The amplitude would keep increasing until limited by the nonlinear effects. To identify the regime where thermoacoustic instability occurs, investigating the feedback mechanism is of crucial importance [213]. In many cases, the propagation of acoustic waves is considered to be a linear phenomenon since the amplitude of pressure oscillations corresponding to the perturbations is relatively low when compared to the mean pressure in the combustor [42]. The flame, however, is more complex due to the inherent nonlinearities associated with the chemical reactions and transport processes of heat and momentum [233]. The response of the flame to the acoustic perturbation is also highly nonlinear, especially in a turbulent environment [42].

Traditionally, modeling of thermoacoustic instability aims to determine the response of the flame to acoustic perturbation. In the past few decades, several low-order models based on a quasi-linear approach were introduced. Among them, the most commonly used models are flame transfer function (FTF) [213, 234–238] and flame describing function (FDF) [213, 239–241]. FTF estimates the linear response of the flame to acoustic perturbations by either experiment or simulations. External velocity perturbation (u') is introduced to the combustor by using actuators (speakers or linear actuators). Then, the response in the form of the fluctuation in the heat release rate ($\dot{q}'$) is measured and evaluated as a function of the forcing frequencies (ω). The flame transfer function, F, is, then, defined as shown in Eq. (6.1), where $\bar{\dot{q}}$ and $\bar{u}$ are the mean heat release rate and the mean velocity at a given condition.

$$F(\omega) \;=\; \frac{\dot{q}'(\omega)/\bar{\dot{q}}}{u'(\omega)/\bar{u}} \;=\; G(\omega)e^{i\varphi(\omega)} \tag{6.1}$$

Once the FTF is estimated, the global dynamical behavior of a thermoacoustic

system can be evaluated by incorporating the acoustic driving due to heat release rate fluctuations (obtained from FTF) into the acoustic field equations. However, established on classic linear stability analysis, FTF cannot capture the nonlinear effect of the thermoacoustic system. Thus the amplitude of limit cycle oscillation, or triggering phenomenon in a subcritical Hopf bifurcation, cannot be estimated using FTF [242]. Subsequently, flame describing function (FDF) was introduced. Originated from theories of control systems [243] and introduced by Dowling et al. [213, 235], FDF extended the framework of FTF to the nonlinear regime. It defines the complex response of the flame as a function of both input frequency (ω) and amplitude ($|u'|$), as shown in Eq. (6.2).

$$F(\omega, |u'|) \;=\; \frac{\dot{q}'(\omega)/\bar{\dot{q}}}{u'(\omega)/\bar{u}} \;=\; G(\omega, |u'|)e^{i\varphi(\omega,|u'|)} \tag{6.2}$$

The FDF approach considers the flame as a nonlinear module coupled to the linear acoustic system. Compared to FTF, FDF can predict the amplitude of limit cycle oscillation. However, FDF is based on a quasi-linear assumption, i.e., for a particular forcing, the flame only responds at the same frequency. In other words, the response of flame at the higher harmonic frequencies resulting from the forcing is ignored [163]. Thus, FDF may not be suitable for modeling complex behaviors that include non-harmonic responses, e. g. chaos, and intermittency. Moreover, in FDF, the flame is forced by acoustic perturbations at different frequencies and amplitude, which similar to FTF, does not include many aspects of the inherent physics of the flame dynamics [244]. For a long time, the conditions of a thermoacoustic system were considered either operational stable or unstable (limit cycle thermoacoustic oscillation). Correspondingly, FTF/FDF approaches mainly focus on finding out the unstable regime and the amplitude of periodic oscillation. However, experimental observations have shown that thermoacoustic systems can exhibit complex dynamical behaviors other than limit cycle oscillations [158, 245, 246]. Many of these behaviors can be identified from laminar thermoacoustic systems. Beyond limit cycle

oscillation, Kabiraj et al. [44] observed a route to chaos through quasi-periodic oscillation in a laminar Rijke tube, which conforms Ruelle-Takens scenario. Various bifurcations in the same system were subsequently investigated [247], and complex behaviors including strange non-chaos were captured [161]. These findings were also supported by other groups. For example, in a separate study, Guan et al. [248] also identified an intermittency route to chaos in a laminar Rijke tube. Collectively, these studies show that even a simple thermoacoustic system can exhibit rich dynamics.

Inspired by the observations, the underlying physics of these complex behaviors in thermoacoustic systems attracts wide research interest. Existing approaches based on one-way coupling and forced response cannot provide plausible explanations for these phenomena. However, an alternative viewpoint based on synchronization is getting attention recently. Pawar et al. [249] showed that the onset of thermoacoustic instability is an outcome of the mutual synchronization between the unsteady heat release rate and acoustic fluctuations. Depending on the dynamical state of the system, the two signals can be either synchronized or de-synchronized. Later studies by Mondal et al. [250] found various synchronization states including phase locking, intermittent phase locking, and phase drifting. Moon et al. [251] presented a thermoacoustic system that consists of two coupled turbulent combustors, and investigated their mutual synchronization. Premraj et al. [252] investigated the effect of system parameters on the synchronization behaviors of coupled oscillators.

These researches paved the way for building new models for thermoacoustic systems using the framework of synchronization. Godvarthi et al. [253] found that while varying the coupling strength, a system of locally coupled grid of chaotic Rossler oscillators coupled globally to a chaotic Van der Pol oscillator can become self-organized and transition to periodic oscillations. Guan et al. [254] introduced a low order model consisting of two Van der Pol oscillators. Our recent work presented a phenomenological model based on the synchronization framework for modeling laminar thermoacoustic systems [244]. We

use a pair of damped linear oscillators to represent the unsteady heat release rate and acoustic fluctuation, the two oscillators are nonlinearly coupled. By adjusting the coupling strength, the model can replicate the Hopf bifurcation in a laminar thermoacoustic system, capture the route to chaos, and predicts states including quasi-periodic oscillation, chaos, and strange non-chaos. In the present work, we attempt to extend the synchronization framework for thermoacoustic systems to the turbulent regime.

In turbulent combustors, turbulent reactive flow always generates low amplitude disordered acoustic fluctuations in the chamber. During stable operation, the sound is known as combustion noise. Traditionally, combustion noise is considered acoustic fluctuations and treated as background noise. However, recent studies [255–257] showed that combustion noise possesses high-dimensional chaotic fluctuations and exhibits multifractal characteristics. These studies indicate that combustion noise is dynamically complex, and should not be considered pure stochastic fluctuation. Meanwhile, an intermittency state was also discovered presaging the transition from combustion noise to limit cycle oscillation [258, 259]. When increasing the flow rate in the combustor, intermittent bursts of periodic oscillations with high amplitude can appear randomly among low amplitude aperiodic oscillations. Upon increasing the flow rate further, the system will finally enter a regime of periodic oscillation. The transition is found to be a process in which the system gradually self-organizes and loses its multifractality, as order emerges from chaos [257, 260]. Meanwhile, several universal power laws were also identified [193, 194, 261]. These studies provide valuable early warning signals to evade combustion instability.

The main goal of this study is to extend our synchronization framework [244] for the laminar thermoacoustic system to the turbulent regime. Because the model is phenomenological, it should qualitatively replicate the observations from experiments. We expect the model to capture the transition from combustion noise to limit cycle oscillation through intermittency. Furthermore, the model should identify the self-organization and loss of multifractality in the transition. In our previous work [244], we showed that a

pair of coupled oscillators with proper coupling strength can model the quasi-periodic route to chaos observed in laminar thermoacoustic systems. Based on that experience, in this work, we use a tuned pair of coupled oscillators to represent the simplified turbulent reactive flow. These two oscillators are then coupled with a third oscillator representing the acoustic field. We will show that, with proper coupling strength, this three-oscillator model can reflect the combustion dynamics arising in a turbulent combustor.

The rest of the manuscript is organized as follows: in Sect. 6.2, we introduce the model based on the synchronization framework; In Sect. 6.3.1, we introduce the experimental setup; In Sect. 6.4, we compare the dynamics observed in the model and the experiment. The results will show that the model can qualitatively replicate the transition from combustion noise to periodic oscillation in a turbulent thermoacoustic system. Power laws associated with self-organization and loss of multifractality are also captured.

6.2 Model construction

Our primary goal is to present a phenomenological, reduced-order model based on a synchronization framework for modeling the transition to thermoacoustic instability in a confined turbulent combustor. In our previous study [244], we proposed a synchronization-based model for a laminar combustor, where the acoustic field and the unsteady heat release rate were represented by a pair of nonlinearly coupled damped oscillators, each of which had a two-dimensional phase space. By varying the coupling strength between the two oscillators, the system could reproduce the route to chaos observed in a laminar combustor [44]. The system also captured multiple bifurcations and different dynamical states, including limit cycle oscillation, quasi-periodic oscillation, strange-non chaos [161], and chaos. Expanding on that work, this study considers the acoustic pressure and unsteady (turbulent) heat release rate as two nonlinearly coupled sub-systems. Unlike in a laminar combustor, a turbulent combustor's heat release rate fluctuations exhibit chaotic

behavior when the coupling between the unsteady heat release rate and the acoustic field is weak. In order to capture this, the unsteady heat release rate in the proposed model for the turbulent combustor is represented using a pair of coupled second-order differential equations (Eqs. (6.3-6.4)). This system of differential equations with appropriate coupling strength exhibits chaotic dynamics in four-dimensional phase space. Hence they can represent the chaotic oscillations corresponding to turbulent heat release rate. Here we consider that the time series of y_2 represents the unsteady heat release rate. Eqs. (6.3-6.4) are further coupled with Eq. 6.5 that represents the acoustic oscillator. Note that y_3 represents the pressure fluctuations.

The system of oscillators has angular frequencies of ω_1, ω_2, and ω_3. We will use the symbol f to denote the frequency, which is related to angular frequency as $\omega = 2\pi f$. The damping coefficients are ζ_1, ζ_2, and ζ_3.

$$\ddot{y}_1 + \zeta_1\omega_1\dot{y}_1 + \omega_1^2 y_1 = C_{12}(1 - {y_2}^2)\dot{y}_1 \tag{6.3}$$

$$\ddot{y}_2 + \zeta_2\omega_2\dot{y}_2 + \omega_2^2 y_2 = R_1 C_{12} y_1^2 + R_2 C_{32} y_3^3 \tag{6.4}$$

$$\ddot{y}_3 + \zeta_3\omega_3\dot{y}_3 + \omega_3^2 y_3 = C_{32}(1 - y_2^2)\dot{y}_3 - \dot{y}_3^3 \tag{6.5}$$

We define $C_{12}, C_{21}, C_{23}, C_{32}$ as the coupling strength. Furthermore, the relative strength of the mutual coupling is defined using the ratio of C_{ij}s, $R_1 = C_{21}/C_{12}$, $R_2 = C_{23}/C_{32}$. The presented reduced-order model is designed to replicate the dynamical states observed in a turbulent combustor exhibiting thermoacoustic instability. We leveraged knowledge gathered from past experiments to help guide the selection of various model parameters. For example, recent studies showed that the coupled interaction between the unsteady heat release rate and the acoustic field is asymmetric [262, 263].

Unsteady heat release rate exerts a stronger influence on the acoustic field than the converse, which implies $C_{32} > C_{23}$ so that $R_2 < 1$. We select the natural frequencies of the three oscillators (ω_1, ω_2, and ω_3) such that the time series of pressure and heat release rate have a similar value and variational trend for the dominant frequency with a change in the control parameter as observed from experiments. To achieve this, we assign a fixed ratio between ω_1 and ω_2 ($\omega_1 = 1.125\omega_2$), resulting in intended aperiodic oscillations when the heat release rate subsystem (Eq. 6.3-6.4) was weakly coupled to the acoustic oscillator (Eq. 6.5). Meanwhile, to ensure that the dominant frequency of $\dot{q}'$ increases during the transition as observed in the experiment, we set a linear relationship between the natural frequency, ω_2 and the coupling strength C_{32} ($\omega_2 = 2\pi C_{32}/20$). The natural frequency of the acoustic field (y_3) is chosen to be constant ($\omega_3 = 1.3 \times 2\pi$) since in the experiments, the dominant frequency of acoustic oscillations is more or less constant. The nonlinear terms $C_{12}(1 - y_2^2)\dot{y}_1$ and $C_{32}(1 - y_2^2)\dot{y}_3$ are inspired by Van der Pol oscillator. The other nonlinear terms, however, are manually selected to match the experimental observation, a more detailed description of this process is given in Sect. 6.4. In essence, we start with nonlinear terms with the lowest exponents and smaller degrees and increase the complexities of the terms until we qualitatively and statistically reproduce the dynamics observed in the experiments (nature of transitions in dynamics, the frequency profile, and the fractal characteristics of p'). The set of parameters we choose is not unique, and it is possible to use another set of better-optimized nonlinear terms with higher degrees and exponents to improve the model. Towards this, a data-driven optimization strategy will be designed in future work. The other parameter values used in Eqs. (6.3-6.5) are selected to be: $\zeta_1 = 0.1$, $\zeta_2 = 0.05$, $\zeta_3 = 0.3$, $C_{12} = 1.62$, $R_1 = 1.2$, and $R_2 = 0.54$. In the study, since Eq. 6.3 and Eq. 6.4 form a subsystem that represents the unsteady heat release rate, C_{12} is fixed. Meanwhile, C_{32} is considered the control parameter which dictates the transitions between different dynamical states of the system. In an experimental turbulent thermoacoustic system, the control parameter is generally the Reynolds number of the flow,

$Re{=}\bar{u}L/\nu$, where L is the characteristic length scale of the burner and ν is the kinematic viscosity of the unburned mixture. With the current model and the value of parameters mentioned above, the transition between various states was observed for the range of C_{32} from 14 to 18. The coupled equations (Eqs: 6.3-6.5) are solved using the 4th-order Runge-Kutta method in Matlab. Gaussian noise with variance $\sigma = 5\%$ is added to the time series. We note that for a fixed C_{32}, the model outputs a normalized time series of heat release rate and pressure fluctuations.

As mentioned earlier, the primary goal of this work is to demonstrate that coupled oscillator models can reproduce combustion dynamics in a turbulent combustor. During the construction of the model, we intended to keep the nonlinear terms as simple (low-order) as possible while qualitatively reproducing the key dynamics observed in experiments. The current forms of nonlinear terms shown in Eqs: 6.3-6.5 and the values of various constants were chosen after manual optimization and satisfied the requirements. We note that, in general, a large number of possible forms of nonlinear terms can be selected. A robust method for identifying and optimizing the nonlinear terms will be a focus of our future work.

6.3 Methodologies

6.3.1 Experimental Details

We primarily use the experimental data from Pawar et al. [249] as a benchmark to validate the model. The experimental study applies to a laboratory-scale turbulent combustor with a bluff body stabilized flame, where liquefied petroleum gas was burned with air. The incoming airflow first passes through a settling chamber. Then, it is premixed with the fuel and sent into the combustion section. The pressure fluctuation (p') in the combustor is estimated using pressure transducers. The heat release rate ($\dot{q}$) is acquired by measuring the chemiluminescence intensity of CH* using a photo-multiplier tube (PMT),

from which its fluctuations ($\dot{q}'$) are calculated. During the experiment, the fuel flow rate was kept constant at 25 slpm, while the air flow rate varied from 400 slpm to 940 slpm, covering Reynolds number (Re) range from 1.09×10^5 to 2.12×10^5. We note that an increase in flow rate (Re) increases the mean heat release rate ($\bar{q}$) of an unconfined (de-coupled from acoustics) turbulent flame due to decreased residence time [264]. Thus, it is appropriate to use heat release rate intensity $\dot{q}'_{rms}/\bar{\dot{q}}$ as the statistical measure of fluctuations. However, the acoustic characteristics of the chamber remain unaffected by the Re. Thus p'_{rms} is a good measure.

The measurements confirm that the combustor exhibited stable operation at low Re. However, the pressure and heat release rates fluctuate at a low amplitude due to the inherent turbulence. This regime refers to high dimensional chaos [265]. As Re increases, the amplitude of pressure oscillation increases continuously. Meanwhile, among aperiodic oscillations, burst and periodic oscillations start emerging in a near-random fashion, which refers to the state of intermittency. When Re further increases, both pressure and heat release rates oscillate periodically and with significantly greater amplitude, corresponding to the onset of thermoacoustic instability.

We will use a second set of experimental data from Nair et al. [258] during our discussion on the power-law behaviors in the transition process (Sec: 6.4.5). This work used a swirl-stabilized burner. The rest of the configuration and experimental technique remained mostly unchanged. The details of this setup can be found in [258].

In experiments, the flow in the combustor is fully developed (constant turbulence intensity, $u'_{rms}/\bar{u}$) and hence, u'_{rms} grows linearly with Re ($u'_{rms} \propto Re$). In these experiments, the measured p'_{rms} and $\dot{q}'_{rms}$, which increase with Re, are composed of the contribution from turbulence and the thermoacoustic instability. The former arises from the RMS of the fluctuations in flow velocity u'_{rms}, and hence can be assumed to be proportional to Re. These turbulence-induced effects are apparent when one measures the pressure in a turbulent flow inside the combustor without the flame or heat release rate in an unconfined

flame, thus no thermoacoustic effects. It is to be noted that the model presented in Eqs: 6.3 - 6.5, only accounts for the coupled dynamics between acoustics and heat release, thus discounts the increase in p'_{rms} and $\dot{q}'_{rms}$ due to turbulence effects. Since these discounted effects are proportional to Re, and in our model, we assumed $C_{32} \sim Re$, for comparison purposes, the experiment equivalent of pressure and heat release rate from our models can be obtained as $p' = y_3 C_{32}$, and $\dot{q}' = y_2 C_{32}$.

6.3.2 Multifractal Detrended Fluctuation Analysis

In Multifractal Detrended Fluctuation Analysis (MFDFA), the signal of $x(i)$ will first be accumulated to generate a new signal (Eq. 6.6), called "the profile".

$$Y_i \;=\; \sum_{k=1}^{i} (x_k - \bar{x}) \tag{6.6}$$

Next, the profile with length N is separated into N_s equal-sized, non-overlapping segments. the segments are detrended by subtracting the local linear fit $\bar{Y}$. Then, a structure function F_s^w of order w and span s can be obtained:

$$F_s^w = \left(\frac{1}{N_s} \sum_{i=1}^{N_s} \left(\frac{1}{s} \sum_{i=1}^{s} \left(Y_i - \bar{Y} \right)^2 \right)^{\frac{w}{2}} \right)^{\frac{1}{w}} \tag{6.7}$$

The generalized Hurst exponent of order w (H^w) is then defined as the slope of the linear regime of F_s^w verses s in a logarithmic plot. Note that the Hurst exponent H^2 corresponds to the generalized Hurst exponent of order 2 (i. e. $w = 2$). In this study, the range of w is chosen from -2 to 2. From the generalized Hurst exponents, we apply Legendre transformation to generate the singularity exponents α and the singularity spectrum $f(\alpha)$ by using the following relations:

$$\tau_w = wH^w - 1; \quad \alpha = \frac{\partial \tau_w}{\partial w}; \quad f(\alpha) = w\alpha - \tau_w \tag{6.8}$$

Further details can be found in [266, 267].

6.4 Results and discussions

The presented synchronization-based three-oscillator model is expected to replicate some of the key features of a turbulent combustor. The model should capture the transition from combustion noise to periodic oscillation, during which the amplitude of pressure and heat release rate oscillation increase monotonically. It should also predict different synchronous states during the transition, which mostly depends on the synchronization states of the pressure and heat release rate. Moreover, in the regime of combustion noise, the model is expected to produce a multifractal behavior in pressure oscillations, which is the hallmark of a stable turbulent combustor. As the system transitions to thermoacoustic instability, self-organization is observed during experiments [193, 194] and the time series shows a scale-independent nature marked by power-law dynamics. We expect the model to be able to predict similar behavior.

In the following subsections, we will analyze the statistics and dynamics of the time series produced by the model and will qualitatively compare them with those of the experimental data. We note that the primary expectation from the model with predefined model parameters is to reproduce the experimental observations qualitatively. The quantitative similarity is not expected, which requires tuning the model parameters based on the experiments.

6.4.1 The temporal transition from combustion noise to periodic oscillation

First, we will use the temporal dynamics and their statistics in assessing the model performance. As mentioned before, in the model, the control parameter is the coupling strength between the unsteady heat release rate and the acoustic oscillator C_{32}. Increasing the coupling strength C_{32}, the system transitions from chaos to periodic limit cycle

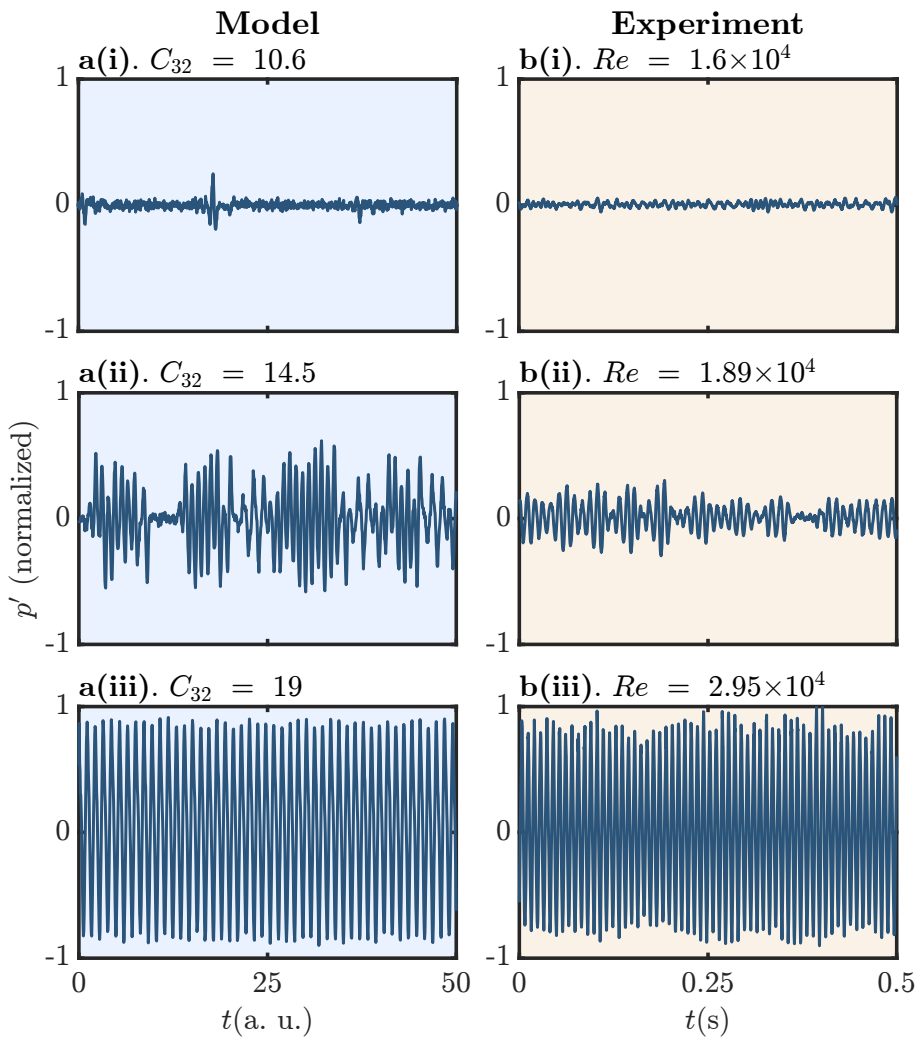


Figure 6.1. Time series obtained from the model and experiments at different dynamical states. Note that Gaussian noise with variance $\sigma = 5\%$ is added to the time series from the model. From left to right: model, experimental results from Pawar et al. [249] From top to bottom: combustion noise (**a(i)**: $C_{32} = 11.05$, **b(i)**: $Re = 1.6 \times 10^4$), intermittency (**a(ii)**: $C_{32} = 14.95$, **b(ii)**: $Re = 1.89 \times 10^4$), limit cycle oscillation (**a(iii)**: $C_{32} = 19.7$, **a(iii)**: $Re = 2.95 \times 10^4$).

oscillation through intermittency, a behavior also observed in experiments. Figures. 6.1a(i, ii, iii) show representative time series of the normalized pressure functions from the model at different C_{32}. These plots also illustrate the changes in the morphology of the time series at different dynamical states. Figures. 6.1b(i, ii, iii) shows a similar time series obtained from experiments ([249]) at different Re, which clearly exhibit very similar qualitative behaviors. As shown in Fig. 6.1a(i), at low C_{32}, the signal is disordered, and the

overall amplitude of p' is small, which corresponds to the regime of combustion noise. In Fig. 6.1a(ii), as C_{32} increases, although the time series remains disordered, the amplitude of the time series increases, and intermittent oscillations appear. During intermittency, the signals are composed of aperiodic, low-amplitude fluctuations interspersed amongst periodic, high-amplitude fluctuations in a near-random fashion. The different parts of the signal have amplitudes with several different orders of magnitudes [258]. Previous studies proposed a route from combustion noise to thermoacoustic instability through intermittency [258], and hence it is important to determine the existence of an intermittency state in the model. When we further increase C_{32}, as shown in Fig. 6.1a(iii) the time series becomes more regular and with a larger amplitude, the periodic oscillation has now become dominant. It indicates that the system has entered the regime of limit cycle oscillation. As mentioned earlier, we observe similar characteristics in the corresponding time series from the experiment, shown in columns Fig. 6.1b(i, ii, iii).

6.4.2 The variation in the *RMS* and dominant frequency of the pressure and the heat release rate fluctuations

One of the hallmarks of thermoacoustic instability is the large increase in the amplitude of pressure and heat release rate fluctuations as the system transitions from combustion noise to the limit cycle oscillation. While this can be visualized qualitatively for three different C_{32} (model) and Re (experiment) in Fig. 6.1, we additionally compare the root mean square values of both pressure fluctuations (p'_{rms}) and heat release rate fluctuations (q'_{rms}) for a range of operating conditions (Fig. 6.2a(i) and b(ii)). Here we evaluate the *RMS* of time series of a quantity, $x(t)$ as

$$x_{\mathrm{rms}} = \sqrt{\frac{1}{M}\sum_{i=1}^{M}(x(t_i)-\bar{x})} \tag{6.9}$$

where $\bar{x}$ is the mean of x and M is the length of the time series. Our model predicts a

continuous increase of p'_{rms} and q'_{rms} with an increase in the control variable, C_{32} (Fig. 6.2a(i)), a trend which is observed for experiments with turbulent combustor (Fig. 6.2b(i)).

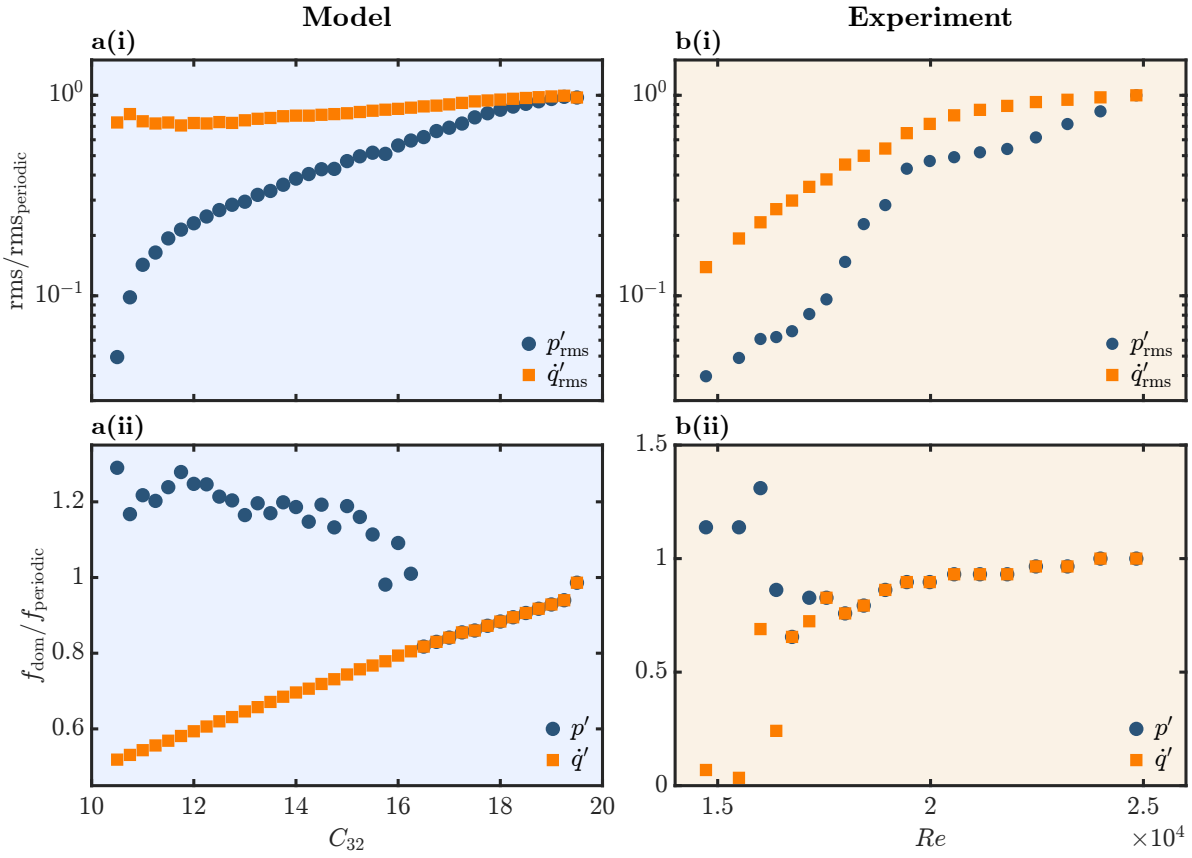


Figure 6.2. **a(i)** and **b(i)**: *RMS* of p' and $\dot{q}'$ at different conditions from model and experiment. As C_{32} or Re increases, p'_{rms} increases monotonically. **a(ii)** and **b(ii)**: dominant frequency of p' and $\dot{q}'$ at different conditions from model and experiment. The dominant frequency of pressure and heat release rate when C_{32} or Re varies. As C_{32} or Re increases and the system transitions to periodic oscillation, both signals start to have the same dominant frequency.

We next analyze the dominant frequency of the pressure and heat release rate signals, which is critical in determining the mode of oscillations in thermoacoustic instabilities. Figure 6.2a(ii) depicts the variations of dominant frequencies of p' and $\dot{q}'$ with C_{32}, predicted by the model. As we can see in the figure, initially at low C_{32} during the state of combustion noise, the two signals exhibit different dominant frequencies, which are far apart. But as C_{32} increases, the two dominant frequencies gradually merge, and finally, both signals

have the same frequency during limit cycle oscillation (high C_{32}). This suggests that the two signals are synchronized with each other (we will quantify this process in the next subsection). Similar behavior of dominant frequency is also observed for experiments as Re is increased (Fig. 6.2b(ii)). Furthermore, we also compare the power spectral density (PSD) of p' at various C_{32} (model) and Re (experiment) in Fig. 6.3. They indeed show a similar trend in that, the peak of the dominant frequency becomes sharper in the spectrum as C_{32} or Re increases, and periodic oscillations become more dominant (seen in Fig. 6.1). The sharpened peak indicates that the energy is gradually concentrated to the dominant frequency from a previously broadband spectrum at low C_{32} or Re. We will quantify and discuss the behavior of spectral condensation in the later section.

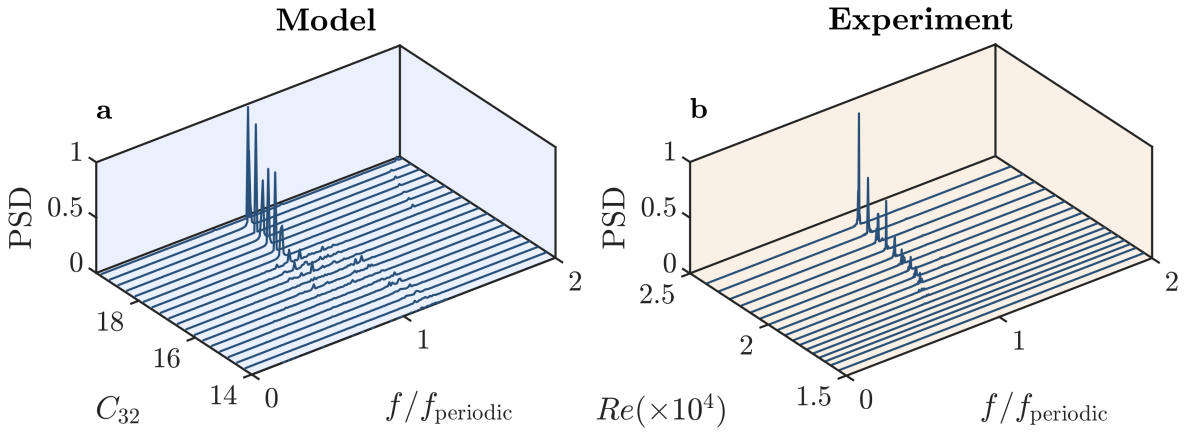


Figure 6.3. The power spectra density of p' at different conditions from model and experiment. As C_{32} or Re increases, the height of the peak increases significantly, where periodic oscillation becomes dominant.

6.4.3 Synchronization characteristics

As mentioned in the introduction, experimental studies have shown that the time series of p' and $\dot{q}'$ exhibit a de-synchronous state during the state of combustion noise, in that the phase of their oscillation varies with time. The studies have also confirmed that these time series become phase synchronized as the system approaches the onset of combustion (thermoacoustic) instability. During limit cycle oscillation, p' and $\dot{q}'$ become

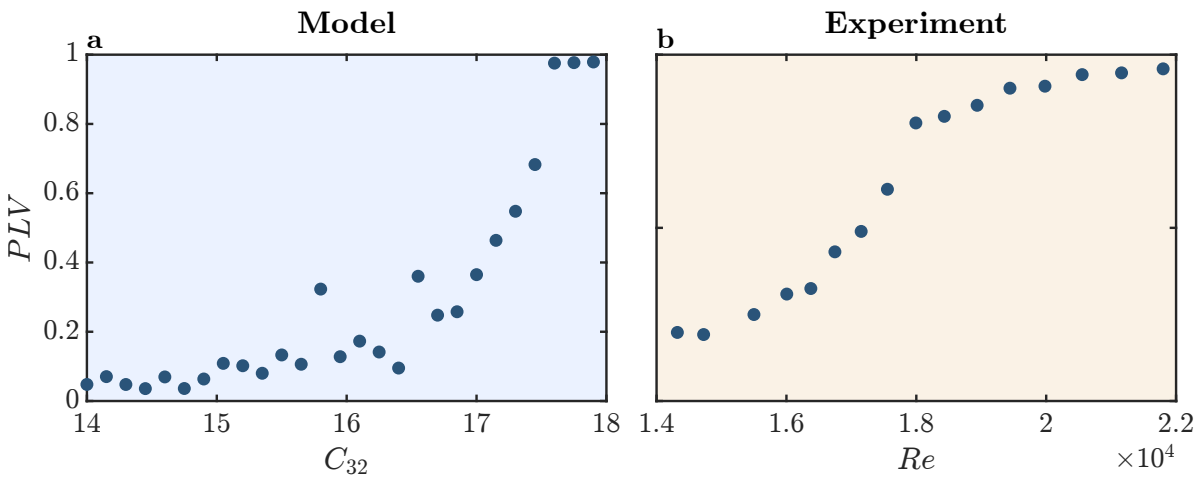


Figure 6.4. PLV between p' and $\dot{q}'$ at different conditions from model (**a**) and experiment (**b**). In the regime of combustion noise, the phase lock value between p' And $\dot{q}'$ is close to 0, which indicates the two signals are desynchronized. As periodic oscillation appears, PLV increases and stays close to 1, which corresponds to synchronization.

completely phase-locked or phase synchronized. The degree of synchronization between p' and $\dot{q}'$ can be evaluated with the *Phase Locking Value* (PLV), which can be calculated using the Hilbert transform and the relation [268],

$$PLV = \frac{1}{M}\left|\sum_{i=1}^{M} e^{j\left(\phi_{p'}(t)-\phi_{\dot{q}'}(t)\right)}\right|, \tag{6.10}$$

where $\phi_{p'}(t)$ and $\phi_{\dot{q}'}(t)$ are the instantaneous phase of the pressure and heat release rate fluctuations. PLV can vary between 0 to 1; a PLV value of 0 indicates that the two signals are desynchronized, and a PLV value of 1 corresponds to perfect phase synchronization. The PLV evaluated based on the experimental data [249] plotted in Fig. 6.4(b), shows low values of PLV at low Re (control parameter for the experiments) and at high Re, PLV approaches 1, suggesting phase synchronization. To assess if our model can predict such characteristics, we calculated the PLV from the model output and then plotted it as a function of the coupling strength, C_{32} in Fig. 6.4(a). The time series of p' and $\dot{q}'$ are de-synchronized at a low C_{32} (combustion noise). Like experiments, the model also predicts an increase in PLV with C_{32} (control parameter for the model). Finally, PLV

becomes almost 1 when $C_{32} > 17$, suggesting phase synchronization during limit cycle oscillations.

6.4.4 Loss of multifractality during transition

In a turbulent combustor, the observed flame dynamics are an outcome of the continuous interaction of multi-scale eddies in the flow with the chemical reaction. Such interaction leads to a broadband low amplitude oscillation in the heat release rate and pressure fluctuations, even in the de-synchronized states. Such broadband oscillations or combustion noise has been traditionally assumed to be stochastic and has been modeled as white or colored noise in many studies [265, 269–271]. However, recent studies have shown that combustion noise is not always stochastic, and it has features of higher-dimensional chaos [255, 272]. Furthermore, experimental data and analyses have also shown that the pressure fluctuations from combustion noise can be self-similar and exhibit multifractality [256, 257, 260]. Such behavior of multifractality is, indeed, a hallmark of turbulent flows [273–275] and turbulent flame dynamics [89, 276, 277]. In other words, combustion noise caused by turbulent reactive flows is dynamically complex and can be considered deterministic. More recent studies showed that the onset of thermoacoustic instability can be characterized as an order emerging from chaos via a state of intermittency [163]. During this transition, the system gradually loses its multifractality [257, 260]. Based on these observations, several techniques are proposed to determine the stability boundaries and to provide early warning signals (EWS) [257]. Since the proposed model aims to replicate the dynamics of turbulent combustors, it is critical to assess if it can reproduce the presence and loss of multifractality in pressure fluctuations in combustion noise and thermoacoustic instability (limit cycle oscillations), respectively.

In time series analysis, the fractal dimensions (D) are often used to characterize fractal behavior, where the value and the length of the data show a self-similarity associated

with a power law, and D is the exponent of the scaling relation. Fractal nature also exists in many complex systems, e.g. time signals with complex dynamics can be self-similar in local fluctuations with multiple scales [278]. In a self-similar time series, the fractal dimension is related to the Hurst exponent (H) as $D = 2 - H$ [279], which evaluates the long-term memory of the time series. However, in many systems involving broadband perturbations (e.g., turbulence), the scaling behavior can be more complex and may depend on the order of the structure function, giving rise to multifractality. A multifractal system, instead of one single Hurst exponent, requires a singularity spectrum consisting of a series of generalized Hurst exponents with multiple orders to describe its characteristics [280]. The singularity spectrum depicts the fractal behaviors of local fluctuations of different magnitudes. In our work, the generalized Hurst exponents are evaluated by multifractal spectrum $f(\alpha)$ versus singularity exponent α using the multifractal detrended fluctuation analysis (MFDFA) [266, 267]. In the appendix, we provide a brief description of MFDFA.

Using MFDFA, the multifractal spectra $f(\alpha)$ for pressure oscillations obtained from our model and previous experiment [249] are plotted as a function of α in Fig. 6.5a and b, respectively. It is to be noted that the width of the spectrum quantifies the degree of multifractality of the time series. Figure 6.5a shows that at low C_{32} (combustion noise) the spectrum is indeed wide, suggesting strong multifractality and hence complexity. This behavior is also observed for experimental data at low Re (Fig. 6.5b). As C_{32} increases, the width of the spectrum shrinks, indicating that the system gradually loses its multifractality as it approaches thermoacoustic instability. At high C_{32}, when the system exhibits limit cycle oscillations, the spectra condense to a point, and hence the multifractality has been lost. This reduction of width and the collapse of the multifractal spectrum can also be seen in experimental data as Re is increased (Fig. 6.5b).

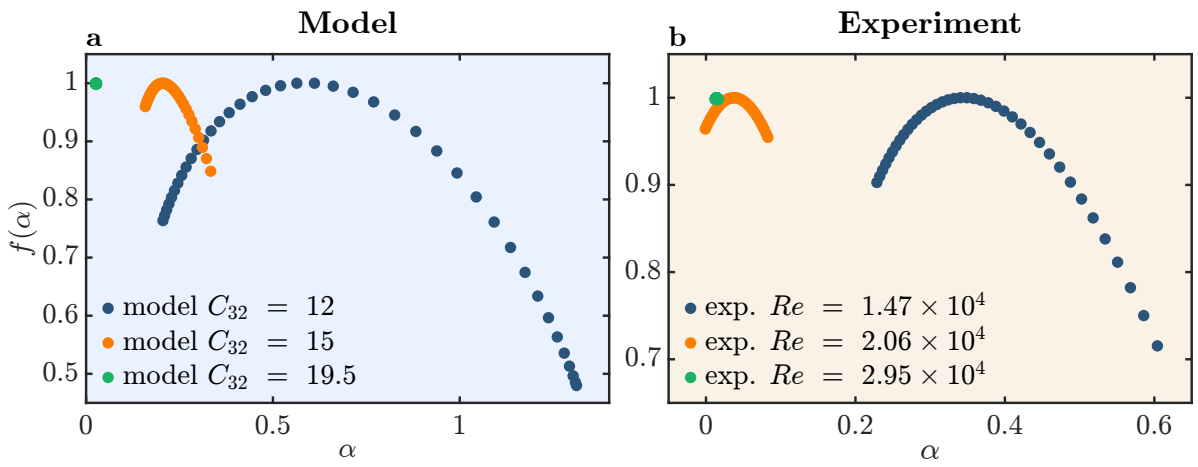


Figure 6.5. Multifractal spectrum at different dynamical states from the model (**a**) and experiment (**b**), as C_{32} or Re increases, the system transitions from combustion noise to periodic oscillation. In the regime of combustion noise, the multifractal profile exhibits a wide range spectrum, corresponding to a dynamically complex state. During the transition, the spectrum shrinks, indicating that the system gradually loses its multifractality.

6.4.5 Power law in self-organization

In this section, we will discuss the recent discoveries of scaling relations observed as a turbulent system transitions to thermoacoustic instabilities, and assess if the proposed coupled oscillator model can also produce such dynamics. Turbulent systems generally contain high-dimensional chaos, and their time series is naturally irregular and disordered. However, when turbulence is coupled to the other subsystems, through their inherent coupling, self-organization may occur, in that the underlying broadband nature is lost. One typical example is the turbulent Rayleigh-Bénard system, where the fluid motion is turbulent at a low-temperature gradient. However, fluid particles may move orderly at a high-temperature gradient and result in large-scale spatial patterns [281]. During self-organization, the positive feedback leads the disordered, chaotic system to transition to an ordered state, and regularly repeating patterns emerge both time-wise and space-wise. The initially disordered state is generally a superposition of a series of motions with a wide range of modes and a broadband energy spectrum. During self-organization, one or more modes gradually emerge and become dominant. Self-organization has been studied extensively

in various turbulent systems including aeroelastic [282] and aeroacoustic [283] systems. In recent years, studies found that the transition from chaotic fluctuations to periodic oscillations in the turbulent thermoacoustic system is also a process of self-organization [260]. Several self-similar behaviors were subsequently identified, including the power laws of Hurst exponent [194] and spectral condensation [193]. To validate the proposed model, we will assess the scaling laws of the Hurst exponents and spectral condensation using the methodology reported by Pavithran et al. [193, 194]. Simultaneously we will use the same measures on two sets of different experiments, bluff-body stabilized [249] and swirl-stabilized [258] combustors.

As discussed in 6.4.4, the Hurst exponent relates to the fractal dimension and can vary between 0 and 1. Time series with $H = 0.5$ refers to uncorrelated random fluctuations. For the upper range ($0.5 < H < 1$), the time series is persistent with a long-term positive auto-correlation, i. e. a high value in the time series is likely to be followed by another high value. On the other hand, for $0 < H < 0.5$, the time series is antipersisitent, i. e. it tends to switch between high and low values. In recent studies [193, 261], an inverse power-law relation between the spectral amplitude of the dominant mode (A) and the Hurst exponent ($H \propto A^n$) was reported in turbulent systems that exhibit a transition from the chaotic state to periodic state and thus, self-organization. Interestingly, the exponent n was found to be almost constant and $n \approx -2$ for a series of different systems, including aeroacoustic, aeroelastic, and thermoacoustic systems. Here, we calculated the Hurst exponent and spectral amplitude of the dominant mode during the transition from the data produced by the model. The results are compared with the experimental data from the bluff-body and swirler combustors, as shown in Fig. 6.6. We, indeed, observe a power law with an exponent close to -2 for both the model and the experiments. Such agreement implies that the model is capable of capturing the underlying path in the transition to thermoacoustic instability in turbulent combustors.

Next, we investigate the model's capability in capturing the self-organization

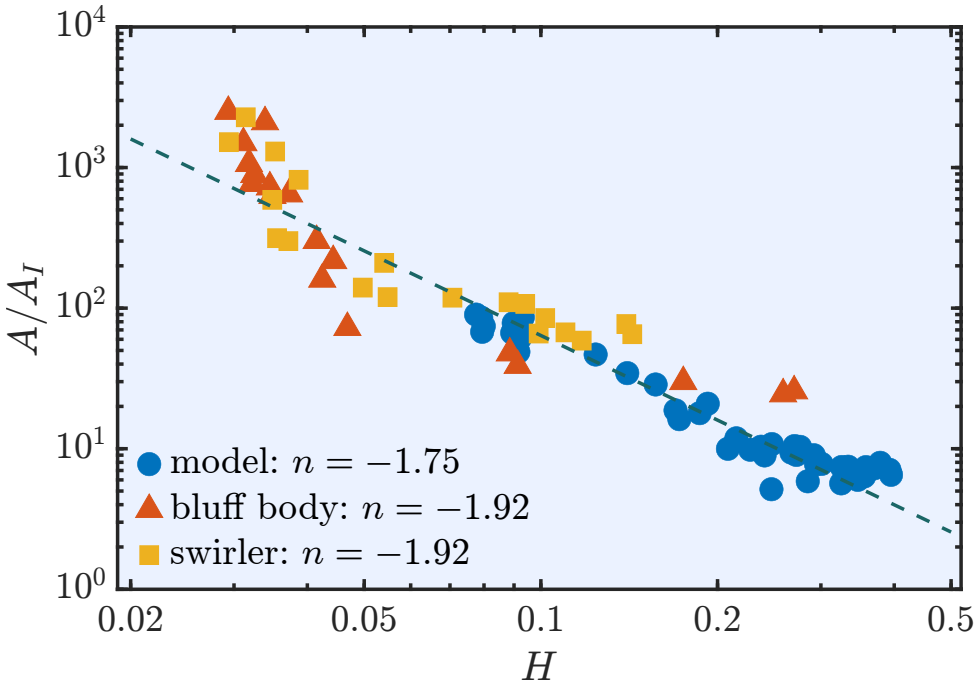


Figure 6.6. The spectral amplitude of the dominant mode (A) versus Hurst exponents (H) at different control parameters during the transition to thermoacoustic instability. Note that both A and H are plotted on a logarithmic scale, and A is normalized by the A_I, which is the y-intercept of linear regression: $\log(A) = n\log(H) + \log(A_I)$. We observed that an inverse power law, $A/A_I \propto H^n$ with an exponent $n = -2$ (dashed line) fits the data from both model and the two experimental studies. Experimental data are from the bluff-body-stabilized combustor by Pawar et al. [249], and swirl-flow combustor by Nair et al. [258].

using another measure reported in [194, 261]. In the regime of combustion noise, the time series is aperiodic, with a low amplitude, and show a broadband profile in the power spectrum. However, when the system undergoes limit cycle oscillation due to thermoacoustic instability, the time series become periodic, the amplitude increases significantly, and the natural frequency shifts slightly and becomes dominant in the power spectrum. During the transition, the profile of the power spectrum narrows from a broad peak centered around the natural frequency to a single sharp peak (Fig. 6.3). The measurement of spectral condensation quantifies how the power spectrum condenses during the transition by calculating the m^{th} moment of the power spectrum, evaluated as

$$[\mu_m^x \mu_n^y] = \left[\int_{-\delta F}^{+\delta F} \frac{P(F)}{P_0} \left|\frac{F}{f_0}\right|^m dF\right]^x \times \left[\int_{-\delta F}^{+\delta F} \frac{P(F)}{P_0} \left|\frac{F}{f_0}\right|^n dF\right]^y \tag{6.11}$$

μ_m here is the m^{th} moment of the power spectrum, f is the frequency, f_0 is the dominant frequency of time series, $P_0 = P(f_0)$ is the dominant peak of the power spectrum, and $F = f - f_0$ is the modified frequency. $[\mu_m^x \mu_n^y]$ here are the products of higher-order moments of the power spectrum. In Fig. 6.7, we compare a few high-order moments statistics obtained from the model and the experiments. The figure shows that for all the moments, the model and the experiments do follow a similar behavior in that during the transition from combustion noise to periodic oscillation, the variation of $\mu_m^x \mu_n^y$ follows a power law. The exponents of the power law are not the same constant across the model and the two experiments, primarily due to underlying coupling mechanisms. Nevertheless, the comparison confirms that the coupled oscillators can capture the underlying higher-order statistics of spectral condensation observed during the transition to the periodic states.

6.4.6 Summary and outlook

In this study, we introduced a phenomenological model for modeling turbulent thermoacoustic systems. The model is based on the synchronization framework, consisting of three oscillators. The first two oscillators are coupled nonlinearly at a fixed coupling strength and form a sub-system representing the unsteady heat release rate from the turbulent reactive flow. Meanwhile, the third oscillator represents the acoustic field. The acoustic field and the unsteady release are coupled with a variable coupling strength. The model can replicate the transition from stable operation to thermoacoustic instability in a turbulent combustor by adjusting the coupling strength. When the coupling strength is small, the model can produce chaotic oscillation with multifractal characteristics corresponding to combustion noise. As the coupling strength increases, the system loses multifractality and transitions to periodic oscillation with higher amplitude through inter-

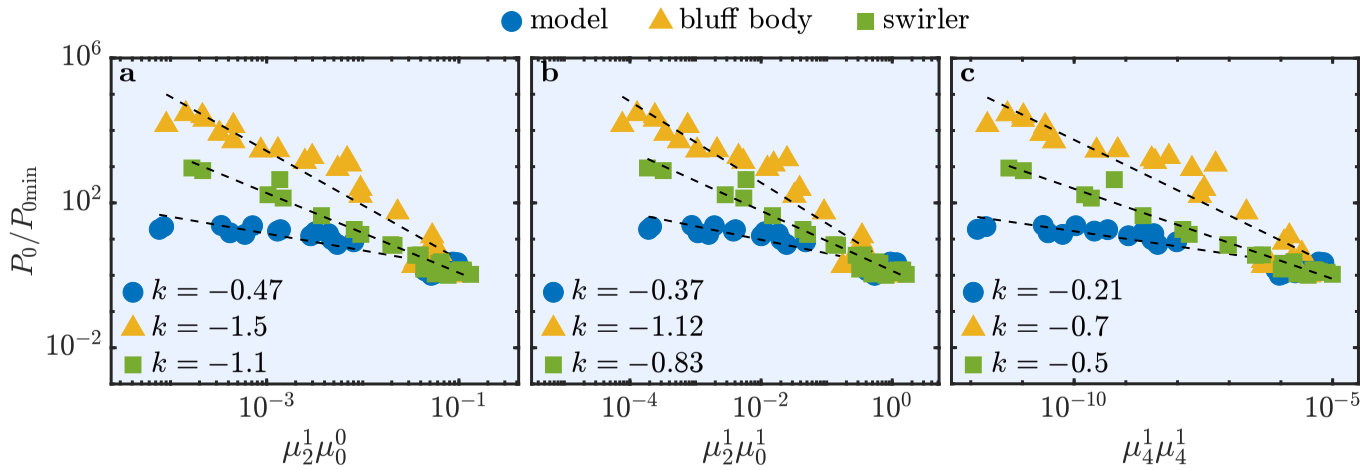


Figure 6.7. Scaling behaviors of spectral condensation from the model and experiments, which follows $\log(P_0) = k\log([\mu_m^x\mu_n^y]) + C$. Note that both P_0 and $[\mu_m^x\mu_n^y]$ are plotted on a logarithmic scale, and P_0 is normalized by $P_{0\min}$. Experimental data are from the bluff-body-stabilized combustor by Pawar et al. [249], and swirl-flow combustor by Nair et al. [258]. From left to right: $\mu_2^1\mu_0^0$, $\mu_2^1\mu_0^1$, $\mu_4^1\mu_4^1$.

mittency. These behaviors are consistent with the experimental observations. Furthermore, we analyzed the self-organization behavior during the transition by calculating the scale of spectral condensation. The scale shows power laws similar to the ones reported in the experiments. In contrast to FTF/FDF, the developed model focuses on capturing the transition to thermoacoustic instability through intermittency. Currently, we have not tried to perform system identification and predict the unsteady regime or amplitude of oscillation in practical combustors. However, the model provides a new configuration for modeling thermoacoustic systems, which considers the unsteady heat release rate as an independent sub-system, instead of a quasi-steady response to the acoustic perturbation. With the help of data-driven methods, the model can be further improved and optimized for real combustors.

This chapter is a reprint of the following published article:

Weng, Y., Unni, V. R., Sujith, R. I., Saha, A. (2023). Synchronization-based model for turbulent thermoacoustic systems. *Nonlinear Dynamics, 111*, 12113–12126.

Chapter 7

Detecting early warning signals of turbulent thermoacoustic systems using modal analysis

7.1 Introduction

In modern combustors such as gas turbines, rocket engines, and industrial burners, combustion occurs in confined spaces, and with high energy densities. Under certain conditions, the unsteady heat release rate (HRR) from the reactive flow couples with the acoustic field and form a feedback loop. The feedback could be positive and leads the system to large amplitude pressure oscillation that can disrupt stable engine operation and potentially damage hardware [1, 10–12]. In recent decades, lean-premixed-prevaporized (LPP) combustors have been widely used in gas turbine combustors and industrial burners to minimize emissions. However, due to the increased sensitivity of lean flames to perturbations, these combustors are more susceptible to thermoacoustic instability. As a result, addressing thermoacoustic instability has become a significant challenge in the design of modern combustors. Numerous studies have focused on predicting, mitigating, and suppressing thermoacoustic instabilities.

In many cases, the propagation of acoustic waves is considered a linear phenomenon since the amplitude of pressure oscillations is relatively low compared to the mean pressure

in the combustor [42]. However, comparing to the acoustic fluctuation, reactive flow is more complex due to its inherent association with multiple factors in practical combustors, including flame dynamics [24, 39], hydrodynamics [284–287], and turbulence [21]. Each of these factors can be viewed as an individual subsystem with its own distinct time and length scales, and many of them exhibit significant nonlinearity. The interaction of these subsystems often leads to rich dynamics. For instance, in laminar thermoacoustic systems like the Rijke tube, sub-critical bifurcations, quasi-periodic, and aperiodic oscillations are observed and have been studied extensively with various control parameters, including the location of the flame [44], flow rate [164], and flame conditions [167].

For practical engines, the combustors generally have a turbulent environment. Turbulent flow and turbulent flame introduce disordered fluctuations with low amplitude, even when the system is at stable operation, traditionally known as combustion noise. As the flow rate increases, the system could transition to the regime of thermoacoustic instability, where the amplitude of the fluctuation increases monotonically and the broad band fluctuation transition to limit cycle oscillation (LCO) with single dominant frequency [257]. Turbulent flow and turbulent flame introduce aperiodic fluctuations with low amplitude, even when the system is at stable operation. For a long time, thermoacoustic instability was primarily addressed as an acoustic problem. Combustion noise is viewed as a stochastic fluctuation added to the system, either white noise or pink noise etc. [288], and the transition from stable operation to instability is considered a fixed point to a limit cycle oscillation (LCO), with discussions limited to these two dynamical states. However, recent research has shown that combustion noise exhibits higher-order chaotic behavior. For instance, Nair et al. [257] discovered the multifractality of combustion noise and observed that the system gradually loses such behavior as it transitions to instability. These studies indicates that combustion noise should not be viewed merely as a stochastic fluctuation. As a result, the emergence of limit cycle oscillations (LCO) during the transition is a phenomenon where a dominant mode arises from a chaotic

system with a broadband spectrum, both spatially and temporally. This observation indicates that the transition is a process of self-organization [192], where multiple modes with different frequencies, related to various physical behaviors, redistribute their energies into a few dominant modes [289–291]. Previous studies by Pavithran et al.quantified these behaviors in turbulent thermoacoustic system through scaling laws related to spectral condensation [193] and Hurst exponents [194] during the transition to instabilities, making it a potential early warning signal to instability. These observations are also found to be universal across multiple systems, extending beyond just thermoacoustic instability.

Based on these observations, several important questions arise. One of the most significant is: How do the various modes in the regime of combustion noise interact with each other, redistribute their energy, and lead to the system's transition to LCO? To address this question, we need to obtain full state measurements of the entire system to resolve the higher-dimensional phase space. However, most investigations on thermoacoustic instability rely solely on time series measurements of pressure fluctuations and unsteady heat release rates (HRR) because obtaining comprehensive field measurements of various variables in the combustor is typically challenging. Therefore, many studies [44, 292–294] reconstruct the phase space from time series data using a delayed coordinate system, as described by Takens's theorem. In these studies, the time lag for the delayed coordinates is determined by calculating the average mutual information (AMI), and the corresponding minimum embedding dimension is then identified using the false nearest neighbor (FNN) algorithm. [187] This approach has been frequently applied in previous research, uncovering multiple distinct dynamical states in thermoacoustic systems, and making it possible to adopt methods from complex system studies, especially in laminar cases. However, this approach can be challenging when processing data from the regime of combustion noise, the system dynamics are naturally turbulent and possess high dimensional structure. With experimental data inevitably containing intrinsic noise, determining the optimized time lag and minimum embedding dimensions can be rather difficult.

In this work, we employ Hankel matrices to reconstruct the phase space using delayed coordinates and then apply PCA to rank the components based on orthogonality and energy content. This delay embedding method has its roots in the 1980s [186, 295]. By performing singular value decomposition (SVD) on the Hankel matrix, we achieve a low-rank linear modal decomposition of the entire system dynamics [296]. This approach eliminates the need to compute an optimized time lag, which can be particularly challenging for turbulent systems. Additionally, the method is robust to noise due to the use of PCA. Furthermore, it enables the decomposition of time series data through low-rank approximation via SVD, providing deeper insights into the various orthogonal components of the phase space that represent the underlying physics. As we will demonstrate later in this paper, each orthogonal component corresponds to different frequency bands, allowing for easy identification of their physical counterparts.

The primary objective of this study is to decompose the principal components from the reconstructed phase space using the aforementioned approach and conduct an analysis based on these components. Our aim is to identify critical transitions in the modes during the transition phase and to provide potential early warning signals for impending instability.

7.2 Experimental details

In this study, we analyzed experimental data from Pawar et al. [249], which was obtained from a lab-scale premixed turbulent combustor equipped with a bluff body flame holder and fueled by liquefied petroleum gas. The incoming airflow was premixed with the fuel after passing through a settling chamber before being directed into the combustion section. Pressure fluctuations (p') were measured using pressure transducers, while the time series of heat release rate ($\dot{q}'$) was obtained by measuring the chemiluminescence of CH^* using a photo-multiplier tube (PMT). The data acquisition for p' and $\dot{q}'$ was

synchronized, with both signals sampled at a frequency of 10 kHz. In the experiment, as the airflow rate varied, the Reynolds numbers (Re) for the combustor ranged from 1.43×10^5 to 2.95×10^5. At low Reynolds numbers, the combustor operated stably, with p' exhibiting low-amplitude aperiodic oscillations due to the turbulent environment within the chamber, and the power spectrum exhibits broadband profile, as shown in Fig. 7.1 **a1**, **b1**. As Re increased, the amplitude of pressure oscillations gradually grew, and bursts of periodic oscillations began to emerge sporadically among the low-amplitude aperiodic oscillations, known as teh state of intermittency (Fig. 7.1 **a2**). With further increases in Re, the oscillation became periodic with one dominant frequency (Fig. 7.1 **a3**, **b3**.), the system exhibits LCO.

7.3 Methods

In this study, one of the main goal is to reconstruct the higher dimensional phase space from time time series. According to Takens's Theorem [186], one can reconstruct topologically equivalent phase space by introducing a delayed coordinate system. In many studies, phase space reconstruction aims to find an optimized delayed coordinate system that captures the system's dynamics with the minimum number of dimensions. This process involves determining two key parameters: the embedding dimension d and the optimal time lag τ for the given time series. Previous research on thermoacoustic instability [44, 159, 297] has often employed methods like average mutual information (AMI) and False Nearest Neighbor (FNN) to determine these parameters. However, as mentioned in the introduction, the low amplitude of signals and unavoidable measurement noise can make it challenging to accurately determine the optimal τ and d. It is important to note, however, that according to Takens' theorem, it is not strictly necessary to use the minimum embedding dimension for phase space reconstruction. Theoretically, the phase space can be reconstructed with more dimensions using any given time lag. To

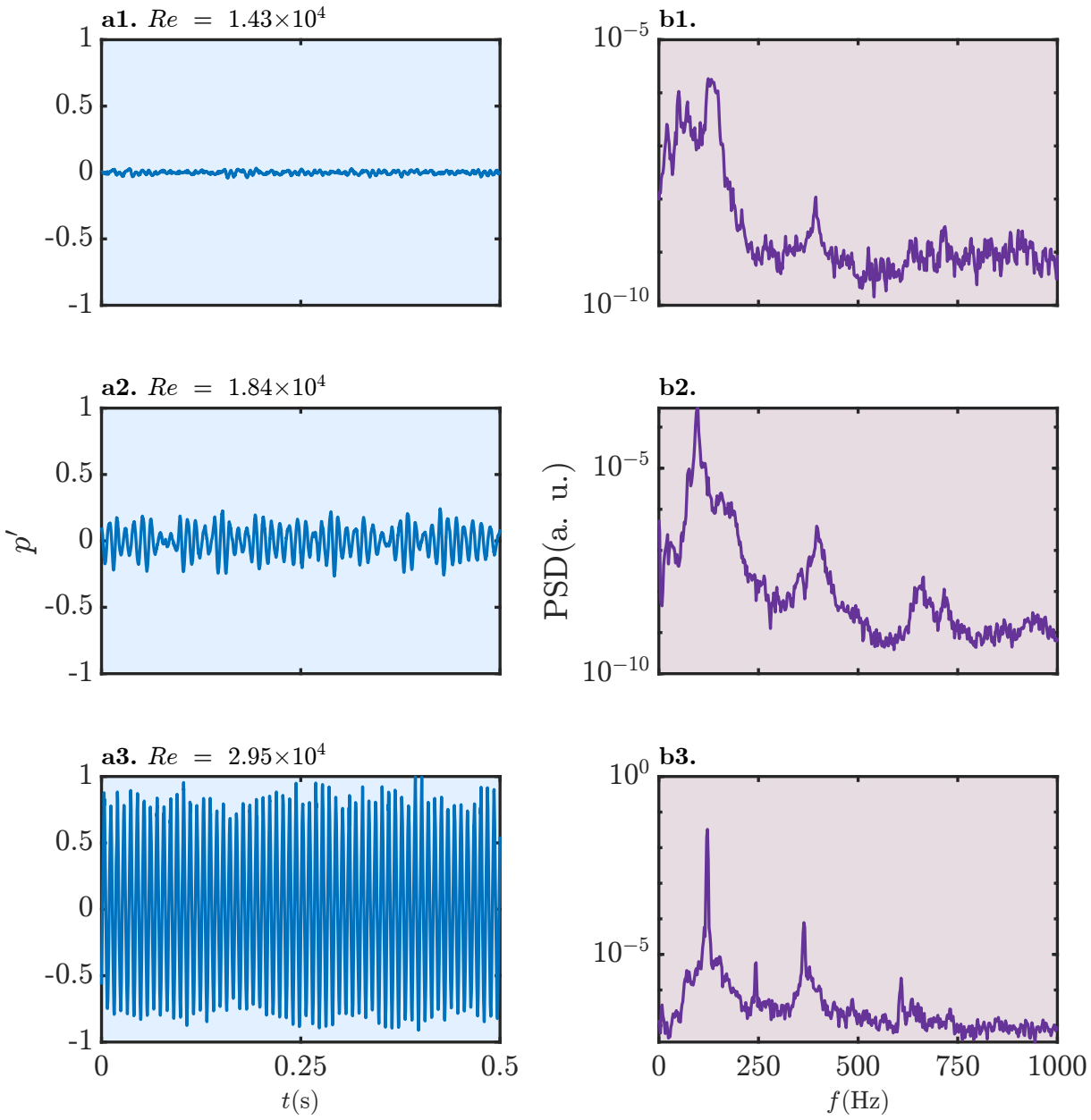


Figure 7.1. Typical dynamics at different Re in the experiment, from top to bottom: Combustion noise, intermittency, LCO

address these challenges, we use the sampling time scale as the time lag and employ a large number of dimensions for phase space reconstruction. This approach avoids the need to compute the embedding dimension and optimal time lag [298], particularly in the context of combustion noise. The reconstructed phase space is represented as a Hankel matrix. In particular, we construct the Hankel matrix by placing delayed vectors $\mathbf{x}$ side-by-side as

follows. It is well-known that delayed vectors can provide more information regarding the overall dynamical system through correlation analysis between each delayed vectors [299].

$$\mathbf{H} = \begin{bmatrix} x_1 & x_2 & x_3 & \cdots & x_m \\ x_2 & x_3 & x_4 & \cdots & x_{m+1} \\ x_3 & x_4 & x_5 & \cdots & x_{m+2} \\ \vdots & \vdots & \vdots & \ddots & \vdots \\ x_n & x_{n+1} & x_{n+2} & \cdots & x_{n+m-1} \end{bmatrix} \tag{7.1}$$

Since each column of the Hankel matrix represents only a single time step difference, they are not independent of one another [300]. Therefore, it is essential to include a sufficient number of columns to ensure that the minimum embedding phase space is a subset of the Hankel matrix. After performing a sensitivity analysis on our dataset, we determined that using 200 columns in our Hankel matrix ensures the validity of the reconstructed phase space. However, with such a large number of dimensions, where each dimension carries practically the same information, it is necessary to decompose the system and convert the coordinate system based on the rank of different modes. To achieve this, we employ principal component analysis (PCA). First proposed by Pearson in 1901 [301], the PCA algorithm decomposes the dataset into directions of maximum correlations with measurements, providing insights into low-dimensional structures from high-dimensional datasets. In dynamical systems, we often work with high-dimensional experimental measurements. However, the underlying physics may be sparse; therefore, one needs a way to distinguish between the principal components and the noisy components of the dynamical system. The PCA algorithm is similar to the singular value decomposition (SVD) and goes as follows: given some data matrix $\mathbf{X} \in \mathbb{R}^{n \times m}$, assuming $n \gg m$, one can

apply SVD to the zero-mean data matrix $\mathbf{B} = \mathbf{X} - \overline{\mathbf{X}}$ to obtain:

$$\mathbf{B} = \mathbf{U}\boldsymbol{\Sigma}\mathbf{V}^*. \tag{7.2}$$

where $\mathbf{U}$ gives a new orthogonal basis for $\mathbf{B}$ and can be interpreted as principal components of $\mathbf{B}$. The singular value matrix $\boldsymbol{\Sigma}$ represents the magnitude/energy of each principal component u_i. $\mathbf{V}^*$ denotes the Hermitian transpose of the matrix $\mathbf{V}$, where $\mathbf{V}$ contains the orthogonal basis of the data matrix. Hence, SVD allows us to transform the data into a new coordinate system by

$$\mathbf{B}\mathbf{V} = \mathbf{U}\boldsymbol{\Sigma}. \tag{7.3}$$

By ranking the components according to their singular values, we can more effectively visualize the first three components in a 3D plot, providing clearer insight into the phase space topology, as illustrated in Fig. 7.2. The topology of the phase space undergoes significant changes as the Reynolds number Re varies. At low Re, in the regime of combustion noise, the phase trajectory is multi-dimensional, with the singular values of the first three components being of the same order of magnitude (as indicated in the plot). As Re increases, the singular values of the first two dimensions increase drastically compared to the third, causing the phase space trajectory to flatten out, eventually forming a two-dimensional ring, which is characteristic of limit cycle oscillations (LCO). To more effectively quantify the changes in phase space topology, we normalize the singular values such that the 2-norm of the normalized singular value $\hat{\boldsymbol{\sigma}}$ is equal to one (Eqn. 7.4).

$$\|\hat{\boldsymbol{\sigma}}\|_2 = 1. \tag{7.4}$$

In addition to analyzing the phase space topology, this can also be interpreted as the normalized mode energy derived from applying PCA to the Hankel matrix—in other words, the total energy contained in the components of the reconstructed phase space. As

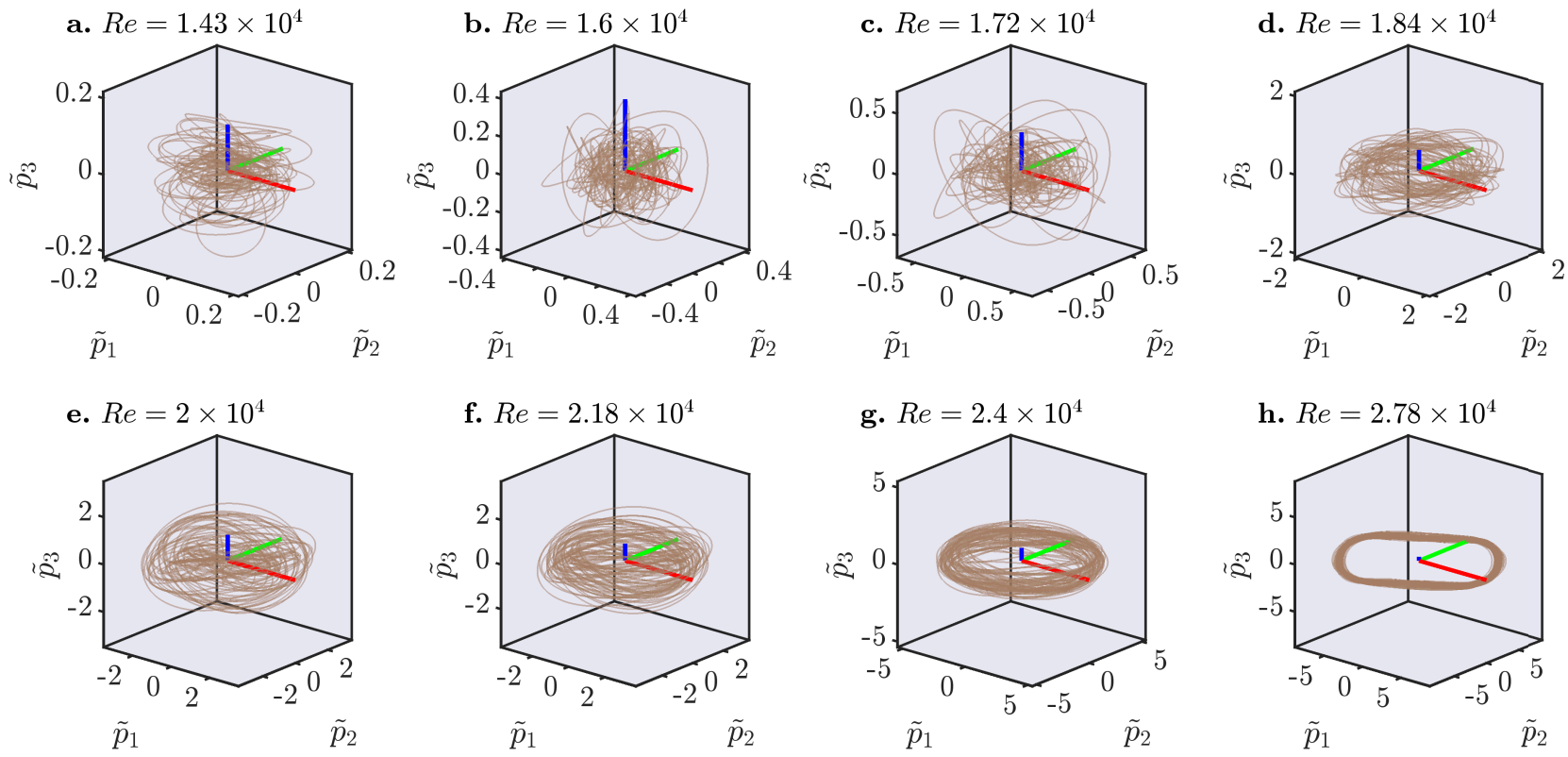


Figure 7.2. Phase Space change as the system transitions from combustion noise to intermittency, and finally reaching limit cycle oscillation.

shown in Fig. 7.3, we present the sum of the $\hat{\sigma}$ values for the first six modes across several representative cases.

This then allows us to compare across different phase space geometries and define a quantity flatness η in the third principal component direction using the normalized singular values $\hat{\sigma}_i$:

$$\eta = \frac{\hat{\sigma}_1}{\hat{\sigma}_3}. \tag{7.5}$$

Note that the vector σ_i is ordered in descending fashion based on the energy of each corresponding PCA mode. Additionally, as the system approaches thermoacoustic instability, the pressure time series becomes more of a periodic oscillation, rendering the phase space to flatten and become a circle (Fig. 7.4). We will refer to this process as a loss of dimensionality during the route to chaos. In Fig. 7.4, the green vector corresponds to σ_3, while the blue and red vectors correspond to σ_1 and σ_2 respectively. In the limit of perfect periodic oscillation (i.e. sinusoidal time series), the phase space becomes completely flat with $\hat{\sigma}_1 = \hat{\sigma}_2 = \frac{1}{\sqrt{2}}$ and

$$\lim_{\hat{\sigma}_3 \to 0} \eta = \infty. \tag{7.6}$$

We may also examine the frequency spectrum of each mode in the columns of $\mathbf{U}$. Applying the Fourier transform to $\mathbf{U}$ is the same as applying the DFT matrix $\mathbf{F}$, which is another orthogonal matrix.

$$\mathbf{B} = \mathbf{U}\mathbf{\Sigma}\mathbf{V}^* \underbrace{\mathbf{F}\mathbf{B}}_{\mathbf{B_F}} = \underbrace{\mathbf{F}\mathbf{U}}_{\mathbf{U_F}} \mathbf{\Sigma}\mathbf{V}^*. \tag{7.7}$$

Noticing that $\mathbf{U_F}$ is simply another orthogonal matrix, therefore forms a valid singular value decomposition

$$\mathbf{B_F} = \mathbf{B_F}\mathbf{\Sigma}\mathbf{V}^*. \tag{7.8}$$

Notice that the singular values did not change. Hence, the Fourier-transformed modes are still ranked based on the original energy levels. Thus, we may examine the dominant frequencies in each mode and understand how the physics changed from combustion noise to limit cycle oscillation, allowing us to understand the transferring of energy between different physical phenomenons by looking at the frequencies present in each mode.

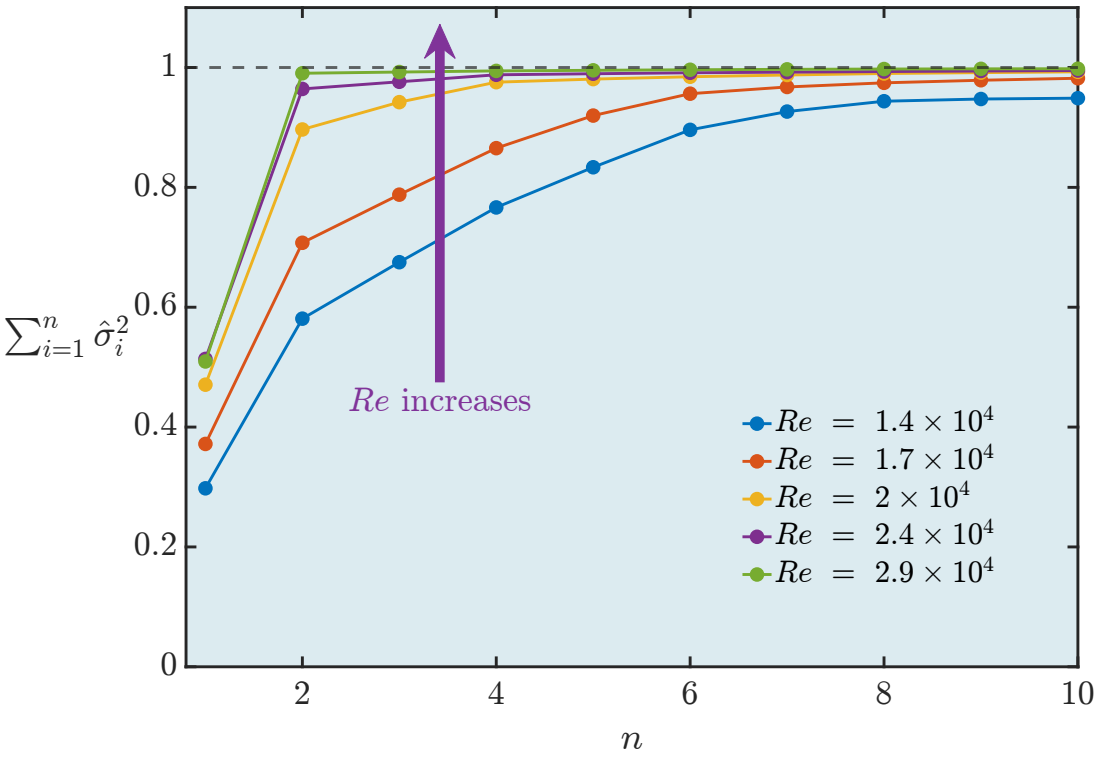


Figure 7.3. Cumulative sum of normalized singular values $\hat{\sigma}_i^2$. The sum up to $n = N$ should equal 1 since we normalized the 2-norm to be 1.

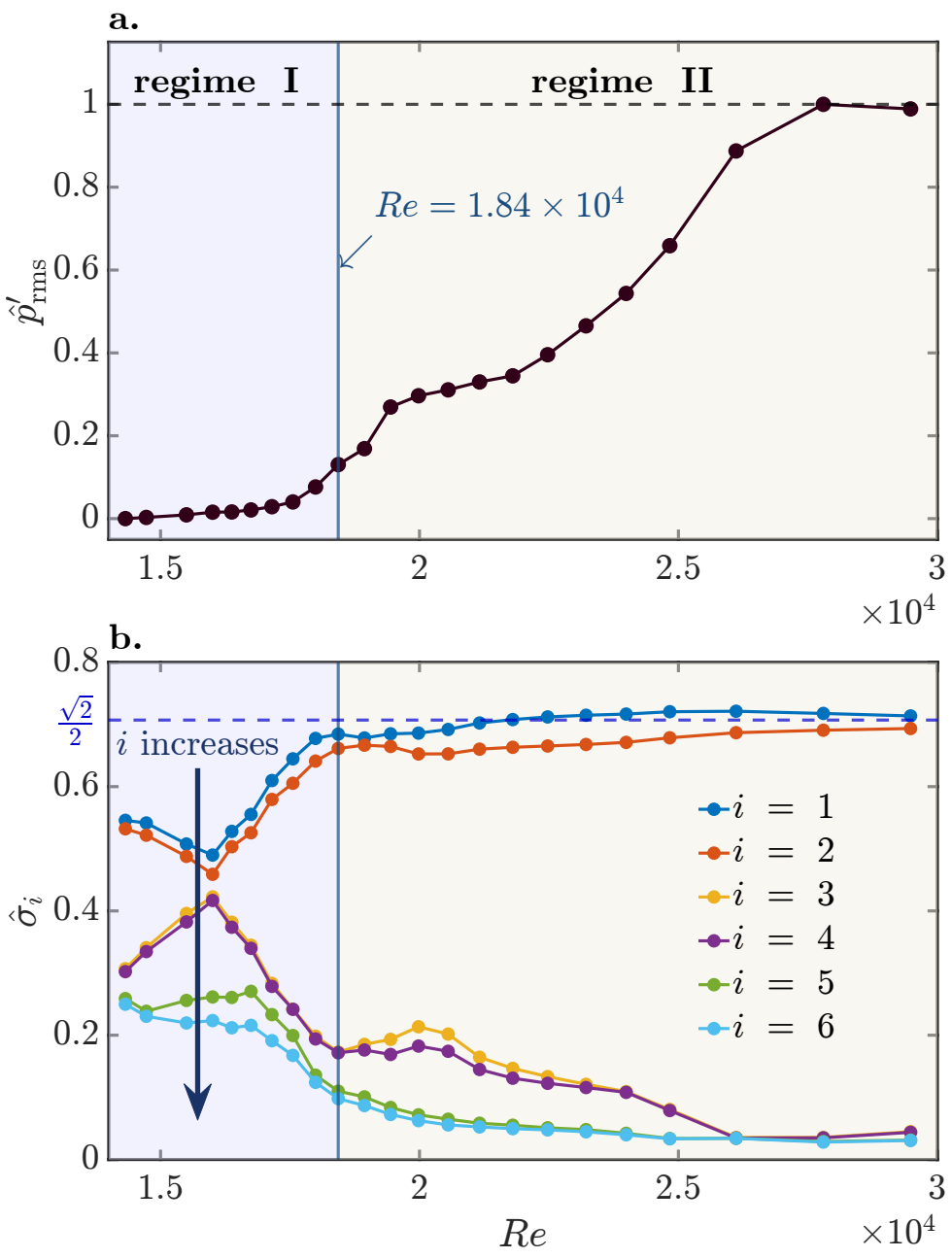


Figure 7.4. Evolution of the first six singular values as a function of Re. Observe that in Regime I, the singular values fluctuates; while in Regime II, $\hat{\sigma}_1$ and $\hat{\sigma}_2$ stabilizes to around $\frac{\sqrt{2}}{2}$. This separation region can be compared to $\hat{p}'_{\mathrm{rms}}$, the rms of the normalized pressure time series. We can see the saturation of $\hat{\sigma}_1$ and $\hat{\sigma}_2$ can be a useful signal in predicting a rapid increase in the amplitude of pressure oscillation. The non-monotonicity in Regime I will be discussed later.

7.4 Power Law of Self-Organization

Now we derive a theoretical power from eqn. (7.4). Rewriting it using the definition of η from eqn. (7.5), we obtain:

$$\frac{\hat{\sigma}_1^2 + \hat{\sigma}_2^2}{\hat{\sigma}_3^2} + 1 + \frac{\sum_{i=4}^{N} \hat{\sigma}_i^2}{\hat{\sigma}_3^2} = \frac{1}{\hat{\sigma}_3^2} \tag{7.9}$$

Let us denote

$$k = \frac{\sum_{i=4}^{N} \hat{\sigma}_i^2}{\hat{\sigma}_3^2}.$$

Examining Fig. 7.4, we see that $\hat{\sigma}_1 \approx \hat{\sigma}_1$ for all cases. And now using the definition of the flatness ratio η, we can say $\frac{\hat{\sigma}_1^2+\hat{\sigma}_2^2}{\hat{\sigma}_3^2} \approx 2\eta^2$. Then eqn. (7.9) becomes:

$$2\eta^2 + 1 + k = \hat{\sigma}_3^{-2} \tag{7.10}$$

Thus,

$$\eta = \frac{1}{\sqrt{2}} \sqrt{\hat{\sigma}_3^{-2} - 1 - k}. \tag{7.11}$$

Finally, we just need to examine the value of k. First, consider the perfectly periodic regime where $\hat{\sigma}_1 \approx \hat{\sigma}_2 \approx \frac{1}{\sqrt{2}} \gg \hat{\sigma}_i$ for all $i \geq 3$. Therefore we may perform an expansion about infinity for $\hat{\sigma}_3^{-2}$ on eqn. (7.11), and obtain the linearized equation for η:

$$\eta = \frac{1}{\sqrt{2}} \hat{\sigma_3}^{-1}. \tag{7.12}$$

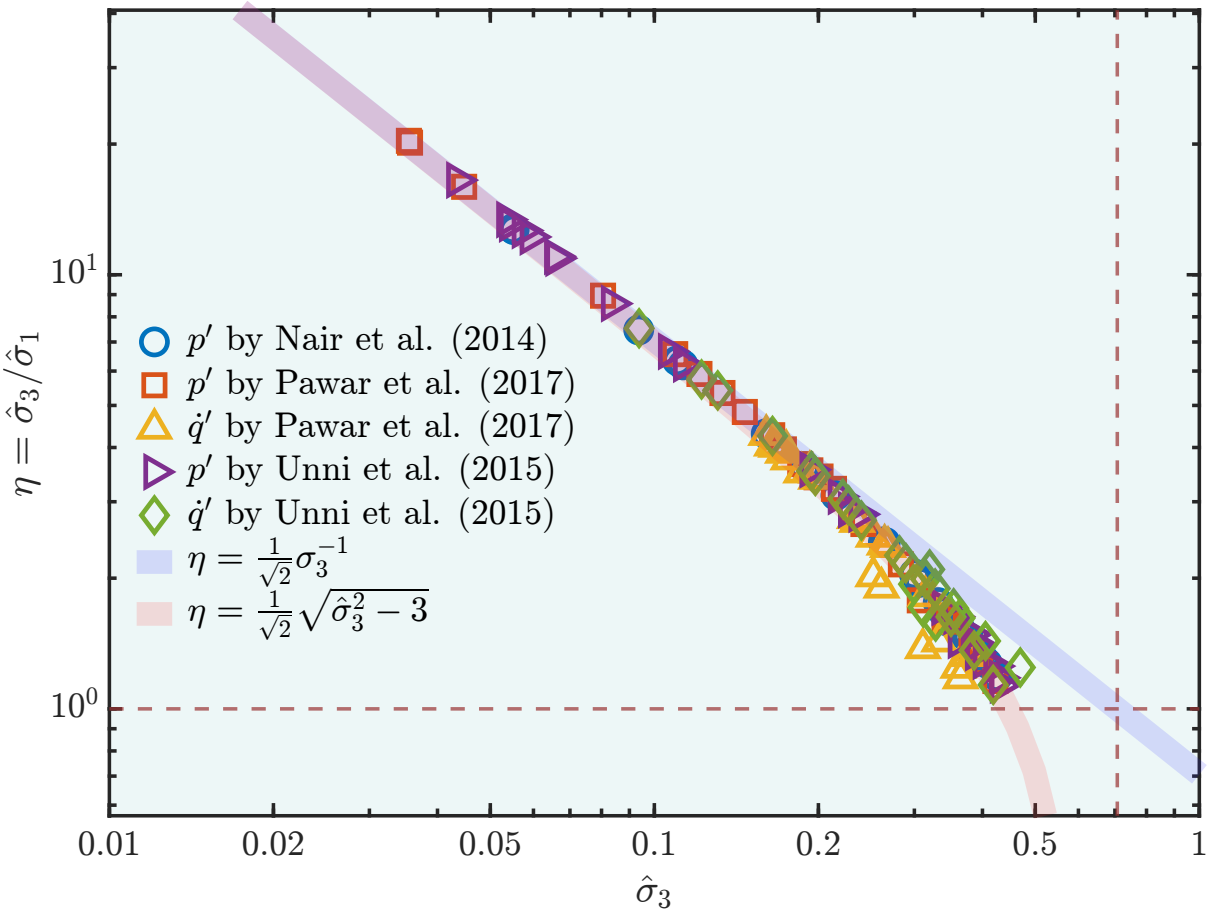


Figure 7.5. Experimental Data overlapped with theoretical lines (Eqns. (7.12), and (7.13))

Now again, looking at Fig. 7.4, we observe that $\hat{\sigma}_3 \approx \hat{\sigma}_4 \gg \hat{\sigma}_i$ for all $i \geq 5$. Therefore, $k \sim \mathcal{O}(1)$. Experimentally, we determined $k \approx 2$ matches well with data, as shown in Fig. 7.5.

$$\eta = \frac{1}{\sqrt{2}}\sqrt{\hat{\sigma_3}^{-2} - 3}. \tag{7.13}$$

Moreover, eqn. (7.11) is generalizable to any phase space trajectories. Let us experiment with an artificial signal of the following form:

$$x(t) = sin(2\pi f t) + a \cdot N_{comb}, \tag{7.14}$$

where f is the frequency, $a \geq 0$ is a scalar, and N_{comb} denotes a unit amplitude combustion

noise time series taken from experimental data. Clearly, the phase space trajectory will be a perfect circle when $a = 0$. Now, considering the non-trivial case of $a > 0$, as we increase a, the weight between the sinusoidal dynamics and the combustion noise changes. Looking at Fig. 7.5, we see extremely good matching between this artificial time series and experiential data. This also gives the PCA analysis an interpretable physical meaning, such that the PCA algorithm helps us to decompose the dynamics into sinusoidal oscillation and combustion noise. This is seen from Fig. 7.5 too denoted with the two power-law curves. At the earlier stage, the power law deviates from that derived for periodic oscillation (Eqn. (7.12)) due to combustion noise. Therefore, it is possible to represent bulk of the dynamics using just combinations of sinusoid and combustion noise. The higher order effects are less important, hence with smaller singular values and are ignored here.

7.5 Regime Separation in Singular Value Spectrum

Previous studies have shown that there exists a rather smooth transition from combustion noise to periodic oscillation in a turbulent thermoacoustic system. Moreover, many routes to chaos were observed, one of them is frequency spectrum condensation, in which one frequency gradually dominates the entire frequency domain, hence achieving periodic oscillation.

Here, we propose a regime partition based on the singular value spectrums observed in Fig. 7.4. As divided in the figure, there exists two regimes: a) combustion noise, b) increasing of $\hat{\sigma}_1$ and $\hat{\sigma}_2$. Overlaying the figure with the gradually increasing amplitude of the pressure field, we noticed that the beginning of regime (b) is earlier than that of amplitude increasing, making this a possible early warning signal. Moreover, noticing that in regime (b), $\hat{\sigma}_1$ and $\hat{\sigma}_2$ both asymptotes to the value $\frac{1}{\sqrt{2}}$. This is clear from eqns. (7.12), and (7.13).

Therefore, one may employ the early warning signal by selecting some parameter ϵ

such that for some case index, or system parameter index (ex. Re) $n \geq N$, $\left|\hat{\sigma}_{1,n} - \frac{1}{\sqrt{2}}\right| < \varepsilon$. In other words, we have shown that for systems following such self-organization behavior, the function $\hat{\sigma}_1$ converges to $\frac{1}{\sqrt{2}}$. This function can be well described by the derived equations in (7.12), and (7.13).

7.6 Synchronization Analysis

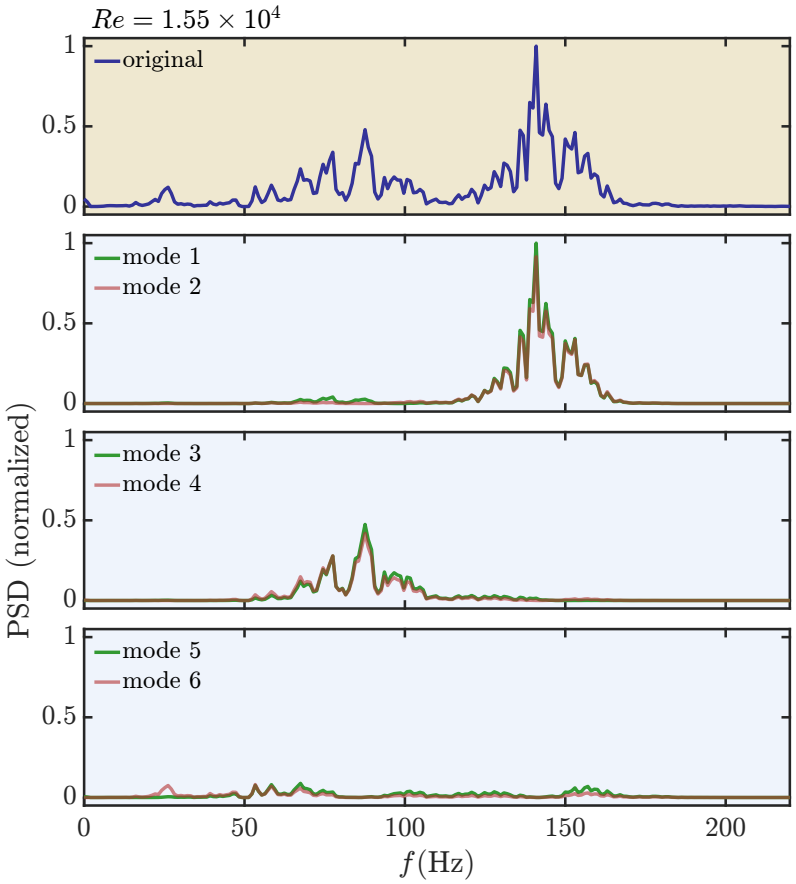


Figure 7.6. From top to bottom: An example of the PSD of the original time series and the first 6 modes after PCA, note that $Re = 1.55 \times 10^4$ in this case, which is a typical case in the regime of combustion noise.

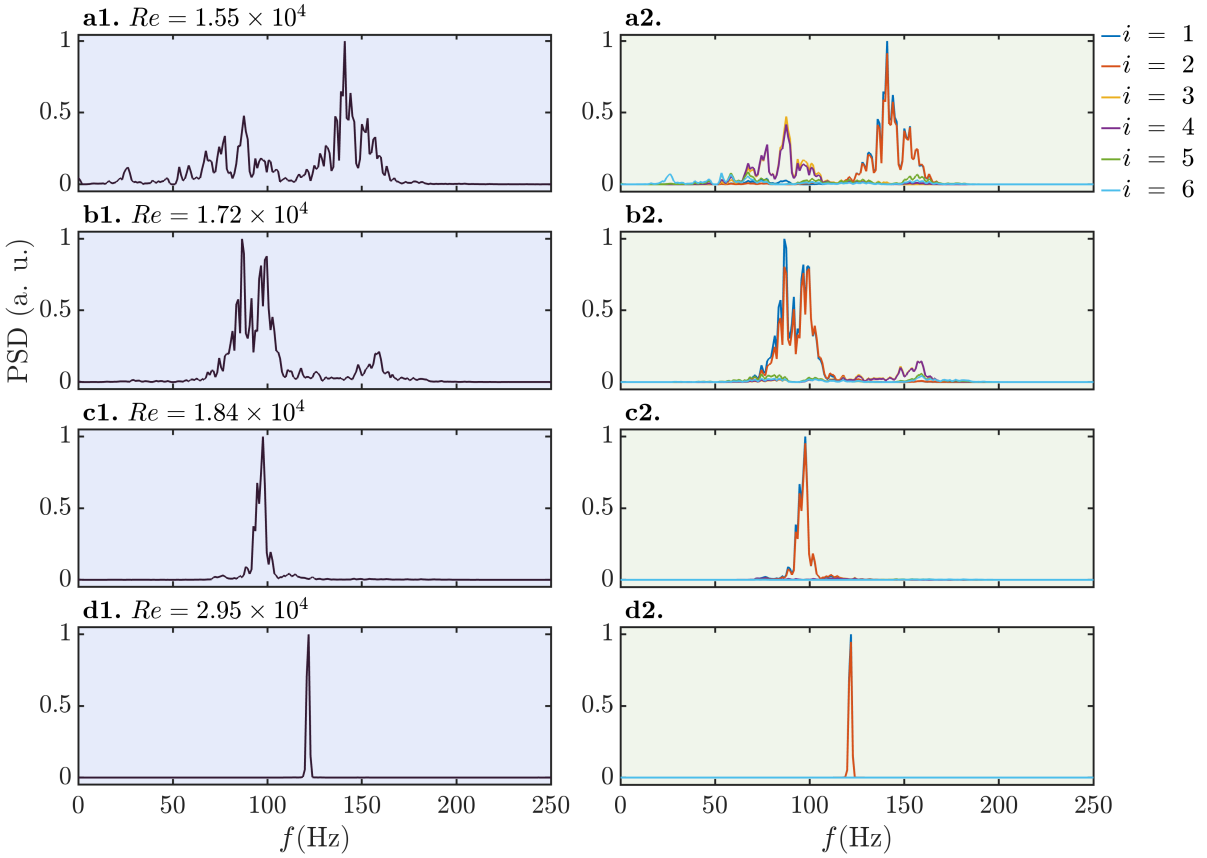


Figure 7.7. On the left shows the PSD plots of the pressure time series at different Re. On the right, we decomposed the time series into various components through PCA, and computed the PSD plot of each component. Notice that mode $2n-1$ and $2n$ share almost identical frequency content.

Different from the Fourier Transform, which decomposes a signal into its frequency component, PCA decomposes the signal based on its energy content and maintains orthogonality between components, as shown in Fig. 7.6, and Fig. 7.7. Physically, when one examines the PSD plot, like those shown in the left half of Fig. 7.7, one may suspect that different frequency bands represent different physical behaviors. For example, a low-frequency broadband may represent combustion noise, whereas a narrower frequency band may represent periodic oscillation.

To our surprise, the PCA algorithm can decompose frequency peaks into broadband that are easy to interpret. In Fig. 7.7(a1), we see two distinct frequency bands. Then in

Fig. 7.7(a2), the PSD plots for the extracted modes correctly capture the frequency bands. Moreover, they also come in pairs, like those shown in Fig. 7.4, where the $2n-1$ and $2n$-th modes share similar singular values. Here the frequency spectrum is decomposed by the mode pairs, and each pair shares almost the same frequency content and power. Similarly, for Fig. 7.7(b,c,d), we also see how the PCA modes successfully decompose the frequency bands into sections.

Physically speaking, we can see that mode pairs 1,2 captures the frequency bands with the highest energy content, and 3,4 captures those with the second highest energy content, and so on. This is evident from the fact that the energy of the Fourier transformed modes remains ranked, as shown in Eqn. (7.8). Hence, the frequencies contained in each mode can also be used to interpret the most dominant physical mechanism present under that operation condition.

As demonstrated by both Fig. 7.4 and Fig. 7.7, the modes come in pairs, in terms of energy and frequency content. For any arbitrary matrices $\mathbf{B}$ with rank N, SVD gives the low rank approximation:

$$\mathbf{B}_r = \sum_{i=1}^{r} \sigma_i u_i v_i^*, \quad r \leq N. \tag{7.15}$$

Here, in our thermoacoustic data set, the modes come in pairs. Therefore we would like to group them to reconstruct the time series corresponding to each pair. Recall that in our Hankel matrix formulation, the first column of $\mathbf{B}$ represents the original time series. For example, if we choose to group modes 3 and 4 to reconstruct the low-rank Hankel matrix and corresponding low-rank time series $x(t)$:

$$\mathbf{H}_{3,4} = \sum_{i=3}^{4} \sigma_i u_i v_i^*, \tag{7.16}$$

Then,

$$x_{3,4} = \mathbf{H}_{3,4}(:, 1). \tag{7.17}$$

In general, for any mode pair $2n-1$ and $2n$, we reconstruct the corresponding low-rank phase space and time series:

$$\mathbf{H}_{2n-1,2n} = \sum_{i=2n-1}^{2n} \sigma_i u_i v_i^*, x_{2n-1,2n} = \mathbf{H}_{2n-1,2n}(:, 1). \tag{7.18}$$

Clearly, the summation of all of these modes gives the full-order Hankel matrix, since we are just regrouping different modes. In our analysis, only the first six modes (first three pairs) will be considered, as they provide us the majority of the energy. Such grouping provides us a way to perform meaningful synchronization analysis between each mode, and relate them to actual physical mechanisms.

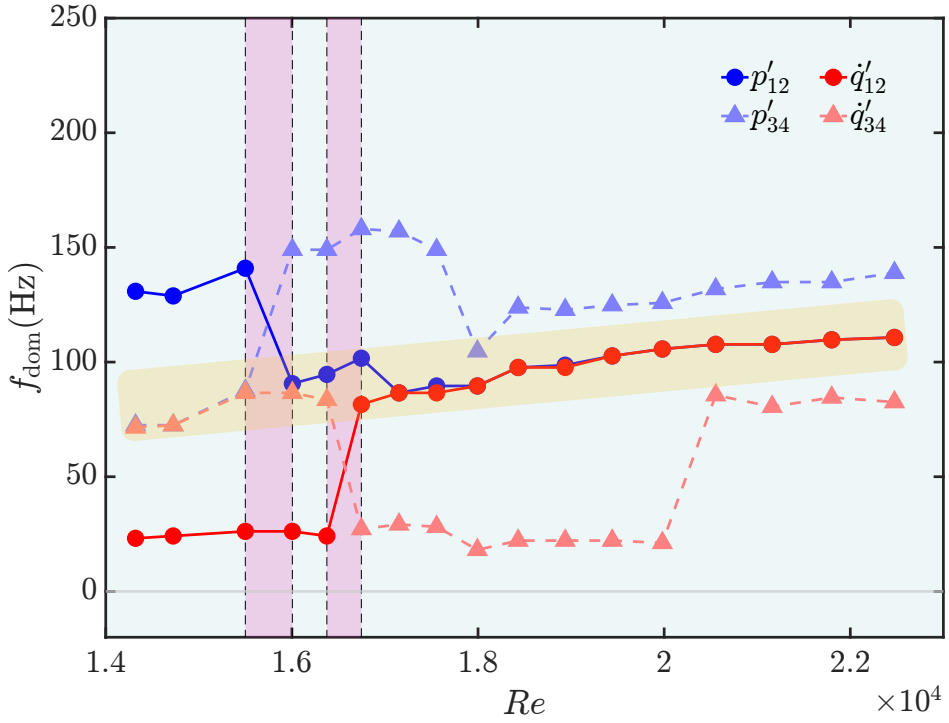


Figure 7.8. Dominant frequencies for p'_{12}, p'_{34}, $\dot{q}'_{12}$, and $\dot{q}'_{34}$ constructed based on eqn. (7.18). Clearly, a pair of synchronized modes exists, as highlighted here. Initially, $\dot{q}'_{34}$ is synchronized to p'_{34}, because at the beginning the combustion noise energy is lower than the synchronized components. After a certain Re, the synchronized modes show up as p'_{12} and $\dot{q}'_{12}$, meaning that the synchronized components now have more energy. The phase locking value details for this band of synchronized modes are shown in Fig. 7.10.

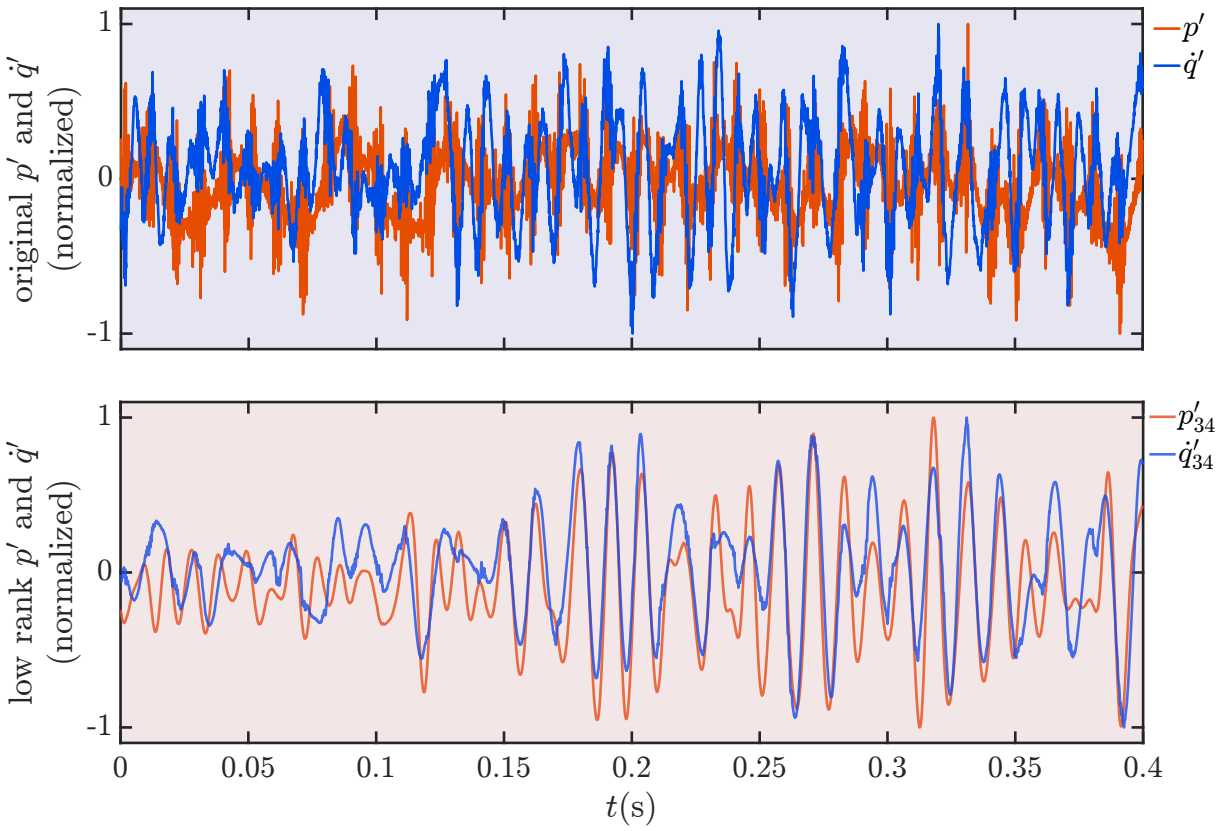


Figure 7.9. Example time series for p'_{34} and $\dot{q}'_{34}$, and their full order time series in low Re regimes ($Re = 1.47 \times 10^4$). Clearly, there exists synchronized parts between p'_{34} and $\dot{q}'_{34}$, and the asynchronous parts assume lower amplitudes compared to the synchronized parts.

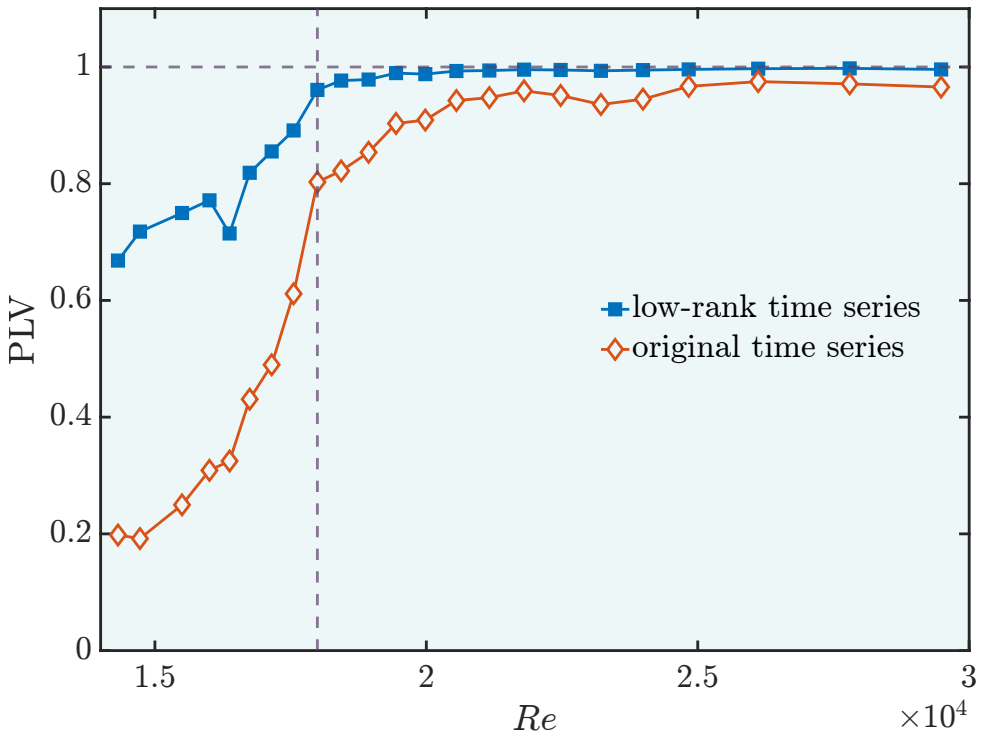


Figure 7.10. Phase Locking Valve vs. Re. The low-rank time series is reconstructed from the low-rank Hankel matrix

Closely examining Fig. 7.4, we observe a cusp in regime I, where the two branches of $i = 1, 2$ and $i = 3, 4$ seem to almost touch. Therefore, we suspect a crossing, or a change of importance between these two sets of singular values, such that the initial set of modes corresponding to $i = 3, 4$ increases its amplitude and eventually overtakes the set $i = 1, 2$. This is demonstrated in Fig. 7.8, where we present the change of dominant frequency for mode 2 and 4 (dominant frequencies for mode 1 and 3 are omitted here since they are identical to that of 2 and 4).

At the early stages of the combustor (before the cusp), the two dominant frequencies in the pressure time series are the fundamental frequency of the chamber ($\approx 130Hz$) and a subharmonic ($\approx 87Hz$). As the flow rate increases, we observe that the crossing occurs after case 3, where the energy contained in the 4th mode of pressure time series overtakes that in the 2nd mode. So now the frequency with the higher singular value becomes the subharmonic, and the frequency with the lower singular value is the fundamental frequency

of the combustor.

Similar crossing behavior is observed in the heat release rate graph, where the switch occurs after case number 5. Notice the synchronization behavior between mode number 2 of both pressure and heat release rate very early on. Therefore, we compute the Phase Locking Value (PLV) between each mode. PLV serves as a statistical tool to investigate long-term synchronization behavior between correlated data, and it was first introduced by Lachaux et al. in 1999 [302].

For a given time series $x(t)$, its Hilbert transform $\mathcal{H}[x(t)]$ is complex-valued and can be written as follows, where A represents amplitude and ϕ represents the instantaneous phase angle.

$$\mathcal{H}[x(t)] = A(t)e^{i\phi(t)}.$$

Then by looking at the difference between the phase angle between two signals x_1 and x_2, one can obtain the instantaneous phase locking value (PLV):

$$PLV = \frac{1}{N}\left|\sum_{n=1}^{N} e^{i\Delta\phi(t)}\right|,$$

where N is the length of the time series and $\Delta\phi = \phi_{x_1} - \phi x_2$ is the instantaneous phase difference. As demonstrated by Weng et al. [244], PLV and $\Delta\phi$ have different trends in different regimes. In the periodic oscillation regime, both pressure and heat release rate are perfectly synchronized and $\Delta\phi \approx 0$, making $PLV \approx 1$. On the other hand, in the combustion noise regime, $\Delta\phi$ may grow unboundedly, making PLV close to 0. Therefore, these are good metrics for determining synchronization behaviors between time series.

Fig. 7.10 shows the phase locking value graph based on Re. One can see that the low-rank time series of pressure and heat release rate, both reconstructed from the low-rank Hankel matrix, remain synchronized even during the combustion noise regime.

Traditionally, this regime is considered to have no synchronization behavior, which is demonstrated through the curve for the original time series.

7.7 Discussion

As seen from Fig. 7.5, the theoretical line matches all experimental data fairly well. In Fig. 7.4, we see that the singular value data can be broken up into two parts: one is the combustion noise part, and the other is the true dynamics part. At early case id (low Re number), we see that the combustion noise is comparable to the true dynamics. However, as we increase Re, the true dynamics begin to dominate, hence observed as a circle in phase space. Moreover, we see that the magnitude of the singular values of the true dynamics is much larger than that of the combustion noise; therefore, we observe a loss of dimensionality. This allows the interpretation of $\hat{\sigma}_i$ to be part of the background noise for $i \geq 3$. Then, the induced dynamics between η and $\hat{\sigma}_3$ can be interpreted as phase space flatness vs. amplitude of background noise. This phase space flatness quantity η can inform us about the dimensionality reduction of the dynamical system, which can then be used as an early warning signal. Physically, the increase in η represents a relative decrease in the combustion noise.

Recall Fig. 7.8 where the dominant frequencies between each mode are shown. Clearly, at certain Re, the energy-containing modes (the second mode) synchronize to the fundamental frequency of the chamber. Therefore we suspect synchronization behavior between the modes.

This chapter is a part of the following ongoing research and is currently being prepared for submission for publication:

Weng, Y., Zhu, Y., Unni, V. R., Sujith, R. I., Saha, A., Deriving early warning signals for turbulent thermoacoustic systems using principal component analysis. Under preparation

Bibliography

[1] T. C. Lieuwen and V. Yang. *Combustion instabilities in gas turbine engines: operational experience, fundamental mechanisms, and modeling*. American Institute of Aeronautics and Astronautics, 2005.

[2] P. Pelce and P. Clavin. Influence of hydrodynamics and diffusion upon the stability limits of laminar premixed flames. *J. Fluid Mech.*, 124:219–237, 1982.

[3] M. Matalon and B. Matkowsky. Flames as gasdynamic discontinuities. *J. Fluid Mech.*, 124:239–259, 1982.

[4] M. Matalon and B. Matkowsky. On the stability of plane and curved flames. *SIAM Journal on Applied Mathematics*, 44(2):327–343, 1984.

[5] M. Frankel and G. Sivashinsky. The effect of viscosity on hydrodynamic stability of a plane flame front. *Combust Sci Technol*, 29(3-6):207–224, 1982.

[6] M. P. Boyce. *Gas turbine engineering handbook*. Elsevier, 2011.

[7] R. Royce. *The jet engine*. John Wiley & Sons, 2015.

[8] P. P. Walsh and P. Fletcher. *Gas turbine performance*. John Wiley & Sons, 2004.

[9] A. H. Lefebvre. *Gas turbine combustion*. CRC press, 1998.

[10] J. C. Oefelein and V. Yang. Comprehensive review of liquid-propellant combustion instabilities in F-1 engines. *J Propul Power*, 9(5):657–677, 1993.

[11] T. J. Poinsot, A. C. Trouve, D. P. Veynante, S. M. Candel, and E. J. Esposito. Vortex-driven acoustically coupled combustion instabilities. *J Fluid Mech*, 177:265–292, 1987.

[12] S. M. Candel. Combustion instabilities coupled by pressure waves and their active control. In *Symp (Int) Combust*, volume 24, pages 1277–1296, 1992.

[13] M. Barrere and F. Williams. Comparison of combustion instabilities found in various types of combustion chambers. In *Symposium (International) on Combustion*, volume 12, pages 169–181. Elsevier, 1969.

[14] F. A. Williams. *Combustion theory*. CRC Press, 2018.

[15] C. K. Law. *Combustion Physics*. Cambridge University Press, 2006.

[16] J. Abraham, F. A. Williams, and F. V. Bracco. A discussion of turbulent flame structure in premixed charges. *SAE transactions*, pages 128–143, 1985.

[17] R. Borghi. On the structure and morphology of turbulent premixed flames. In *Recent Advances in the Aerospace Sciences*, pages 117–138. Springer, 1985.

[18] G. Andrews, D. Bradley, and S. Lwakabamba. Turbulence and turbulent flame propagation—a critical appraisal. *Combustion and Flame*, 24:285–304, 1975.

[19] Y.-C. Chen, N. Peters, G. Schneemann, N. Wruck, U. Renz, and M. S. Mansour. The detailed flame structure of highly stretched turbulent premixed methane-air flames. *Combustion and flame*, 107(3):223–IN2, 1996.

[20] N. Peters. Laminar flamelet concepts in turbulent combustion. In *Symposium (International) on Combustion*, volume 21, pages 1231–1250. Elsevier, 1988.

[21] N. Peters. *Turbulent Combustion*. Cambridge Monographs on Mechanics. Cambridge University Press, 2000.

[22] L. De Goey, T. Plessing, R. Hermanns, and N. Peters. Analysis of the flame thickness of turbulent flamelets in the thin reaction zones regime. *Proceedings of the Combustion Institute*, 30(1):859–866, 2005.

[23] S. R. Turns et al. *Introduction to combustion*, volume 287. McGraw-Hill Companies, 1996.

[24] S. Chaudhuri, V. Akkerman, and C. K. Law. Spectral formulation of turbulent flame speed with consideration of hydrodynamic instability. *Physical Review E*, 84(2):026322, 2011.

[25] S. Yang, A. Saha, Z. Liu, and C. K. Law. Role of darrieus–landau instability in propagation of expanding turbulent flames. *Journal of Fluid Mechanics*, 850:784–802, 2018.

[26] S. B. Pope. *Turbulent flows*. Cambridge university press, 2000.

[27] R. Borghi. On the structure and morphology of turbulent premixed flames. In *Recent advances in the Aerospace Sciences*, pages 117–138. Springer, 1985.

[28] T. Poinsot, D. veyynante, and S. Candel. Diagrams of premixed turbulent combustion based on direct simulation. In *Symposium (international) on Combustion*, volume 23, pages 613–619. Elsevier, 1991.

[29] R. Abdel-Gayed, D. Bradley, and F.-K. Lung. Combustion regimes and the straining of turbulent premixed flames. *Combustion and Flame*, 76(2):213–218, 1989.

[30] H. Kobayashi, T. Tamura, K. Maruta, T. Niioka, and F. A. Williams. Burning velocity of turbulent premixed flames in a high-pressure environment. In *Symposium (international) on combustion*, volume 26, pages 389–396. Elsevier, 1996.

[31] P. Clavin. Dynamic behavior of premixed flame fronts in laminar and turbulent flows. *Progress in energy and combustion science*, 11(1):1–59, 1985.

[32] B. Videto and D. Santavicca. Flame-turbulence interactions in a freely-propagating, premixed flame. *Combustion Science and Technology*, 70(1-3):47–73, 1990.

[33] S. Zhang and C. J. Rutland. Premixed flame effects on turbulence and pressure-related terms. *Combustion and Flame*, 102(4):447–461, 1995.

[34] A. M. Steinberg, J. F. Driscoll, and S. L. Ceccio. Measurements of turbulent premixed flame dynamics using cinema stereoscopic piv. *Experiments in Fluids*, 44(6):985–999, 2008.

[35] C. Fureby. A fractal flame-wrinkling large eddy simulation model for premixed turbulent combustion. *Proceedings of the Combustion Institute*, 30(1):593–601, 2005.

[36] P. E. Hamlington, A. Y. Poludnenko, and E. S. Oran. Interactions between turbulence and flames in premixed reacting flows. *Physics of Fluids*, 23(12):125111, 2011.

[37] B. Bobbitt, S. Lapointe, and G. Blanquart. Vorticity transformation in high karlovitz number premixed flames. *Physics of Fluids*, 28(1):015101, 2016.

[38] S. Chaudhuri, F. Wu, D. Zhu, and C. K. Law. Flame speed and self-similar propagation of expanding turbulent premixed flames. *Physical review letters*, 108(4):044503, 2012.

[39] Z. Liu, V. R. Unni, S. Chaudhuri, R. Sui, C. K. Law, and A. Saha. Self-turbulization in cellularly unstable laminar flames. *Journal of Fluid Mechanics*, 917, 2021.

[40] C. K. Law. *Combustion physics*. Cambridge university press, 2010.

[41] M. Matalon. Intrinsic flame instabilities in premixed and nonpremixed combustion. *Ann. Rev. Fluid Mech.*, 39:163–191, 2007.

[42] R. I. Sujith and S. A. Pawar. *Thermoacoustic Instability: A Complex Systems Perspective*. Springer Nature, 2021.

[43] E. Freitag. *On the measurement and modelling of flame transfer functions at elevated pressure*. PhD thesis, Technische Universität München, 2009.

[44] L. Kabiraj, A. Saurabh, P. Wahi, and R. I. Sujith. Route to chaos for combustion instability in ducted laminar premixed flames. *Chaos*, 22(2):023129, 2012.

[45] S. B. Pope. Turbulent premixed flames. *Annual Review of Fluid Mechanics*, 19(1):237–270, 1987.

[46] M. Fairweather, M. Ormsby, C. Sheppard, and R. Woolley. Turbulent burning rates of methane and methane–hydrogen mixtures. *Combustion and Flame*, 156(4):780–790, 2009.

[47] J. F. Driscoll. Turbulent premixed combustion: Flamelet structure and its effect on turbulent burning velocities. *Progress in Energy and Combustion Science*, 34(1):91 – 134, 2008.

[48] A. Masri, R. Dibble, and R. Barlow. The structure of turbulent nonpremixed flames revealed by raman-rayleigh-lif measurements. *Progress in Energy and Combustion Science*, 22(4):307–362, 1996.

[49] J. B. Bell, M. S. Day, and J. F. Grcar. Numerical simulation of premixed turbulent methane combustion. *Proceedings of the Combustion Institute*, 29(2):1987–1993, 2002.

[50] J. B. Bell, M. S. Day, J. F. Grcar, M. J. Lijewski, J. F. Driscoll, and S. A. Filatyev. Numerical simulation of a laboratory-scale turbulent slot flame. *Proceedings of the Combustion Institute*, 31(1):1299–1307, 2007.

[51] S. A. Filatyev, J. F. Driscoll, C. D. Carter, and J. M. Donbar. Measured properties of turbulent premixed flames for model assessment, including burning velocities, stretch rates, and surface densities. *Combustion and Flame*, 141(1-2):1–21, 2005.

[52] R. Prasad and J. Gore. An evaluation of flame surface density models for turbulent premixed jet flames. *Combustion and Flame*, 116(1-2):1–14, 1999.

[53] H. Pitsch. Large-eddy simulation of turbulent combustion. *Annual Review of Fluid Mechanics*, 38:453–482, 2006.

[54] P. Clavin. Dynamic behavior of premixed flame fronts in laminar and turbulent flows. *Progress in Energy and Combustion Science*, 11(1):1–59, 1985.

[55] R. Borghi. Turbulent combustion modelling. *Progress in Energy and Combustion Science*, 14(4):245–292, 1988.

[56] A. Y. Poludnenko and E. S. Oran. The interaction of high-speed turbulence with flames: Global properties and internal flame structure. *Combustion and Flame*, 157(5):995–1011, 2010.

[57] A. W. Skiba, T. M. Wabel, C. D. Carter, S. D. Hammack, J. E. Temme, and J. F. Driscoll. Premixed flames subjected to extreme levels of turbulence part i: Flame structure and a new measured regime diagram. *Combustion and Flame*, 189:407–432, 2018.

[58] Z. Liu, V. R. Unni, S. Chaudhuri, C. K. Law, and A. Saha. Local statistics of laminar expanding flames subjected to darrieus–landau instability. *Proceedings of the Combustion Institute*, 38(2):1993–2000, 2021.

[59] Y. Weng, A. Potnis, and A. Saha. Regime and morphology of polyhedral bunsen flames. *Combustion and Flame*, 248:112585, 2023.

[60] A. Steinberg, J. Driscoll, and S. Ceccio. Temporal evolution of flame stretch due to turbulence and the hydrodynamic instability. *Proceedings of the Combustion Institute*, 32(2):1713–1721, 2009.

[61] S. Chaudhuri, V. Akkerman, and C. K. Law. Spectral formulation of turbulent flame speed with consideration of hydrodynamic instability. *Physical Review E*, 84(2):026322, 2011.

[62] Z. Liu, S. Yang, C. K. Law, and A. Saha. Cellular instability in $le < 1$ turbulent expanding flames. *Proceedings of the Combustion Institute*, 37(2):2611–2618, 2019.

[63] F. Charlette, C. Meneveau, and D. Veynante. A power-law flame wrinkling model for les of premixed turbulent combustion part i: non-dynamic formulation and initial tests. *Combustion and Flame*, 131(1-2):159–180, 2002.

[64] H. Weller, G. Tabor, A. Gosman, and C. Fureby. Application of a flame-wrinkling les combustion model to a turbulent mixing layer. In *Symposium (international) on Combustion*, volume 27, pages 899–907. Elsevier, 1998.

[65] E. R. Hawkes, O. Chatakonda, H. Kolla, A. R. Kerstein, and J. H. Chen. A petascale direct numerical simulation study of the modelling of flame wrinkling for large-eddy simulations in intense turbulence. *Combustion and Flame*, 159(8):2690–2703, 2012.

[66] C. J. Mueller, J. F. Driscoll, D. L. Reuss, M. C. Drake, and M. E. Rosalik. Vorticity generation and attenuation as vortices convect through a premixed flame. *Combustion and Flame*, 112(3):342–358, 1998.

[67] P.-H. Renard, D. Thevenin, J.-C. Rolon, and S. Candel. Dynamics of flame/vortex interactions. *Progress in Energy and Combustion Science*, 26(3):225–282, 2000.

[68] A. Lipatnikov and J. Chomiak. Turbulent flame speed and thickness: phenomenology, evaluation, and application in multi-dimensional simulations. *Progress in Energy and Combustion Science*, 28(1):1–74, 2002.

[69] S. Hemchandra and T. Lieuwen. Local consumption speed of turbulent premixed flames–an analysis of "memory effects". *Combustion and Flame*, 157(5):955–965, 2010.

[70] H. Kobayashi, T. Nakashima, T. Tamura, K. Maruta, and T. Niioka. Turbulence measurements and observations of turbulent premixed flames at elevated pressures up to 3.0 mpa. *Combustion and Flame*, 108(1-2):104–117, 1997.

[71] H. Kobayashi, K. Seyama, H. Hagiwara, and Y. Ogami. Burning velocity correlation of methane/air turbulent premixed flames at high pressure and high temperature. *Proceedings of the Combustion Institute*, 30(1):827–834, 2005.

[72] F. Wu, A. Saha, S. Chaudhuri, and C. K. Law. Propagation speeds of expanding turbulent flames of c4 to c8 n-alkanes at elevated pressures: Experimental determination, fuel similarity, and stretch-affected local extinction. *Proceedings of the Combustion Institute*, 35(2):1501–1508, 2015.

[73] S. B. Pope. Pdf methods for turbulent reactive flows. *Progress in Energy and Combustion Science*, 11(2):119–192, 1985.

[74] E. Baum, B. Peterson, C. Surmann, D. Michaelis, B. Böhm, and A. Dreizler. Investigation of the 3d flow field in an ic engine using tomographic piv. *Proceedings of the Combustion Institute*, 34(2):2903–2910, 2013.

[75] N. Liu, K. Zhou, and L. Ma. 3d tomography integrating view registration and its application in highly turbulent flames. *Combustion and Flame*, 221:429–440, 2020.

[76] D. Ebi and N. T. Clemens. Simultaneous high-speed 3d flame front detection and tomographic piv. *Measurement Science and Technology*, 27(3):035303, 2016.

[77] G. Lu, A. Steinberg, and M. Yano. A sparse optical flow inspired method for 3d velocimetry. *Experiments in Fluids*, 64(4):66, 2023.

[78] P. Ahmed, B. Thorne, M. Lawes, S. Hochgreb, G. V. Nivarti, and R. S. Cant. Three dimensional measurements of surface areas and burning velocities of turbulent spherical flames. *Combustion and Flame*, 233:111586, 2021.

[79] Y. Zheng, L. Weller, and S. Hochgreb. 3d flame surface measurements in low-turbulence bunsen flames via scanning and orthogonal cross-planar techniques. *Combustion and Flame*, 258:113103, 2023.

[80] I. Trueba-Monje and J. A. Sutton. Flame structure and broadening in turbulent premixed jet flames. *Combustion and Flame*, 251:112676, 2023.

[81] N. Chakraborty, G. Hartung, M. Katragadda, and C. Kaminski. Comparison of 2d and 3d density-weighted displacement speed statistics and implications for laser based measurements of flame displacement speed using direct numerical simulation data. *Combustion and Flame*, 158(7):1372–1390, 2011.

[82] A. M. Steinberg, B. Coriton, and J. Frank. Influence of combustion on principal strain-rate transport in turbulent premixed flames. *Proceedings of the Combustion Institute*, 35(2):1287–1294, 2015.

[83] P. E. Hamlington, R. Darragh, C. A. Briner, C. A. Towery, B. D. Taylor, and A. Y. Poludnenko. Lagrangian analysis of high-speed turbulent premixed reacting flows: Thermochemical trajectories in hydrogen–air flames. *Combustion and Flame*, 186:193–207, 2017.

[84] S. Pope. The evolution of surfaces in turbulence. *International Journal of Engineering Science*, 26(5):445 – 469, 1988.

[85] S. Chaudhuri. Life of flame particles embedded in premixed flames interacting with near isotropic turbulence. *Proceedings of the Combustion Institute*, 35(2):1305 – 1312, 2015.

[86] S. Chaudhuri, A. Saha, and C. K. Law. On flame–turbulence interaction in constant-pressure expanding flames. *Proceedings of the Combustion Institute*, 35(2):1331 – 1339, 2015.

[87] A. Upatnieks, J. F. Driscoll, C. C. Rasmussen, and S. L. Ceccio. Liftoff of turbulent jet flames—assessment of edge flame and other concepts using cinema-piv. *Combustion and Flame*, 138(3):259–272, 2004.

[88] J. Weinkauff, D. Michaelis, A. Dreizler, and B. Böhm. Tomographic piv measurements in a turbulent lifted jet flame. *Experiments in Fluids*, 54:1–5, 2013.

[89] A. Saha, S. Chaudhuri, and C. K. Law. Flame surface statistics of constant-pressure turbulent expanding premixed flames. *Physics of Fluids*, 26(4), 2014.

[90] G. P. Smith, D. M. Golden, M. Frenklach, N. W. Moriarty, B. Eiteneer, M. Goldenberg, C. T. Bowman, R. K. Hanson, S. Song, W. C. Gardiner, and et al. GRI 3.0, 1999.

[91] T. Poinsot and D. Veynante. *Theoretical and numerical combustion*. RT Edwards, Inc., 2005.

[92] M. Nguyen, D. Yu, and S. Shy. General correlations of high pressure turbulent burning velocities with the consideration of lewis number effect. *Proceedings of the Combustion Institute*, 37(2):2391–2398, 2019.

[93] F. Williams. Recent advances in theoretical descriptions of turbulent diffusion flames. *Turbulent Mixing in Nonreactive and Reactive Flows*, pages 189–208, 1975.

[94] M. Matalon. On flame stretch. *Combustion Science and Technology*, 31(3-4):169–181, 1983.

[95] S. M. Candel and T. J. Poinsot. Flame stretch and the balance equation for the flame area. *Combustion Science and Technology*, 70(1-3):1–15, 1990.

[96] F. Creta and M. Matalon. Propagation of wrinkled turbulent flames in the context of hydrodynamic theory. *Journal of Fluid Mechanics*, 680:225–264, 2011.

[97] D. Lohse and S. Grossmann. Intermittency in turbulence. *Physica A: Statistical Mechanics and its Applications*, 194(1-4):519–531, 1993.

[98] G. Haller and G. Yuan. Lagrangian coherent structures and mixing in two-dimensional turbulence. *Physica D: Nonlinear Phenomena*, 147(3-4):352–370, 2000.

[99] G. Haller. Distinguished material surfaces and coherent structures in three-dimensional fluid flows. *Physica D: Nonlinear Phenomena*, 149(4):248–277, 2001.

[100] G. Haller. Lagrangian coherent structures. *Annual Review of Fluid Mechanics*, 47:137–162, 2015.

[101] H. L. Daveynate, A. Mohan, and S. Chaudhuri. Genesis and evolution of premixed flames in turbulence. *Combustion and Flame*, 196:386–399, 2018.

[102] A. N. Kolmogorov. A refinement of previous hypotheses concerning the local structure of turbulence in a viscous incompressible fluid at high reynolds number. *Journal of Fluid Mechanics*, 13(1):82–85, 1962.

[103] A. Obukhov. Some specific features of atmospheric turbulence. *Journal of Geophysical Research*, 67(8):3011–3014, 1962.

[104] R. A. Antonia and K. R. Sreenivasan. Log-normality of temperature dissipation in a turbulent boundary layer. *Physics of Fluids*, 20(11):1800–1804, 11 1977.

[105] J. O. Abe, A. Popoola, E. Ajenifuja, and O. Popoola. Hydrogen energy, economy and storage: review and recommendation. *Int. J. Hydrogen Energy*, 44(29):15072–15086, 2019.

[106] H. Plass Jr, F. Barbir, H. Miller, and T. Veziroğlu. Economics of hydrogen as a fuel for surface transportation. *Int. J. Hydrogen Energy*, 15(9):663–668, 1990.

[107] G. A. Karim. Hydrogen as a spark ignition engine fuel. *Int. J. Hydrogen Energy*, 28(5):569–577, 2003.

[108] L. Das. Hydrogen-oxygen reaction mechanism and its implication to hydrogen engine combustion. *Int. J. Hydrogen Energy*, 21(8):703–715, 1996.

[109] D. Cecere, E. Giacomazzi, and A. Ingenito. A review on hydrogen industrial aerospace applications. *Int. J. Hydrogen Energy*, 39(20):10731–10747, 2014.

[110] P. Clavin. Dynamic behavior of premixed flame fronts in laminar and turbulent flows. *Prog. Energ. Combust.*, 11(1):1–59, 1985.

[111] G. I. Sivashinsky. On the intrinsic dynamics of premixed flames. *Philos. Trans. Royal Soc. A*, 332(1624):135–148, 1990.

[112] G. Darrieus. Propagation d'un front de flamme. *La Technique Moderne*, 30:18, 1938.

[113] L. Landau. On the theory of slow combustion. *Acta physicochim. URSS*, 19(1):77–85, 1944.

[114] G. I. Sivashinsky. Diffusional-thermal theory of cellular flames. *Combust. Sc. Tech.*, 15(3-4):137–145, 1977.

[115] G. I. Sivashinsky. Instabilities, pattern formation, and turbulence in flames. *Ann. Rev. Fluid Mech.*, 15(1):179–199, 1983.

[116] G. I. Sivashinsky. Some developments in premixed combustion modeling. *Proc. Combust. Inst.*, 29(2):1737–1761, 2002.

[117] G. Troiani, F. Creta, and M. Matalon. Experimental investigation of darrieus–landau instability effects on turbulent premixed flames. *Proc. Combust. Inst.*, 35(2):1451–1459, 2015.

[118] Z. Liu, V. Unni, S. Chaudhuri, C. Law, and A. Saha. Local statistics of laminar expanding flames subjected to Darrieus–Landau instability. *Proc. Combust. Inst.*, https://doi.org/10.1016/j.proci.2020.06.118, 2020.

[119] C. K. Law, G. Jomaas, and J. K. Bechtold. Cellular instabilities of expanding hydrogen/propane spherical flames at elevated pressures: theory and experiment. *Proc. Combust. Inst.*, 30:159–167, 2005.

[120] M. Haq. Correlations for the onset of instabilities of spherical laminar premixed flames. *J. Heat transfer*, 127(12):1410–1415, 2005.

[121] Z.-Y. Sun, F.-S. Liu, X.-C. Bao, and X.-H. Liu. Research on cellular instabilities in outwardly propagating spherical hydrogen-air flames. *Int. J. Hydrog. Energy*, 37(9):7889–7899, 2012.

[122] C. Clanet and G. Searby. First experimental study of the Darrieus-Landau instability. *Phys. Rev. Lett.*, 80(17):3867, 1998.

[123] J. Yu, R. Yu, X. Fan, M. Christensen, A. Konnov, and X.-S. Bai. Onset of cellular flame instability in adiabatic ch4/o2/co2 and ch4/air laminar premixed flames stabilized on a flat-flame burner. *Combust. Flame*, 160(7):1276–1286, 2013.

[124] D. Bradley. Instabilities and flame speeds in large-scale premixed gaseous explosions. *Philos. Trans. Royal Soc. A*, 357(1764):3567–3581, 1999.

[125] F. Wu, G. Jomaas, and C. K. Law. An experimental investigation on self-acceleration of cellular spherical flames. *Proc. Combust. Inst.*, 34(1):937–945, 2013.

[126] S. Yang, A. Saha, F. Wu, and C. K. Law. Morphology and self-acceleration of expanding laminar flames with flame-front cellular instabilities. *Combust. Flame*, 171:112–118, 2016.

[127] J. Beeckmann, R. Hesse, S. Kruse, A. Berens, N. Peters, H. Pitsch, and M. Matalon. Propagation speed and stability of spherically expanding hydrogen/air flames: Experimental study and asymptotics. *Proc. Combust. Inst.*, 36(1):1531–1538, 2017.

[128] C. R. Bauwens, J. M. Bergthorson, and S. B. Dorofeev. Experimental study of spherical-flame acceleration mechanisms in large-scale propane–air flames. *Proc. Combust. Inst.*, 35(2):2059–2066, 2015.

[129] Y. Gostintsev, A. Istratov, and Y. Shulenin. Self-similar propagation of a free turbulent flame in mixed gas mixtures. *Combust. Explos. Shock Waves*, 24(5):563–569, 1988.

[130] Y. Xie, J. Wang, X. Cai, and Z. Huang. Self-acceleration of cellular flames and laminar flame speed of syngas/air mixtures at elevated pressures. *Int. J. Hydrog. Energy*, 41(40):18250–18258, 2016.

[131] N. Fogla, F. Creta, and M. Matalon. Effect of folds and pockets on the topology and propagation of premixed turbulent flames. *Combust. Flame*, 162(7):2758–2777, 2015.

[132] R. Lamioni, P. Lapenna, G. Troiani, and F. Creta. Flame induced flow features in the presence of Darrieus-Landau instability. *Flow Turbul. Combust.*, 101(4):1137–1155, 2018.

[133] S. Ishizuka, K. Miyasaka, and C. K. Law. Effects of heat loss, preferential diffusion, and flame stretch on flame-front instability and extinction of propane/air mixtures. *Combust. Flame*, 45:293–308, 1982.

[134] G. I. Sivashinsky, C. K. Law, and G. Joulin. On stability of premixed flames in stagnation-point flow. *Combust. Sc. Tech.*, 28(3-4):155–159, 1982.

[135] A. Smithells. Xvi.—note on the structure of luminous flames. *J. Chem. Soc. Trans.*, 61:217–226, 1892.

[136] H. Guenoche and G. Markstein. Nonsteady flame propagation. *Pergamon Press, New York*, page 107, 1964.

[137] J. Buckmaster. Polyhedral flames—an exercise in bimodal bifurcation analysis. *SIAM J Appl. Math.*, 44(1):40–55, 1984.

[138] S. Sohrab and C. K. Law. Influence of burner rim aerodynamics on polyhedral flames and flame stabilization. *Combust. Flame*, 62(3):243–254, 1985.

[139] M. Gorman, C. Hamill, M. El-Hadi, and K. Robbins. Rotating and modulated rotating states of cellular flames. *Combust. Sc. Tech.*, 98(1-3):25–35, 1994.

[140] N. Bouvet, F. Halter, C. Chauveau, and Y. Yoon. On the effective lewis number formulations for lean hydrogen/hydrocarbon/air mixtures. *International journal of hydrogen energy*, 38(14):5949–5960, 2013.

[141] W. K. Lewis. The evaporation of a liquid into a gas. *Trans. ASME.*, 44:325–340, 1922.

[142] C. K. Law, G. Jomaas, and J. K. Bechtold. Cellular instabilities of expanding hydrogen/propane spherical flames at elevated pressures: theory and experiment. *Proceedings of the combustion institute*, 30(1):159–167, 2005.

[143] S. Muppala, M. Nakahara, N. Aluri, H. Kido, J. Wen, and M. Papalexandris. Experimental and analytical investigation of the turbulent burning velocity of two-component fuel mixtures of hydrogen, methane and propane. *international journal of hydrogen energy*, 34(22):9258–9265, 2009.

[144] F. Dinkelacker, B. Manickam, and S. Muppala. Modelling and simulation of lean premixed turbulent methane/hydrogen/air flames with an effective lewis number approach. *Combust Flame*, 158(9):1742–1749, 2011.

[145] R. Addabbo, J. Bechtold, and M. Matalon. Wrinkling of spherically expanding flames. *Proc. Combust. Inst.*, 29(2):1527–1535, 2002.

[146] S. Chaudhuri, A. Saha, and C. K. Law. On flame–turbulence interaction in constant-pressure expanding flames. *Proc. Combust. Inst.*, 35(2):1331–1339, 2015.

[147] M. Z. Haq. *Fundamental studies of premixed combustion*. PhD thesis, University of Leeds, 1998.

[148] S. Gutman, R. Axelbaum, and G. I. Sivashinsky. On bunsen burner polyhedral flames. *Combust. Sc. Tech.*, 98(1-3):57–70, 1994.

[149] V. Kurdyumov, E. Fernandez, and A. Linan. Flame flashback and propagation of premixed flames near a wall. *Proc. Combust. Inst.*, 28(2):1883–1889, 2000.

[150] V. Kurdyumov, E. Fernandez-Tarrazo, J.-M. Truffaut, J. Quinard, A. Wangher, and G. Searby. Experimental and numerical study of premixed flame flashback. *Proc. Combust. Inst.*, 31(1):1275–1282, 2007.

[151] M. Matalon and B. J. Matkowsky. Flames as gasdynamic discontinuities. *Journal of Fluid Mechanics*, 124:239–259, 1982.

[152] M. Matalon and B. Matkowsky. On the stability of plane and curved flames. *SIAM Journal on Applied Mathematics*, 44(2):327–343, 1984.

[153] M. Frankel and G. Sivashinsky. The effect of viscosity on hydrodynamic stability of a plane flame front. *Combustion Science and Technology*, 29(3-6):207–224, 1982.

[154] J. D. Buckmaster and G. S. S. Ludford. *Theory of Laminar Flames*. Cambridge Monographs on Mechanics. Cambridge University Press, 1982.

[155] L. Rosen and R. Axelbaum. Suppression of cellular structure in slot-burner flames. *Combustion and flame*, 126(1-2):1433–1444, 2001.

[156] J. O'Connor, V. Acharya, and T. Lieuwen. Transverse combustion instabilities: Acoustic, fluid mechanic, and flame processes. *Prog Energy Combust Sc*, 49:1–39, 2015.

[157] S. R. Stow and A. P. Dowling. Thermoacoustic oscillations in an annular combustor. In *Turbo Expo: Power for Land, Sea, and Air*, volume 78514, page V002T02A004. ASME, 2001.

[158] J. D. Sterling. Nonlinear analysis and modelling of combustion instabilities in a laboratory combustor. *Combust Sci Technol*, 89(1-4):167–179, 1993.

[159] H. Gotoda, H. Nikimoto, T. Miyano, and S. Tachibana. Dynamic properties of combustion instability in a lean premixed gas-turbine combustor. *Chaos*, 21(1), 2011.

[160] K. Kashinath, I. C. Waugh, and M. P. Juniper. Nonlinear self-excited thermoacoustic oscillations of a ducted premixed flame: bifurcations and routes to chaos. *J Fluid Mech*, 761:399–430, 2014.

[161] D. Premraj, S. A. Pawar, L. Kabiraj, and R. I. Sujith. Strange nonchaos in self-excited singing flames. *EPL (Europhysics Letters)*, 128(5):54005, 2020.

[162] Y. Guan, M. Murugesan, and L. K. Li. Strange nonchaotic and chaotic attractors in a self-excited thermoacoustic oscillator subjected to external periodic forcing. *Chaos*, 28(9), 2018.

[163] M. P. Juniper and R. I. Sujith. Sensitivity and nonlinearity of thermoacoustic oscillations. *Annual Review of Fluid Mechanics*, 50:661–689, 2018.

[164] R. Wildemans, V. Kornilov, P. de Goey, and I. L. Arteaga. Nonlinear dynam of pure intrinsic thermo-acoustic modes. *Combust Flame*, 251:112703, 2023.

[165] Z. Yu, A. J. Jaworski, and A. S. Abduljalil. Fishbone-like instability in a looped-tube thermoacoustic engine. *The Journal of the Acoustical Society of America*, 128(4):EL188–EL194, 2010.

[166] Y. Matsui. An experimental study on pyro-acoustic amplification of premixed laminar flames. *Combust Flame*, 43:199–209, 1981.

[167] P. Kasthuri, V. R. Unni, and R. Sujith. Bursting and mixed mode oscillations during the transition to limit cycle oscillations in a matrix burner. *Chaos*, 29(4):043117, 2019.

[168] C. Chen and S. Sohrab. Upstream interactions between planar symmetric laminar methane premixed flames. *Combust Flame*, 101(3):360–370, 1995.

[169] T. Echekki, J. H. Chen, and I. Gran. The mechanism of mutual annihilation of stoichiometric premixed methane-air flames. In *Symp (Int) Combust*, volume 26, pages 855–863. Elsevier, 1996.

[170] W. Culler, X. Chen, S. Peluso, D. Santavicca, J. O'Connor, and D. Noble. Comparison of center nozzle staging to outer nozzle staging in a multi-flame combustor. In *Turbo expo: Power for land, sea, and air*, volume 51050, page V04AT04A024. ASME, 2018.

[171] F. Richecoeur, P. Scouflaire, S. Ducruix, and S. Candel. High-frequency transverse acoustic coupling in a multiple-injector cryogenic combustor. *J Propul Power*, 22(4):790–799, 2006.

[172] L. Crocco and S.-I. Cheng. Theory of combustion instability in liquid propellant rocket motors. Technical report, Princeton Univ Nj, 1956.

[173] T. Chen, X. Guo, J. Jia, and J. Xiao. Frequency and phase characteristics of candle flame oscillation. *Sci Rep*, 9(1):342, 2019.

[174] D. M. Forrester. Arrays of coupled chemical oscillators. *Sci Rep*, 5(1):16994, 2015.

[175] K. Manoj, S. A. Pawar, S. Dange, S. Mondal, R. I. Sujith, E. Surovyatkina, and J. Kurths. Synchronization route to weak chimera in four candle-flame oscillators. *Phys. Rev. E*, 100:062204, Dec 2019.

[176] A. Bhattacharya, S. Mondal, S. De, A. Mukhopadhyay, and S. Sen. Synchronisation behaviour between two candle flame oscillators with similar and dissimilar amplitudes of oscillations. *Combust Theor Model*, 27(3):291–316, 2023.

[177] R. Addabbo, J. Bechtold, and M. Matalon. Wrinkling of spherically expanding flames. *Proc Combust Inst*, 29(2):1527–1535, 2002.

[178] C. K. Law, G. Jomaas, and J. K. Bechtold. Cellular instabilities of expanding hydrogen/propane spherical flames at elevated pressures: theory and experiment. *Proc Combust Inst*, 30(1):159–167, 2005.

[179] Y. Weng, A. Potnis, V. R. Unni, and A. Saha. Assessing local statistics of a premixed turbulent bunsen flame. *AIAA Journal*, pages 1–9, 2024.

[180] P. Brearley, U. Ahmed, and N. Chakraborty. The relation between flame surface area and turbulent burning velocity in statistically planar turbulent stratified flames. *Phys. Fluids*, 32(12), 2020.

[181] R. D. Knight. *Physics for scientists and engineers: A Strategic Approach with modern physics*. Pearson New York, NY, 2017.

[182] D. Noh, E. Karlis, S. Navarro-Martinez, Y. Hardalupas, A. Taylor, D. Fredrich, and W. Jones. Azimuthally-driven subharmonic thermoacoustic instabilities in a swirl-stabilised combustor. *Proc Combust Inst*, 37(4):5333–5341, 2019.

[183] J. Moeck, M. Oevermann, R. Klein, C. Paschereit, and H. Schmidt. A two-way coupling for modeling thermoacoustic instabilities in a flat flame rijke tube. *Proc Combust Inst*, 32(1):1199–1207, 2009.

[184] J. H. Feldhoff, R. V. Donner, J. F. Donges, N. Marwan, and J. Kurths. Geometric detection of coupling directions by means of inter-system recurrence networks. *Phys. Letts. A*, 376(46):3504–3513, 2012.

[185] J.-P. Eckmann, S. O. Kamphorst, D. Ruelle, et al. Recurrence plots of dynamical systems. *World Scientific Series on Nonlinear Science Series A*, 16:441–446, 1995.

[186] F. Takens. Detecting strange attractors in turbulence. In D. Rand and L.-S. Young, editors, *Dynamical Systems and Turbulence, Warwick 1980*, pages 366–381, Berlin, Heidelberg, 1981. Springer Berlin Heidelberg.

[187] M. B. Kennel, R. Brown, and H. D. Abarbanel. Determining embedding dimension for phase-space reconstruction using a geometrical construction. *Phys. Rev. A*, 45(6):3403, 1992.

[188] R. Sujith and S. A. Pawar. *Thermoacoustic instability: A complex systems perspective*. Springer Nature, 2021.

[189] V. Godavarthi, S. A. Pawar, V. R. Unni, R. Sujith, N. Marwan, and J. Kurths. Coupled interaction between unsteady flame dynamics and acoustic field in a turbulent combustor. *Chaos*, 28(11), 2018.

[190] S. Dange, S. A. Pawar, K. Manoj, and R. Sujith. Role of buoyancy-driven vortices in inducing different modes of coupled behaviour in candle-flame oscillators. *AIP Advances*, 9(1), 2019.

[191] S. A. Pawar, A. Seshadri, V. R. Unni, and R. Sujith. Thermoacoustic instability as mutual synchronization between the acoustic field of the confinement and turbulent reactive flow. *J Fluid Mech*, 827:664–693, 2017.

[192] M. C. Cross and P. C. Hohenberg. Pattern formation outside of equilibrium. *Reviews of modern physics*, 65(3):851, 1993.

[193] I. Pavithran, V. R. Unni, A. J. Varghese, D. Premraj, R. I. Sujith, C. Vijayan, A. Saha, N. Marwan, and J. Kurths. Universality in spectral condensation. *Scientific Reports*, 10(1):1–8, 2020.

[194] I. Pavithran, V. R. Unni, A. J. Varghese, R. I. Sujith, A. Saha, N. Marwan, and J. Kurths. Universality in the emergence of oscillatory instabilities in turbulent flows. *EPL (Europhysics Letters)*, 129(2):24004, 2020.

[195] J. C. Oefelein and V. Yang. Comprehensive review of liquid-propellant combustion instabilities in F-1 engines. *Journal of Propulsion and Power*, 9(5):657–677, 1993.

[196] T. Lieuwen and V. Yang. *Combustion Instabilities in Gas Turbine Engines: Operational Experience, Fundamental Mechanisms, and Modeling (Progress in Astronautics and Aeronautics)*. 01 2005.

[197] T. Lieuwen and N. Murray. Unsteady combustor physics. *The Journal of the Acoustical Society of America*, 134:1431, 08 2013.

[198] Rayleigh, J.W.S. The Explanation of Certain Acoustical Phenomena. *Nature*, 18(455):319–321, Jul 1878.

[199] K. McManus, T. Poinsot, and S. Candel. A review of active control of combustion instabilities. *Progress in Energy and Combustion Science*, 19(1):1 – 29, 1993.

[200] T. Lieuwen. Experimental investigation of limit-cycle oscillations in an unstable gas turbine combustor. *Journal of Propulsion and Power*, 18, 01 2002.

[201] N. Ananthkrishnan, S. Deo, and F. E. Culick. Reduced-order modeling and dynamics of nonlinear acoustic waves in a combustion chamber. *Combustion science and technology*, 177(2):221–248, 2005.

[202] S. H. Strogatz. *Nonlinear Dynamics and Chaos: With Applications to Physics, Biology, Chemistry and Engineering*. Westview Press, 2000.

[203] H. Torres, T. Lieuwen, C. Johnson, B. Daniel, and B. Zinn. *Experimental investigation of combustion instabilities in a gas turbine combustor simulator*.

[204] J. D. Sterling. Nonlinear analysis and modelling of combustion instabilities in a laboratory combustor. *Combustion Science and Technology*, 89(1-4):167–179, 1993.

[205] S. Candel. Combustion dynamics and control: Progress and challenges. *Proceedings of the Combustion Institute*, 29(1):1 – 28, 2002. Proceedings of the Combustion Institute.

[206] W. Cheung, G. Sims, R. Copplestone, J. Tilston, C. Wilson, S. Stow, and A. Dowling. Measurement and analysis of flame transfer function in a sector combustor under high pressure conditions. pages 187–194, 01 2003.

[207] M. A. Macquisten, M. Whiteman, S. R. Stow, and A. J. Moran. Exploitation of measured flame transfer functions for a two-phase lean fuel injector to predict thermoacoustic modes in full annular combustors. volume Volume 4A: Combustion, Fuels and Emissions of *Turbo Expo: Power for Land, Sea, and Air*, 06 2014.

[208] C. Paschereit, B. Schuermans, W. Polifke, and O. Mattson. Measurement of transfer matrices and source terms of premixed flames. *J. Eng. Gas Turbines Power*, 124:239–247, 04 2002.

[209] B. D. Bellows, M. K. Bobba, J. M. Seitzman, and T. Lieuwen. Nonlinear Flame Transfer Function Characteristics in a Swirl-Stabilized Combustor. *Journal of Engineering for Gas Turbines and Power*, 129(4):954–961, 12 2006.

[210] A. P. Dowling. Nonlinear self-excited oscillations of a ducted flame. *Journal of Fluid Mechanics*, 346:271–290, 1997.

[211] A. P. Dowling. A kinematic model of a ducted flame. *Journal of Fluid Mechanics*, 394:51–72, 1999.

[212] A. F. Gelb and W. E. V. Velde. Multiple-input describing functions and nonlinear system design. pages 137–139, 1968.

[213] A. P. Dowling. Nonlinear self-excited oscillations of a ducted flame. *Journal of Fluid Mechanics*, 346:271–290, 1997.

[214] N. Noiray, D. Durox, T. Schuller, and S. Candel. A unified framework for nonlinear combustion instability analysis based on the flame describing function. *Journal of Fluid Mechanics*, 615:139–167, 2008.

[215] M. P. Juniper and R. I. Sujith. Sensitivity and nonlinearity of thermoacoustic oscillations. *Annual Review of Fluid Mechanics*, 50(1):661–689, 2018.

[216] L. Kabiraj, A. Saurabh, P. Wahi, and R. I. Sujith. Route to chaos for combustion instability in ducted laminar premixed flames. *Chaos (Woodbury, N.Y.)*, 22:023129, 06 2012.

[217] P. Kasthuri, V. R. Unni, and R. I. Sujith. Bursting and mixed mode oscillations during the transition to limit cycle oscillations in a matrix burner. *Chaos (Woodbury, N.Y.)*, 29:043117, 04 2019.

[218] L. Kabiraj and R. I. Sujith. Nonlinear self-excited thermoacoustic oscillations: Intermittency and flame blowout. *Journal of Fluid Mechanics*, 713:376–397, 12 2012.

[219] K. Kashinath, I. Waugh, and M. P. Juniper. Nonlinear self-excited thermoacoustic oscillations of a ducted premixed flame: Bifurcations and routes to chaos. *Journal of Fluid Mechanics*, 761:399–430, 12 2014.

[220] D. Premraj, S. A. Pawar, L. Kabiraj, and R. I. Sujith. Strange nonchaos in self-excited singing flames. *arXiv e-prints*, page arXiv:1910.06916, Oct 2019.

[221] R. Gopal, A. Venkatesan, and M. Lakshmanan. Applicability of 0-1 test for strange nonchaotic attractors. *Chaos: An Interdisciplinary Journal of Nonlinear Science*, 23(2):023123, 2013.

[222] S. Pawar, A. Seshadri, V. R. Unni, and R. I. Sujith. Thermoacoustic instability as mutual synchronization between the acoustic field of the confinement and turbulent reactive flow. *Journal of Fluid Mechanics*, 827:664–693, 09 2017.

[223] S. Mondal, S. Pawar, and R. I. Sujith. Synchronous behaviour of two interacting oscillatory systems undergoing quasiperiodic route to chaos. *Chaos: An Interdisciplinary Journal of Nonlinear Science*, 27:103119, 10 2017.

[224] A. Raaj, J. Venkatramani, and S. Mondal. Synchronization of pitch and plunge motions during intermittency route to aeroelastic flutter. *Chaos: An Interdisciplinary Journal of Nonlinear Science*, 29(4):043129, 2019.

[225] V. Godavarthi, S. A. Pawar, V. R. Unni, R. I. Sujith, N. Marwan, and J. Kurths. Coupled interaction between unsteady flame dynamics and acoustic field in a turbulent combustor. *Chaos: An Interdisciplinary Journal of Nonlinear Science*, 28(11):113111, 2018.

[226] Y. Guan, M. Murugesan, and L. K. B. Li. Strange nonchaotic and chaotic attractors in a self-excited thermoacoustic oscillator subjected to external periodic forcing. *Chaos: An Interdisciplinary Journal of Nonlinear Science*, 28(9):093109, 2018.

[227] G. Gottwald and I. Melbourne. On the implementation of the 0–1 test for chaos. *SIAM Journal on Applied Dynamical Systems*, 8(1):129–145, 2009.

[228] H. Kantz and T. Schreiber. *Nonlinear Time Series Analysis*. Cambridge University Press, 2 edition, 2003.

[229] U. Feudel, S. Kuznetsov, and A. Pikovsky. *Strange Nonchaotic Attractors*. World Scientific, 2006.

[230] G. A. Gottwald and I. Melbourne. On the implementation of the 0–1 test for chaos. *SIAM Journal on Applied Dynamical Systems*, 8(1):129–145, 2009.

[231] G. A. Gottwald and I. Melbourne. A new test for chaos in deterministic systems. *Proceedings of the Royal Society of London. Series A: Mathematical, Physical and Engineering Sciences*, 460(2042):603–611, 2004.

[232] Rayleigh, J.W.S. The Explanation of Certain Acoustical Phenomena. *Nature*, 18(455):319–321, Jul 1878.

[233] X. Wu, M. Wang, P. Moin, and N. Peters. Combustion instability due to the nonlinear interaction between sound and flame. *Journal of Fluid Mechanics*, 497:23–53, 2003.

[234] S. Candel. Combustion dynamics and control: progress and challenges. *Proceedings of the Combustion Institute*, 29(1):1–28, 2002.

[235] A. P. Dowling and S. R. Stow. Acoustic analysis of gas turbine combustors. *Journal of Propulsion and Power*, 19(5):751–764, 2003.

[236] S. Ducruix, D. Durox, and S. Candel. Theoretical and experimental determinations of the transfer function of a laminar premixed flame. *Proceedings of the Combustion Institute*, 28(1):765–773, 2000.

[237] T. Lieuwen. Modeling premixed combustion-acoustic wave interactions: A review. *Journal of Propulsion and Power*, 19(5):765–781, 2003.

[238] W. Cheung, G. Sims, R. Copplestone, J. Tilston, C. Wilson, S. R. Stow, and A. P. Dowling. Measurement and analysis of flame transfer function in a sector combustor under high pressure conditions. In *Turbo Expo: Power for Land, Sea, and Air*, volume 36851, pages 187–194, 2003.

[239] S. R. Stow and A. P. Dowling. Low-order modelling of thermoacoustic limit cycles. In *Turbo Expo: Power for Land, Sea, and Air*, volume 41669, pages 775–786, 2004.

[240] N. Noiray, D. Durox, T. Schuller, and S. Candel. A unified framework for nonlinear combustion instability analysis based on the flame describing function. *Journal of Fluid Mechanics*, 615:139–167, 2008.

[241] X. Han, J. Li, and A. S. Morgans. Prediction of combustion instability limit cycle oscillations by combining flame describing function simulations with a thermoacoustic network model. *Combustion and Flame*, 162(10):3632–3647, 2015.

[242] S. H. Strogatz. *Nonlinear dynamics and chaos with student solutions manual: With applications to physics, biology, chemistry, and engineering*. CRC press, 2018.

[243] W. E. Vander Velde et al. Multiple-input describing functions and nonlinear system design. *McGraw lill*, 1968.

[244] Y. Weng, V. R. Unni, R. I. Sujith, and A. Saha. Synchronization framework for modeling transition to thermoacoustic instability in laminar combustors. *Nonlinear Dynamics*, 100:3295–3306, 2020.

[245] R. Keanini, K. Yu, and J. Daily. Evidence of a strange attractor in ramjet combustion. In *27th Aerospace Sciences Meeting*, page 624, 1989.

[246] C. C. Jahnke and F. E. Culick. Application of dynamical systems theory to nonlinear combustion instabilities. *Journal of Propulsion and Power*, 10(4):508–517, 1994.

[247] L. Kabiraj, R. I. Sujith, and P. Wahi. Bifurcations of Self-Excited Ducted Laminar Premixed Flames. *Journal of Engineering for Gas Turbines and Power*, 134(3), 12 2011. 031502.

[248] Y. Guan, V. Gupta, and L. K. B. Li. Intermittency route to self-excited chaotic thermoacoustic oscillations. *Journal of Fluid Mechanics*, 894:R3, 2020.

[249] S. A. Pawar, A. Seshadri, V. R. Unni, and R. I. Sujith. Thermoacoustic instability as mutual synchronization between the acoustic field of the confinement and turbulent reactive flow. *Journal of Fluid Mechanics*, 827:664, 2017.

[250] S. Mondal, S. Pawar, and R. I. Sujith. Synchronous behaviour of two interacting oscillatory systems undergoing quasiperiodic route to chaos. *Chaos: An Interdisciplinary Journal of Nonlinear Science*, 27(10):103119, 2017.

[251] K. Moon, Y. Guan, L. K. Li, and K. T. Kim. Mutual synchronization of two flame-driven thermoacoustic oscillators: Dissipative and time-delayed coupling effects. *Chaos: An Interdisciplinary Journal of Nonlinear Science*, 30(2):023110, 2020.

[252] D. Premraj, K. Manoj, S. A. Pawar, and R. Sujith. Effect of amplitude and frequency of limit cycle oscillators on their coupled and forced dynamics. *Nonlinear Dynamics*, 103(2):1439–1452, 2021.

[253] V. Godavarthi, P. Kasthuri, S. Mondal, R. I. Sujith, N. Marwan, and J. Kurths. Synchronization transition from chaos to limit cycle oscillations when a locally coupled chaotic oscillator grid is coupled globally to another chaotic oscillator. *Chaos: An Interdisciplinary Journal of Nonlinear Science*, 30(3):033121, 2020.

[254] Y. Guan, K. Moon, K. T. Kim, and L. K. Li. Low-order modeling of the mutual synchronization between two turbulent thermoacoustic oscillators. *Physical Review E*, 104(2):024216, 2021.

[255] H. Gotoda, M. Amano, T. Miyano, T. Ikawa, K. Maki, and S. Tachibana. Characterization of complexities in combustion instability in a lean premixed gas-turbine model combustor. *Chaos: An Interdisciplinary Journal of Nonlinear Science*, 22(4):043128, 2012.

[256] V. Nair, G. Thampi, S. Karuppusamy, S. Gopalan, and R. I. Sujith. Loss of chaos in combustion noise as a precursor of impending combustion instability. *International Journal of Spray and Combustion Dynamics*, 5(4):273–290, 2013.

[257] V. Nair and R. I. Sujith. Multifractality in combustion noise: predicting an impending combustion instability. *Journal of Fluid Mechanics*, 747:635–655, 2014.

[258] V. Nair, G. Thampi, and R. I. Sujith. Intermittency route to thermoacoustic instability in turbulent combustors. *Journal of Fluid Mechanics*, 756:470, 2014.

[259] V. Nair and R. I. Sujith. Identifying homoclinic orbits in the dynamics of intermittent signals through recurrence quantification. *Chaos: An Interdisciplinary Journal of Nonlinear Science*, 23(3):033136, 2013.

[260] V. R. Unni and R. I. Sujith. Multifractal characteristics of combustor dynamics close to lean blowout. *Journal of Fluid Mechanics*, 784:30–50, 2015.

[261] I. Pavithran, V. R. Unni, A. Saha, A. J. Varghese, R. I. Sujith, N. Marwan, and J. Kurths. Predicting the amplitude of thermoacoustic instability using universal scaling behavior. *Journal of Engineering for Gas Turbines and Power*, 143(12), 2021.

[262] V. Godavarthi, S. A. Pawar, V. R. Unni, R. I. Sujith, N. Marwan, and J. Kurths. Coupled interaction between unsteady flame dynamics and acoustic field in a turbulent combustor. *Chaos: An Interdisciplinary Journal of Nonlinear Science*, 28(11):113111, 2018.

[263] T. Kurosaka, S. Masuda, and H. Gotoda. Attenuation of thermoacoustic combustion oscillations in a swirl-stabilized turbulent combustor. *Chaos: An Interdisciplinary Journal of Nonlinear Science*, 31(7):073121, 2021.

[264] N. Peters. *Turbulent combustion*. Cambridge university press, 2000.

[265] J. Tony, E. Gopalakrishnan, E. Sreelekha, and R. I. Sujith. Detecting deterministic nature of pressure measurements from a turbulent combustor. *Physical Review E*, 92(6):062902, 2015.

[266] J. W. Kantelhardt, S. A. Zschiegner, E. Koscielny-Bunde, S. Havlin, A. Bunde, and H. E. Stanley. Multifractal detrended fluctuation analysis of nonstationary time series. *Physica A: Statistical Mechanics and its Applications*, 316(1-4):87–114, 2002.

[267] E. A. F. E. Ihlen. Introduction to multifractal detrended fluctuation analysis in matlab. *Frontiers in Physiology*, 3:141, 2012.

[268] P. F. Panter. Modulation, noise, and spectral analysis. *New York, McGraw-Hill Book Co. P-759*, 1965.

[269] N. Noiray. Linear growth rate estimation from dynamics and statistics of acoustic signal envelope in turbulent combustors. *Journal of Engineering for Gas Turbines and Power*, 139(4), 2017.

[270] P. Clavin, J. Kim, and F. Williams. Turbulence-induced noise effects on high-frequency combustion instabilities. *Combustion Science and Technology*, 96(1-3):61–84, 1994.

[271] X. Zhang, Y. Xu, Q. Liu, J. Kurths, and C. Grebogi. Rate-dependent bifurcation dodging in a thermoacoustic system driven by colored noise. *Nonlinear Dynamics*, 104(3):2733–2743, 2021.

[272] H. Gotoda, Y. Okuno, K. Hayashi, and S. Tachibana. Characterization of degeneration process in combustion instability based on dynamical systems theory. *Physical Review E*, 92(5):052906, 2015.

[273] K. Sreenivasan. Fractals and multifractals in fluid turbulence. *Annual review of fluid mechanics*, 23(1):539–604, 1991.

[274] C. Meneveau and K. Sreenivasan. Simple multifractal cascade model for fully developed turbulence. *Physical Review Letters*, 59(13):1424, 1987.

[275] R. Prasad, C. Meneveau, and K. Sreenivasan. Multifractal nature of the dissipation field of passive scalars in fully turbulent flows. *Physical Review Letters*, 61(1):74, 1988.

[276] M. Raghunathan, N. B. George, V. R. Unni, P. Midhun, K. Reeja, and R. I. Sujith. Multifractal analysis of flame dynamics during transition to thermoacoustic instability in a turbulent combustor. *Journal of Fluid Mechanics*, 888, 2020.

[277] V. R. Unni, C. K. Law, and A. Saha. A cellular automata model for expanding turbulent flames. *Chaos: An Interdisciplinary Journal of Nonlinear Science*, 30(11):113141, 2020.

[278] B. B. Mandelbrot and B. B. Mandelbrot. *The fractal geometry of nature*, volume 1. WH freeman New York, 1982.

[279] B. J. West and W. Deering. Fractal physiology for physicists: Lévy statistics. *Physics Reports*, 246(1-2):1–100, 1994.

[280] D. Harte. *Multifractals: theory and applications*. Chapman and Hall/CRC, 2001.

[281] A. Pandey, J. D. Scheel, and J. Schumacher. Turbulent superstructures in Rayleigh-Bénard convection. *Nature Communications*, 9(1):1–11, 2018.

[282] M. H. Hansen. Aeroelastic instability problems for wind turbines. *Wind Energy: An International Journal for Progress and Applications in Wind Power Conversion Technology*, 10(6):551–577, 2007.

[283] G. A. Flandro and J. Majdalani. Aeroacoustic instability in rockets. *AIAA Journal*, 41(3):485–497, 2003.

[284] J. O'Connor. Understanding the role of flow dynamics in thermoacoustic combustion instability. *Proceedings of the Combustion Institute*, 39(4):4583–4610, 2023.

[285] C.-M. Ho and P. Huerre. Perturbed free shear layers. *Annual review of fluid mechanics*, 16:365–424, 1984.

[286] P. Huerre and P. A. Monkewitz. Absolute and convective instabilities in free shear layers. *Journal of Fluid Mechanics*, 159:151–168, 1985.

[287] P. Huerre and P. A. Monkewitz. Local and global instabilities in spatially developing flows. *Annual review of fluid mechanics*, 22(1):473–537, 1990.

[288] I. Waugh, M. Geuß, and M. Juniper. Triggering, bypass transition and the effect of noise on a linearly stable thermoacoustic system. *Proceedings of the Combustion Institute*, 33(2):2945–2952, 2011.

[289] V. Croquette. Convective pattern dynamics at low prandtl number: Part i. *Contemporary Physics*, 30(2):113–133, 1989.

[290] J. S. Kelso. *Dynamic patterns: The self-organization of brain and behavior*. MIT press, 1995.

[291] C. Sun, S. Jia, C. Barsi, S. Rica, A. Picozzi, and J. W. Fleischer. Observation of the kinetic condensation of classical waves. *Nature Physics*, 8(6):470–474, 2012.

[292] Y. Weng, V. R. Unni, R. Sujith, and A. Saha. Synchronization framework for modeling transition to thermoacoustic instability in laminar combustors. *Nonlinear Dynam*, 100(4):3295–3306, 2020.

[293] Y. Guan, K. Moon, K. T. Kim, and L. K. Li. Synchronization and chimeras in a network of four ring-coupled thermoacoustic oscillators. *Journal of Fluid Mechanics*, 938:A5, 2022.

[294] Z. Yang, B. Yin, Y. Guan, S. Redonnet, and L. K. Li. Chaos via type-ii intermittency in a forced globally unstable jet. *Journal of Fluid Mechanics*, 984:R8, 2024.

[295] N. H. Packard, J. P. Crutchfield, J. D. Farmer, and R. S. Shaw. Geometry from a time series. *Physical review letters*, 45(9):712, 1980.

[296] S. L. Brunton, B. W. Brunton, J. L. Proctor, E. Kaiser, and J. N. Kutz. Chaos as an intermittently forced linear system. *Nature communications*, 8(1):19, 2017.

[297] Y. Guan, V. Gupta, M. Wan, and L. K. Li. Forced synchronization of quasiperiodic oscillations in a thermoacoustic system. *Journal of Fluid Mechanics*, 879:390–421, 2019.

[298] J. F. Gibson, J. Doyne Farmer, M. Casdagli, and S. Eubank. An analytic approach to practical state space reconstruction. *Physica D: Nonlinear Phenomena*, 57(1):1–30, 1992.

[299] H. Ye, R. J. Beamish, S. M. Glaser, S. C. H. Grant, C. hao Hsieh, L. J. Richards, J. T. Schnute, and G. Sugihara. Equation-free mechanistic ecosystem forecasting using empirical dynamic modeling. *Proceedings of the National Academy of Sciences*, 112(13):E1569–E1576, 2015.

[300] P. Frame and A. Towne. Space-time pod and the hankel matrix. *Plos one*, 18(8):e0289637, 2023.

[301] K. P. F.R.S. Liii. on lines and planes of closest fit to systems of points in space. *Philosophical Magazine Series 1*, 2:559–572, 1901.

[302] J.-P. Lachaux, E. Rodriguez, J. Martinerie, and F. J. Varela. Measuring phase synchrony in brain signals. *Human brain mapping*, 8(4):194–208, 1999.